Quantitative methods to elucidate and characterize various aggregation pathways of an IgG1 monoclonal antibody

By

Cavan K. Kalonia

Submitted to the graduate degree program in Pharmaceutical Chemistry and the Graduate Faculty of the University of Kansas in partial fulfillment of the requirements for the degree of Doctor of Philosophy.

_____

Chairperson: David B. Volkin, Ph.D

_____

C. Russel Middaugh, Ph.D

_____

Teruna J. Siahaan, Ph.D

_____

Cory J. Berkland, Ph.D

_____

Eric J. Deeds, Ph.D

Date Defended: January 11, 2016

The Dissertation Committee for Cavan K. Kalonia

certifies that this is the approved version of the following dissertation:

Quantitative methods to elucidate and characterize various aggregation pathways of an IgG1 monoclonal antibody

_____

Chairperson: David B. Volkin, Ph.D

Date approved: January 11, 2016

Abstract

The term protein aggregation is used in pharmaceutical biotechnology literature to describe a collection of different mechanisms that produce non-native, net irreversibly associated protein molecules. The presence of protein aggregates in therapeutic protein drugs is problematic because certain protein aggregates may induce an anti-drug immune response in patients. The work described in this Ph.D. thesis is focused on developing quantitative tools and theoretical models to better characterize and understand protein aggregation as a function of formulation conditions (solution pH, ionic strength, excipients, etc.) and external stresses (e.g., temperature, agitation, light, etc.). The methods developed here are then applied to develop a comprehensive understanding of the aggregation pathways of an IgG1 monoclonal antibody (mAb) under various conditions.

Depending upon the protein itself, the formulation composition and the processing stress, protein aggregation may produce heterogeneous distribution of aggregates with different sizes and morphological properties. This work presents a novel data visualization method to monitor aggregate size, morphology, and concentration as a function of formulation variables such as solution composition, type of external stress, and stress duration. Such data visualization methods can be useful for isolating the effect of single variables. Another complementary method to determine the mass of subvisible particles (large aggregates with an equivalent spherical diameter of ~1-100 μm) was also developed in this work to better relate protein subvisible particle numbers to sample stability. Such calculation methods are often necessary because particle mass is often too low to be measured experimentally. When combined, these two methodologies serve as a set of powerful tools to better analyze protein aggregation because stressed samples with high particle numbers and small masses suggest that aggregate nucleation

(monomers forming aggregate seeds) mechanisms are dominant. On the other hand, stressed protein samples with low particle numbers and large masses may point to aggregate growth mechanisms being dominant.

Application of the data visualization and mass calculation methods to better characterize mAb aggregation led to a striking experimental observation that certain formulations could stabilize the IgG1 mAb against elevated temperatures but destabilize it against mechanical agitation. This, among other observations, led to the hypothesis that elevated temperatures promoted aggregation of this mAb in the bulk solution while mechanical agitation induced mAb particle formation at the air-solution interface.

To better understand how formulation affected temperature induced aggregation of this mAb, kinetic models describing nucleation and growth processes were fit to mAb aggregation data collected at several incubation temperatures (25, 40 and 57 °C). The results of this study suggested that partially unfolded intermediates are an important driver of both aggregate nucleation and growth. Protein-protein interactions, on the other hand, only appeared to affect aggregate growth for this mAb.

To further elucidate how mechanical agitation of mAb solutions could induce protein particle formation, controlled compression-expansion cycles were applied to the air water interface of mAb solutions. In this study, in collaboration with the Dhar laboratory, slow compression-expansion rates were found to induce aggregate formation at the air-solution interface. Faster compression-expansion rates appeared to disrupt the air-solution interface releasing protein particles into the bulk mAb solution. In addition, formulation composition was observed to affect the tendency of this IgG1 mAb to aggregate at the air-solution interface.

Dedicated to:

My father,

Davy Kalonia,

for being my role model and source of inspiration.

Acknowledgements

I would first and foremost like to thank my advisor and mentor Professor David Volkin for providing me the opportunity to develop as a pharmaceutical scientist under his guidance. He generously afforded me the freedom to pursue some of my own research ideas while providing wisdom and support. David always emphasized the importance of clear communication, experimental design and scientific collaboration. I feel confident knowing that he has prepared me well for the future. This thesis would not have been possible without his patience, trust, knowledge and experience.

In addition to David, several other professors have played a significant role in my development as a scientist. Professor Russ Middaugh always encouraged me to ask questions and challenge scientific assertions regardless of who was making them. He has been a valued source of knowledge, encouragement, and critical analysis. My father, Professor Davy Kalonia at the University of Connecticut, has been an amazing source of wisdom and inspiration. He encouraged me to develop a strong knowledge of the fundamental concepts relevant to my research. Professor Prajnaparamita Dhar introduced me to the fields of interfacial science and rheology. These fields will be a main focus of my postdoctoral fellowship at the National Institute of Standards and Technology.

The past and present members of my thesis committee have played an important role in shaping and directing my research. Therefore, I would like to acknowledge Professor David Volkin, Professor Russ Middaugh, Professor Teruna Siahaan, Professor Jennifer Laurence, Professor Cory Berkland and Professor Eric Deeds for serving on my committee and supervising

my research. Their collective experience and knowledge has helped me to develop as a better scientist.

The Macromolecule and Vaccine Stabilization Center (MVSC) contributed to my scientific development in several very meaningful ways. Most notably, the center provided me with the resources and environment to pursue research without analytical or financial constraints. I would like to thank Dr. Sangeeta Joshi, the associate director, for her hard work towards sustaining and improving the center. I value the advice, wisdom, and support that she provided during my graduate education. Dr. Ozan Kumru was another great mentor and source of knowledge. He spent a great deal of time training me in the lab and helping me to improve my manuscripts. I would like to acknowledge Jayant Arora for being a great source of both support and scientific insight. We spent countless hours discussing subjects from colloidal interactions to arginine effects. Additionally, Dr. Ron Toth, Dr. Srivalli Telikepalli (former MVSC member), Dr. Jae Kim, Dr. Newton Wahome (former MVSC member), Vishal Toprani, Indira Prajapati and Ian Gabel are all recognized for their various contributions to my research projects.

The research contained in this thesis was supported by several important collaborations. I would like to acknowledge and thank Professor Prajnaparamita Dhar and her graduate student Saba Ghazvini from the School of Engineering at the University of Kansas for their help in characterizing protein at the air-solution interface. Dr. Roman Mathaes and Dr. Julia Engert from the Ludwig Maximillian University of Munich provided me with non-spherical polystyrene standards to test mathematical models to calculate particle volume from a 2-D image. I would also like to thank Professor Christopher Roberts from the University of Delaware for reviewing some of my thesis work and discussing how to best model protein aggregation.

Last, but definitely not least, I would like to thank my fiancée, Justine Surh, for being incredibly supportive and a major source of motivation. I also want to thank my Maltese, Snowbelle, for helping me to smile after every day.

Table of Contents

Chapter 1: Introduction

Chapter 2: Radar Chart Array Analysis to Visualize Effects of Formulation Variables on IgG1 Particle Formation as Measured by Multiple Analytical Techniques

Chapter 3: Calculating the Mass of Subvisible Protein Particles with Improved Accuracy Using Microflow Imaging Data

Chapter 4: Evaluating the Role of the Air-Solution Interface on the Mechanism of Subvisible Particle Formation Caused by Mechanical Agitation for an IgG1 mAb

Chapter 1: Introduction

1.0. Overview

The presence of protein aggregates in biopharmaceutical drug products raises clinical and regulatory concerns about potentially increasing risk of unwanted anti-drug immunogenicity responses in patients upon administration (1, 2). The work outlined in this thesis is focused on developing quantitative tools and theoretical models to better characterize and understand the protein aggregation process. The models and methods developed are applied to elucidate the effect of pharmaceutically relevant variables (e.g., formulation composition, varying external stress conditions) on the aggregation of an Immunoglobulin-1 (IgG1) monoclonal antibody (mAb).

This review will focus on discussing the role of colloidal interactions, protein structural integrity, and interfacial surfaces on the protein aggregation pathway, with a focus on the formation of larger aggregates called subvisible particles (defined here as 1-100 microns in equivalent circular diameter). In the first section, colloidal stability will be defined in terms of intermolecular interactions and the pharmaceutical relevance of such interactions will be discussed. The second section will cover the role of protein structure, conformational stability, and/or adsorption to the air-solution interface on aggregation rates and mechanisms, especially in the case of monoclonal antibodies (mAbs). In the final section of the introduction, we focus our attention on the formation of a particular subset of protein aggregates, subvisible particles, and review the current understanding published in the biopharmaceutical literature and discuss outstanding challenges (and opportunities) that remain to be addressed.

1.1. Colloidal Interactions

In general, intermolecular interactions govern the kinetics and thermodynamics of non-specific association (aggregation/coalescence) between colloidal particles (3). Any object with linear dimensions between 1 nm and 1 μm can be classified as a colloidal particle (CP). Aggregation refers to a process in which two or more CPs come together while largely retaining their individual physical identity. For example, the total solvent exposed surface area of aggregated CPs is not substantially reduced compared to the same number of non-aggregated CPs (although specific interfaces can become sequestered from the solvent). This more general definition of colloidal aggregation will become important for better understanding and modeling mechanisms of protein aggregation as described below.

1.1.1. Intermolecular Interactions and Colloidal Stability

Colloidal stability, the ability of CPs to resist aggregation/coalescence, is related to the long and short range forces between CPs (4). In a dilute solution, the colloidal stability of CPs can be described by the pairwise potential of mean force. The potential of mean force (W_{22}) describes the net pairwise interaction between two colloidal particles as a function of center-to-center distance(r). Mathematically, W_{22} can be expressed as

$$W_{22}(r) = W_{HS}(r) + W_Z(r) + W_{disp}(r) + W_{osmotic}(r) + W_{dipole}(r) + W_{assoc}(r), \qquad (1.01)$$

where $W_{HS}, W_Z, W_{disp}, W_{osmotic}, W_{dipole}, W_{assoc}$ represent pairwise interaction potentials arising from hard sphere, electrostatic, dispersion, osmotic, dipole and specific interactions, respectively (5, 6).

For a sufficiently dilute solution of uniform colloidal spheres, the interaction potential arising from electrostatic interactions (W_Z) can be modeled as

3

$$W_z(r) = \frac{(ze)^2 \exp[-\kappa(r-d)]}{4\pi r \varepsilon_o \varepsilon_r (1+\frac{1}{2}\kappa d)^2} \quad \text{for } r > d,$$
(1.02)

where z, e, κ, ε_o, and ε_r represent the net charge, elemental charge, inverse Debye length, dielectric permittivity of a vacuum and dielectric constant of water, respectively (7). For this relationship to hold, the center-to-center distance (r) between CPs must remain larger than their diameter (d). From Equation 1.02, it is apparent that increasing the net charge (z) will increase the repulsive electrostatic potential energy between two colloidal particles. The value of W_z can also be increased by reducing the value of the inverse Debye length (κ). For dilute salt solutions (ionic strength <0.1 M), the value of κ can be calculated using

$$\kappa = \sqrt{\frac{2e^2 N_A I}{k_b T \varepsilon_o \varepsilon_r}},$$
(1.03)

where N_A is Avogadro's number, I is ionic strength, k_b is Boltzmann's constant, and T is the absolute temperature (8). This calculation can be simplified to $\kappa = 3.27 * 10^7 \sqrt{I}$ at 20 °C (9). Equation 1.02 demonstrates that increased ionic strength should decrease both the range and strength of repulsive interactions between CPs.

The rate of collisions between colloidal particles (CPs) is directly proportional to the colloidal stability of a system. For uniformly charged spheres that stick upon contact, the rate of colloidal aggregation (k) can be described by the theory of slow coagulation (3). The expression relating the rate of colloidal aggregation (k) to colloidal stability (W_{22}) is

$$k \approx \frac{4\pi(D)}{\int_{2R_S}^{\infty} \exp\{W_{22}(r)/k_b T\}\frac{dr}{r^2}},$$
(1.04)

where D is the diffusion coefficient, R_s is the radius of the CP, and the other terms have been defined in the previous section (3). If there are no interactions between CP in solution ($W_{22} = 0$), but the CP associate (aggregate) upon contact, then Equation 1.04 reduces to its diffusion limited form

$$k \approx 8\pi(D)R_s = \frac{4k_bT}{3\eta}, \tag{1.05}$$

where η is the solution viscosity. The theory of slow coagulation theoretically demonstrates that increasing repulsive intermolecular interactions (quantified by W_{22}) can be an effective way to stabilize thermodynamically unfavorable colloidal dispersions against aggregation.

1.1.2. Pharmaceutical Relevance of Colloidal Stability for Protein Drugs

Protein aggregation, reversible self-association (RSA), and phase separation (PS) are undesirable outcomes that result from unwanted protein associations (10). These physical processes can prohibit the successful pharmaceutical development of therapeutic protein candidates (11). Aggregation, for example, can reduce drug efficacy and/or increase immunogenicity reactions of therapeutic proteins in patients (1, 2, 12-14). RSA, on the other hand, can produce networks of associated species which can affect viscoelastic properties of the solution (5, 15). This increase in the elasticity can manifest as an apparent increase in solution viscosity leading to pharmaceutical challenges in terms of manufacturing (e.g., filterability) and patient delivery (e.g., syringeability) (16-20). Extensive RSA can cause phase separation which can negatively affect homogeneity of formulations containing therapeutic proteins and excipients (21-23) leading to protein instability and solution turbidity.

Increasing the colloidal stability between protein molecules has been shown to be an effective method of disrupting protein aggregation and/or RSA within experimentally measured timescales (4, 5). In other words, an unstable solution phase can become a metastable solution phase provided that the interaction potential between molecules is sufficiently large. In such situations, the implications on the storage stability of biopharmaceutical protein drugs are critical: i.e., the thermodynamics of protein association may not always affect product shelf-life (i.e., the extent of aggregate formation) because the protein solution might not reach equilibrium within that timescale (i.e., the expiry date and storage temperature).

One common approach to design stable formulations of protein drugs is to maximize colloidal stability by increasing/decreasing the solution pH relative to the isoelectric point of a specific protein. Such changes in the solution pH can increase electrostatic repulsions (given by W_Z) between protein molecules by increasing their overall net charge. This behavior is roughly captured by Equation 1.02. It is important to note, however, that Equation 1.02 poorly describes W_Z for most proteins (with the possible exception of extreme pH values for proteins that can maintain their higher-order structure under such conditions) because it assumes spherical geometry with uniformly distributed charge.

In general, proteins tend to have anisotropic charge distributions and can have oppositely charged "patches" that introduce specific interaction contributions (W_{assoc}) to the potential of mean force (24). Theoretically such attractive interactions reduce the potential of mean force (W_{22}) at particular molecular orientations (25). Such clustered "patches" of charged or hydrophobic amino acid residues can be responsible for low apparent solubility and/or reversible self-association of certain proteins (20, 26, 27).

1.1.3. Experimental Parameters as Indicators of Colloidal Stability

The second osmotic virial coefficient (B_2) and diffusion interaction parameter (κ_D) are two commonly used, experimentally obtained values to quantify the interactions between protein molecules under different solution conditions. In the following sections, the measurement of these parameters and their relationship to colloidal stability will be reviewed.

1.1.3.1. The Second Osmotic Virial Coefficient

The osmotic pressure (π), i.e., the pressure required to prevent the diffusion of solute molecules in an ideal solution, can be expressed as

$$\pi = \frac{RTc}{M}, \tag{1.06}$$

where R is the ideal gas constant, T is the absolute temperature, c is the concentration of solute molecules (mass/volume), and M is the number averaged molecular weight. Intermolecular interactions between colloidal particles cause values of π to systematically deviate from the values predicted by Equation 1.06.

The osmotic pressures of non-ideal solutions are fit using a truncated virial expansion of Equation 1.06:

$$\pi = RTc\left(\frac{1}{M} + B_2 c\right) \tag{1.07}$$

where B_2 is the second osmotic virial coefficient. Equation 1.07 is only valid for dilute solution conditions where pairwise molecular interactions dominate (28). In concentrated or crowded solutions, short intermolecular distances can give rise to each solute molecule "feeling" forces from multiple solute molecules (29).

The second osmotic virial coefficient can be related to the pairwise potential of mean force (W_{22}) using statistical mechanics. This virial coefficient can be expressed as

$$B_2 = -\frac{N_A}{2M^2} \int \{exp[-W_{22}(r)/k_B T] - 1\} 4\pi r^2 dr, \tag{1.08}$$

where N_A is Avogadro's number, M is the molecular weight of the solute, and $W_{22}(r)$ is the orientation averaged potential of mean force (6, 28, 30). From this statistical mechanical definition of B_2, it is clear that B_2 is an indirect measure of W_{22} (and therefore of colloidal stability). Furthermore, when there are no intermolecular interactions (e.g., $W_{22} = 0$), the value of B_2 reduces to 0. When the net intermolecular interactions are either repulsive or attractive, the B_2 values are then or negative, respectively.

1.1.3.2. Static Light Scattering and B_2

The Zimm equation can be used to determine an apparent second virial coefficient from static light scattering (SLS) data measured at multiple protein concentrations (31). This relationship is given by

$$\frac{K^* c_2}{R(\theta)} = \frac{1}{M_w} + 2A_2 c_2 , \tag{1.09}$$

where K^* is an optical constant, $R(\theta)$ is the experimentally determined excess Rayleigh ratio, c_2 is the protein concentration (mass/volume), M_w is the weight averaged molecular weight, and A_2 is the apparent second virial coefficient. Although A_2 and B_2 differ in terms of their statistical mechanical definitions (30, 32, 33), SLS remains one of the most common experimental measures of colloidal stability. This is because $A_2 \approx B_2$ at sufficiently dilute protein concentrations (33-35). When measured at higher protein concentrations, A_2

measurements can still be used qualitatively to rank order solutions in terms of colloidal stability because it systematically overestimates repulsive interactions (and systematically underestimates attractive interactions) (33).

Virial coefficients (both A_2 and B_2) can also be reported as normalized values. Normalization is performed to account for the excluded volume of hard spheres to better capture other weak intermolecular interactions such as electrostatic interactions (36, 37). Using statistical mechanics, the excluded volume contribution to B_2 can be expressed as

$$B_2 = \frac{N_A u}{2M^2},$$ (1.10)

where u is the excluded volume, N_A is Avogadro's number and M is the molecular weight (3, 9). One possible normalization approach is described by

$$a_2 = \frac{A_2 - B_2{}^{exc}}{B_2{}^{exc}},$$ (1.11)

where a_2 the normalized second virial coefficient and $B_2{}^{exc}$ is the calculated contribution of excluded volume on the second virial coefficient. Normalizing virial coefficients is a practical approach because contributions from excluded volume can dominate the value of B_2 when other intermolecular interactions are weak making it difficult to determine whether intermolecular interactions are attractive or repulsive (38).

1.1.3.3. The Diffusion Interaction Parameter

In a dilute ideal solution, the diffusion coefficient of non-interacting spherical particles is given by the Stokes-Einstein relationship,

$$D_s = \frac{k_B T}{6\pi\eta R_s},$$ (1.12)

where D_s is the 'self-diffusion coefficient', k_B is the Boltzmann constant, T is the absolute temperature, η is the solution viscosity, and R_s is the radius of the spherical particles (3, 8). In more concentrated environments, particles begin to prevent each other from randomly diffusing (i.e., the frictional coefficient increases). In such a case, the frictional coefficient, denoted by f, can be described by

$$f = f_0(1 + f_1 c + \cdots),\qquad(1.13)$$

where f_0 is the frictional coefficient of particles in an infinitely dilute solution and the other coefficients correct for concentration dependent effects (39).

In protein solutions, intermolecular interactions may also affect diffusion in a concentration dependent manner. The relationship can be described by

$$D_m = D_s(1 + \kappa_D c + \cdots),\qquad(1.14)$$

where D_m is typically referred to as the 'collective' or 'mutual' diffusion coefficient, c is the solute concentration (mass/volume), and κ_D is the diffusion interaction parameter (34, 40).

The diffusion interaction parameter is often used as an experimental value in biopharmaceutical formulation research to quantify protein-protein interactions under different conditions (15, 41-43). Theoretically, the diffusion interaction parameter can be related to the second osmotic virial coefficient (B_2) by the expression

$$\kappa_D = 2B_2 M - f_1 - 2\nu,\qquad(1.15)$$

where M is the molecular weight of the protein, ν is the partial specific volume, and f_1 is given in Equation 1.13 (39, 43). Using Equation 1.08 to substitute for B_2, κ_D can be defined in terms of the potential of mean force (W_{22}) as

$$\kappa_D = -\frac{N_A}{M} \int \{exp[-W_{22}(r)/k_B T] - 1\} 4\pi r^2 dr - f_1 - 2\nu. \qquad (1.16)$$

From Equation 1.16, it is apparent that the diffusion interaction parameter is related to colloidal stability (through W_{22}) provided that f_1 and ν remain constant between different formulation conditions.

1.1.3.4. Dynamic Light Scattering and κ_D

The most common experimental approach to determine κ_D values for various protein solutions is by dynamic light scattering (DLS). The calculated correlation function $g_1(s, t_d)$ for light scattering intensity fluctuations over time can be related to the diffusion coefficient (D_m) of monodisperse spherical particles through the relationship

$$g_1(s, t_d) = exp(-s^2 D_m t_d), \qquad (1.17)$$

where s is the magnitude of the scattering vector and t_d is the time delay used in the calculation of the correlation function (3). Using Equation 1.14, it is possible to determine κ_D by plotting 'mutual' diffusion coefficient (D_m) vs. protein concentration (c). The y-intercept (extrapolation to zero protein concentration) provides D_s and the slope divided by D_s provides the value of κ_D. This approach only holds true for dilute protein concentrations where the plot of D_m vs. c is linear.

1.2. Protein Aggregation

The term "protein aggregation" is generally used by pharmaceutical scientists to describe unwanted, non-native, irreversible processes where conformationally altered protein molecules agglomerate through multiple conformational rearrangement and colloidal association steps (10, 44, 45). Protein aggregation is important to minimize in biotherapeutic products because such aggregates can decrease potency and are theoretically posited to increase patient immunogenicity (1, 2). Experimental evidence supporting such arguments that formation of anti-drug antibodies in patients is related to the presence of protein drug aggregates has been suggested using both in-vitro and animal models (12-14, 46, 47). It is important to note, however, that not all aggregates are necessarily equal in regard to their immunogenic potential in patients and that the determination of such physicochemical and immunological properties remains an active area of research (14).

1.2.1. Protein Aggregation Mechanisms

The thermodynamics and kinetics of protein aggregation have been classically interpreted using the Lumry-Eyring model (4, 48-50). In this model, proteins undergo a reversible conformational change prior forming "irreversible" aggregates. The reversible conformational change is generally expressed as

$$M \xleftrightarrow{K_{unf}} U \tag{1.18}$$

where M represents native monomer, U represents a conformationally altered monomer, and K_{unf} represents the equilibrium constant for this reaction. Two conformationally altered proteins are then able to associate to form a thermodynamically "irreversible" aggregate.

$$2U \xrightarrow{k_{agg}} A_2 \tag{1.19}$$

where k_{agg} is the rate aggregate formation, and A_2 is a dimeric aggregate. Protein aggregation

that follows the Lumry-Eyring model can be conceptualized in a simple reaction coordinate

energy diagram (Figure 1.1).
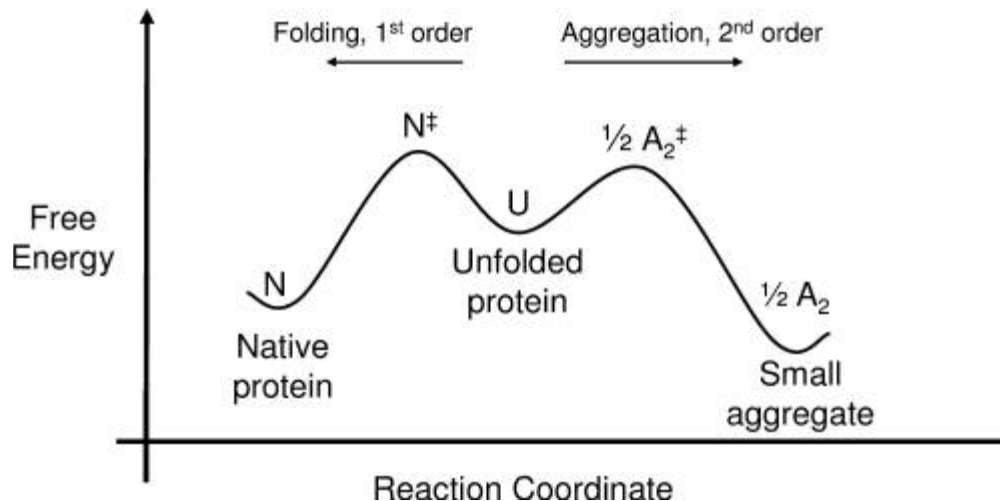
Figure 1.1. Theoretical reaction coordinate energy diagram for the Lumry-Eyring model of

protein aggregation (Ref (51): Reproduced with permission from Elsevier).

Thermodynamic stabilization of protein monomers (against aggregation) can theoretically be

achieved by increasing the free energy of partially unfolded intermediate and/or small aggregate

states (Figure 1.1). Based on these considerations, one common formulation approach to

stabilize proteins against aggregation is by adding inert excipients which are preferentially

excluded from the surface of the protein and thus destabilize the unfolded intermediate (U) (11,

51, 52). The difference in excipient concentration at the surface of the protein and in the bulk

solution can induce an osmotic stress if the local chemical potentials are unbalanced. In such an

event it becomes less favorable for water to hydrate the protein thereby destabilizing structurally

expanded unfolded states which have more surface area than the folded, more compact native

state (53).

Proteins which aggregate according to the Lumry-Eyring model can also be kinetically

stabilized by increasing the activation energy of the unfolding and/or associations steps. In

Figure 1.2, the initial activation energy of the association step is similar to the activation energy

of the unfolding step (solid trace). When the activation energy of the association step is

increased (dotted trace), it becomes the rate limiting step of the protein aggregation process.
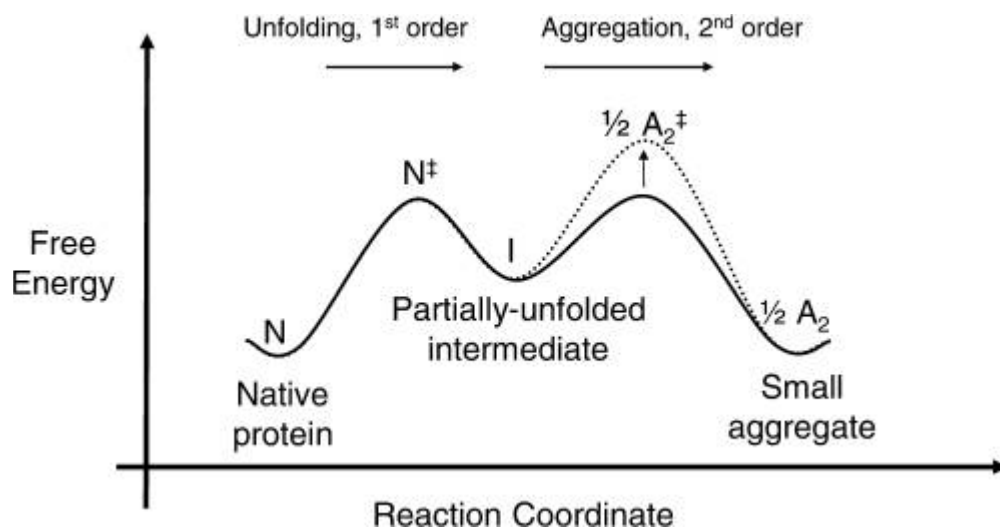
Figure 1.2. Theoretical reaction coordinate energy diagram for the Lumry-Eyring model of

protein aggregation. Dotted trace reflects increased activation energy for the associated

transition state. (Ref (51): Reproduced with permission from Elsevier).

According to the theory of slow coagulation presented in section 1.1.1., the rate of association

should decrease (increased activation energy) when the potential of mean force between

molecules is increased (increased colloidal stability). The arguments outlined above establish a

theoretical basis for why solution conditions resulting in increased colloidal stability appears to

influence protein aggregation in some situations (4, 54, 55), but not in others (56, 57).

Although the Lumry-Eyring model is useful for a basic conceptual understanding of protein aggregation, actual mechanisms are rarely as straightforward. Protein aggregation generally involves simultaneous competing aggregation pathways which can be initiated by conformational changes (44, 58), chemical changes (44), native associations (44, 59, 60), and/or adsorption to interfaces (air-solution, container-solution, etc.) (44, 61-65). Furthermore, protein aggregates may range in size from small, soluble non-native dimers to large, insoluble visible particulates (66). The size of aggregates and extent of aggregation are predominantly a function of protein sequence (67, 68), the solution environment (51, 54, 69), and exposure to different environmental variables (e.g., temperature, light, agitation) (54, 66, 70, 71).

1.2.2. Aggregation of Monoclonal Antibodies

Monoclonal antibodies are becoming increasingly important class of protein drugs used in the ongoing effort to improve human health. As of 2013, there were 35 approved mAb products on the market that have been approved to treat a wide variety of indications (72). Protein aggregation is a formulation development challenge that must be overcome to successfully bring a product candidate mAb to market. Additionally, mAbs are also being developed as antibody-drug-conjugate (ADC) therapies, where cytotoxic small molecules drugs are covalently conjugated to the antibodies using a chemical linker (73, 74). These ADC can be more prone to aggregation because they often have reduced conformational stability and solubility compared to unconjugated antibodies (75, 76).

1.2.2.1. IgG1 mAb Structure and Conformational Stability

IgG1 mAb molecules are "Y shaped" proteins that are composed of two identical "heavy" polypeptide chains and two identical "light" polypeptide chains. The protein is thus a

15

homodimer, has a molecular weight of approximately 150 kDa, and is held together by 4 inter

chain and 12 intra chain disulfide bonds.
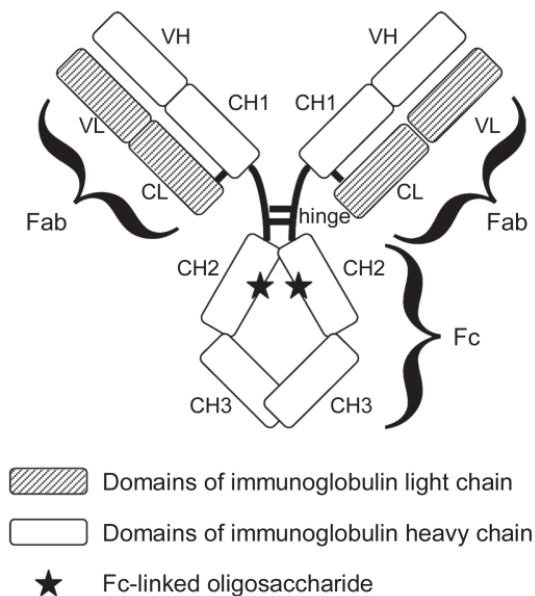
Figure 1.3. Structure of a human IgG1 mAb (Ref (77): Reproduced with permission from Dove

Press).

As shown in Figure 1.3, the molecule is folded such that the heavy chain has one variable

domain (VH) and three constant domains (CH1, CH2, CH3) which are conserved across

different IgG1 mAbs. The light chain has one variable domain (VL) and one constant domain.

The VH, VL, CH1, and CL domains of a heavy chain-light chain pair compose the fragment

antigen binding (Fab) region and the CH2 and CH3 domains of the heavy chains compose the

fragment crystallizable (Fc) region. The CH2 domain also contains two N-linked glycosylation

sites (i.e., one per each heavy chain).

The Lumry-Eyring model of protein aggregation requires individual protein monomers to

partially unfold, and multiple structurally altered monomers associate to form small aggregates.

16

Therefore, conformational stability of mAb molecules is expected to be an important parameter for aggregation pathways which follow a similar process. Thermodynamically, conformational stability reflects the difference in free energy between native and partially unfolded monomer states. At equilibrium, the concentration of partially unfolded monomer (N^*) can be expressed as

$$[N^*] = \frac{[m_{tot}]e^{-\Delta G/RT}}{1+e^{-\Delta G/RT}}, \tag{1.20}$$

where m_{tot} reflects the total monomer concentration, R is the ideal gas constant, T is the absolute temperature, and ΔG reflects the free energy difference between native and partially unfolded states.

The conformational stability of IgG1 mAbs is commonly evaluated using a variety of biophysical techniques monitoring mAb structural integrity as a function of temperature including differential scanning calorimetry (DSC) (78, 79). In general, the irreversible nature of mAb unfolding vs. temperature precludes reversible 2-state thermodynamic analysis of DSC data. If irreversibility is caused by Lumry-Eyring protein aggregation and the unfolding process is much faster than aggregation, such analysis may still provide reasonable results (48, 49). On the other hand, if aggregation is much faster than unfolding, DSC thermograms may reflect unfolding kinetics. Despite the challenges outlined above, DSC remains as an effective tool to evaluate relative differences in the conformational stability of different mAb domains/regions as well as to compare different mAbs, and effect of different solutions conditions (80).

1.2.2.2. Aggregation Mechanisms for mAbs in Bulk Solution

Aggregation of mAb molecules in bulk solution is a multistep process that can involve several competing aggregation pathways (57, 81, 82). As shown in Figure 1.4, mAb aggregation can be initiated by formation of native clusters and/or partial unfolding of specific domain/regions of the mAb.
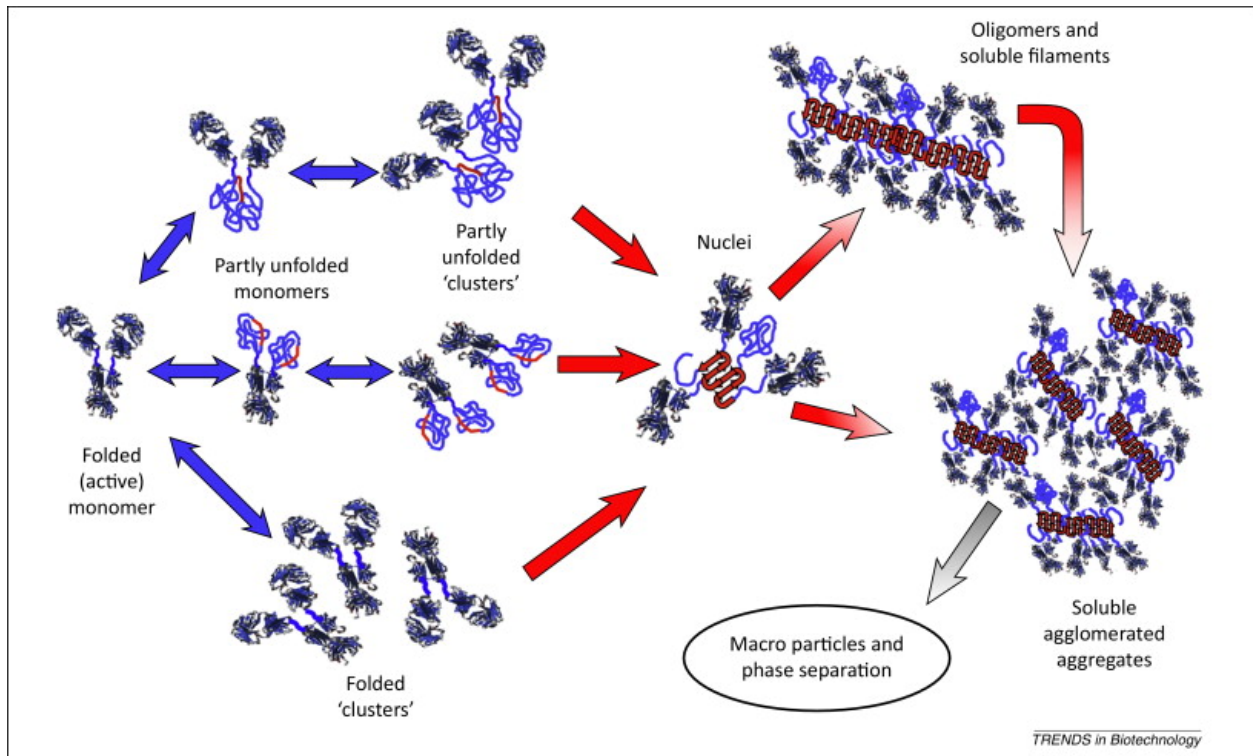
Figure 1.4. Schematic representation of mAb aggregation in bulk solution (Ref (83): Reproduced with permission from Elsevier).

Unlike the Lumry-Eyring model, more advanced models of protein aggregation also consider aggregate growth by monomer addition and/or aggregate-aggregate addition (84-87). Similar to actual experimental results, it tends to be less clear how experimental surrogate parameters for conformational and/or colloidal stability will affect aggregation kinetics for these models (71).

Additionally, excipients may directly interact with the protein which can complicate predictions based on colloidal models or simulations (35, 88-90). Thus, accurately predicting the effect of formulation on the long term aggregation behavior of mAbs remains an outstanding challenge.

1.2.2.3. Adsorption of mAbs to the Air-Solution Interface and Aggregation

In addition to bulk solution pathways, mAb aggregation may also occur at the air-solution interface (62, 91, 92). Since mAbs are amphipathic molecules, they can preferentially accumulate at interfaces which can result in very high local concentrations. In the absence of added detergents, preferential accumulation of mAb molecules may cause the air-solution interface to display high surface pressures values (62, 92). Surface pressure, or the decrease in surface tension of the solution due to monolayer formation, represents a decrease in the free energy of the air-water surface (8). Therefore, surface pressure will increase when amphipathic molecules adsorb to the interface and when they have favorable interactions at the surface. As the air is much more hydrophobic than water, this can result in protein molecules partially unfolding forming structurally altered species leading to subsequent protein aggregation at the air-solution interface (92).

1.3. Subvisible and Submicron Protein Particles

Very large protein aggregates are often called protein particles in the pharmaceutical literature (93, 94). This term is completely unrelated and should not be confused with colloidal particles as reviewed above. Protein particles can be large enough to be seen by eye (~having linear dimensions greater than 100 microns), and are called visible particles, or they can be smaller in size and are not visually detectable and are further classified as submicron or subvisible particles (54, 93, 94). The exact size range of particles described by the terms

"submicron" and "subvisible" tends to vary depending upon the research group as well as the type of instrumentation used. In this review, we define submicron particles as having an equivalent spherical diameter (diameter of a sphere that has equivalent volume to the protein particle) ranging from 0.1-1 µm and subvisible particles as having a 2-dimensional cross sectional area which ranges from 1-100 µm in equivalent circular diameter (diameter of a circle that has equivalent area to a 2-dimensional image of the protein particle). These definitions of particle size accommodate the analytical instruments currently used to detect and quantify the particle size distributions of protein aggregates (95).

Particles with dimensions in the range of 0.1-10 µm are especially important to monitor because of their potential to stimulate immunogenic responses in patients (1, 13, 14). This is because such particles are the optimal size to be internalized by antigen presenting cells and they may also display repeating arrays antigenic motifs (96). Determining the particular physicochemical properties which make protein particles more or less immunogenic remains an outstanding challenge of the field (97).

The purpose of this review is to propose a methodology of how to efficiently interpret and communicate certain types of protein particle data. This review is geared towards protein pharmaceutical researchers that are already proficient with protein particle analysis. The focus will be directed towards communicating and interpreting measurements of protein particle "size" and "density" across different instruments.

1.3.1. Protein Particle Density

The density of an IgG1 mAb has been approximated at 1.41 g/ml, and the density of proteins can be empirically described as a function of molecular weight (98). Folzer et al.

recently measured the density of protein particles with "sizes" ranging from approximately 0.2 to

5 μm in diameter using resonant mass measurement and found that the density of the protein

particles ranged from 1.28 and 1.33 g/ml (99). The results published by Folzer et al., highlight

the critical importance of how protein particle boundaries are defined to determine particle

density.
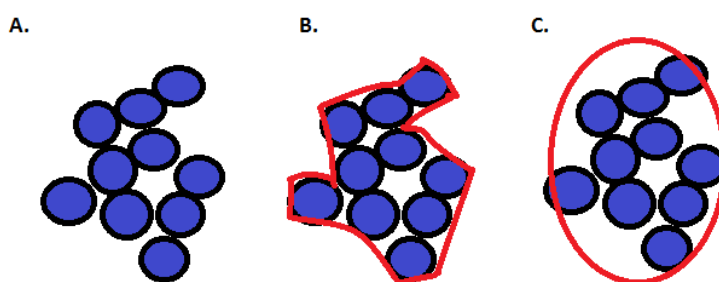
Figure 1.5. Various ways to define protein particle boundaries for density determination

In Figure 1.5, all three schematics of protein particles are identical, but the density determined

for each of the particles will be dramatically different due to differences in the defined

boundaries. The boundary of a protein particle is defined by the "measuring stick" or probe used

to determine such a boundary. For example, a probe the size of a solvent molecule would likely

determine a particle boundary resembling Figure 1.5A. The density values reported by Folzer et

al., reflects such a boundary. On the other hand, instruments using a larger probe such as visible

light may detect boundaries which more closely resemble Figure 1.5B or C.

Let's hypothetically consider a situation in which the solvent has a density of 1.00 g/ml

and the protein has a density of 1.35 g/ml. Further, let's assume that the boundary of Figure

1.5A is so precise that the particle is defined as 100 % protein. Next let's assume that the

boundary defining Figure 1.5B contains 30% solvent and 70 % protein and that the boundary

defining Figure 1.5C contains 70% solvent and 30% protein. The density values for the protein

particle will be either 1.35, 1.24, and 1.11 g/ml, depending on the assumption used. Technically,

none of these density values are wrong depending upon how particle boundary size is defined.

On the other hand, use of different density values for protein particles will dramatically affect

results when provided as an input for other calculations such as particle weight.   Therefore, we

emphasize caution in interpreting published density values for protein particles and suggest that

extra consideration be given to the size of the probe used to establish particle boundary

conditions.

1.3.2. Protein Particle Size

The accurate detection and sizing of protein particles is limited by current analytical

instrumentation (100, 101). Some of the properties which make protein particles challenging to

size/count is their heterogeneous morphology, low contrast (particle refractive index similar to

solution refractive index), wide size distribution, unclear density value (see previous section),

and high number (54, 102-104). These properties necessitate that multiple analytical instruments

be used to characterize the full size range protein particles. The basic operation and principles of

current particle counting instruments have been extensively reviewed elsewhere (95, 105-111).

Each instrument uses a different measurement principle to detect and quantify the size of protein

particles based on certain properties of protein particles. In this section, we demonstrate how

particle properties such as shape and density can affect the quantification of protein particle size

for commonly used instruments.

1.3.2.1 Nanoparticle Tracking Analysis (NTA)

In nanoparticle tracking analysis, particles suspended in solution are illuminated by a laser and light scattered from particles within the field of view is focused and tracked. The motion of the scattering centers is captured using a CCD camera and related to a hydrodynamic radius through a 2-dimensional Stokes-Einstein equation

$$\overline{(x,y)^2} = \frac{2k_BT}{3r_h\pi\eta},$$
(1.21)

where $\overline{(x,y)^2}$ is the mean-squared speed of the particle, T is the temperature, k_B is the Boltzmann constant, r_h is the hydrodynamic radius, and η is the solution viscosity (105).

Stokes law, given by $f = 3r_h\pi\eta$ in this example, describes the frictional coefficient (f) of spherical particles. As protein particles are non-spherical, particle size is reported as a 'fictitious' sphere with the same diffusion coefficient as the actual particle. This approach provides valid values but can make comparisons of size between different instruments challenging. For example, an ellipsoidal particle will have a different frictional coefficient than a spherical particle. The effect of asymmetry on the frictional coefficient ($\frac{f}{f^*}$) of a prolate ellipsoid of revolution $\left(\frac{b}{a} < 1\right)$ can be calculated using

$$\frac{f}{f^*} = \frac{\left[1-\left(\frac{b}{a}\right)^2\right]^{1/2}}{\left(\frac{b}{a}\right)^{2/3} ln\left(\frac{1+[1-(b/a)^2]^{1/2}}{b/a}\right)},$$
(1.22)

where b is the minor axis and a is the major axis of the prolate ellipsoid of revolution (3). Therefore, a prolate ellipsoid of revolution with an aspect ratio of 0.1, 0.2, or 0.3 will have a calculated friction ratio 1.54, 1.25, or 1.14 times larger than that of an equivalent volume sphere,

respectively. Therefore, a fiber-like protein aggregate with an equivalent spherical diameter of 200 nm and an aspect ratio of 0.1, 0.2, or 0.3 could be measured by NTA as having a hydrodynamic diameter of ~309, 250, or 227 nm, respectively.

1.3.2.2. Resonant Mass Measurement (RMM)

Resonant mass measurement is performed by passing a solution through a microfluidic channel in a cantilever resonator (106, 112). When a particle in solution travels through the resonator, there is a drop in the frequency which can result in the detection of a particle depending upon the assigned limit of detection. The buoyant mass of a particle travelling through the resonator is calculated using

$$M_B = \Delta f * S \tag{1.23}$$

where Δf describes the frequency drop and S is a parameter accounting for the sensitivity of the resonator. The mass of the particle is then calculated using entered values of particle density (p_p) and solution density (p_s) by the equation

$$M = \frac{M_B}{1 - \frac{p_s}{p_p}}. \tag{1.24}$$

The particle diameter (D) is then calculated using

$$D = \sqrt[3]{\frac{6M}{\pi * p_p}}. \tag{1.25}$$

Equations 1.23, 1.24, and 1.25 were obtained from the Archimedes user manual. It is important to note that the buoyant mass is an experimentally measured parameter determined by RMM and that reported size values are calculated using a user entered value for protein particle density. For example, using the protein density values calculated from Figure 1.5, user inputted density

values of 1.35, 1.24, or 1.11 g/ml, describing the same protein particle, could result in a particle size detection of 379, 438, or 558 nm equivalent spherical diameter for a buoyant mass of 10^{-11} g, respectively.

1.3.2.3. Flow Microscopy

In flow microscopy experiments, sample is passed through a flow cell using a peristaltic/syringe pump and illuminated using an LED. Snapshots of the flow cell are captured using a high definition digital camera and particles are identified using image analysis. Particle size is determined using proprietary image analysis algorithms based upon the 2-dimensional particle image. Particle morphology will clearly affect the sizing results because a sphere will be homogenously sized regardless of particle rotation whereas an ellipse or fiber-like particle will be randomly oriented and display a much wider distribution of particle sizes.

The assumption that an equivalent circular diameter of protein particles can be equated to an equivalent spherical diameter has been demonstrated to be very inaccurate (104). The volume of protein particles with spherical or prolate ellipsoid of revolution morphology can be calculated using equivalent circular diameter or area based diameter and circularity by

$$V = \frac{\pi}{6} * d^3 * \sqrt{1.70763 - 1.70864 * (1 - C)^{0.45} - 0.70638 * C} \quad ,$$

where V is the volume, d is the diameter, and C is the circularity (104).

1.3.3. Size and Density Conclusions

In this section, we have theoretically demonstrated how both measurement principles and user based assumptions about particle properties can affect the determination of protein particle size and/or density. A spherical protein particle with a 2.6 μm diameter that is 30%

protein/volume when measured by flow microscopy could be measured at 1.76 μm diameter by resonant mass measurement if the density is assumed to be 100% protein/volume. If the particle morphology is similar to a prolate ellipsoid of revolution, the resonant mass measurement would not be affected, but equivalent circular diameter could increase to 4.95 μm if the largest cross section possessing an arbitrary circularity of 0.2 was imaged.

Therefore, it is quite plausible that the same protein particle could be measured at 1.76 μm equivalent spherical diameter by resonant mass measurement and 4.95 μm equivalent circular diameter by flow microscopy. This theoretical example demonstrates why perfect correlation between different analytical instruments, such as resonant mass measurement and flow microscopy, should not be expected in most cases. Certain examples do exist in the literature where resonant mass measurement and flow microscopy measurements show good correlations between particle size values from the two instruments, but this should not be the case when protein particle morphologies become heterogeneous and thus notably deviate from a spherical shape (109).

Resonant mass measurement and nanoparticle tracking analysis data are also theoretically expected to show poor correlation in protein particle size depending on the assumptions used. As illustrated in the previous sections, particle morphology has a large effect on the particle size output of nanoparticle tracking analysis, but will not affect the size output from resonant mass measurements. In contrast, during resonant mass measurements, solvent molecules are the probe of particle boundaries whereas in nanoparticle tracking analysis, the boundaries are defined in terms of the external dimensions of the particle. Therefore, the different sizes presented by the two techniques inherently assume different particle densities.

Chapter 2: Radar Chart Array Analysis to Visualize Effects of Formulation Variables on IgG1 Particle Formation as Measured by Multiple Analytical Techniques

2.1. Introduction

Improving our basic understanding of protein aggregate and particle formation pathways during the manufacturing and storage of therapeutic protein candidates is of increasing interest to protein formulation scientists and regulators alike. This interest primarily arises from the potential ability of these particles to induce an unwanted, humoral immune response resulting in the production of anti-drug antibodies that reduce the efficacy of the administered therapy (1). Previous investigators have shown that particles generated by different stresses vary in average size, shape, concentration, transparency, and chemical modifications, however, the physicochemical properties of a protein particle that potentially elicit an immune response remain elusive (66, 113, 114). The immunogenic potential of particle subpopulations is difficult to study because separating and isolating species from a highly heterogeneous population, while maintaining their structural integrity, is technically challenging (114). Additionally, sample handling must be minimized during particle characterization to preserve the integrity of the measured particle populations (101, 115). Because of these challenges, formulation development strategies for protein therapeutics are increasingly focused on reducing the number of submicron and subvisible particle degradants that form during manufacturing and storage (97). The formation of proteinaceous particles can be reduced by increasing both the conformational and colloidal stability of the protein in solution as well as by decreasing the number of nucleating species (4). Non-native aggregation is often initiated by partially unfolded or misfolded monomers that associate if there is a favorable change in the free energy of the system (44, 68, 81, 87, 116, 117). Certain anions (e.g., chloride) preferentially accumulate on the surface of proteins and can influence both the conformational and colloidal stability of proteins in solution (90, 118).

Multiple analytical instruments are needed to measure the full range of aggregates and particles in solution because no single technique is currently capable of providing an accurate, quantitative description of the entire aggregation profile of a protein solution (95, 100, 108, 119). Subvisible and submicron are terms used to classify particles that are 1-100 µm and 0.1 to <1 µm, respectively (97). Microflow digital imaging (MFI) has become a popular technique to characterize subvisible particles and has been used to study particle formation in monoclonal antibody formulations (120-123). MFI captures digital images of particles from a solution passing through a flow cell and uses algorithms to measure a wide variety of parameters including, but not limited to, equivalent circular diameter, concentration, counts, circularity, aspect ratio, and intensity. These parameters provide an advantage over other subvisible particle counting techniques because morphological filters can be used to discriminate between proteinaceous particles and non-proteinaceous silicone oil droplets or air bubbles (124). A limitation of MFI, however, is the possible undercounting of particles that have a refractive index similar to that of the solvent (110). This experimental artifact can be partially corrected through the proper use of the optimize illumination function (107, 110, 121). A complementary technology is the Archimedes Particle Metrology System, which uses the principle of resonant mass measurement (RMM) to measure the buoyant mass of particles from a solution passing through a suspended microchannel resonator (SMR). SMR technology complements MFI because it detects submicron particles from 200 nm to subvisible particles <5 µm in equivalent spherical diameter. and has also been used to study submicron particle as low as $\sim 10^4$ particles/ml in a monoclonal antibody formulation (106). Both RMM and MFI provide high resolution particle size and concentration data by counting individual particles, but the large quantity of data produced makes it challenging to compare trends across multiple data sets.

Data visualization methods have been developed to aid in the formulation development of protein-based therapeutic drugs and vaccines. The empirical phase diagram (EPD) visualizes macromolecule structural changes as a shift in colors as a function of environmental stresses (e.g., temperature and solution pH). The EPD visually summarizes biophysical stability data from multiple techniques that have been reduced in dimensionality through principle components analysis (125, 126). There are several reports in which the EPD has been used to visualize changes in mAb conformational stability and dynamics (127-129). Additional data visualization methods have more recently been developed to examine protein stability data including radar chart analysis and comparative signature diagrams (130, 131). Radar charts have the advantage of displaying multidimensional data without truncating the data or using statistical methods such as principle components analysis.

In this report, we apply radar chart array analysis to compare multiple, large data sets from different analytical methods to determine the effect of formulation variables on the nature of IgG1 mAb aggregates and particles generated through different stress conditions. First, we assess the effect of solution pH and NaCl on the concentration, size, and formation kinetics of subvisible particles, measured by MFI, created due to stirring and shaking of the solutions. Additionally, we use radar chart array analysis to evaluate how IgG1 mAb particle morphology, i.e., the particle's aspect ratio (a measure of elongation) and intensity (a measure of particle transparency), are affected by formulation conditions. Lastly, we examine the potential of radar chart analysis to visualize formation of the particles and aggregates across the entire size profile, from subvisible and submicron sized particles to small soluble aggregates as measured by MFI, RMM, and size exclusion high performance liquid chromatography (SE-HPLC), respectively.

2.2. Experimental Procedures

2.2.1. Materials and Sample Preparation

An IgG1 mAb (pI ~9) was supplied by Janssen Biotech Inc. (Horsham, PA) at ~40 mg/ml. Working mAb solutions were made by diluting the stock solution into 20 mM citrate-phosphate buffer to a final protein concentration of 1.0 mg/ml. Individual samples were prepared at pH 4.0, 6.0 and 8.0 and NaCl concentrations of 0, 0.15, and 1.0 M. These working solutions (3 mL) were prepared in glass vials (37.7 x 16.75 mm) from Schott (Lebanon, PA) and capped with 20 mm lyophilization vial stoppers (West Pharmaceutical Services, Exton, PA).

2.2.2. Generation of Aggregates

Heat stressed aggregates were generated by incubating samples at 65°C for 10, 120, and 240 min. Stirred stressed aggregates were generated by stirring samples with teflon coated micro spinbars (Fisher) for 10, 120, and 240 min. The stirring speed was adjusted to setting 5 on a Pierce Reacti-Therm III from Thermo Scientific (West Palm Beach, FL). Shaking stressed protein aggregates were made by shaking samples side to side at 300 RPM for 10, 120, and 240 min using a HS 260 shaker from IKA Works Inc. (Wilmington, NC).

2.2.3. Differential Scanning Calorimetry

DSC was performed with 1.0 mg/ml protein samples, prior to stress exposure, using a high throughput capillary VP-DSC (MicroCal, Piscataway, NJ). Thermograms were obtained by scanning from 10° to 90°C at a rate of 60°C/hr as described previously (132). T_m values were obtained by iteratively fitting the thermogram to a non-2-state model for unfolding. T_o values were obtained by determining the point at which a specific interpolated tangent line intersects the horizontal axis.

2.2.4. Extrinsic Fluorescence Spectroscopy

IgG1 mAb samples were diluted to 0.1 mg/ml in their corresponding buffers and a 20 molar excess of 1-anilinonaphthalene-8-sulfonate (ANS, Sigma) was added.   The fluorescence emission was measured using a QM-40 spectrofluorometer from Photon Technology International (Birmingham, NJ) as described previously (120).

2.2.5. Size Exclusion High Performance Liquid Chromatography

A Tosoh Bioscience TSKgel G3000SWx1 stainless steel column (San Francisco, CA) along with the corresponding guard column (TSKgel SWxl guard column) operated at 30°C was used in all experiments. A Shimadzu Prominence UFLC HPLC system (Kyoto, Japan) connected to a diode array detector was used.   Twenty five µL of each sample were injected into a column that was equilibrated with at least 10 column volumes of 20 mM sodium phosphate buffer (pH 6.8). The flow rate was 0.7 mL/min and the measurement time was 30 minutes. LC Solution software was used for data analysis and peak integration. Total area loss, percent monomer loss of the solution, and percent soluble aggregates of the solution were reported as described previously (133).

2.2.6. Resonant Mass Measurement

An Archimedes Particle Metrology System (Affinity Biosensors, Santa Barbara, CA) was used to quantify submicron and small subvisible particles from 0.275 to 1.85 µm. A Hi-Q micro sensor, calibrated using 1.03 µm polystyrene beads (Affinity Biosensors), was used for all measurements. Reference solutions of 1:20 D_2O:H_2O or pure H_2O were used depending upon the solution density of the sample being measured. Prior to daily measurements, the accuracy of the Hi-Q microsensor was tested using the 1.03 µm bead standard. Before each measurement,

the sensor and the micro tubing, was rinsed with 2% PCC-54 detergent, by applying high

pressure on the sample and reference vials to clean the bypass channels. In addition to the high

pressure applied to the sample and reference vials, low pressure was also applied to the sample

waste vial to induce a flow to rinse the sensor with 2% PCC-54 detergent. This process was

applied until a clean frequency trace was achieved. The sensor was then loaded with particle

free water and two "sneeze" operations were performed. The sample was loaded for 30 s, and a

stop trigger of 200 particles or 30 min measurement time was used. The limit of detection was

empirically determined (0.035 Hz) and used throughout the study. The density value for the

mAb was estimated at 1.41g/ml based on protein molecular weight (98).

2.2.7. Microflow Digital Imaging

A DPA-4200 flow microscope (Protein Simple, Santa Clara, CA) was used to capture

digital images of subvisible particles with ECD from 2-70 µm. Before each measurement, the

flow cell was primed in the following manner: particle free water was flushed through the flow

cell at the maximum flow rate until the flow cell was observed to be particle free for at least 30 s.

The optimize illumination function was then used to ensure the proper level of solvent

illumination. Samples underwent the minimal required amount of sample handling prior to

measurement and were degassed by exposure to a vacuum chamber for 10 min. To prevent

clogging of the flow cell, samples containing approximately 50 or more visible particles

(observed through visual inspection) were set aside for 30 min to allow the largest particles to

settle. Samples with particle concentrations over the limit of quantitation (900,000

counts/ml)(121) were diluted and the results were corrected for the dilution factor (samples

subjected to 240 min of stirring were diluted 1:3, and samples stressed for $\geq$120 min by heat

were diluted 1:10). Particle statistics were generated using MFI View Analysis Suite (MVAS)

version 1.3 (Protein Simple, Santa Clara, CA). Each MFI measurement was separated into five subpopulations based upon particle equivalent circular diameter (ECD); $2 \leq x < 5$, $5 \leq x < 10$, $10 \leq x < 25$, $25 \leq x < 50$, and $50 \leq x < 70$ μm.

2.2.8. Radar Chart Construction

Radar charts were generated using software developed in our laboratory (MiddaughSuite) as described previously (131). This report is, however, the first time that radar chart arrays have been applied to protein aggregation and particle formation data sets from MFI, RMM and SEC. To create the MFI particle number and size range radar charts, particle concentration data, obtained from analysis using MVAS 1.3 software described above, were pre-processed by calculating the mean, standard deviation, and mean minus standard deviation (m-SD) for the five particle size populations listed in the previous section. The mean and m-SD values were then uploaded to MiddaughSuite software. The radar charts were set to a log scale and each axis was defined to have a minimum of 10 and a maximum of 1,000,000 particles. Radar charts were generated for both the mean and the m-SD values and then precisely superimposed using pixel alignment in Adobe Photoshop CS6 (Adobe Systems, San Jose, CA). The purpose of superimposing the two radar charts was to include an indication of error for n=3 replicate experiments because particle measurements are often highly variable. The m-SD was chosen because m+SD would be hard to visualize because positive error bars appear smaller on a log scale.

Particle morphology radar charts were created using the average mean intensity and aspect ratio values for each of the five particle size populations (obtained through the filter manager tool in MVAS 1.3). These data were pre-processed and the mean and m+SD values were uploaded to MiddaughSuite. The axes of this radar chart were set to an inverted linear

scale and each axis was defined to have a minimum value of 0.35 and a maximum of 0.85. Axes with an insufficient number of particles (empirically determined to be < 25 counted) were highlighted with a light red background color. The mean and the m+SD particle morphology radar charts were also superimposed using Adobe Photoshop to indicate variability between n=3 measurements. The m+SD were used to maintain the consistency of radar chart interpretation because the morphology radar chart arrays use an inverted linear axis.

To create the "multiple instruments" radar chart, data from SEC, RMM, and MFI were preprocessed to obtain the mean and the m-SD for each condition. The data were then uploaded to MiddaughSuite and each axis was highlighted with a background color according its scale. Axes 1 and 2, corresponding to total area loss and monomer loss were set to an inverted linear scale between 0 and 100%. Axis 3, the soluble aggregate content, was set to a linear scale between 0 and 25%. Axes 4-6, representing submicron and small subvisible particle concentrations between 0.275 and 1.85 µm were set to a log scale with a minimum value of 10^4 and a maximum value of 10^9 particles (approximate limit of quantitation for the Archimedes). Lastly, axes 7-9, representing subvisible particles from 2-70 µm, were set to a log scale with a minimum of 100 and a maximum of 10^7 particles. The mean and m-SD radar charts were generated and superimposed using Adobe Photoshop to indicate error between the n=3 measurements.

2.3. Results

2.3.1. Conformational Stability of IgG1 mAb vs. Solution pH and NaCl Concentration

Prior to examining the effect of formulation variables on particle formation, differential scanning calorimetry was used to study the relative conformational stability of the IgG1 mAb in

solutions with varying pH and NaCl concentrations. For example, at pH 4, three thermal melting events were observed at 56.1, 70.7, and 72.6 °C, which are referred to as T_{m1}, T_{m2}, and T_{m3}, respectively (See Figure 2.1). The effects of solution pH and NaCl on the observed Tm values for the mAb are summarized in Table 2.1. mAb solutions at pH 4 had the lowest thermal melting value (and onset temperatures) while the addition of 0.15 and 1 M NaCl to the pH 4 solutions caused further reductions in melting and onset temperatures (Table 2.1). At pH 6 and 8 with no NaCl, only T_{m2} and T_{m3} were reproducibly detected. Addition of 0.15 M NaCl appeared to slightly lower the melting and onset temperatures, and the addition of 1 M NaCl resulted in detection of T_{m1}. In addition, fluorescence measurements using ANS as an extrinsic probe were used to determine if solution pH and NaCl concentration influenced ANS interactions with hydrophobic surfaces within the mAb (or potentially between mAbs). No major differences in ANS fluorescence intensity were observed in the various mAb solutions described above, suggesting no major alterations of mAb's overall tertiary structure (or self-associations) across the pH range of 4-8 and NaCl concentrations of 0 to 1M (data not shown).

2.3.2. Radar Chart Analysis of Effects of Solution pH, NaCl Concentration, and Stress on IgG1 mAb Particle Formation as Measured by MFI

2.3.2.1. Particle Number and Size

Radar Charts were initially constructed to visualize various data sets of subvisible particle formation as obtained by MFI with an IgG1 mAb under different formulation conditions. First, we present some generic MFI data to demonstrate how to interpret a radar chart. Figure 2.2A shows a commonly used graphical representation of generic MFI data from one experimental condition, i.e., a histogram of particle concentration (log scale) as function of particle size

(grouped together in different size bins). Figure 2.2B shows the same MFI data in the form of a radar chart. The numbered axes of the radar chart correspond to the same numbered size bins on the histogram (e.g., number one refers to particle size bin 2-5 microns in both Figures 2.2A and 2.2B). The axes of radar charts are linearly connected so that the data set can be visualized as a polygon. In addition, particle concentration is displayed in this radar chart using concentric rings positioned from the center to the edge of the circle. For example, as shown in Figure 2.2C, each ring shows a ten-fold increase in particle concentration.

In Figure 2.3, radar chart analysis was used to elucidate the effect of varying solution pH, NaCl concentration, and stress conditions on the kinetics of subvisible particle formation (number and the size distribution as measured by MFI) for an IgG1 mAb. Prior to stress, a low number (i.e., 100 to 3,000) subvisible particles were detected in the various protein samples with samples at pH 4 having fewer particles than pH 6 regardless of the NaCl concentration. After 10 min of shaking stress (left panel of Figure 2.3), more than 5,000 particles (2-25 µm) had formed at pH 4 with no added NaCl. Samples containing 0.15 M NaCl formed particles at a similar rate, however, ~50 particles from 25-50 µm had also formed. Samples in the presence of 1 M NaCl had the highest particle concentration in size range of 2-25 µm as well as >100 particles/ml from 25-50 µm. The concentration of subvisible particles, generated through shaking, increased over the time of shaking with increased values noted at 120 min. Particle formation decelerated after 120 min (no longer forming at a logarithmic rate) with the 240 min shaking sample showing similar particle concentrations and size distributions across the pH and NaCl conditions examined. The presence of 1 M NaCl had a more pronounced effect on IgG1 mAb samples at pH 4 that were shaken for more than 2 h since an average of 10,000 particles from 25-50 µm and 1,000 particles from 50-70 µm had formed. In general, the presence of 1 M NaCl at pH 4, 6 or 8

caused larger subvisible particles to form when these protein samples were shaken (Figure 2.3, left panel and Figure 2.11).

The IgG1 mAb samples stirred at pH 4 resulted in an entirely different subvisible particle distribution, compared to shaking under the same solution conditions (Figure 2.3, middle panel). For example, particles generated from stirring stress tended to be primarily 2-25 µm in size. After 10 min of stirring, samples with 0 M NaCl had the least amount of subvisible particles, 0.15 M NaCl had ~10^4 particles/ml, and 1 M NaCl had >10^4 particles. The concentration of small particles noticeably increased between 2 and 4 h of stirring. After 4 h of stirring, for IgG1 mAb samples with 1 M NaCl, the most subvisible particles (> 10^6 particles/ml from 2-5 µm) were formed, while samples with 0.15 M NaCl formed ~300,000 particles/ml from 2-5 µm and samples with no NaCl formed <50,000 particles/ml (Figure 2.3, middle panel).

Samples stirred at pH 6 (Figure 2.3, right panel) and pH 8 (Figure 2.10, right panel) exhibited very different behaviors in terms of the effect of NaCl on particle formation compared to pH 4. Samples at pH 6 in the absence of NaCl had the highest concentration of subvisible particles over 4 h (particle concentrations >10^6 particles/ml). In contrast, the presence 1 M NaCl greatly reduced the concentration of subvisible particles to ~50,000/ml. At pH 8, the presence of either 0.15 or 1M NaCl greatly reduced the concentration of subvisible particles for IgG1 mAb samples stirred for 2 and 4 h (Figure 2.10).

2.3.2.2. Particle Morphology

Representative particle images captured by MFI demonstrate formation of low, medium, and high aspect ratio/intensity valued protein particles in the IgG1 mAb solutions depending on the formulation and stress (Figure 2.4). Model ellipses that correspond to particle aspect ratio values are also presented as a simplified method to visualize particle elongation (i.e., aspect

ratio). We present some MFI data to demonstrate how to interpret a radar chart for particle morphology. In Figure 2.5A, these data are presented in a manner similar to other reports with published MFI morphological data (134). Figure 2.5A shows scatter plots (for the first 3,000 particles counted by MFI, n=1) of particle size vs. a morphological parameter, one plot for particle aspect ratio and the other for particle intensity. Morphological data from additional particles cannot be added to these scatter plots since resolution would be lost as additional data points merge into one continuous color (not shown). In contrast, the aspect ratio and intensity values from the same experiment, but this time using the entire, complete data set (>200,000 particles/ml, n =3) are presented as an radar chart (Figure 2.5B) showing particle size vs. morphological parameter, using a scale for the morphology parameters as shown in Figure 2.5C (i.e., aspect ratio or intensity/1000). Regions shaded in light red in the radar charts in Figure 2.5B denote insufficient particles were present in the samples (empirically defined as < 25 particles as measured by MFI) to effectively compare the effect NaCl, pH, and stress on particle morphology. One reason this was done was so that the few subvisible particles present at time zero did not affect the radar chart analysis of the morphological properties of particles formed from stress and solution conditions over time.

 As an example, radar chart analysis of MFI particle morphological parameters are shown for IgG1 mAb samples stressed for 4 h with varying pH, NaCl, and stress conditions (Figure 2.6). As shown on the left panel, the average particle aspect ratio and intensity values did not change with NaCl concentration when samples were stirred for 4 h at pH 4. As another example, the addition of 1 M NaCl had a profound effect on particle morphology when the samples were subjected to 4 h of shaking at pH 4 and 8. When the mAb samples were shaken at pH 4 (Figure 2.6, middle panel), the presence 1 M NaCl caused the average aspect ratio of all size ranges in

39

the particle distribution to decrease (i.e., the particle elongation increases). Particles larger than 25 µm had an average aspect ratio of less than 0.35 (refer to the ellipse models presented in Figure 2.4). Additionally, the intensity of subvisible particles in the size range from 25-50 µm increased (became more transparent) in the presence of 1M NaCl when compared with both 0 M and 0.15 M NaCl. Samples of IgG1 mAb subjected to the same shaking stress but now at pH 8 (Figure 2.6, right panel), in the presence of 0 M and 0.15M NaCl, contained particles with low intensity (i.e., were not transparent) and had a high aspect ratio (i.e., more globular). Interestingly, the presence of 1 M NaCl at pH 8 caused a large increase in average intensity and a substantial reduction in the aspect ratios for particles in the size range over 10-50 µm.

2.3.3. Radar Charts Incorporating Protein Aggregate and Particle Formation Data from Multiple Analytical Techniques

Radar chart array analysis was then applied to data sets from multiple analytical techniques, which measured mAb particle and aggregate formulation over different size ranges. The 'multiple-instruments radar chart' was designed to provide mechanistic information relating to the potential interrelationships of soluble aggregate and particle formation. A representative example of the multiple-instrument radar chart is shown in Figure 2.7. For SEC, Figure 2.7A shows a typical bar graph of SEC data for pH 6, 0.15 M NaCl mAb samples that were heated for 2 h. SEC data includes the percent of monomer loss, total area loss (insoluble aggregate), and soluble aggregates formed. The same SEC data are also presented in radar chart form in Figure 2.7D (axes 1-2 in the purple region, and axis 3 in the blue region, of the radar chart in Figure 2.7D correspond to bars 1-3 in Figure 2.7A). Similarly for submicron particle data, Figure 2.7B is a histogram of RMM data, for the same heat stressed mAb sample, providing particle size data in the submicron range up to particles with an equivalent spherical radius of 1.85 µm. The

numbered size bins (4-6) in Figure 2.7B correspond to axes 4-6 in the yellow region of the corresponding radar chart (Figure 2.7D). Finally, Figure 2.7C is a histogram of MFI particle size and concentration data for the heat stressed mAb sample for subvisible particles of size 2-70 µm. The particle size bins numbered 7-9 in the histogram (Figure 2.7C) correspond to axes 7-9 in the red region of the radar chart (Figure 2.7D). A more detailed key showing the labeling of the multiple-instruments radar chart in terms of scale and measurements, are provided in Figure 2.7E.

An example of utilizing a 'multiple-instruments radar chart' to characterize aggregate and particle formation is shown for heat and stirring stresses of an IgG1 mAb solution at pH 6 with varying NaCl concentrations (left panel of Figure 2.8). At time zero (at all NaCl concentrations), the mAb samples contained <1,000 subvisible particles, >10^5 submicron particles, and were > 99% monomer with <0.2% soluble aggregates. After 10 min of heat stress at 65˚C, mAb samples without NaCl showed a ~10% total peak area loss as well as a ~10% monomer loss as measured by SEC, and after 2 h of heating, the samples had 35% total area loss, 40% monomer loss, and 5% soluble aggregates. In addition, an extremely high concentration of subvisible particles (>10^7 particles/ml) was now observed. Interestingly, under the same conditions, the addition of 0.15 M NaCl increased soluble aggregate levels to 10% based on SEC with a concomitant decrease the total concentration of subvisible particles by ~10 fold as measured by MFI (and did not substantially change the amount of submicron particles). The presence of 1 M NaCl in the mAb solution greatly increased the levels of soluble aggregates to ~22% while the measured total area loss was approximately 20%, and the monomer loss was ~50% as measured by SEC. In addition, the 1M NaCl containing mAb samples showed a greatly reduced concentration of subvisible particles (<50,000 measured by MFI), as well as a reduced

41

concentration of submicron particles by more than 10x as measured by RMM. After 4 h of heating, there was essentially complete aggregation and the monomer species was virtually undetectable by SEC (left panel of Figure 2.8).

The effect of stirring stress on IgG1 mAb solutions is shown in the right panel of Figure 2.8. In contrast to heating stress, no major changes in soluble aggregate levels were observed (with less than 10% total area loss) by SEC in the majority of samples subjected to stirring stress. This result in itself suggests different aggregation mechanisms are dominant for heating and stirring stresses. After 10 min of stirring, $\sim 10^6$ submicron sized particles formed in all of the samples, and the mAb sample without NaCl had formed the most subvisible particles ranging from 2-10 µm. After 2 and 4 h of stirring, the particle number and size distributions in the mAb samples with 0 and 0.15 M NaCl appeared similar, but samples with 1 M NaCl showed a ~ 50 fold reduction of subvisible particles along with a substantially increased number of submicron particles ($\sim 10^8$ particles/ml) as shown in right panel of Figure 2.8. Finally, mAb samples were shaken at pH 4 and displayed a third dominant aggregation mechanism (See Supplemental Figure 2.3): no soluble aggregates were detected by SEC, while submicron particle formation leveled off after 10 min as measured by Archimedes. The subvisible sized particle populations continued increasing over time as measured by MFI. Under these conditions, the addition of 1 M NaCl caused increased formation of subvisible particles in the 25-70 µm size range.

2.4. Discussion

2.4.1. Utility of Radar Chart Arrays to Summarize and Analyze Protein Aggregate and Particle Formation Data Sets from Different Instruments

The ability of radar charts to better visualize protein aggregation and particle formation results for an IgG1 mAb in different formulations, as measured by multiple analytical

instruments, was investigated in this report. We first used radar charts to examine the effect of pH, NaCl concentration, stress type, and length of stress exposure on the size and concentration of the sub-visible particles that were formed as measured by MFI. A broader application of radar charts incorporating data from multiple analytical instruments was also investigated. Radar chart array analysis was shown to be an effective tool for characterizing the effect of individual formulation composition and environmental stress variables on protein growth kinetics and particle size distribution. For example, the pH dependent behavior of particle formation (number and size distribution) as a function of NaCl and stress (i.e., shaking and stirring) was established for an IgG1 mAb. It is important to emphasize the utility of radar charts to plot large data sets of MFI data and compare trends across formulation conditions. For example, the MFI data in Figure 2.3 represents 36 different experimental conditions (e.g., time, stress type, formulation composition) performed in triplicate resulting in a total of 108 experiments. If histograms were to be used as shown in Figure 2.2A, many plots would be needed to summarize the results and compare the effects of time, stress type, and formulation composition on mAb particle formation (including particle concentration and size distribution) in solution. This makes analysis of trends in particle size, concentration and morphology more challenging. Using radar chart array analysis, however, all of these results are displayed, and trends across the 36 conditions are summarized in a single figure (Figure 2.3). The radar chart arrays in this paper were modified to display statistical variability, in the form of standard deviation, of the various data sets. The ability to display the error makes these modified radar-chart arrays a more powerful tool to study protein aggregation than other data visualization methods such as the empirical phase diagrams.

Another application of radar chart analysis is to analyze the effect of formulation composition and environmental stresses on the average morphology of any subvisible particle

size range. MFI is capable of measuring multiple particle morphological parameters such as intensity, feret diameter, aspect ratio, circularity, etc. Unfortunately, these data remain largely underutilized, especially in comparison to particle concentration and size range measurements. This is largely due to unfamiliarity with the parameters and the difficulty in presenting such large data sets in an organized fashion. Several reports have recently presented MFI morphological data using scatter plots and line graphs (107, 134). These graphical methods are effective at presenting a few morphological data sets, however, scatter plots and line graphs become cumbersome to interpret as the quantity of particles and/or the number of data sets (e.g., formulation conditions and time points) increase. Other data visualization methods used for displaying biophysical stability data, such as the EPD, would also be inefficient at visualizing particle morphological trends because principle components analysis would complicate data interpretation since all of morphological parameters correlate to varying degrees. Radar chart analysis was successful in elucidating the effect of buffer composition (pH and NaCl concentration) and stress conditions (shaking and stirring) on the morphology of sub-visible particles (aspect ratio and intensity) formed from IgG1 mAb solutions (Figure 2.6). Radar-chart-array analysis could be applied in the future to elucidate the effect of similar formulation variables on other particle parameters including particle mass, reversibility (defined as a decrease in particle size when diluted to stable pH conditions) (66), density, and surface irregularity (fractal dimension); such work is currently underway in our laboratory.

Radar chart arrays were also used to visualize results from multiple analytical instruments that monitor protein aggregate and particle formation across size ranges from mAb soluble aggregates (SEC), to submicron particles (RMM), and to subvisible particles (MFI). To our knowledge, there are no other data visualization methods available which provide such a

comprehensive picture of protein aggregation data across a wide size range. Although radar

chart array analysis provided qualitative comparisons of the effect of formulation variables on

mAb aggregation, one limitation of this approach is that SEC, RMM and MFI use different

measurement methods and provide information on different numerical scales. For example,

RMM measures a frequency shift caused by a particle passing through a resonator and calculates

the buoyant mass based on the shift and the sensitivity of the resonator. An equivalent spherical

diameter is calculated using the appropriate density value and the buoyant mass (refer to Burg et

al. for further explanation) (112). MFI measures the 2-dimensional area of particles and, through

image analysis, calculates the equivalent circular diameter (ECD) of the particle (135). ECD is

not directly related to spherical diameter, and assuming such may result in an overestimation of

particle volume. Another current analytical limitation is the presence of a detection gap because

of the inability to accurately measure very small particles from ~50 nm to 275 nm. The

application of nanoparticle tracking analysis (NTA) or dynamic light scattering would be of

interest in future studies to address a more complete size range. NTA requires, however, a high

minimum concentration of submicron particles ($>10^6$/ml) and would likely be applied to select

samples. Nonetheless, radar chart analysis was an effective tool for probing complex protein

growth mechanisms monitored by multiple analytical techniques (Figures 2.7 and 2.8) and, in

general, offered the ability to more easily follow trends in the data, thus providing some

additional insights as described below.

2.4.2. Effects of pH, NaCl and Stress on IgG1 mAb Aggregate and Particle Formation and Morphology

The focus of this work was on the development of radar chart data visualization

techniques for MFI data on subvisible particle formation (concentration, size range, and

45

morphology) due to different stresses (shaking, stirring, heating). Once developed, however, interesting trends in the physical instability of this model IgG1 mAb were readily apparent. For example, the pH and stress-type dependence of the NaCl effect on the aggregation profile of this IgG1 mAb was striking. During stirring and heating, but not shaking, the presence of 1 M NaCl promoted particle growth at pH 4, but inhibited particle growth at pH 6 and 8 (refer to Figure 2.8 and Figure 2.9). In contrast, during shaking stress, the presence of NaCl increased the size and concentration of particles present at pH 4, 6, and 8 (refer to Figure 2.11). This pH-dependent effect of NaCl on the physical instability of this IgG1 mAb was also observed by separate turbidity measurements (data not shown).

Studies have previously shown that anion binding promotes aggregation of an IgG mAb through charge shielding and by affecting conformational stability (118). In this work, the presence of NaCl (> 0.15 M) destabilized the conformational of the mAb at pH 4 as measured by DSC in terms of Tonset and three Tm values (See Table 2.1). NaCl had a much less pronounced effect on Tonset and Tm values for this IgG1 mAb at pH 6 and 8 (See Table 2.1). The observed decrease in conformational stability provides some insight into why the presence of NaCl destabilizes this mAb at pH 4 during stress. It does not, however, necessarily address the observed effects of NaCl on slowing particle formation during heating or stirring at pH 6 or 8. Kroetsch et al. showed that soluble aggregates of alpha-chymotrypsinogen A rapidly coalesce to form insoluble aggregates once a critical salt concentration was reached (116). Our results suggest that addition of 1 M NaCl at pH 6 actually increases the colloidal stability of this mAb since the particles formed during heating and stirring are on average much smaller in size compared to samples with or without 0.15 M NaCl. Accurate particle mass (or density) measurements/calculations, however, are needed in addition to particle size, to more

conclusively understand the effect of NaCl on the colloidal stability of this mAb. Such measurements and calculations, combined with radar chart array analysis of the results, are currently underway.

Another interesting observation is that the average morphology of subvisible particles formed varies with solution pH and NaCl for shaking, but not stirring stress. The particles created through stirring appear to form by a similar mechanism since they have similar size and morphology across the pH values and NaCl concentrations as measured by MFI. In contrast, subvisible particles created through shaking have a diverse morphology (i.e., aspect ratio, intensity) that is sensitive to both the pH and NaCl concentration. This result suggests that in addition to changing the conformational and colloidal stability of a mAb, the formulation composition can also influence the mechanism of aggregation under certain stresses, potentially by influencing the nature of the interactions between the associating molecules.

Since formation of aggregates and particulates during long-term and accelerated stability studies affect formulation composition choices and decisions about storage conditions and shelf life, radar chart analysis could assist in these important comparisons during formulation development. Stability data are also a key part of comparability assessments, since changes in mAb drug product formulations or primary containers may affect the protein's physical stability (136, 137). Radar charts could potentially assist in these types of comparisons as well. For example, the effect of formulation impurities from prefilled syringes such as silicon oil (64, 138) and tungsten (139) on protein particle formation could be evaluated by radar chart analysis using appropriate filters of the MFI data to separate silicon oil droplets from protein particles (109, 124).

2.5. Conclusions

When conducting high throughput screening studies of protein instability under various formulation conditions, data visualization methods are crucial to quickly and effectively interpret large quantities of physical stability data (140, 141). Radar chart analysis offers an exciting opportunity to improve the throughput and effectiveness of analyzing protein aggregation and particle formation studies. Additionally, there is potential to combine particle size/concentration data sets with more accurate measurements/approximations of protein particle volume, partial specific volume, and mass (in development). Radar chart analysis should also provide an improved understanding of the effect of formulation composition and environmental stresses on the mechanisms of mAb particle formation.

2.6. Figures and Tables

2.6.1 Tables

pH	[NaCl] (M)	T_{onset}	SD	T_{m1}	SD	T_{m2}	SD	T_{m3}	SD
4.0	0.00	48.1	0.9	56.1	0.1	70.7	0.2	72.6	0.1
	0.15	46.6	0.4	53.0	0.1	68.3	0.1	70.8	0.1
	1.00	44.7	0.2	50.9	0.1	67.3	0.1	68.5	0.1
6.0	0.00	66.1	0.1	ND	ND	73.0	<0.1	83.4	0.3
	0.15	65.4	0.2	ND	ND	72.7	<0.1	83.3	<0.1
	1.00	62.6	0.5	69.9	0.1	74.3	<0.1	84.1	<0.1
8.0	0.00	66.0	0.2	ND	ND	72.3	<0.1	82.7	<0.1
	0.15	66.0	0.3	ND	ND	71.9	<0.1	82.7	<0.1
	1.00	64.5	0.1	71.0	<0.1	73.6	<0.1	83.6	<0.1

Table 2.1. Effect of Solution pH and NaCl Concentration on Thermal Onset (Tonset) and Thermal Melting (Tm1, Tm2, Tm3) Temperatures of an IgG1 mAb as Determined by DSC. See methods section for experimental details. SD is standard deviation from triplicate (n=3) experiments. ND indicates a Tm value could not be determined from experimental data.

2.6.2. Figures
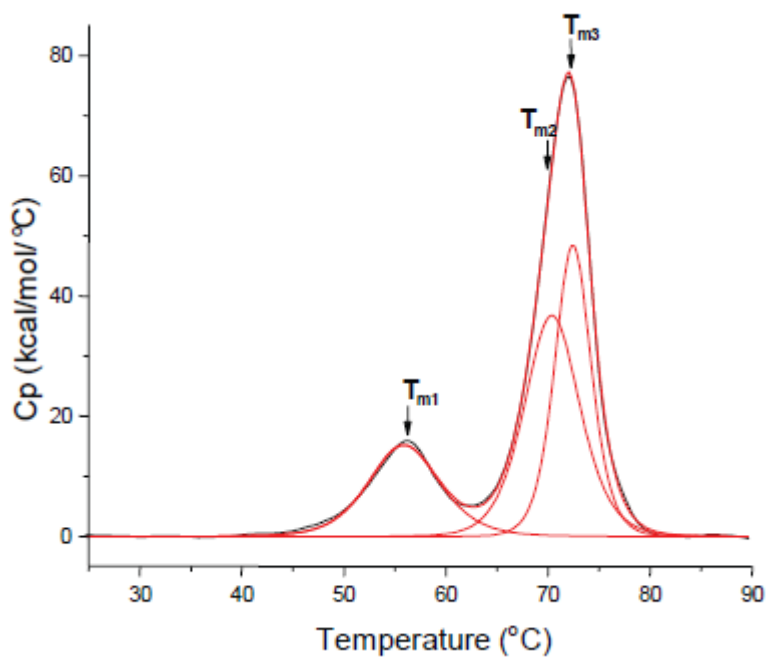
Figure 2.1. Representative DSC Thermogram of the IgG1 mAb. DSC thermogram of the IgG1 mAb (1 mg/mL) in a 20 mM citrate phosphate buffer, pH 4.0, no NaCl. T_{m1}, T_{m2}, and T_m are labeled and correspond to the deconvoluted peaks as indicated in figure.
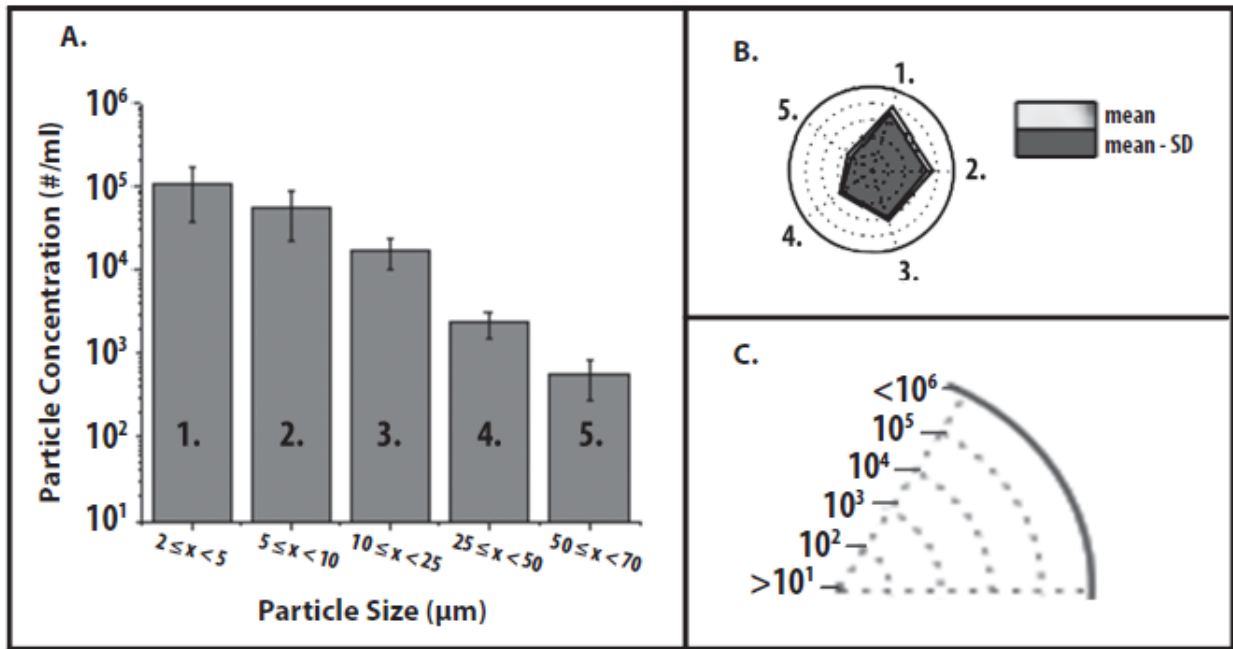
Figure 2.2. Application of Radar Chart array Analysis to Evaluate Subvisible Particle Concentration and Size Distribution Data Measured by MFI. (a) Histogram (n=3) of representative MFI data plotting particle concentration versus particle size (ECD) for an IgG1 mAb solution containing 20 mM citrate-phosphate buffer at pH 8.0 and 1 M NaCl subjected to 4 hours of shaking. (b) Radar chart presentation of the same data set; each axis is labeled with a number and is the same size range as the corresponding numbered bin size in the histogram. The values along the each axis of the radar chart are connected linearly to visualize the data set as a polygon. The perimeter of the outermost polygon represents the mean particle concentration, the polygon labeled 'mean - SD' represents the mean minus one standard deviation, and the distance between the perimeters of the two polygons (along an axis) is equivalent to the lower error bar in the equivalent bin of the histogram (one standard deviation). (c) Illustration of the particle concentration (log scale) used in the radar charts in this work to display experimentally measured micro flow imaging subvisible particle concentrations.
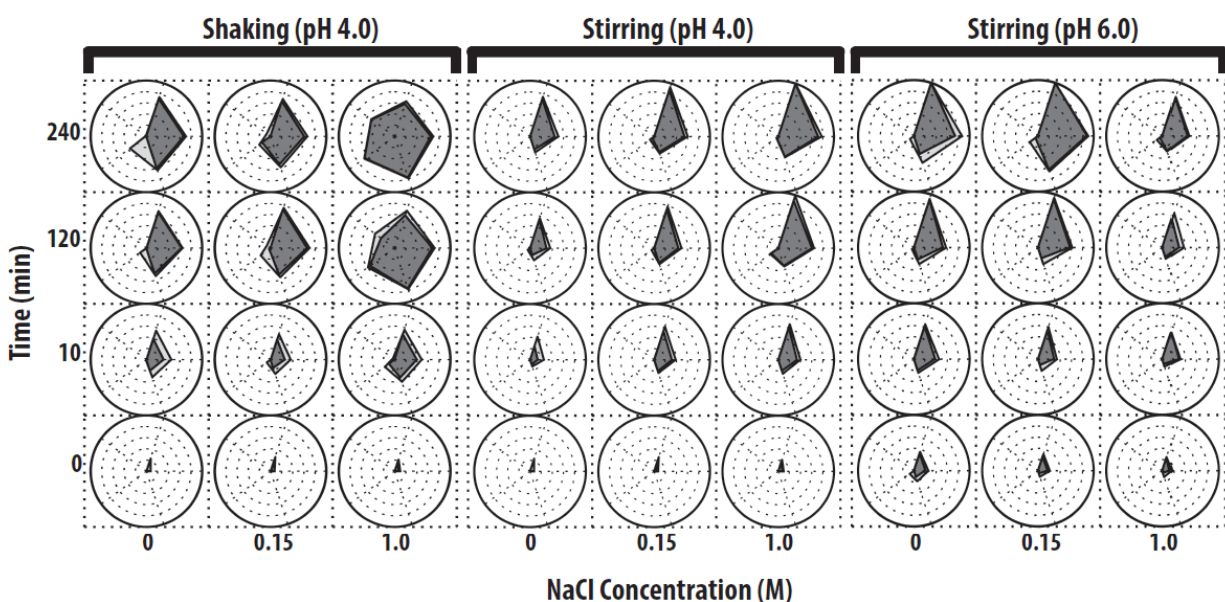
Figure 2.3. Radar Chart Array Analysis of Subvisible Particle Concentration and Size Data for IgG1 mAb Solutions as Measured by MFI. IgG1 mAb solutions of varying pH values and NaCl concentrations were exposed to different stress types over time as indicated in the figure (n=3), and resulting formation of subvisible particles was measured by MFI. The Y-axis represents the amount of time the formulations were stressed (in minutes), the X-axis represents NaCl concentrations, and each radar chart panel (left, middle, right) signifies a change in stress or pH. See methods for experimental details of MFI measurements from each of these accelerated stress studies. Refer to Figure 2.2 for an explanation of MFI particle concentration and size range scales/units shown in individual radar charts.
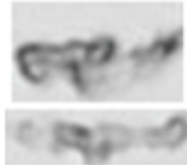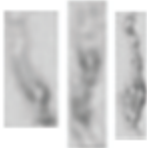
Aspect Ratio			Mean Intensity	
Values	Model Ellipse	IgG1 Particles	Values (ILU)	IgG1 Particles
0.85			800	
0.65			650	
0.35			400	

Figure 2.4. Representative Morphological Parameters for Protein Particles from MFI Analysis. Examples of three different aspect ratios and intensity values (low, moderate, and high) are presented along with corresponding IgG1 mAb particle images from MFI. Model ellipses of equivalent aspect ratios are presented to help visualize changes in particle shape. For ease of presentation, protein particle images from MFI are not presented to scale.
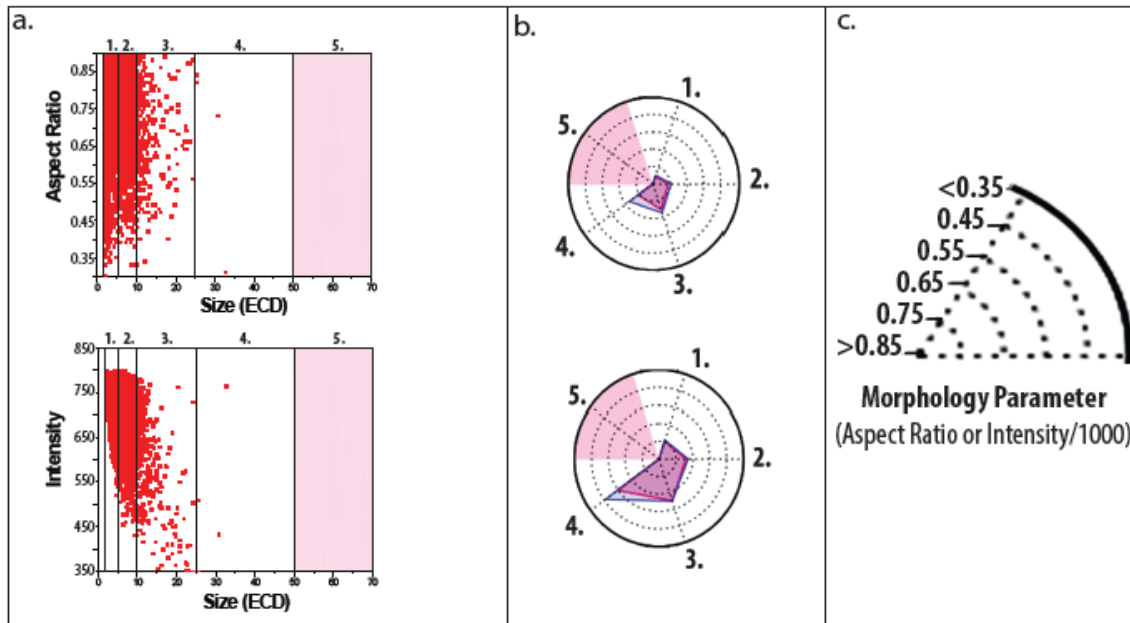
Figure 2.5. Application of Radar Chart Array Analysis to Evaluate Subvisible Protein Particle Morphological Parameters Measured by MFI. (a) Scatter plots of a subset of particle data displaying aspect ratio (top) and intensity (bottom) versus ECD (first 3,000 from n=1 experiments) counted within an IgG1 mAb solution containing 20 mM citrate buffer at pH 8.0 and 0.15 M NaCl subjected to 4 h of shaking. Light red shading represents size bins with insufficient data as defined by x < 25 particles counted. (b) Radar chart presentations of the same experiment showing average aspect ratio (top) or intensity/1000 (bottom) per size range except with the complete data set (~200,000 particles, n=3); each numerical axis in the radar chart is an equivalent size range to the corresponding numbered region in the scatter plots. The perimeter of the outermost polygon displays the mean morphology parameter, the perimeter of the polygon labeled 'mean + SD' displays the mean plus one standard deviation, and the distance between the perimeters of the two polygons (along an axis) is one standard deviation. (c) Illustration of the scale/units used in the radar charts to display experimentally measured (MFI) subvisible particle aspect ratio and intensity/1000 values.

54
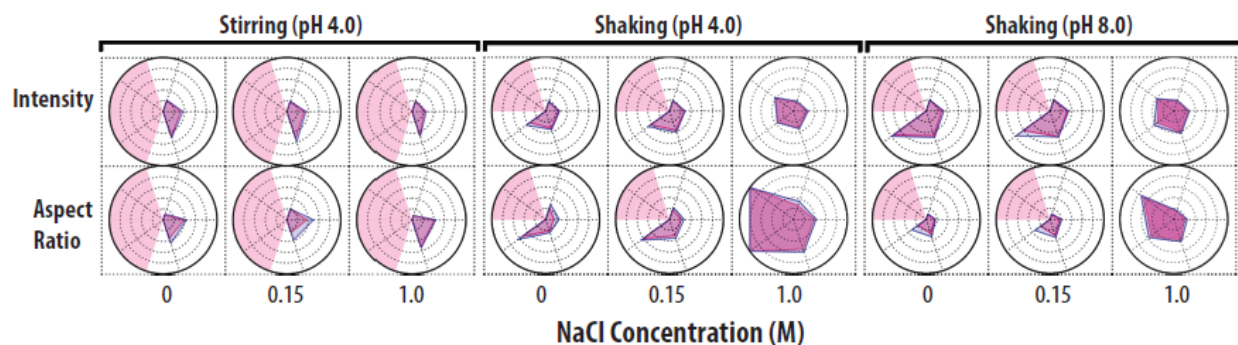
Figure 2.6. Radar Chart Array Analysis of Protein Particle Morphological Parameters Versus Particle Size for IgG1 mAb Solutions as Measured by MFI. IgG1 mAb solutions (at indicated pH and salt concentration) were stressed to generate protein particles (n=3), and solutions were analyzed by MFI. See methods section for experimental details of each accelerated stress study. The Y-axis is labeled with the morphological parameter, the X-axis represents the NaCl concentration, and each panel (left, middle, right) represents a change in stress or pH as indicated. The numerical value/units of each concentric circle in this radar chart is shown in Figure 2.5C. Light red shading represents a region where an insufficient number of particles (x < 25) were counted. Refer to Figure 2.5 for an explanation of particle morphological parameters shown in individual radar charts.
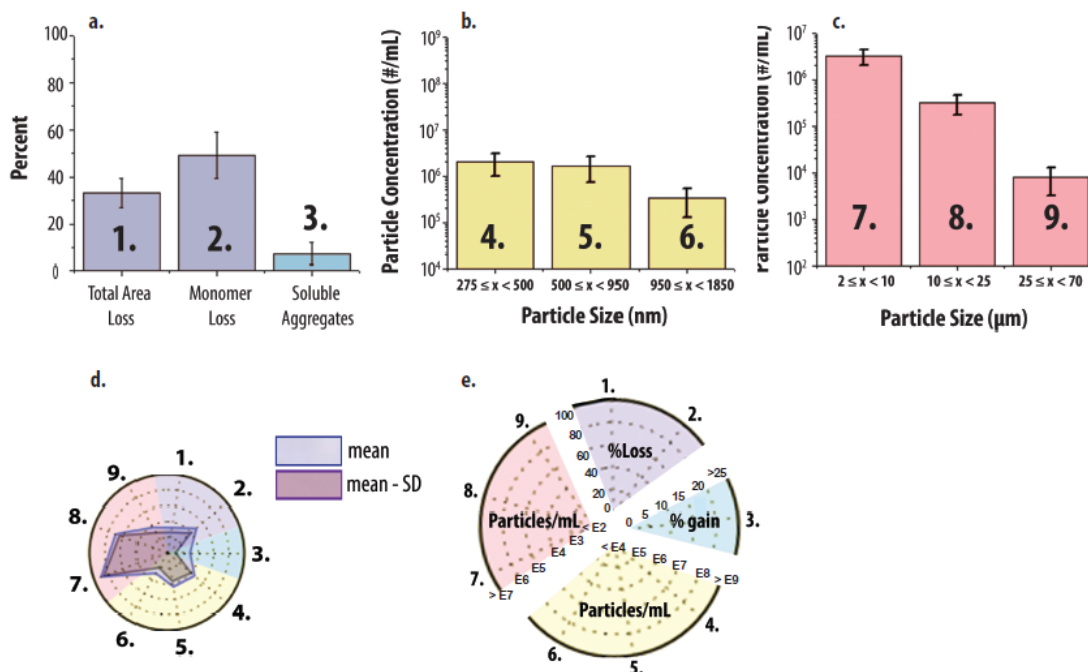
Figure 2.7. Application of Radar Chart Array Analysis to Protein Aggregate and Particle Formation Data from Multiple Analytical Techniques. An IgG1 mAb solution containing 20 mM citrate phosphate buffer (pH 6.0) and 0.15 M NaCl was heated at 65˚C for 120 min and the levels of soluble aggregates, submicron and subvisible particles were measured using SEC, RMM and MFI, respectively. (a, b, c) Bar graph (n=3) of SEC, RMM particle concentrations (0.275-1.85 µm) and MFI particle concentrations (2-70 µm). (d) Radar chart presentation of the same data sets shown bar graphs (a,b,c). The SEC, RMM and MFI data denoted 1-3, 4-6 and 7-9 in the bar charts (a, b, c, respectively) corresponds to axes 1-3, 4-6 and 7-9 in the corresponding radar chart (d). The perimeter of the outermost polygon in the radar chart displays the mean value (particle concentration or area gain/loss), the perimeter of the polygon labeled 'mean - SD' represents the mean value minus one standard deviation, and the distance between perimeters of the two polygons (along an axis) is one standard deviation. (e) Illustration of the numerical scales and units for the radar chart axes with different scales being highlighted with distinct background colors for results from SEC (1,2,3), RMM (4,5,6) and MFI (7,8,9), respectively.
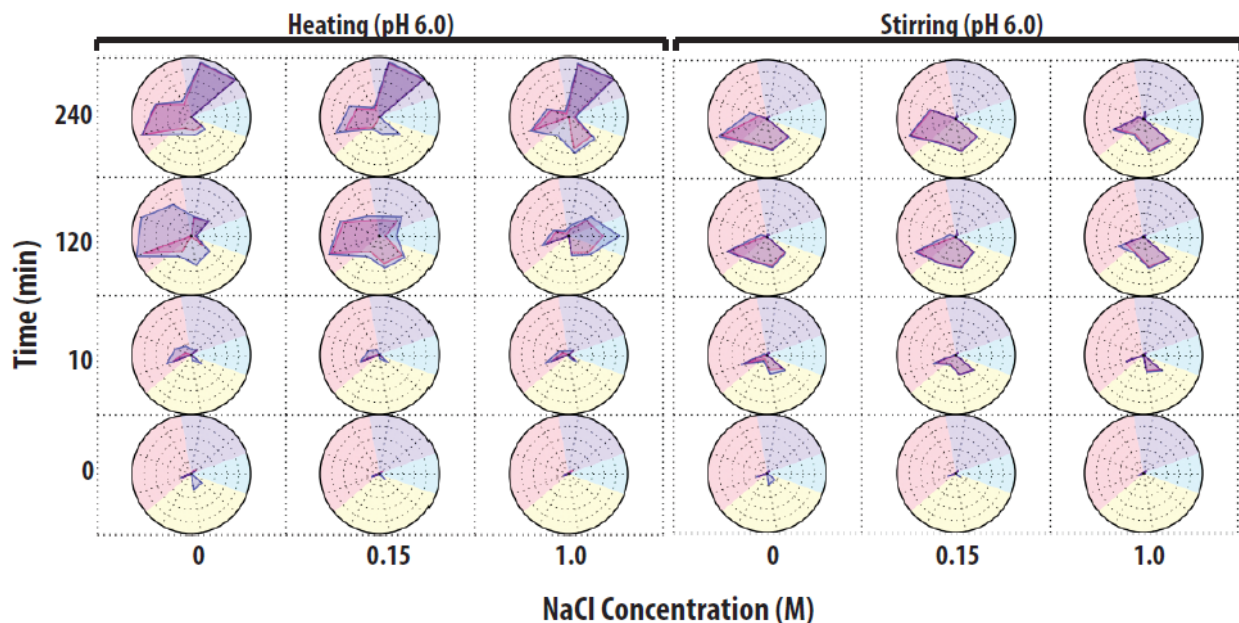
Figure 2.8. Radar Chart Analysis of Protein Aggregate and Particle Formation Data from Multiple Analytical Techniques to Visualize the Extent of IgG1 Physical Instability. IgG1 mAb solutions containing 20 mM citrate phosphate buffer (pH 6.0) and varying NaCl concentrations were stressed by either heat at 65˚C or stirring over time (n=3). Samples were evaluated by a combination of SEC, RMM and MFI. See methods section for experimental details of each accelerated stress study. The Y-axis represents the amount of time the samples was stressed (in minutes), the X-axis represents NaCl concentration, and each radar chart panel (left and right) denotes heating and stirring, respectively. Refer to Figure 2.7 for an explanation of units and scales used in the individual radar charts for each analytical method (SEC, RMM and MFI data).
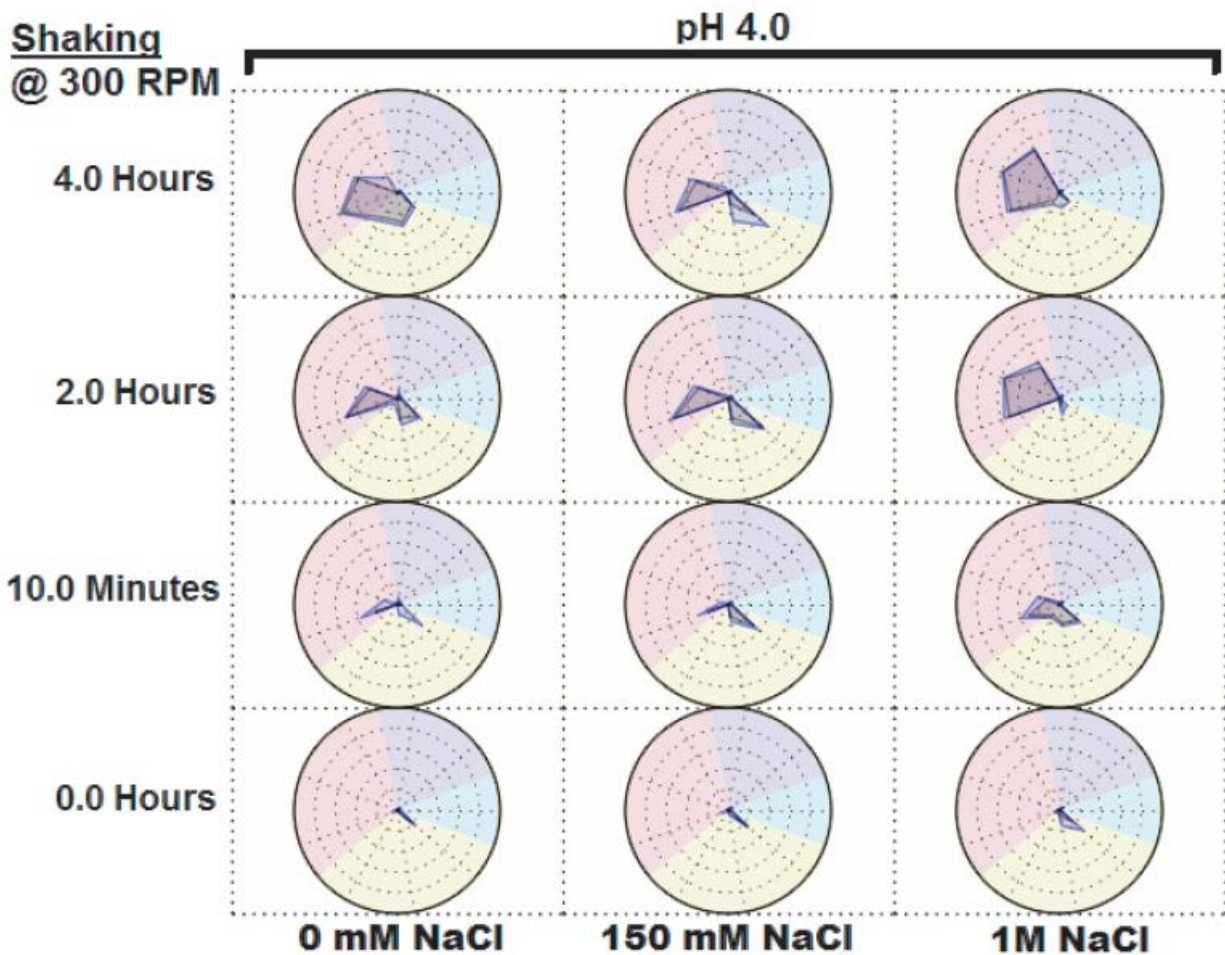
Figure 2.9. Multiple Instruments Radar Chart Array Analysis for Accelerated Stress Study with IgG1 mAb. IgG1 mAb solutions containing 20 mM citrate phosphate buffer (pH 4.0) and varying NaCl concentrations were stressed by shaking side-to-side at 300 RPM over time (n=3). Samples were evaluated by a combination of SEC, RMM and MFI. The Y-axis represents the amount of time the samples was stressed (in minutes), the X-axis represents NaCl concentration. Refer to Figure 2.7 for an explanation of units and scales for the individual radar charts for each analytical method (SEC, RMM and MFI data).
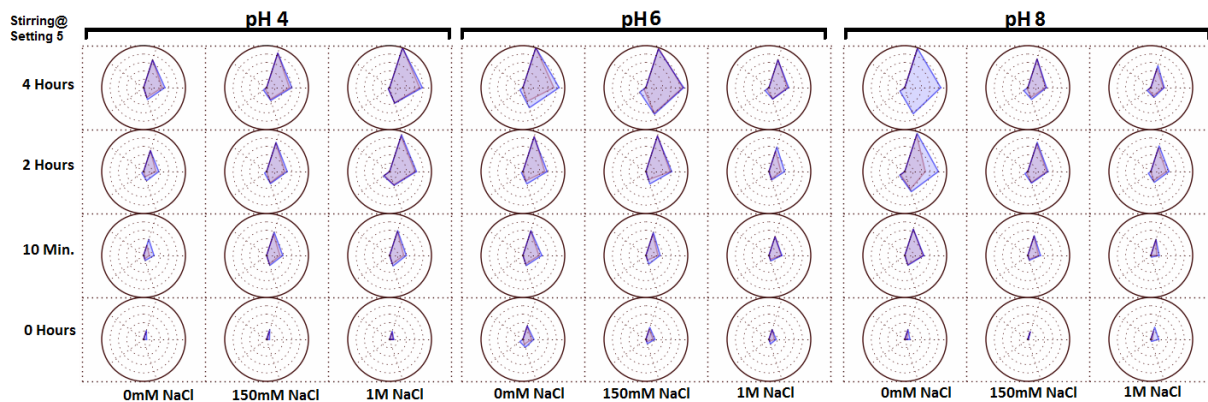
Figure 2.10. Radar Chart Array Analysis of Subvisible Particle Concentration and Size for Particles Created by Stirring. IgG1 mAb solutions of varying pH values and NaCl concentrations were exposed to stirring with a Teflon bar for up to 4 h (n=3). The Y-axis represents the amount of time the formulations were stressed (in minutes), the X-axis represents NaCl concentrations, and each radar chart panel (left, middle, right) signifies a change in pH. Refer to Figure 2.2 for an explanation of particle concentration and size scales shown in individual radar charts.
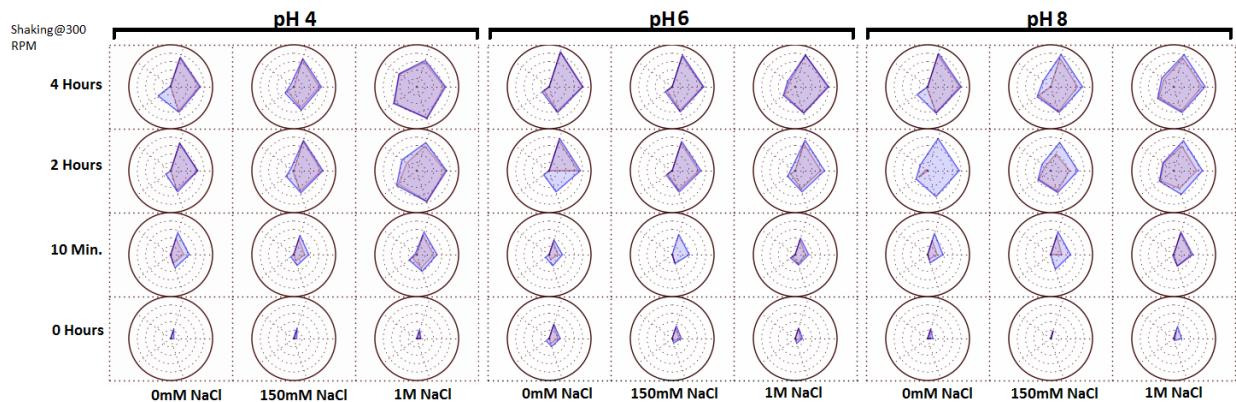
Figure 2.11. Radar chart array analysis of subvisible particle concentration and size for particles created by shaking. IgG1 mAb solutions of varying pH values and NaCl concentrations were exposed to side-to-side shaking at 300RPM for up to 4 h (n=3). The Y-axis represents the amount of time the formulations were stressed (in minutes), the X-axis represents NaCl concentrations, and each radar chart panel (left, middle, right) signifies a change in pH. Refer to Figure 2.2 for an explanation of particle concentration and size scales shown in individual radar charts.

Chapter 3: Calculating the Mass of Subvisible Protein Particles with Improved Accuracy Using Microflow Imaging Data

3.1. Introduction

The formation of subvisible particles (1-100 µm in diameter) in therapeutic protein products has the potential to impact the clinical utility of these parenteral administered therapies. One major concern with monoclonal antibody (mAb) drugs is that subvisible particles could induce an immune response that results in the formation of neutralizing anti-drug antibodies that limit efficacy (1). This presents as a unique formulation challenge because protein degradants can form not only during manufacturing, storage and shipping, but potentially during administration as a result of improper handling or dilution into an IV bag (120, 142, 143).   There have been numerous studies and reviews devoted to characterizing and classifying protein-based subvisible particles (66, 70, 95, 97, 100, 106, 108, 113).   Recently, the potential risks of different types of protein subvisible particles in inducing immune responses have been evaluated in various preclinical models including cell culture and animal studies (12, 13, 144, 145).

Subvisible particles tend to be fragile associations of native-like or non-native protein molecules that typically represent only a small fraction of the entire protein mass in solution (e.g., ~0.01%) (122, 123, 134). Consequently, isolating or enriching specific particle subpopulations by size or morphology is technically challenging. The extent of protein particle formation can be modulated by changing the conformational and/or colloidal stability of a given protein in solution (4). Controlling the size or morphology of the particles, however, is challenging since protein aggregation can occur by a number of different mechanisms that may vary based upon the protein, the formulation, exposure to nucleation sites, and the external stress applied (44, 54, 68, 81, 87, 134). Joubert et al.(66) and Luo et al.(113) have shown that different stress conditions create particles that vary in size, concentration, degree of structural perturbation, and extent of chemical modifications.   The effect of stress on the size,

morphology, and concentration of subvisible particles is also sensitive to formulation (e.g. pH, NaCl concentration) (54, 70). Additionally, the initial presence of soluble aggregates(116) and/or submicron(146) particles can facilitate subvisible particle formation. Finally, solution formulation conditions and sample handling encountered during experimental measurements can affect the size and number of subvisible particles observed. For example, both flow microscopy and light obscuration decrease in accuracy when the refractive index (RI) of solution approaches the RI of particles (110, 147). Analytical methods should minimize sample handling to preserve the integrity of the resulting particles (101), while dilution and/or de-gassing procedures may be necessary to accommodate instrument capabilities.

The number and size range of subvisible particles in parenteral products have traditionally been measured by light obscuration, but when applied to monitoring protein particles, accuracy may be limited since protein particles act as phase objects and primarily scatter visible light in the forward direction which can result in poor contrast (95, 108, 148, 149). Flow microscopy has emerged as a more effective method to count and characterize large, proteinaceous subvisible particles because contrast is enhanced by interference that results from the recombination of diffracted light waves that differ in phase (149, 150). Particles can then be more accurately sized by combining positive and negative contrast thresholds with a neighborhood analysis algorithm (150). Microflow imaging (MFI) is often selected for flow microscopy measurements (107, 121, 123). Through automated image analysis, MFI provides various size, morphology and transparency parameters which can be applied to discriminate between proteinaceous particles and other contaminants such as silicone oil droplets (124).

Wuchner et al reported a calculation of protein particle weight based on MFI data using simple assumptions of spherical shape and a reported value of protein partial specific volume

(123). These calculations were comparable to experimentally determined levels in a high

concentration IgG1-mAb solution after long-term storage at 2-8°C. Barnard et al.,(122) used a

similar approach to calculate the mass of individual protein particles in solution based on data

from MFI measurements. In their calculations, it was assumed that protein particles are spherical

in shape, composed of 75% protein, and have a density of 1.43 g/ml (determined by Quillin et al)

(151). In this work, we sought to build on these reports by combining a new approach to

calculate particle volume from MFI data with updated assumptions of protein particle

composition and density. The applications, shortcomings, and advantages of this new

calculation method, as well as comparisons to the Barnard et al.(122) method, are also discussed.

3.2. Experimental Procedures

3.2.1. Materials and Sample Preparation

An IgG1 mAb (pI ~ 9) was provided by Janssen Biotech Inc. (Horsham, Pennsylvania) at

a concentration of ~40 mg/ml. The stock mAb solution was diluted to a final concentration of 1

mg/ml using 20 mM citrate-phosphate buffer (C-P buffer) prepared at pH 4.0, 6.0, or 8.0 with 0,

0.15 or 1.0 M NaCl. The samples were filled into glass vials (Schott, Lebanon, Pennsylvania),

stoppered and then subjected to 2 h of shaking or stirring stress as described previously (54).

All buffers were sterile filtered (0.2 μm) prior to use. Polystyrene spheres (3, 5, 10, 25, 50 and

70 μm in diameter) obtained from Thermo-Fisher Scientific (Waltham, Massachusetts) were

used for method development. Extensively aggregated control samples were prepared by

shaking samples containing 1 mg/ml IgG in pH 5.0, 20 mM acetate buffer with 150 mM NaCl

for 115 h.

Elongated PS particles were produced from polystyrene (PS) spheres (Microparticles, Berlin, Germany) and polyvinyl alcohol (PVA) from (Sigma-Aldrich, Steinheim, Germany) by using a film-stretching method in hot oil (152). Briefly, PVA (10% w/v) and glycerol (2.5% w/v) were dissolved in water at 85°C. Spherical PS particles were added to this solution at a concentration of 0.1% (w/v). 15 ml of the mixture was poured into a 75 cm² film-casting mold and dried for 72h at 25°C. PS particle films were cut into 5 x 4 cm sections and stretched using a manual film-stretching device build in-house. The device consists of 2 metal clamps in an oil bath (120°C) and a screw, which separates the two clamps during the stretching process. Particles were recovered by dissolving the film in water, followed by several washing steps with water / 0.01% SDS cleaning solution.

3.2.2. Microflow Digital Imaging (MFI)

A DPA-4200 MFI flow microscope (Protein Simple, Santa Clara, California) was used to image and count subvisible IgG particles with an equivalent circular diameter (ECD) from 2-70 µm. Prior to measurement, particles were de-gassed in a vacuum chamber for 10 min. Particle counting and sizing statistics were obtained using MFI View Analysis Suite MVAS 1.3 (Protein Simple, Santa Clara, California) and assigned to five size bins based on particle ECD values as described previously (54). Particle data across each of the five size bins, which covered the entire IgG1 particle distribution were used to calculate the particle mass (as described below). Prior to measurement, the extensively aggregated control mAb sample was diluted 1:10 to reduce particle levels to within the instrument detection limit (< 900,000/ml).

MFI measurements were also performed on spherical and non-spherical polystyrene standards. These samples were not degassed, and the data was exported into a spreadsheet for analysis. For the non-spherical polystyrene samples, MVAS software was used to implement

morphology filters to remove impurities (e.g., small air bubbles, fragmented and dimeric standards) from the datasets to ensure accurate and representative particle statistics corresponding to the non-spherical standards. The Gaussian shaped peak corresponding to the non-spherical standard was saved while the Gaussian shaped peaks corresponding to dimers and small fragments were removed. The results were visually confirmed to ensure that no standard images were removed and that no digital images corresponding to polystyrene dimers remained.

3.2.3. Radar Chart Construction

Radar chart arrays visualizing subvisible particle data from MFI (particle concentration vs. size and particle morphology vs. size) were generated as described previously using in-house software (Middaugh Suite) (54). In addition, a radar chart array displaying the calculated particle mass vs. measured particle size was prepared using particle mass data calculated using the ellipsoid-volume and Barnard et al., analysis methods described later. This was pre-processed by calculating the mean, standard deviation, and mean minus standard deviation (mean-Sdev) for the particles within the following ECD bins: $2 \leq x < 5$, $5 \leq x < 10$, $10 \leq x < 25$, $25 \leq x < 50$, and $50 \leq x < 70$ μm (later referred to as bins 1, 2, 3, 4 and 5, respectively). The mean and m-SD values were uploaded to Middaugh Suite and the radar charts were set to a log scale. Each axis was set to display minimum and maximum masses of $10^{-1.5}$ μg/ml (~0.032) and 10 μg/ml, respectively.

3.2.4. Experimental Determination of IgG1 mAb Mass Loss Due to Mechanical Stress

Prior to mechanical stress, the protein concentration of the IgG1 mAb samples was determined by measuring the absorbance at 280 nm ($\varepsilon^{0.1\%} = 1.37$) using an 8453 UV-Vis

Spectrophotometer (Agilent, Santa Clara, California). Baseline correction was applied by subtracting the average value over the range of 320 to 400 nm (Light scattering correction as suggested by Mach et al. was attempted, but not implemented because it resulted in reduced spectra quality due to the extremely low optical density at 350 nm after centrifugation) (153). After the samples were stressed (and particles were measured by MFI from an aliquot of the sample), the remaining sample fractions were subjected to centrifugation at 17,000 x g for 15 min. The supernatant fractions of the samples were collected and the centrifugation step repeated. This centrifugation procedure removed >99.5% of subvisible particles and essentially 100% of subvisible particles larger than 10 µm from the stress condition that produced the most particles (data not shown). The difference in concentration between the unstressed and stressed IgG1 samples was then calculated. The UV-Visible spectrophotometer accurately measured the loss of IgG at >15 µg/ml.

3.2.5. Calculation of Particle Mass from MFI Data by Assuming Spherical Volume

The mass of a protein particle was calculated using the equation developed by Barnard et al (122). The assumptions being that protein particles possess a spherical volume, and are composed of 75% protein and 25% solvent. The mass of a single particle can be described by equation 3.1:

$$M = 0.75 * \frac{4}{3}\pi(d/2)^3 * 1.43\frac{g}{ml} \tag{3.1}$$

where M represents the calculated mass of a particle and d represents the equivalent circular diameter. The total mass of particles was calculated by summing the calculated particle masses and correcting for the analyzed volume.

3.2.6. Calculation of Particle Mass from MFI Data Using the Ellipsoid-Volume Method

The ellipsoid-volume method uses individual subvisible particle values of size and morphology (determined from two dimensional images captured by MFI) to calculate the mass of the three dimensional particle. To this end, each subvisible particle is modeled as a 2-dimensional ellipse with equivalent area and circularity, which is then rotated about its minor axis, to calculate the volume of a prolate ellipsoid of revolution. This calculated volume of the particle is then used to calculate particle mass. This requires values of the particle density and composition (see below). Because of the novel nature of this method, we provide both a theoretical derivation in the methods section and a case study using an MFI data set in the results section to illustrate the utility of the method.

3.2.6.1. Theoretical Derivation

In this section of the derivation, we determine the relationship between circularity and aspect ratio for an ellipse. This relationship can be applied to calculate the aspect ratio (AR) of an ellipse with an equivalent circular diameter (*d*) and circularity (*C*) equal to the particle.

Using an approximation, the perimeter of an ellipse can be written:

$$\text{Perimeter} = \pi \left[3 * \left(a + b \right) - \sqrt{(a + 3b)(3a + b)} \right]$$

This equation has ~0.41% error for ellipses with very high eccentricities. "a" denotes the major axis and "b" denotes the minor axis. The aspect ratio of an ellipse can be expressed as $AR = \frac{b}{a}$ and b can be expressed in terms of a as $b = a * AR$.

The radius of a circle with equivalent area to an ellipse can be written as $r = a\sqrt{AR}$. Thus, a can be expressed in terms of equivalent circular diameter as $a = \frac{d}{2 \times \sqrt{AR}}$.

Therefore,

$$\text{Perimeter} = \pi * \frac{d}{2\sqrt{AR}} * [(3 + 3 * AR) - \sqrt{(3 + 10 * AR + 3 * AR^2)}]$$
(3.2)

The perimeter of an ellipse is related to circularity by the expression $C = \frac{2 * \pi * \frac{d}{2}}{\text{Perimeter}}$.

Substituting circularity into (2) yields,

$$C = \frac{1}{\frac{1}{2 * \sqrt{AR}} * [(3 + 3 * AR) - \sqrt{(3 + 10 * AR + 3 * AR^2)}]}.$$
(3.3)

The values generated by this mathematical relationship were plotted as aspect ratio as a function of circularity and fit using Mathematica 8.0 (Wolfram, Champaign, Illinois) to obtain a function that describes aspect ratio (AR) of a model ellipse as a function of particle circularity. The mathematical fit describing aspect ratio in terms of circularity is described by equation 3.4:

$$AR = 1.70763 - 1.70864 \times (1 - C)^{0.45} - 0.70638\, C$$

(3.4)

In the following part of the derivation, we model the ellipse defined by equation 3.4 as a prolate ellipsoid of revolution to approximately calculate particle volume.

The volume of a prolate ellipsoid of revolution can be written as follows:

$$V = \frac{4}{3}\pi ab^2 = \frac{4}{3}\pi \frac{b^3}{AR}$$

The minor axis, *b*, can be expressed in terms of d as $b = \frac{d*\sqrt{AR}}{2}$ by equating the area of an ellipse

to the area of a circle. Using this relationship we can calculate the volume of a prolate ellipsoid

of revolution with d and AR:

$$V = \frac{\pi}{6} \times d^3 \sqrt{AR} \tag{3.5}$$

Combining the volume equation with our fitted function yields:

$$V = \frac{\pi}{6} \times d^3 \times \sqrt{1.70763 - 1.70864 \times (1 - C)^{0.45} - 0.70638\,C} \tag{3.6}$$

Using this equation (above), the volume of a distribution of particles ranging from fiber-like to

spherical can be more accurately calculated by removing the assumption of spherical volume and

considering particle morphology.

To calculate particle mass from the modeled volume for protein particles, a value of 1.41

g/ml was used as the density of IgG as recommended by Fischer et al. (98), and we assume the

proteinaceous particles contain 20% protein and 80% solvent. The rationales for these

assumptions are presented in the discussion section. Based on the ellipsoid volume calculations

combined with these assumptions of protein density and particle composition, the mass of an

individual subvisible particle can be calculated using equation 3.7:

$$\text{Mass of particle k } (M_k) = \frac{\pi}{6} \times d^3 \times \sqrt{1.70763 - 1.70864 \times (1 - C)^{0.45} - 0.70638\,C} \, * \, 1.41\frac{g}{ml} * f \tag{3.7}$$

Where f represents the fraction of protein bound within a prolate ellipsoid of equal equivalent

circular diameter and circularity (i.e., a value of 0.2 for f as described above). The total mass of

subvisible particles in solution was then calculated by summing the masses of the individual

particles and then dividing the sum by the sample volume that was analyzed (V_a, in mL) as shown in equation 3.8:

$$\text{Mass of n particles per ml} = \frac{\sum_{k=1}^{n} M_k}{V_a} \tag{3.8}$$

It is important to note that experimentally measured aspect ratio could also be used to calculate particle mass by substituting equation 3.4 into equation 3.7. The application of the ellipsoid-volume method to determine particle mass only requires the use of equations 3.7 and 3.8 and is simple to implement in standard spread sheet software. This is illustrated in the results section using representative MFI data from shake stressed IgG1 mAb solutions.

3.3. Results

3.3.1. Ellipsoid-Volume Method Applied to a Representative Subvisible Particle MFI Dataset

We selected an IgG1 mAb sample (1.0 mg/mL) in a pH 4 citrate-phosphate buffer containing 1 M NaCl that was shaken for 2 h, as a representative MFI data set to illustrate the ellipsoid volume method of calculating particle mass. This condition produced a heterogeneous mix of subvisible particles with various morphologies that ranged from fiber-like to spherical as well as other irregular shapes. A graphical representation of equation 3.4 (red curve) is provided to visualize the relationship between aspect ratio and circularity for an ellipse of varying circularity (Figure 3.1A). Corresponding model ellipses are depicted along the curve in addition to values for actual digital images of IgG subvisible particles (shown as green dots). Some of the particles show a small deviation from the red curve, and these particles tended to have slight surface irregularities. The particles that displayed larger deviations from the ellipse curve tend

71

to have tangled, bent, or branched fiber-like morphology, which result in measured aspect ratio (from MFI) to be inaccurate (Figure 3.1A). These findings resulted in the selection of particle circularity, rather than its aspect ratio, to fit the measured subvisible particle digital images into an ellipse model to calculate their volume. As outlined in the methods section, circularity obtained from an MFI digital image of a subvisible particle was used to model the particle as an ellipse along the red curve (i.e., Equation 3.4). Figure 3.1B provides a step-by-step illustration of the ellipsoid-volume method to calculate particle mass as described by equations 3.7 and 3.8. Figure 3.1C is a representative scatter plot of an MFI dataset acquired (blue diamonds) from the shake stressed mAb solution described above.

To calculate the total mass of subvisible particles in this solution, the calculation methodology would be applied to each particle and then summed up across the entire data set (Figure 3.1B). It is important to note that the ellipsoid-volume method functions by modelling the particles as ellipsoids along the power function curve (red diamonds) based upon their circularity. By comparison, if it is assumed that the subvisible particles are perfectly shaped spherical particles (i.e., Barnard et al, 2011), then all the subvisible particles will be modeled at the coordinates (1.0, 1.0).

3.3.2. Experimental and Calculated Mass of Subvisible Particles Formed from Stressing IgG1 mAb Solutions

A comparison of the calculated values for subvisible particle mass using a combination of the Barnard et al.(122) method and the ellipsoid-volume method described above, were used along with an approach to experimentally measure the mass of protein particles present in solution. For the experimental approach, the concentration of protein in solution was monitored

before and after stress (and extensive centrifugation) by UV-visible absorption spectroscopy. Three different conditions were selected that resulted in the formation of different levels of particles. First, mAb samples (pH 4 in a citrate-phosphate buffer) were stirred for 4 h resulting in ~one microgram of particles per ml (Figure 3.2A). Second, mAb samples (pH 4 in a citrate-phosphate buffer with 1M NaCl) were shaken for 4 h resulting in tens of microgram of particles (Figure 3.2B). Finally, mAb samples (pH 5 in a sodium acetate buffer with 0.15M NaCl) were shaken for 115 hours resulting in hundreds of microgram of particles (Figure 3.2C).

For the pH 4.0 mAb samples stirred for 2h (Figure 3.2A), the average calculated particle mass per ml for the Barnard et al. equation and the ellipsoid-volume equation were ~3.0 and ~0.4 µg/mL. This value was below the limit of quantitation (LOQ) of the experimental method of <15 µg/ml. This result highlights the potential utility of such methods to estimate particle mass using experimentally measured particle number results at relatively low levels.

For other two mAb sample conditions, which resulted in higher concentrations of subvisible particles, especially >25 µm, the total mass calculated by the Barnard et al.(122) equation greatly exceeded the experimentally determined mass loss. For example, for the mAb samples at pH 4.0 containing 1M NaCl and shaken for 2h, the calculated average particle mass per ml for the Barnard et al. equation and the ellipsoid-volume equation were approximately 370 and 26 µg/mL, respectively (Figure 3.2B). It can be seen the latter result is much more closely aligned with the experimentally determined value of ~34 µg/mL. Similarly, for the mAb samples at pH 5.0 containing 0.15M NaCl and shaken for 115h, the average calculated particle mass per ml for the Barnard et al. equation and the ellipsoid-volume equation were approximately 2400 and 280 µg/mL, respectively (Figure 3.2C). Again, the latter result is much more closely aligned with the experimentally determined value of ~290 µg/mL.

For some of these conditions, low numbers of visible particles with > 70 µm ECD were observed by MFI, but not included in the particle mass calculations because these values were below the limit of quantitation for this flow imaging instrument. For example, including visible particles > 70 microns in the calculations for the mAb samples at pH 4, 1M NaCl shaken for 2 h increased the total calculated mass by ~240% for the Barnard et al. method and ~80% for ellipsoid-volume method (data not shown).

3.3.3. Additional Verification of Particle Mass Calculations Using Polystyrene Bead Standards

We used spherical and non-spherical polystyrene bead standards to more extensively evaluate the performance of the ellipsoid-volume equation versus simply assuming a spherical volume. The ellipsoid volume equation and an assumption of spherical volume were used to predict the equivalent spherical diameters (ESD) of the polystyrene bead standards analyzed by MFI as shown in Table 3.1. The ellipsoid-volume method calculated a more accurate ESD for the non-spherical standards. The most inaccurate results of the standards tested resulted in a ~64, and 200% estimation of the true volume for the ellipsoid-volume method (10 µm spheres) and assumption of spherical volume (10 µm, 3x stretched particles) , respectively. The reason that the ellipsoid-volume method calculated slightly less accurate ESD values for the spherical standards than the assumption of spherical volume is presented in the discussion section.

3.3.4. Application of Calculation Methods to Estimate Particle Mass Formed in a Variety of IgG1 mAb Formulations Based on MFI Data

The concentration, size range, morphological parameters (aspect ratio and intensity) of subvisible particles were measured by MFI as formed after shaking or stirring IgG1 mAb

solutions with different pH values (pH 4.0, 6.0, 8.0) and salt concentrations (0, 0.15, and 1.0 M)

over a 2 h time period. The data were then used to calculate the total mass of the particles. The

subvisible particle concentration and size distribution at t = 0 and the morphology for this IgG1

mAb have been reported previously at t = 4 h, and these experiments showed qualitatively

similar results (54). A radar chart array was used for data visualization of these large data sets to

display the effect of pH, NaCl, and stress type on subvisible particle formation in terms of

particle concentration and size (Figure 3.3). A total of 9 mAb solution conditions and two

different stresses were investigated in triplicate resulting in 54 separate experiments containing a

total of ~1.28 million digital images. It can be seen in Figure 3.3 that shaking stress produced

larger but fewer subvisible particles compared to stirring the same mAb formulations under most

conditions. Formulations containing increasing amounts of NaCl at both pH 6 and 8 had a fewer

number of particles form.

A second radar chart array was generated to visualize the same MFI data set to evaluate

how formulation composition and stress type affected the morphology of subvisible particles in

relation to particle size (Figure 3.4). The aspect ratio of the particles decreases as a function of

increasing particle size for all of the formulation and stress conditions (i.e., the particles become

more elongated as size increases). The shaking of mAb formulations at pH 4 decreased the

aspect ratio for most size ranges relative to pH 6 or 8, while 1M NaCl also decreased the aspect

ratio for most size ranges compared to samples containing no or 0.15 M NaCl. Thus, the

combination of shaking stress on a sample at pH 4, 1 M NaCl reproducibly produced particles

with the lowest average aspect ratio. For the stirred samples, across all of the formulation

conditions, the majority of subvisible particles produced were more circular in nature (high

aspect ratio) with only a few of the larger particles having a moderately smaller aspect ratio

(~0.5). In terms of the morphology parameter of particle intensity, no obvious trends were discernible for either stress or formulation composition. In general, however, a decrease in particle intensity (decreased transparency) was noted as particle size increased.

The distribution of total mass as a function of particle size as calculated from MFI data by the two mass determination methods is presented in radar chart array format for mAb samples subjected to stirring stress (Figure 3.5). For the same mAb samples exposed to shaking stress, both particle number and particle weight (ellipsoid volume method) from MFI data are shown. The radar chart arrays display the calculated mass distribution of the particles as a function of particle size: the particles are placed into five different particle size bins (i.e., 2-5, 5-10, 10-25, 25-50 and 50-70 microns), and the average particle characteristics are calculated for each size bin to estimate the total mass. In addition, the total calculated masses of the particles generated under each condition are provided in Table 3.2. In this case, the total mass is calculated by summing the results of calculated particle mass from the measured particle numbers in the individual size bins in Figures 3.5 and 3.6.

As shown in Figure 3.5 and Table 3.2, the ellipsoid volume method and the Barnard et al. equation generate notably different particle mass distributions as a function of particle size. The Barnard et al. method shows greater bias towards more mass in the larger sized particles. For example, using the pH 4, 1 M NaCl sample subjected to 2 h of stirring (Figure 3.6), the calculated mass of subvisible particles within bin 5 (50-70 micron sized particles) is ~1 µg/ml for the Barnard et al.(122) method, while the mass is calculated to be ~0.09 µg/ml by the ellipsoid-volume method. In general, when using the ellipsoid-volume method, the largest mass fraction of the subvisible particles generated from 2 h of stirring is the smaller sized particles (i.e., 2 to 10 µm) for the mAb formulation conditions examined (Figure 3.6).

As a final example, the distribution of subvisible particles formed by shaking (2 h) different mAb solutions (pH 4, 6, 8 with varying NaCl levels) is displayed in Figure 3.6: the experimentally measured particle concentration and the calculated mass particle mass (ellipsoid-volume method) are displayed as function of particle size using a radar chart array. Across the solution conditions, particle concentrations were highest in the smallest size ranges of 2-5 and 5-10 microns (see size bins 1 or 2 in Figure 3.6). One exception was samples shaken at pH 4 with 1 M NaCl, which produced similar concentrations of particles across the wider size range of 2-50 microns (size bins 1-4 in Figure 3.6). Interestingly, the particle size range with the highest calculated particle mass across the samples was 10-25 microns (located in bin 3 in Figure 3.6). In addition, the larger size range of 25-50 and 50 to 70 microns (Bins 4 and 5 in Figure 3.6), also contained a relatively large fraction of mass. These results demonstrate the utility of radar chart arrays to summarize the size distribution of subvisible particles formed in terms of both particle concentration and their corresponding estimated particle mass.

3.4. Discussion

The morphology of proteinaceous subvisible particles can be highly heterogeneous within a given stressed mAb sample (54). Proteinaceous subvisible particles are often non-spherical and have a wide range of forms that include globular, fiber-like, branched, and ribbon-like structures (154). The assumption that protein particles in solution are spherical (i.e., ECD values from MFI is equivalent to particle ESD), as assumed in the method proposed by Barnard et al.,(122) can lead to calculations of mass and volume with limited accuracy and precision. As demonstrated in this study, improvements in particle mass calculations are possible by accounting for the non-spherical nature of these particles. In addition, the mean and the variance of the morphological parameters may vary depending upon the individual mAb being evaluated,

77

the formulation and the type of stress exposure. Thus, particle morphology measurements from MFI can be further used to develop mathematical models to improve calculated estimates of particle volume, surface area, and mass.

In the Barnard et al. method (122), it was not only assumed that protein particles were spherical in nature, but to determine the mass it was assumed the protein particles had a density of 1.43 g/ml (determined by Quillin et al) (151), and that they were composed of 75% protein and 25% water. For our methods, we not only used MFI data to account for the non-spherical nature of the particles, we also implemented some updated assumptions about the composition of protein particles. First, we used a mAb density value of 1.41 g/ml. This value was obtained using an equation developed by Fischer et al that accounts for the empirical dependency of protein density on its molecular weight (98). Second, we estimated the volume fraction of protein in a protein particle to be 0.2 based on several considerations: (1) protein crystals have large interstitial volumes that are around 50% of the total volume (155), (2) using a RI of 1.41(110) and dn/dc of 0.19 ml/g(156) at 589 nm for protein particles, we can estimate the volume fraction of protein in a particle suspended in water as ~28% because the relationship should still be linear at this concentration (103, 157), and (3) the density of IgG layers adsorbed to different surfaces were measured to be 1.05-1.10 g/ml(158) which corresponds to volume fractions of ~10-24% in pure water. By assuming 0.2 to be the fraction of protein in a particle, the protein mass values calculated by Barnard et al. method(122) is reduced by ~3.75 fold. It would be beneficial in the future to develop an analytical method to determine the average fraction of protein contained within particles generated from different stresses to further improve the accuracy of these particle mass calculation methods.

The particle mass calculation used in this work is referred to as the ellipsoid-volume method. Based on the observation that subvisible particles tend to range from fiber-like to roughly spherical, we tested the hypothesis that subvisible particles can be adequately modeled using calculated ellipses of different sizes and aspect ratios (Figure 3.1). Although a number of particles were found to substantially deviate from the calculated ellipse curve, the majority of these particles were observed to be tangled or bent fibers or ribbon-like structures (data not shown). The two dimensional ellipse shapes, calculated using particle circularity and ECD values from MFI, were used to model particles as different prolate ellipsoids of revolution. Therefore, the ellipsoid-volume method improved the particle volume calculation of subvisible protein particles to more accurately determine their mass compared to a spherical model. Using the ellipsoid-volume method on spherical and non-spherical polystyrene particles resulted in calculated ESD values that deviated from 0.8 to 14% of the true value (Table 3.1). The relatively higher values of error for the spherical standards were probably because MFI often measures the circularity of spherical standards to be less than 0.95 when they should theoretically be 1.0. In the case of these inflexible polystyrene bead standards, using measured aspect ratio would have greatly improved the accuracy of the ellipsoid-volume calculations (data not shown).

To compare the accuracy and precision of the two particle mass calculations (Barnard et al. (122), and the ellipsoid volume methods), we compared the calculated results (from MFI data) to an experimental procedure that was optimized to measure protein mass loss as a result of particle formation. The experimental procedure with stressed samples of IgG1 mAb was shown to have a limit of quantitation of 15 µg/ml, and therefore was not sensitive enough to detect particle mass loss under most experimental conditions (Figure 3.2A). At these low concentrations, experimental results could be complicated by adsorption of the protein particles

79

to the cuvette and/or centrifuge tube in some circumstances (data not shown). Therefore, we generated more extensively aggregated samples to compare the accuracy and precision of the relevant particle mass equations (Figure 3.2B and 3.2C). We found that the Barnard et al.(122) method had lower accuracy, and under certain conditions, could even approximate the mass of particles to be equal to or greater than the total mass of protein in solution. The variability in the total mass calculations displayed in Figure 3.2 is primarily due to the variability of the MFI measurements for the number of particles > 25 µm ECD in each sample. Since the Barnard et al. equation uses the assumption of spherical volume, it had the largest relative standard deviation. Although variability is commonly observed in particle counting experiments, the experimental approach to determine mass loss showed better precision than the calculation methods for the extensively aggregated sample (Figure 3.2C). Another possible explanation could be that the average protein particle density may not be constant from vial to vial (similar to variability in particle number from vial to vial).

The applicability and assumptions of the calculation methods to estimate the mass subvisible particles in a protein formulation are summarized in Table 3.3. The ellipsoid volume method would be the method of choice from the practical point of view that it is simple to implement and provides better estimates of protein particle mass compared to the Barnard et al. equation. In samples that have a large concentration of highly irregular particles due to extensive protein structural perturbation (e.g., heat stress), the ellipsoid volume method could also be inaccurate. In such circumstances, a different shape model such as a cylinder could be evaluated.

The primary advantage of implementing a calculation approach to estimate protein particle mass utilizing flow microscopy is that determination of subvisible particle concentration, size and particle mass come from the same experiment making direct comparisons

straightforward. Otherwise, the fact that different instruments can have entirely different measurement principles and can vary in sensitivity, direct comparison between particle concentrations and mass can be extremely challenging. Using this approach, protein particle mass can be calculated regardless of the concentration and size range of subvisible particles present in a given formulation, offering an ability to estimate particle mass when levels are below the experimental limits of quantification using UV absorbance detection. In addition, individual particle masses can be assigned to specific particles populations within different size ranges. Figure 3.6 illustrates that radar chart arrays can be used to compare the distribution of particles (size, number and weight) formed in different IgG1 mAb formulations during shaking. In addition, Figure 3.6 also displays the contribution of different particle sizes to the total particle mass. For example, although subvisible particles produced by shaking generally showed the highest particle number in the 2-5 micron size bin, this size range contains a small fraction of the total calculated particle mass. It would be of interest to generate a data base of such radar charts for different mAbs, different proteins, different formulations, and/or during accelerated and real-time stability studies. Such studies would facilitate better comparisons of the number, size and weight of subvisible particles that form during manufacturing and storage of protein therapeutic candidates.

3.5. Figures and Tables

3.5.1. Tables

Particle Standards (n=3)	Representative Image from MFI	Spherical Calculated ESD (μm)	E-V Calculated ESD (μm)
70 μm spheres		72.1 ± 0.7	63.9 ± 0.7
50 μm spheres		49.9 ± 0.6	44.4 ± 1.9
25 μm spheres		24.5 ± 0.5	21.5 ± 0.5
10 μm spheres		9.9 ± 0.4	8.7 ± 0.4
5 μm spheres		5.1 ± 0.2	4.4 ± 0.2
3 μm spheres		3.2 ± 0.2	2.7 ± 0.1
25 μm non-spherical 4x stretched particles		31.3 ± 3.2	25.2 ± 1.6
25 μm non-spherical 3x stretched particles		29.1 ± 1.9	24.6 ± 1.3
10 μm non-spherical 3x stretched particles		12.6 ± 2.2	10.4 ± 1.7
10 μm non-spherical 2x stretched particles		11.8 ± 1.5	10.8 ± 1.3

Table 3.1. Calculated and Known Equivalent Spherical Diameters (ESD) for Spherical and Non-Spherical Polystyrene Standards. The spherical ESD values represent the average and standard deviation of 3 replicates of MFI measurements using the assumption that ECD values are equivalent to ESD. The E-V (ellipsoid volume) calculated ESD values are the average volume and standard deviation of 3 measurements calculated using the volume term of ellipsoid-volume method.

82

IgG1 mAb Formulations	Stirring (2 h.)		Shaking (2 h.)	
	Barnard Mass (n=3) (µg/ml)	Ellipsoid-Volume Mass (n=3) (µg/ml)	Barnard Mass (n=3) (µg/ml)	Ellipsoid-Volume Mass (n=3) (µg/ml)
pH 4	2.9 ± 2.1	0.4 ± 0.3	10.2 ± 3.5	1.1 ± 0.5
pH 4 w/0.15 M NaCl	13.9 ± 3.3	1.9 ± 0.5	19.7 ± 18.8	1.1 ± 1.0
pH 4 w/ 1 M NaCl	21.3 ± 2.5	2.7 ± 0.2	365.8 ± 257.0	26.2 ± 16.1
pH 6	20.0 ± 5.6	2.8 ± 0.8	6.3 ± 1.3	0.7 ± 0.1
pH 6 w/0.15 M NaCl	4.5 ± 0.7	0.5 ± 0.1	2.0 ± 1.1	0.2 ± 0.1
pH 6 w/ 1 M NaCl	2.8 ± 0.1	0.3 ± 0.1	8.9 ± 2.2	0.5 ± 0.1
pH 8	5.9 ± 1.6	0.8 ± 0.2	10.5 ± 1.1	0.7 ± 0.2
pH 8 w/0.15 M NaCl	5.8 ± 2.2	0.7 ± 0.3	12.2 ± 6.0	0.7 ± 0.3
pH 8 w/ 1 M NaCl	7.0 ± 3.8	0.7 ± 0.4	19.9 ± 0.5	1.3 ± 0.1

Table 3.2. Calculated Total Mass of Subvisible Particles Formed in Various IgG1 mAb Formulations Subjected to 2 h of Shaking or Stirring Stress. The total calculated mass of protein particles is determined by summing the calculated mass of particles of different sizes (the five size bins in Figures 3.5 and 3.6) measured by MFI. The mass of the size bins was determined using the Barnard and ellipsoid-volume methods (see text). The IgG1 mAb formulations contain 1 mg/mL protein in 20 mM citrate phosphate buffer at the indicated solution pH and NaCl concentration.

Method:	Particle Type				Application	Assumptions
	S	F	B	R		
Barnard et. al	+				**Very Easy** (Requires collection of size data)	• Spherical morphology • Static density (1.43 g/ml) • Static particle composition (75% Protein)
Ellipsoid-Volume	+	+	+		**Easy** (Requires collection of size and circularity data)	• Prolate ellipsoid of revolution morphology • Static density (1.41 g/ml) • Static particle composition (20% Protein)

Table 3.3. Summary of the Applicability and Assumptions of Particle Mass Calculation Methods. S, F, B and R refer to spherical, fiber-like, branched, and ribbon, respectively. See methods section for derivation of the Ellipsoid volume method.

3.5.2. Figures
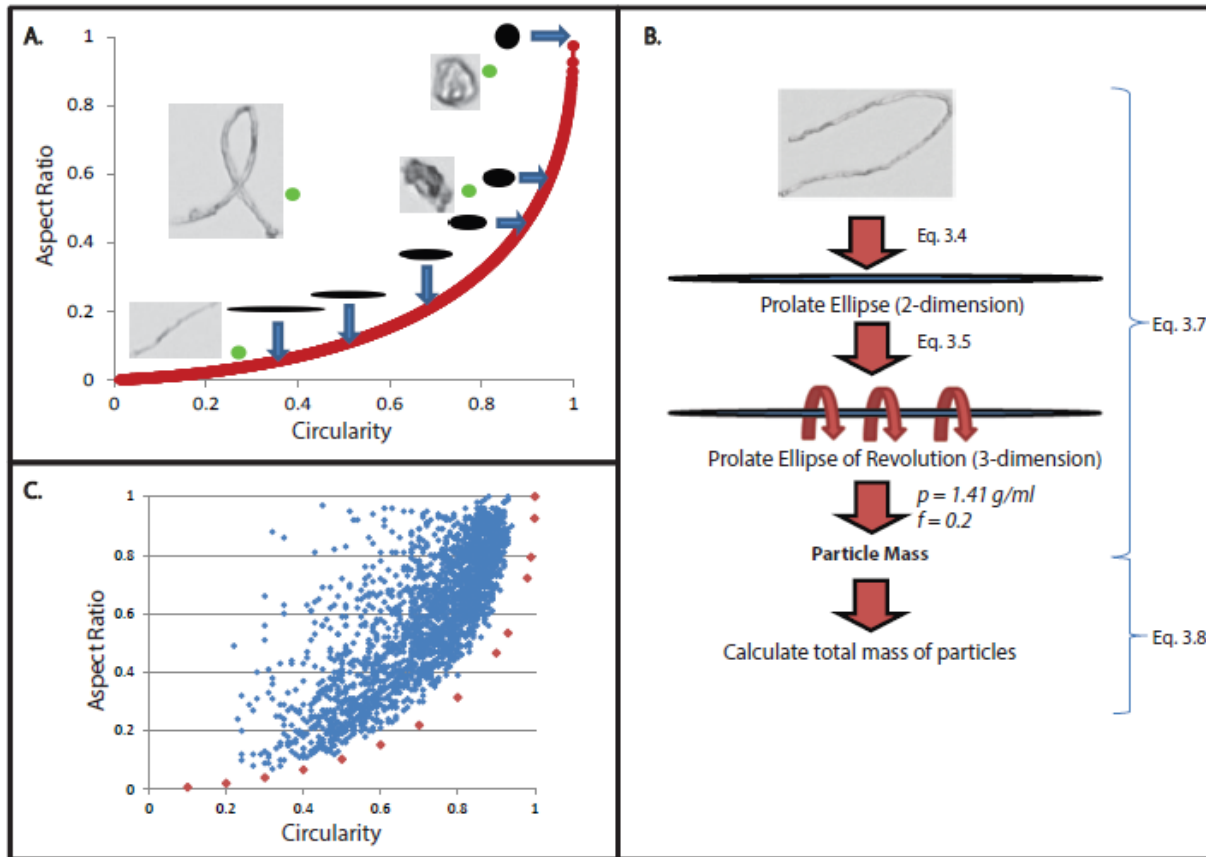
Figure 3.1. The Principle of the Ellipsoid-Volume Mass Calculation Method. (A) The mathematical relationship between aspect ratio and circularity for an ellipse (red curve). Ellipse shapes are illustrated along the curve along with representative IgG1 particle images from MFI analysis to translate this information to particle morphology. The green points represent the location of these IgG particles in relation to the curve. (B) Flow chart to visualize the principles of the ellipsoid-volume method. The entire multi-step process is directly calculated by equation 5. (C) Scatter plot of IgG1 particles created after 2 h of shaking a pH 4.0, 1 M NaCl IgG1 formulation. The ellipse relationship from (A) is traced by the red points. Total mass of subvisible particles in the mAb solution is determined by performing the calculation in (B) for each particle measured by MFI (C) and then summing the results.
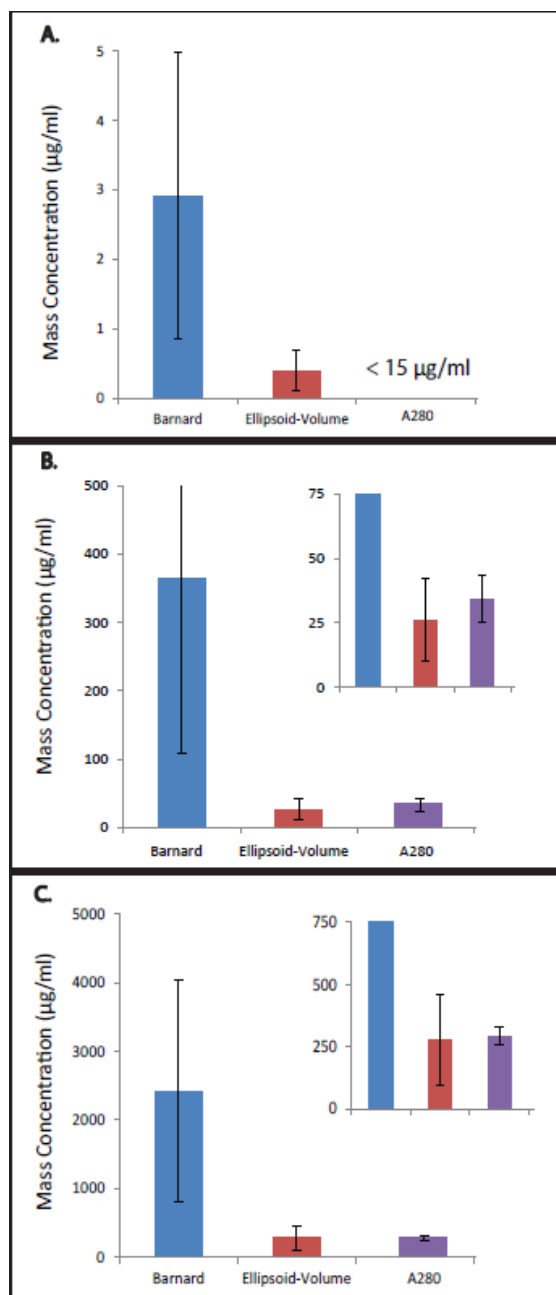
Figure 3.2. Comparison of the Particle Mass Calculation Methods (from MFI Data for Subvisible Particles from 2-70 µm) to Experimentally Determined Values in mAb Formulations with Low, Moderate and Extensive Particle Formation. (A) Values calculated for particles formed by stirring at pH 4.0, 20 mM Citrate-phosphate buffered mAb samples (n=3) for 4 h. (B) Values calculated and experimentally determined for particles formed by shaking

pH 4.0, 1.0 M NaCl, 20 mM Citrate-phosphate buffered mAb samples (n=3) for 4 h. The insert is a zoomed in version of the corresponding bar graph. (C) Values calculated and experimentally determined for particles formed by shaking pH 5, 0.15 M NaCl, 20 mM acetate buffered mAb samples (n=3) for 115 h. The insert is a zoomed in version of the corresponding bar graph.
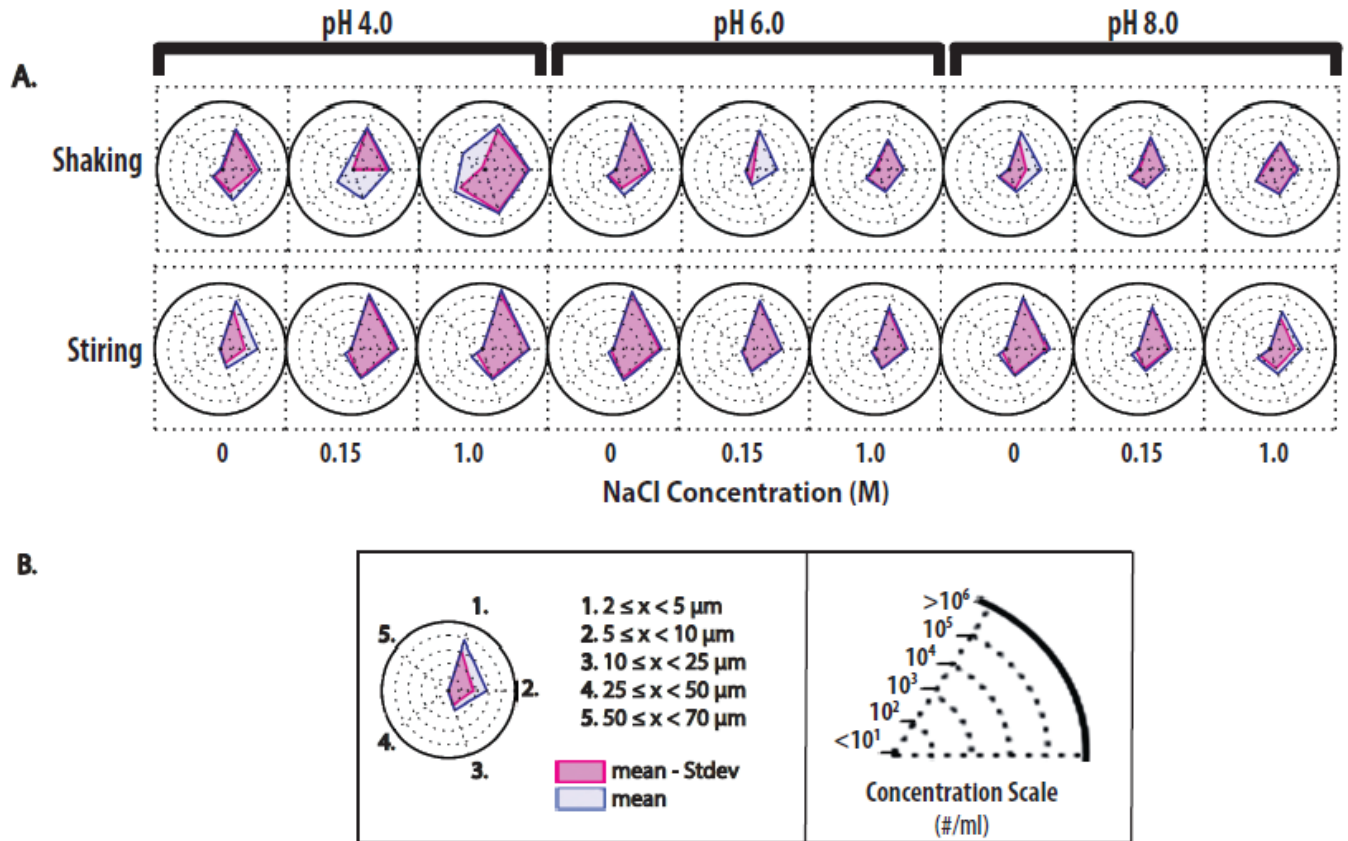
Figure 3.3. The Concentration and Size Range of Subvisible Particles Formed in Different IgG1 mAb Formulations Subjected to Shaking or Stirring. (A) Radar chart array analysis to evaluate the concentration of subvisible particles as measured by MFI. The Y-axis denotes the stress (shaking or stirring), the X-axis denotes the NaCl concentration used, and the brackets (top) group the formulations by pH. (B) A guide for the quantitative interpretation of the radar chart array in (A). (B, left panel) Each numbered axis represents a size bin grouped using particle ECD. The light blue polygon represents the mean concentration (n=3) of subvisible particles within each bin. The pale-fuchsia polygon is the mean – standard deviation to provide an indication of variability. (B, right panel) The concentration of a particular size range can be determined by the size of the polygon along that axis. If the polygon is invisible along the axis there is less than 10 particles/ml in that size range and if the polygon extends to the outer

perimeter of the radar chart there is more than 1,000,000 particles/ml in that size range. Each

concentric ring from the center of the radar chart represents a 10-fold increase in concentration.

The axes are linearly connected to clearly visualize a shift in concentration as a change in shape

of the corresponding polygon.
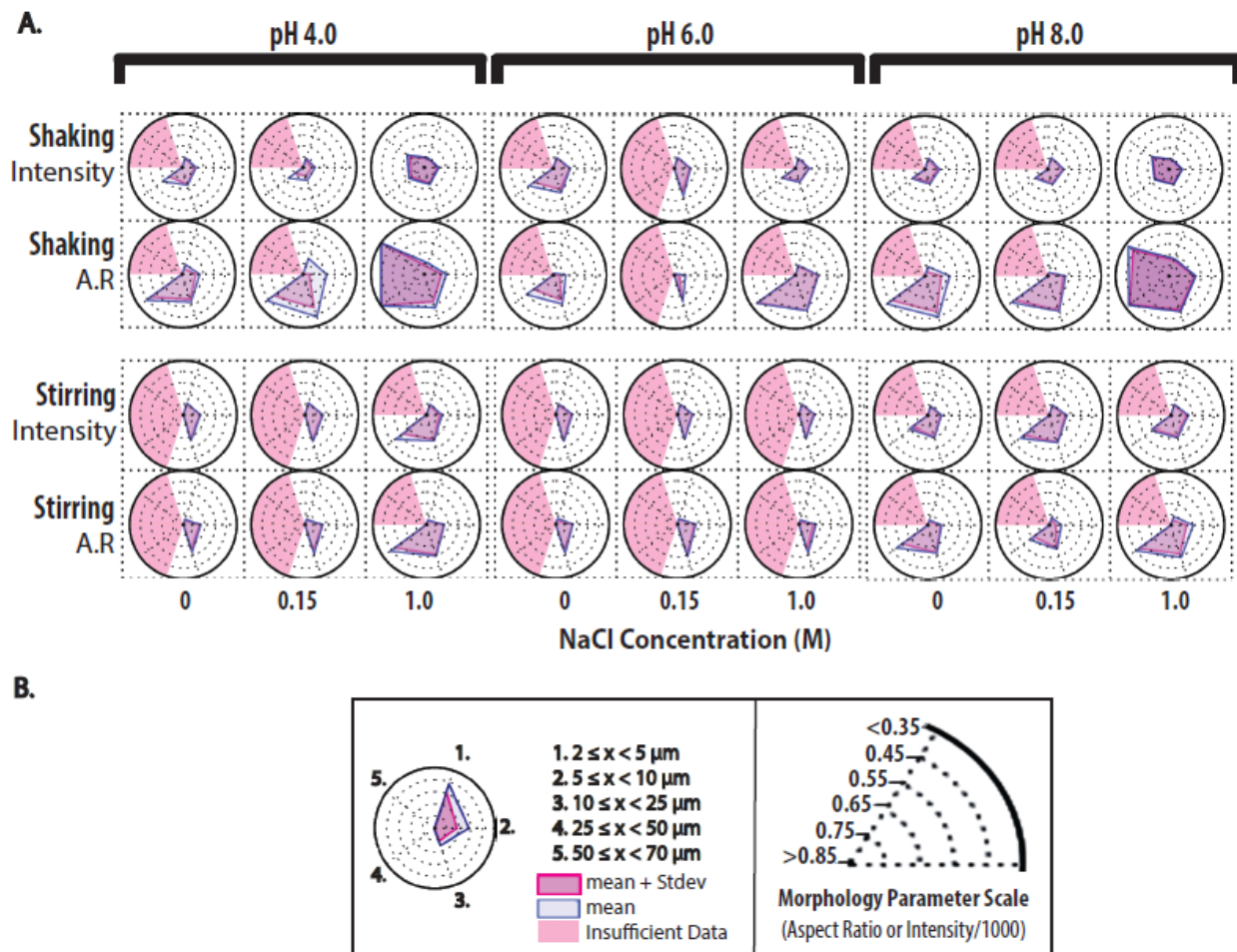
Figure 3.4. The Morphology of Subvisible Particles Formed in Different IgG1 mAb Formulations Subjected to Shaking or Stirring. (A) Radar chart array analysis to evaluate the aspect ratio and intensity of subvisible particles as measured by MFI. The Y-axis denotes the parameter (intensity or aspect ratio) and the stress used (shaking or stirring), the X-axis denotes the NaCl concentration used, the brackets (top) group the formulations by pH. (B) A guide for the quantitative interpretation of the radar chart array in (A). (B, left panel) Each numbered axis represents a size bin grouped using particle ECD. The light blue polygon represents the mean morphology parameter (n=3) for the subvisible particles within each bin. The pale-fuchsia polygon is the mean – standard deviation to provide an indication of variability. An axis shaded

90

in light red denotes that there were insufficient particles (empirically defined as <25 counted) as compared to t=0. (B, right panel) The intensity/1000 or aspect ratio of a particular size range can be determined by the size of the polygon along that axis. If the polygon is invisible along the axis there the parameter is larger than 0.85 in that size range (AR = circular; int = opaque). If the polygon extends to the outer perimeter of the radar chart the parameter is less than 0.35 in that size range (AR = elongated; Int = transparent). Each concentric ring from the center of the radar chart represents a 0.1 decrease in the parameter (increasing elongation or transparency. The axes are linearly connected to clearly visualize a shift in morphology as a change in shape of the corresponding polygon.
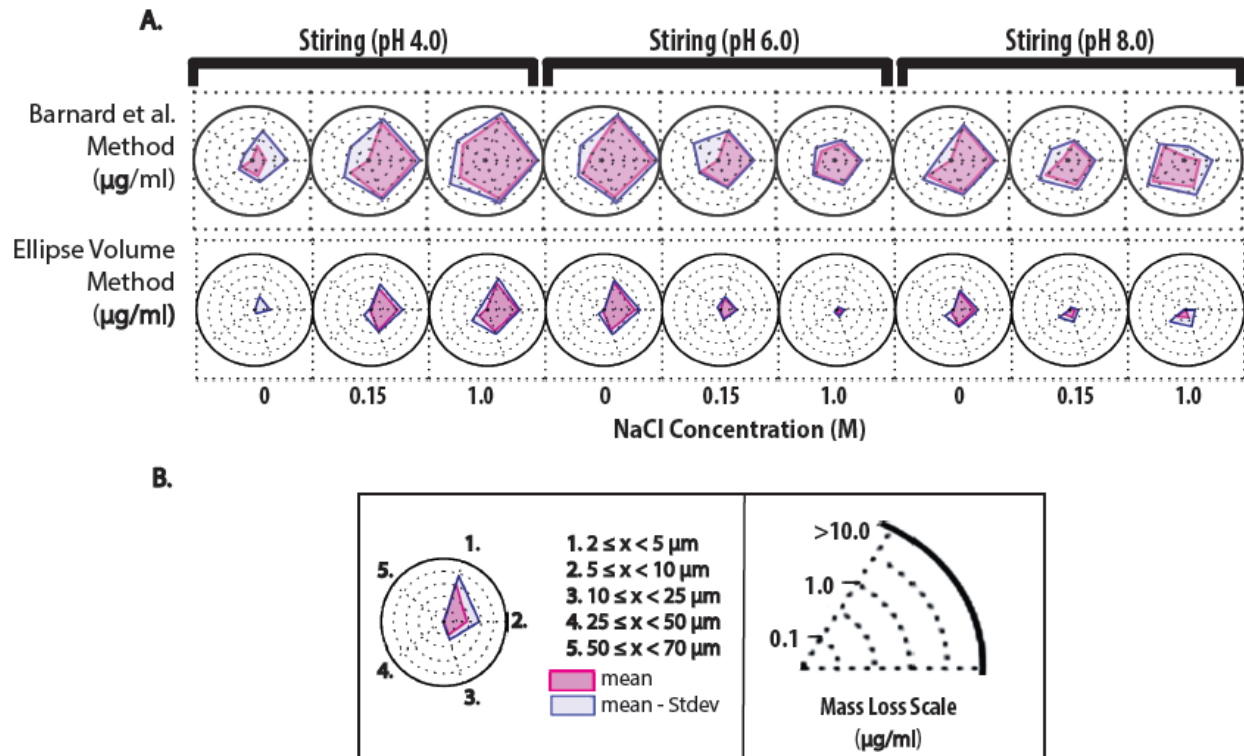
Figure 3.5. Radar chart analysis of the particle mass distributions as a function of particle size as determined by the various calculation methods after stirring different mAb formulations. The mass of particles formed in nine formulations of an IgG1 mAb, n=3, subjected to stirring stress for 2 h, as calculated from MFI data. The Y-axis represents the parameter (i.e., mass calculation method), the X-axis represents the NaCl concentration, and each bracketed group (top) represents a change in pH. (B) Key used for the interpretation of the radar chart array. Each axis in the radar charts corresponds to a particle size range (left panel). The pink polygon represents the mean minus the standard deviation of the parameter, and the blue polygon represents the mean value for the parameter. The radar chart array in (A) uses a defined mass scale (right panel).
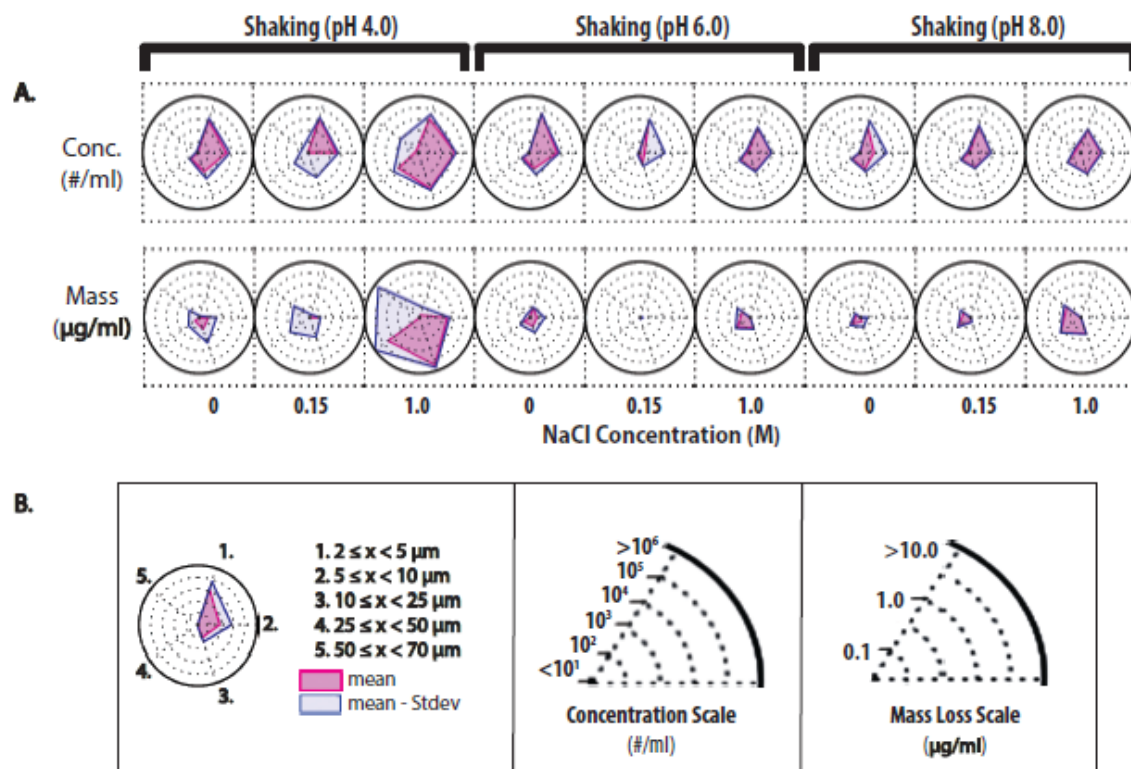
Figure 3.6. **Radar chart analysis of the concentration and calculated mass of particles after shaking different mAb formulations.** (A) Nine formulations of an IgG1, n=3, subjected to shaking stress for 2 h, were evaluated by MFI to determine the concentration and size range of subvisible particles. The Y-axis represents the parameter (i.e. concentration/mass calculation method), the X-axis represents the NaCl concentration, and each bracketed group (top) represents a change in pH. (B) Key used for the interpretation of the radar chart array. Each axis in the radar charts corresponds to a particle size range (left panel). The pink polygon represents the mean minus the standard deviation of the parameter, and the blue polygon represents the mean value for the parameter. The radar chart array in (A) uses a defined concentration scale (middle panel) and mass scale (right panel).

Chapter 4: Evaluating the Role of the Air-Solution Interface on the Mechanism of Subvisible Particle Formation Caused by Mechanical Agitation for an IgG1 mAb[1]

---

[1] This work represents an equal contribution from Cavan Kalonia and Saba Ghazvini, a graduate student from the Bioengineering Department at the University of Kansas under the supervision of Professor Prajnaparamita Dhar. The experiments conducted by Saba are presented to support the conclusions drawn in this chapter.

4.1. Introduction

Protein aggregation and particle formation is a commonly observed degradation pathway of therapeutic mAb drug products, and is a significant cause for concern due to potential adverse effects on product safety and efficacy, either through decreasing potency or by enhancing product immunogenicity (2, 46). Larger protein aggregates, in the size range of >0.1 µm and <100 µm, often called submicron and subvisible protein particles, are widely considered to be important to monitor and control, since particle sizes within this range potentially possess the ability to enhance the efficiency of uptake by antigen presenting cells (1, 12, 13, 96, 159). Characterization of such particles formed by exposure of protein solutions to different stresses (e.g., mechanical, chemical, and thermal) has shown that particles can vary in size, number and shape, as well as the degree of structural perturbation/chemical degradation of protein within the particles, leading to highly heterogeneous samples (66, 70, 113). Preliminary studies attempting to purify fractions of particles based upon size suggest that protein particle immunogenicity potential may be size and concentration dependent as determined by *in vitro* cell-based models (13, 14). As a result, the risk vs. benefit that these protein degradation products pose to patients has emerged as a major consideration during mAb drug formulation design and development (12, 114, 160, 161).

Successful development of protein formulations requires a thorough understanding of protein physical degradation pathways during exposure to different environmental stresses. Numerous studies have resulted in an improved mechanistic understanding of protein aggregation and particle formation in bulk protein solution from a pharmaceutical perspective (44, 59, 162). Models describing protein aggregation and subsequent particle formation in bulk solution typically include nucleation, growth and condensation phases (45, 84, 85) and involve

unfolding and/or association steps. As a result, protein candidates are often formulated to optimize conformational and colloidal stability to reduce the rate of aggregation in bulk solution during manufacturing, storage, transport and administration (4, 71, 163). However, formulation conditions that stabilize some mAbs against aggregation and protein particle formation during thermal stress have been observed to be destabilizing during mechanical agitation(54). Therefore, in addition to evaluating protein interaction mechanisms occurring in the bulk solution, it is also important to consider the air-solution interface as a source of instability for therapeutic protein products (164).

Several recent studies have provided evidence that disruption of a high concentration protein layer at air-solution interface can be responsible for producing protein particles in the bulk solution (62, 91, 92). One of the most common ways to minimize interface induced aggregation of protein molecules has been the addition of nonionic surfactants such as polysorbate 20 or 80 or related surface active compounds(165, 166). Competitive adsorption between the smaller surfactant molecules and the larger protein molecules has been shown to minimize adsorption of the proteins to the air-water interface, thereby reducing protein particle formation at the interface (167). However, polysorbate-based excipients are themselves prone to physicochemical degradation and in some cases may even accelerate the aggregation of certain proteins (168). Other formulation variables such as pH, ionic strength, and poly valent ions have been shown to have a large effect on protein instability during agitation and can impact protein-protein interactions at the air-water interface (118, 169). Therefore, developing a better understanding of how mAb formulation conditions affect air-solution interface mediated particle formation is critical to ultimately reduce the reliance on nonionic surfactant alone to provide stability against agitation induced protein particle formation.

In this work, we seek to further elucidate the mechanism of particle formation initiated at the air-solution interface during mechanical agitation, and to better understand the effect of solution pH and buffer ion type on this aggregation pathway, for a model IgG1 mAb. A Langmuir trough is used to model pharmaceutical instability resulting from mechanical agitation of different formulations of the IgG1 mAb, where controlled compression/dilation cycles ensure that mechanical stresses are applied only to a protein film formed at the air-water interface. Analysis of protein particles formed in the bulk solution after compression/dilation cycles are correlated with high resolution atomic microscopy images of protein films at the interface, to better understand how protein aggregates at the air-solution interface effect the amount of particles present in the bulk solution. In addition, we evaluate the role of formulation conditions on extent of particle formation for this IgG1 mAb at the air-solution interface, with and without mechanical stress, and correlate our results with surface pressure measurements.

4.2. Experimental Procedures

4.2.1. Materials and Sample Preparation

The IgG1 mAb (pI range around ~ 9) used in this study was provided by Janssen Research & Development, LLC (Horsham, Pennsylvania) at a concentration of ~40 mg/ml. Stock buffers of 50 mM citrate and 50 mM histidine were prepared at pH 4.5 and 6.5. The L-histidine was purchased from Sigma-Aldrich (St. Louis, Missouri) and the sodium citrate dihydrate and citric acid anhydrous were purchased from Fisher Scientific (Hampton, New Hampshire). Additionally, 1x phosphate buffered saline (PBS) buffer (Fisher Scientific, Hampton, New Hampshire) was prepared at pH 7.4 according to the manufacturer's recipe, and a second preparation of 1x PBS buffer was titrated using hydrochloric acid to a pH of ~4.5. All

stock buffers were prepared using Milli-Q water (EMD Millipore, Billerica, Massachusetts) and sterile filtered using a 0.2 μm filter.

4.2.2. Mechanical Agitation Studies

The mAb solution was diluted 1:40x into each of the stock buffers to generate working mAb solutions of 1.0 mg/ml. The working mAb solutions were gently inverted and allowed to sit for half an hour to ensure proper mixing. Three ml aliquots of each working solution were pipetted into 37.7×16.75 mm glass vials (Schott, Lebanon, Pennsylvania) and capped with uncoated rubber stoppers (West Pharmaceutical Services, Exton, Pennsylvania). The mAb solutions were agitated using a HS 260 shaker (IKA Works, Inc., Wilmington, North Carolina) at 300 cycles/minute as described previously (70). The aliquots for each formulation condition were agitated for 0, 1 or 3 days (N=3 for each time point).

4.2.3. Interfacial Compression-Expansion Studies[2]

Working IgG1 mAb solutions at 0.37mg/ml were prepared by adding 370 μl of mAb stock solution to 40 ml of buffer (PBS, histidine, or citrate). Working solutions were loaded into a Langmuir trough that was controlled at $23 \pm 2°C$ (Biolin Scientific Inc., Stockholm, Sweden). A Wilhelmy plate was used to measure surface pressure during adsorption and compression-expansion experiments. The compression-expansion cycles began after a 2hr period for adsorption to become saturated. The available interfacial area changed from 87 to 12 cm^2 during each compression-expansion cycle by moving the barriers of the Langmuir trough. The compression ratio, defined as the ratio of the maximum possible area and the minimum area of the trough ($CR=A_{max}/A_{min}$), was held constant at 7.25 for this study. For mAb samples prepared

---

[2] The work described in this section was performed by Saba Ghazvini from the Bioengineering Department at the University of Kansas. The work is included in this thesis to support the conclusions drawn in this chapter.

in 1x PBS, the "slow" compression-expansion rate was 50 cycles/6 hours and the "fast" compression-expansion rate was 750 cycles/6 hours. For the mAb samples prepared in histidine or citrate buffers, the "slow" compression-expansion rate was 50 cycles/6 hours and the "fast" compression-expansion rate was 1000 cycles/6 hours.

4.2.4. Size-Exclusion Chromatography

A Prominence UFLC HPLC (Shimadzu, Kyoto, Japan) with a diode array detector was used with a TSKgel G3000SWx1 stainless steel column (Tosoh Biosciences, San Francisco, California) and TSKgel SWxI guard column for size exclusion chromatography. The column was operated at 30°C and separation was achieved at a flow rate of 0.7 ml/min. The areas of the stressed sample chromatograms were normalized to the total area of the unstressed sample chromatograms to detect a loss of total area. A pH 6.8, 0.2 M phosphate buffer was selected as the mobile phase because the buffer has been shown to minimize protein adsorption to the column (133).

4.2.5. Flow Microscopy

A VS Series FlowCam (Fluid Imaging Technologies, Scarborough, Maine) benchtop flow microscope was used to count and characterize particles ≥ 1 μm but ≤ 100 μm in area based diameter (ABD). A 10x objective was used with a 100 μm x 2 mm flow cell. The sample volume analyzed was 0.5 ml, the flow rate was 0.15 ml/min, and the capture speed was set at 21 frames per second. Prior to measurement, the instrument was focused using NIST traceable 25 μm Duke Standards (Thermo Fisher Scientific, Waltham, Massachusetts).

4.2.6. Atomic Force Microscopy (AFM) [3]

Freshly cleaved mica (Ted pella Inc., Redding, CA) was used as a support to obtain high resolution images of IgG1 mAb particles isolated from the air-solution interface and the bulk solution. Transferring the IgG1 mAb particles from interface was done by briefly contacting the mica to the air-solution interface. Mica sheets containing mAb particles from the bulk solution were prepared by placing the freshly cleaved mica sheet at the bottom of the trough prior to compression-expansion cycles and collected afterwards. Once collected, the mica sheet for the mAb samples in citrate/histidine were immediately washed with Milli-Q water and dried with compressed air at $23 \pm 2\ ^{\circ}C$. The mica sheets for the mAb samples in 1x PBS were also washed with pH 7.0 acetate buffer prior to drying. The AFM setup used was a Veeco MultiMode V (Veeco Instruments Inc., Plainview, NY). All AFM measurements were performed in a tapping mode using silicon probes (TAP150 Bruker) with a spring constant of 5 Nm^{-1} at 150 kHz. Height analysis of the AFM images was done using Research NanoScope v7.30 (Veeco Instruments Inc., Plainview, NY). Imaging was done in a temperature controlled room maintained at $20^{\circ}C$. To evaluate the height of mAb particles analyzed by AFM, 3 images were collected from each mica sheet prepared during Langmuir trough experiments (N=3 for each sample condition). The combined data points for each condition were plotted as box plots.

4.2.7. Fourier Transform Infrared Microscopy (FTIR)

A Vertex 70 FTIR and Hyperion microscope equipped with a 15x objective (Bruker, Billerica, Massachusetts) were used to image particles isolated from solution and measure their FTIR spectra. Particles were isolated using gold filters with a pore size of 5 µm (Pall

---

[3] The work described in this section was performed by Saba Ghazvini from the Bioengineering Department at the University of Kansas. The work is included in this thesis to support the conclusions drawn in this chapter.

Corporation, Port Washington, New York). Heat-denatured controls were prepared by heating 1 mg/ml mAb in pH 7.4 1x PBS at 90°C for 15 min. Native mAb control FTIR spectra were obtained by performing solution measurements on 5 mg/ml mAb in pH 7.4 1x PBS using the BIO-ATR II attachment for the Vertex 70 FTIR.

4.3. Results

To better understand how protein particle formation is occurring at the air-solution interface during mechanical agitation, a Langmuir trough experimental setup was used where an IgG1 mAb solution is exposed to controlled compression/dilation cycles resulting in mechanical stresses applied only at the air-water interface, and not in the bulk protein solution. These results are then compared to agitation of the same mAb solution filled into glass vials. Figure 4.1 provides an overview of the experimental setup and the Langmuir trough instrument. In both cases, changes in interfacial area available are hypothesized to disrupt the adsorbed mAb layer at the air-solution interface and potentially result in the release of particles into the bulk solution as shown schematically in Figure 4.1.

4.3.1. Particle Formation in the Bulk Solution During Mechanical Agitation in PBS Buffer

First, unstressed mAb samples (0 day), formulated in pH 4.5 or pH 7.4 PBS buffer, were analyzed for levels of protein subvisible particles by flow microscopy and were found to contain >300 subvisible particles/mL with most particles in the 2-5 μm and 5-10 μm particle size range (Figure 4.2, bottom panel). After 3 days of side-to-side shaking in glass vials, however, both mAb samples showed a large, significant increase in particles in the bulk solution, with the mAbs samples at pH 4.5 containing more particles compared to the mAb samples at pH 7.4

(Figure 4.2, top panel). Moreover, particles formed in the agitated mAb sample at pH 4.5 were distributed across the size ranges analyzed. The particle size distribution is shown on a logarithmic scale in Figure 4.2 and can be visualized from the shape of the polygon signal of the radar chart. The average number of particles per ml in the pH 4.5 mAb samples was greater than 100,000 for particles 2-5 μm, ~100,000 for particles 5-10 μm, and ~10,000 for particles ranging in size from 10-15, 15-25, 25-40, 40-50, and 50-100 μm. The mAb sample at pH 7.4, on the other hand, did not have significant particle formation for sizes greater than 25 μm as compared to the unstressed sample (Figure 4.2, top right panel). The average number of particles per ml in the pH 7.4 mAb samples was less than 10,000 for particles ranging from 2-5 μm and 5-10 μm, and less than 1,000 for particles ranging from 10-15 μm and 15-25 μm.

The unstressed and mechanically agitated (at 1 and 3 days) mAb samples in PBS buffer were also analyzed using size exclusion chromatography (SEC). The mAb sample at pH 4.5 had ~1.0 ± 0.3 % monomer loss (N=3) whereas the mAb sample at pH 7.4 did not have significant monomer loss over the 3 days of agitation. Additionally, no high molecular weight species (HMWS) or mAb fragments were observed by SEC (see Figures 4.3 and 4.4 for representative chromatograms and SEC stability data).

4.3.2. Surface Properties of mAb Samples in PBS Buffer [4]

As a next step, we then established techniques to correlate these observed differences in particle formation with differences in the interfacial properties of these mAb samples, in the absence and presence of applied stress to the interface. As shown in Figure 4.5A, the surface pressure-area (Π-A) isotherm of mAb solutions in PBS buffer at pH 7.4 was subjected to slow compression-expansion cycles. Theoretically, the measured surface pressure corresponds to

---

[4] The work described in this section was performed by Saba Ghazvini from the Bioengineering Department at the University of Kansas. The work is included in this thesis to support the conclusions drawn in this chapter.

possible adsorption and rearrangement of mAb molecules at the interface(92, 170).   Upon

decreasing the interfacial area, the surface pressure increases (or the surface tension) decreases

non-linearly. Interfacial area expansion after a compression cycle resulted in an abrupt decrease

in the surface pressure causing a visible hysteresis pattern. The surface pressure at the beginning

of first cycle corresponds to the equilibrium saturation value that was reached after the proteins

were allowed to adsorb to the interface and equilibrate for two hours. This saturation value was

not reached during compression-expansion cycles, because the proteins did not have enough time

to reach their equilibrium value during continuous compression-expansion cycles. The

maximum surface pressure at minimum interfacial area was also found to be the maximum for

the first cycle and decreased steadily over the 50 cycles reported here. Figure 4.6 shows

negligible increase of surface pressure with time for protein-free polysorbate samples at 0.00012

wt% (corresponds to the concentration of polysorbate in the mAb solutions being studied) during

adsorption studies. Similarly, Π-A isotherm studies show that the polysorbate solution itself is

compressible further establishing that the increase in measured surface pressure may be

attributed to the presence of mAb proteins at the air-solution interface.

Figure 4.5B presents the first and last cycle for compression-expansion isotherms plotted

for mAb solutions in PBS buffer at both pH 4.5 and pH 7.4. The hysteresis was found to be

greater in the first cycle compared to the last cycle for both sample conditions. The first (blue

and red) and last (black and pink) cycles in the surface pressure vs. area isotherms overlapped

with no statistically significant difference for the two conditions (Figure 4.5B). Additionally, the

initial and final surface pressures were higher for the first cycle compared to the last cycle for

both sample conditions. Figure 4.5C presents the average area under the isotherm curves for the

first and last cycle of mAb samples in PBS buffer at pH 4.5 and 7.4, used as a measure of the

total hysteresis in these protein films. The average value (N=3) of the total area under the curve for the first cycle was higher than that for the last cycle but the difference was not statistically significant. To investigate the effect of time of exposure of mAb samples to the air-solution interface during compression-expansion cycles, we compared 50 cycles of slow (6 hours) and fast (25 min) rate (Figure 4.6 panel C and D). To further investigate how the rate of the compression influenced the compression-expansion isotherms, we compared the surface pressure vs area isotherms for the 1st and 50th cycles corresponding to compression for 6 hours or 25 minutes (fast). While no difference seen for the first cycles, the 50th cycle shows more hysteresis.

4.3.3. The Effect of Compression Rate on Particle Formation at the Air-Protein Solution Interface and in Bulk Solution

The number and size distribution of subvisible sized protein particles in the bulk solution, as measured by flow digital imaging, for mAb samples at pH 4.5 and pH 7.4 after being subjected to slow (A) or fast (B) compression-expansion cycles during 6 hours in the Langmuir trough, are shown in Figures 4.7A and 4.7B, respectively. The same mAb solutions that were not subjected to the compression/dilatational stresses, but for which all other environment conditions were kept identical (temperature, time of incubation, formulation pH) were used as control samples (Figure 4.7, Panel A/B, red signal). Results show no statistically significant differences between the number and size distribution of particles in the bulk mAb samples subjected to the slow compression-expansion rate when compared to the corresponding control samples. Moreover, the control mAb samples at both pH conditions had similar numbers of particles detected in the bulk solution. In contrast, mAb protein solutions that were subjected to fast interfacial compressive stresses for 6 hours, demonstrated more than an order of magnitude increase in the number of protein subvisible particles detected in the bulk solution. Further, the

104

stressed mAb samples at pH 4.5 were found to contain a broader size range of particles (up to 50 μm), when compared with mAb samples at pH 7.4.

4.3.3.1 Atomic Force Microscopy Results [5]

Representative atomic force microscopy (AFM) images of mAb particle formation at the interface and in the bulk mAb solution, for both stressed mAb samples in PBS buffer at the two pHs, are presented in Figure 4.7, panel C and D. For the slow compression-expansion rate (Panel C), the protein films transferred from the air-water interface contained greater number of protein aggregates compared with mica surfaces placed in the bulk mAb solution, irrespective of the solution pH. In contrast, mica sheets placed in bulk mAb solutions that were subjected to fast compression expansion cycles (Panel D), contained greater number of micron and sub-micron protein aggregates when compared with films transferred from the air-solution interface. Additionally, the mAb pH 4.5 solutions, after being subjected to fast compression-expansion cycles, contained more particles at the interface and in the bulk solution, when compared to the pH 7.4 mAb solutions. Figure 4.8 also shows that the total time of compression, or number of total compression-expansion cycles, plays an important role. Keeping the total number of cycles constant, but applying stress at different rates (slow vs fast), we find that the total number and size distribution of mAb particles is not different both at bulk solution (Figure 4.8 panel A,B) and at the interface (Figure 4.8 panel C, D).

In panels E and F of Figure 4.7, box plots displaying the height (median and range) of mAb particles as measured by AFM are presented to quantitatively compare the AFM images (N=9 for each condition). For the slow compression-expansion rate (Panel E), the box plot of the height of protein particles at the interface of the pH 4.5 mAb sample had a higher median value

---

[5] The work described in this section was performed by Saba Ghazvini from the Bioengineering Department at the University of Kansas. The work is included in this thesis to support the conclusions drawn in this chapter.

than the box plot of the interface for the mAb sample at pH 7.4. For the bulk mAb solutions, the range of protein particle height data is much smaller compared to the range of particle height results at the interface. It should be pointed out that areas that did not contain any particles or a lesser number of particles were included in the analysis thereby exacerbating the apparent standard deviations shown in Figure 4.7E and 4.7F. For the mAb samples exposed to fast compression-expansion rate (Figure 4.7, Panel F), AFM results had similar median values for the height of mAb particles at the interface compared to the mAb samples exposed to low compression-expansion at both pH 4.5 and 7.4 conditions. Furthermore, the median value and the range of the particle height data from AFM for particles in bulk solution were similar between the fast and slow compression rates for the pH 7.4 mAb samples. However, the median and range of height data from AFM analysis of particles in bulk solution increased significantly for mAb pH 4.5 samples that were subjected to fast compression.

4.3.4. Qualitative Comparison of the Morphology of mAb Particles Formed During Mechanical Agitation vs. Interfacial Compression-Expansion

To further compare and characterize the protein particles formed during compression-expansion cycles in the Langmuir trough vs. particles formed during agitation in vials, particle morphology data from flow microscopy digital images were analyzed. Circularity (Hu), a measure of particle perimeter relative to a circle of equivalent area, and aspect ratio, a measure of elongation, were evaluated for particles formed by the two stresses and compared to theoretical values for prolate ellipsoids with varying aspect ratios (Figure 4.9)(104). The solid blue curve is a calculation, described previously from Kalonia et al. 2015, that determines the circularity of theoretical prolate ellipses based on the aspect ratio and is meant to be used as a reference point for characterizing particle morphology as described previously (54). For example, at the

coordinate (1, 1) in Figure 4.9, the blue curve represents a perfectly circular particle. As the

aspect ratio decreases, particle elongation increases and positive deviations from the curve

represent the particle having a larger perimeter than an ellipse of equal aspect ratio (typically

indicating an increase in surface roughness/fractal dimension). The subvisible sized protein

particles detected in the mAb sample subjected to fast compression-expansion were ellipse-like

(circularity and aspect ratios close to the theoretical ellipse curve) and ranged from 1x elongation

to 3x elongation relative to a circular particle of equal area (Figure 4.9, Panel A). Protein

particles generated by side-to-side agitation of the same mAb solution, on the other hand, were

more elongated on average (up to 20x relative to a circular particle of equal area) and were not as

ellipse-like as they showed positive deviations from the theoretical ellipse curve (Figure 4.9,

Panel B) as compared to the same mAb sample exposed to compression in the Langmuir trough

(see Figure 4.10).

Several representative protein particle images from flow microscopy analysis are

presented in Figure 4.9C for a mAb sample subjected to fast compression-expansion in the

Langmuir trough. The protein particles appear to be compact and circular/ellipse-like, consistent

with results as seen in the corresponding morphology scatter plot (Figure 4.9A). On the other

hand, the representative images of protein particles detected in the side-to-side agitated mAb

samples (Figure 4.9, Panel D) appear to be loose, tenuous structures with rough perimeters. The

images of the protein particles caused by agitation of the mAb solution in vials are also

consistent with scatter plot data which showed positive deviations from the theoretical ellipse

curve (Figure 4.9B). Additionally we compared overall secondary structure of the mAb

particles, formed during fast compression, using solution FTIR and FTIR microscopy (Figure

4.11). Comparing interfacial stress-induced mAb particles with control and denatured (by heat)

mAb samples, a slight shift in second-derivative FTIR spectra is monitored in two peaks for intramolecular beta-sheet content (occurring between 1620-1640 and 1690-1700 cm^{-1}) (N=3) (Figure 4.11).

4.3.5. Analysis of the Surface Activity and Surface Pressure vs. Area Isotherms for mAb Samples in Histidine or Citrate Buffer [6]

The previous section presented data for an IgG1 mAb in PBS buffer at two different pH values. As a next step, the effect of histidine and citrate buffers on the aggregation propensity of the same IgG1 mAb was examined. The surface pressure-area (Π-A) isotherm of mAb solutions in citrate buffer at pH 6.5 subjected to dilation cycles at a slow compression-expansion rate as shown in Figure 4.10A. Similar to mAb formulated in PBS buffer, the initial surface pressure value corresponds to the value of the saturated surface pressure after 2 hours of adsorption. The initial and final surface pressures at the minimum and maximum interfacial area during compression-expansion cycles decreased over the 50 cycles.

Figure 4.10, Panel B shows the surface pressure change with change in interfacial area during the first and last (50th) cycles for pH 4.5 and 6.5 mAb samples formulated in citrate buffer. Obvious changes in the shape of the curves as well as the values of the surface pressure were recorded in these samples. The mAb solution in citrate buffer at pH 4.5 demonstrated the maximum protein film compressibility (maximum change in surface pressure with changes in the trough area), while the mAb formulated citrate buffer at pH 6.5 showed protein films at the air-water interface were the least compressible films. Further, for each of the excipient solutions, the

---

lower pH solutions demonstrated increased protein film compressibility at the air-solution interface.

Figure 4.10, Panel C presents a quantitative comparison of the average area (N=3) within the surface pressure vs. area curves during the first and last compression-expansion cycles for mAb samples at pH 4.5 and 6.5 in histidine or citrate buffers. Such measurements represent differences in the hysteresis present in the mAb protein films. The difference between the hysteresis of the first and last compression-expansion cycle was significant for all conditions assessed ($p < 0.005$). In addition, the area under the curve for the first compression-expansion cycle for mAb samples was larger when formulated in buffers at pH 4.5 than at pH 6.5, regardless of the buffer ion type (citrate vs. histidine). Most notably, the area under the isotherms for mAb samples in citrate buffer at pH 4.5 is significantly higher than all the other conditions studied ($p < 0.05$). A summary of the statistical analysis of the differences in these areas is presented in Figure 4.10, Panel D.

4.3.6. The Effect of pH and Buffer Composition of mAb Solution on Particle Formation at the Air-Solution Interface for the Slow Compression Rate [7]

To further explore the interfacial mAb particle formation process, topographical AFM images of protein films transferred from the air-solution interface were recorded. Representative images are presented in Figure 4.12 (top panel). Control mAb samples were incubated at room temperature without the application of interfacial stress. Irrespective of the buffer composition and pH of the mAb samples, the extent of protein aggregates formed at the air-solution interface (represented with lighter colors) was greater after being subjected to compression–expansion

---

[7] The work described in this section was performed by Saba Ghazvini from the Bioengineering Department at the University of Kansas. The work is included in this thesis to support the conclusions drawn in this chapter.

cycles, compared to their corresponding control samples. Additionally, several raised/aggregated features in the AFM images were recorded for proteins at the air-solution interface of compressed mAb samples in citrate buffer compared to histidine, irrespective of the solution pH.

Figure 4.12 (bottom panel) presents a box plot analysis of the height (median and range) of AFM images of mAb particles formed in histidine and citrate buffers at pH 4.5 and 6.5. Comparing the protein particles of control mAb samples there was no significant increase in particle height within the formulation by changing the pH (comparing AFM images A with C as well as E with G). However, when comparing the AFM images of the protein particle formed at the interface of compressed mAb samples, by decreasing the solution pH, the median value of protein particle height from the AFM images increases for mAb samples in both histidine and citrate (comparing AFM images B with D as well as F with H). Compressed mAb samples in citrate buffer at air-solution interface had higher median value and range of particle height compared to mAb solution in histidine buffer (AFM images F and H compared to B and D).

4.3.7. The Effect of pH and Buffer Composition of mAb Solution on Particle Number/Size Distribution in Bulk Solution After Compression-Expansion or Agitation

An analysis of particle formation in the bulk mAb solutions filled in glass vials, before and after 3 days of side-to-side agitation, showed that all four of the mAb samples had substantial particle formation in the bulk, when compared to the unstressed (0 day) control (Figure 4.13, top panel). The mAb solution in citrate buffer at pH 4.5 formed the most subvisible particles as compared to the other three mAb samples (pH 4.5 and 6.5 in histidine buffer and pH 6.5 in citrate buffer). After agitation, the mAb sample in citrate buffer at pH 4.5 had over 100,000 particles per ml from 2-5 μm, ~100,000 particles in each size range from 5-10 μm and

10-15 µm, and ~10,000 particles in each size range from 15-25, 25-40, 40-50, and 50-100 µm. On the other hand, the amount and size distribution of particles in the agitated mAb samples in histidine buffer at pH 4.5 and 6.5, as well as the agitated mAb samples in citrate buffer pH 6.5, were comparable and contained ~10,000 particles per ml from 2-5 µm, ~1,000 particles/ml in each range from 5-10, 10-15, and 15-25 µm, and less than 1,000 particles/ml in each of the larger size ranges. Additionally, the unstressed and mechanically agitated (at 1 and 3 days) mAb samples in citrate and histidine buffer were also analyzed using size exclusion chromatography (SEC) (Figure 4.11). The mAb sample in citrate buffer at pH 4.5 had ~2.0 ± 0.7 % monomer loss (N=3) whereas the mAb samples at pH 6.5 in citrate buffer and histidine buffer (both pH values) did not have significant monomer loss over the 3 days of agitation.

In addition to agitation in vials, mAb samples formulated in the same buffer conditions were subjected to controlled fast or slow compression-expansion rates in the Langmuir trough (see Experimental Procedures). Particle numbers were evaluated for the above conditions (Figure 4.13, bottom panel, black signals) and for a control where the same sample mAb formulations were incubated at room temperature for the same amount of time. Similar to results described above with the mAb samples in the PBS buffer, slow compression of the same mAb in the histidine and citrate buffers did not result in a statistically significant difference in the number of particles in bulk solution as compared to the control samples. On the other hand, the fast compression-expansion caused significant increases in levels of particle observed versus the control samples for all four mAb samples. Interestingly, the mAb samples in histidine buffer at pH 4.5 and 6.5, as well as mAb in citrate buffer at pH 6.5, had similar levels of particles after fast compression. The mAb sample in citrate buffer at pH 4.5 generated the greatest number of subvisible particles as well as larger sized particles compared to the other mAb sample

conditions subjected to fast compression. After the fast compression-expansion cycles, the mAb

sample in citrate buffer at pH 4.5 had over 10,000 particles per ml from 2-5 μm, ~10,000

particles in each size range from 5-10 μm and 10-15 μm, and 15-25 μm, and ~1,000 particles in

each range from 25-40, 40-50, and 50-100 μm (Figure 4.13, bottom panel, black signal).

4.4. Discussion

The primary focus of this work was to elucidate the correlation between interfacial stress

induced protein clustering at air-water interfaces and mechanical agitation induced protein

particle formation in bulk mAb solutions. Specifically, a Langmuir trough was used to induce

controlled dilatational stress to protein films at the air-water interface, while high resolution

imaging techniques were used to characterize, in more detail, protein particles formed at the

interface (by AFM), and in the bulk solution (by flow digital imaging). Using Langmuir troughs

to apply a compression/dilatation stress to mAb protein films at the air-water interface was

recently described by Bee *et al.*, to mimic changes in available surface area during agitation(62).

The Langmuir trough ensures that only protein molecules at the interface, and not the bulk

solution, are subjected to controlled stresses. This isolation of the bulk and interfacial stresses

allowed for correlations to be developed between formation of protein particles in these two

different environments with our model IgG1 mAb (see Figure 4.1 for a schematic of proposed

correlation). In this work, we also explored how changes in the bulk mAb solution conditions

and formulation composition contributed to differences in the formation and morphology of

protein aggregates at the air-solution interface. Based on our results, we conclude that while

interfacial stress initiates protein aggregation at the air-solution interface, the presence of protein

particles in the bulk mAb solution formed as a result of mechanical agitation is only correlated

with mAb solutions subjected to "fast" compression/dilatation cycles over an equal length of

time. Further, both the solution pH and buffer composition control the morphology and size distribution of protein particles formed at the interface and in the bulk solution for this IgG1 mAb. These conclusions are discussed in more detail below.

Based on a combination of light scattering and calorimetry characterization studies (data not shown), the four selected solution conditions (citrate and histidine buffer at pH 4.5 and 6.5) result in a range of conformational and colloidal stability values for this IgG1 mAb. The lack of correlation between the mAb's biophysical parameters under these conditions (such as normalized second virial coefficient data from static light scattering and the apparent thermal onset and melting temperature obtained from DSC) and protein particle formation during thermal incubation will be described in an companion manuscript (Chapter 5). Since mAb samples in histidine and citrate buffer at pH 4.5 and 6.5 are representative of a range of physical stability properties in the bulk solution, differences in protein-protein interactions at the air-water interface, and not conformational and colloidal stability, better predict the physical stability of mAb samples subjected to the mechanical stresses. In this paper we describe methodologies to thoroughly characterize the protein films formed at the air-water interface (e.g., Langmuir trough data and atomic force microscopy analysis) with this IgG1 mAb in PBS buffer (pH 4.5 and 7.4), in the absence and presence of interfacial stress, to better correlate the observed changes in particle formation in bulk mAb solutions to differences in interfacial protein film properties. We then not only examine the effect of solution pH and buffer ion types (histidine and citrate buffers at pH 4.5 and 6.5) on the propensity of this IgG1 mAb to form aggregates and particles at the interface and in bulk solution, but also evaluate their effects on the resulting protein particle number, size and morphology.

4.4.1. Analysis of Surface Pressure Changes During Compression-Expansion Cycles [8]

As a first step towards analyzing interfacial phenomenon in various solutions of this gG1 mAb, we measured the surface activity of the protein films in a Langmuir trough experimental setup (Figure 4.1). The equilibrium surface pressure measurements show that even at a concentration of 0.37 mg/ml, the IgG1 mAb samples were surface active when formulated in different buffers and pH values. These results suggest that surface pressure measurements alone do not correlate with protein particle formation. Shieh *et al.* have recently shown, in fact, that equilibrium surface pressure values were not an adequate predictor of a different mAb sample's susceptibility to aggregate (92). Instead, the kinetics of antibody rearrangement after adsorbing to the interface was shown to be better correlated with the extent of observed aggregation(92). In this work, we present a comparison of how differences in the application of surface stresses, as well as protein solution composition, influence protein particle formation in the bulk solution. Particularly, surface pressure vs. area isotherms during the compression-expansion cycles were recorded and analyzed in detail to determine evidence of strong attractive antibody-antibody interactions that may result from mechanical agitation or stresses. Specifically, we compared the difference between the hysteresis of the first and last cycle of surface pressure vs. area isotherms that could potentially indicate the extent of particle loss from the interface. The isotherms indicate the formation of an incompressible film at the interface while the hysteresis indicates the likely possibility of formation of irreversible protein associations during a compression-expansion cycle. Further, mAb samples in citrate buffer at pH 4.5 were found to possess the largest difference in hysteresis between first and last cycles, suggesting the most associations

---

[8] The work described in this section was performed by Saba Ghazvini from the Bioengineering Department at the University of Kansas. The work is included in this thesis to support the conclusions drawn in this chapter.

between the proteins at the air-water interface in this solution. Figure 4.6 also conclusively established that the observed phenomena are due to protein-protein interactions, and not due to the presence of surfactant (polysorbate).

4.4.2. Analysis of Protein Particles Formed at the Air-Water Interface or in Bulk Solution

The analysis of the interfacial properties of the protein films were complemented with high resolution AFM imaging of protein aggregates. Our AFM images confirmed the formation of protein aggregates at the air-water interface in mAb samples that were mechanically stressed in the Langmuir trough. The lack of any notable raised features in the AFM images of mAb samples not subjected to mechanical stresses confirmed that application of interfacial stresses was the key to protein aggregate formation at the air-protein solution interface. It was also interesting to note that protein films transferred from mAb solutions in citrate buffer at pH 4.5 produced the maximum number of protein aggregates, particularly fold-like fibrils, that resemble collapsed protein, polymer or lipid films at air-water interfaces, when they are subjected to very high compression(171, 172) . Therefore, both the presence of compressive stresses, as well as different bulk mAb solution composition (pH and buffer ion type) contributes to the protein aggregate formation at the air-solution interface. [9]

Differences in the formation of protein particles in bulk solution, as measured by radar chart analysis of digital flow imaging data, for the slow and fast compressions, together with the AFM images of the protein aggregates at the interface and bulk solution for slow and fast compressions, establish that in addition to being subjected to interfacial stresses, the protein

---

[9] The work described in this paragraph was performed by Saba Ghazvini from the Bioengineering Department at the University of Kansas. The work is included in this thesis to support the conclusions drawn in this chapter.

particles can be lost from the interface into the bulk and serve as nucleation points only if the interface is sufficiently perturbed. When the number of cycles was kept constant at 50, but the stress was applied for different amounts of time, no difference is observed in the formation of mAb particles, at the interface or in the bulk, further establishing the need for extensive perturbation of the interface. Additionally, hysteresis in the protein films corresponds well with presence of protein particles in bulk protein samples. For example, not only did the mAb sample in citrate buffer at pH 4.5 have the largest difference in hysteresis, suggesting the highest protein-protein associations, the bulk mAb solution for this formulation also had the highest particle formation among mechanically agitated samples (see Figure 4.13). These observations, along with the direct visual evidence of protein aggregates at mechanically stressed air-protein solution interfaces, further establish that while mechanical agitation to the interfacial protein film alone is sufficient to cause protein particle formation, even in relatively dilute solutions of this IgG1 mAb, continuous and aggressive disruption of the interfacial film is also necessary for more extensive protein particle formation in the bulk mAb solution.

Further analysis of the high resolution AFM images of the protein films transferred from the air-water interface suggest that protein particles present at air-water interface of mAb samples formulated in citrate buffer were more fibril-like compared to protein particles present in mAb samples in PBS buffer and larger compared to fibrils formed in mAb samples in histidine buffer (see Fig. 4.7 and 4.12). Interestingly, similar fibril/filament morphology of protein particles with a different mAb in citrate buffer has been reported using other techniques such as electron scanning imaging (88, 173). Interestingly, subvisible particle images of our model IgG1 mAb particles in bulk solution, using flow digital imaging measurements, showed similar fibril morphology for mAb samples in citrate buffer, which further suggests the possibility of

116

detachment of mAb particles from the interface to the bulk solution. Additionally, the compact morphology of mAb particles formed as a result of interfacial stresses compared to those formed by agitation of the same mAb samples in glass vials (Figure 4.9) suggests that the larger compression ratio of the Langmuir trough compared to vials possibly influences the morphology of the observed protein particles in these mAb samples. Differences in the rate and nature of interfacial perturbation between shaking and interfacial compression-expansion cycles could also be responsible for the different particle morphologies observed. Protein molecules that associate rapidly tend to form loose, tenuous aggregate structures whereas molecules that associate slowly have more time to reorient and tend to form more compact aggregates (174).

4.4.3. Impact of Buffer Ion and pH Conditions of mAb Samples on Protein Particle Formation

To better explain the observed differences in the morphology and number of protein particles formed at the air-solution interface, we turn our attention to protein-protein interactions observed in highly concentrated bulk protein solutions. Although one might argue that the bulk protein solution in our studies is very dilute, the two-dimensional air-water interface is in fact highly concentrated, because of the saturation of this interface with protein molecules. Literature survey of highly concentrated mAb protein solution suggests that increased protein-protein interactions in highly concentrated mAb solutions can in fact be correlated with bulk viscosity measurements at high protein concentrations (88, 173, 175-177). For example, Esue *et al.* reported on the appearance of large bulk elasticity for a mAb solution in citrate buffer at a mAb concentration higher than 25 mg/ml at pH 6.0. The elastic modulus of the protein solution was not affected by ionic strength of the formulation but concentration of carboxylate ions (88). On the other hand, decreases in bulk viscosity of mAb samples in histidine buffer have been reported

117

at pH 6.0 (175-177). Esue *et al.* further reported that while the highest elastic modulus or gel-like behavior was found in the mAb protein solution in the pH range 4-6, deprotonation of histidine residue decreased the ability of mAb to interact with citrate ion (with a net negative charge) (173). As a result, the mAb samples in histidine buffer had lower protein-ion interaction, resulting in lower gel-like properties. These observations, although with a different IgG1 mAb, are consistent with particle formation at the air-solution interface observed in this work. Surface pressures vs. area isotherms demonstrate the highest hysteresis for mAb solution in citrate buffer, suggesting the formation of the elastic gel-like film at the interface. Further, mAb samples in citrate buffer at pH 4.5 displayed gel-like fibril formation, rather than clusters at the interface. Moreover, compared to citrate, mAb samples in histidine buffer showed less hysteresis at each of the solution pH values studied. In addition, AFM images of mAb proteins in solutions containing histidine ions formed more loose thread-like structures at the interface.

4.5. Conclusions

In this work, we have examined protein particle formation in bulk solution and in interfacial protein films for a model IgG1 mAb in different formulations, as a means to correlate how stresses and protein interactions at the air-water interface may be attributed to differences in protein particle levels in mechanically agitated mAb solutions. Our results demonstrate that the buffer type and the solution pH of mAb samples affect the extent and morphology of mAb particle formation at the air-solution interface, which in turn affects the levels and shape of protein particles detected in the bulk mAb solution. Comparison of particle formation between mechanical agitated and interfacial stressed mAb protein samples in this work confirmed previous findings with other mAbs on the significant role of interfacial stress in protein particle formation in bulk mAb solutions (62, 91). One common approach to stabilize mAb formulations

118

from agitation stress is to avoid/reduce the surface activity of mAb samples, by adding more thermodynamically favorable compounds, such as non-ionic surfactants such as polysorbates, that compete with mAb molecules for the air-water interface (178, 179). However, these additives are difficult to remove, may accelerate other protein degradation/aggregation pathways, and are labile and prone to self-degrade (168, 178). Although this study focused on mAb particle formation in response to changes in buffer type and pH, future work will include addition of different concentrations of polysorbates and other surface active molecules. Finally, we suggest that the experimental methodology, as summarized Figure 4.1, could be an effective screening tool of various excipient classes and types to identify combinations of additives to minimize interfacial particle formation and thus develop more stable therapeutic protein drug formulations.

4.6. Figures
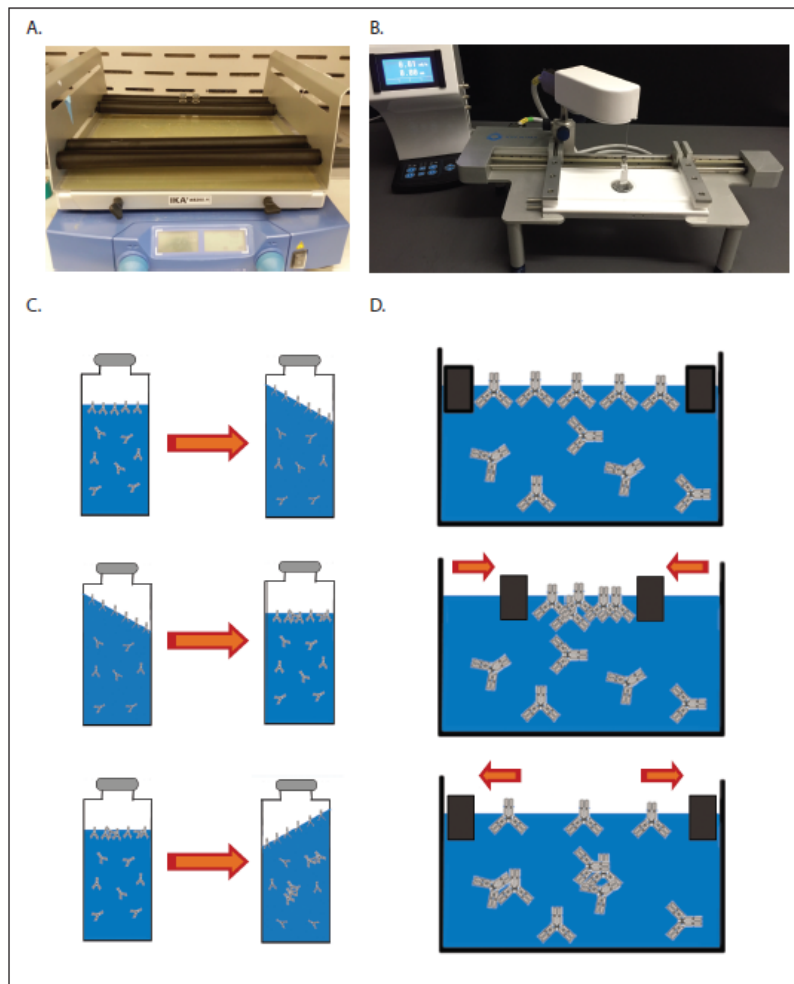
Figure 4.1. Schematic illustration of interfacial stress and subsequent protein particle formation during mechanical agitation of mAb samples in glass vials vs. controlled compression-expansion in a Langmuir trough. (A) System used to shake sample vials in a side-to-side motion. (B) Image of the Langmuir trough connected to a pressure sensor used to apply interfacial mechanical stress and monitor the surface pressure with changes in interfacial area. Panel C and D are schematic illustrations of the potential correlation between mechanisms of protein particle formation in mAb samples subjected to (C) mechanical agitation in vials, and (D) interfacial stress in a Langmuir trough.
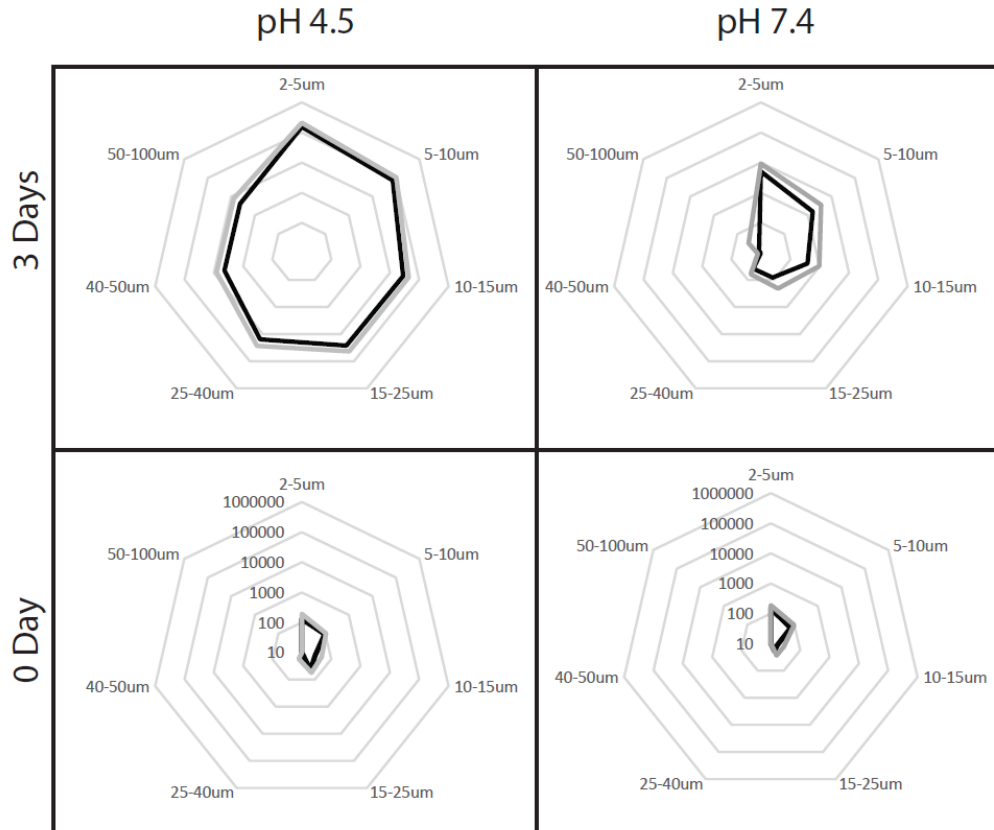
Figure 4.2. Radar chart analysis of flow digital images of subvisible particles formed in mAb solutions in PBS buffer at pH 4.5 or 7.4 at time 0 or after 3 days of side-to-side shaking in glass vials. Each axis of the radar charts represent a particular particle size range (labelled on figure). The black signal represents the average number of protein particles (n=3) and the grey signal represents average plus the standard deviation. The radar charts in this figure use a logarithmic scale with the center of chart representing 10 particles/ml and each concentric polygon of the chart marking a 10x increase in the particle number. The outermost polygon comprising each radar chart marks a particle concentration of 1,000,000 particles/ml for each corresponding size range.
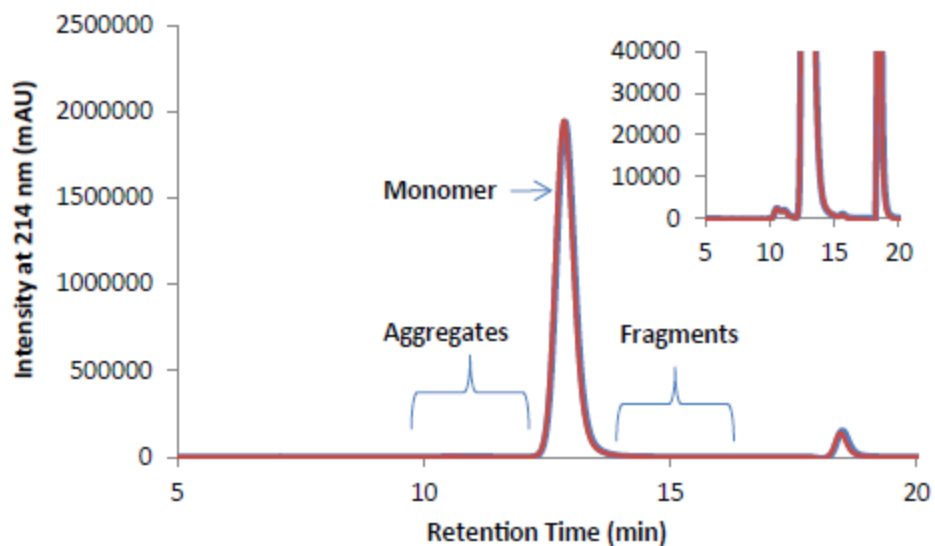
Figure 4.3. Representative SEC chromatogram overlay for mAb samples in pH 7.4 PBS buffer that were shaken in vials side-to side for 3 days (blue) and the corresponding unstressed control (red). The insert is a zoomed in view of the chromatograms. Aggregates are also referred to as high molecular weight species (HMWS) in the text.

A.
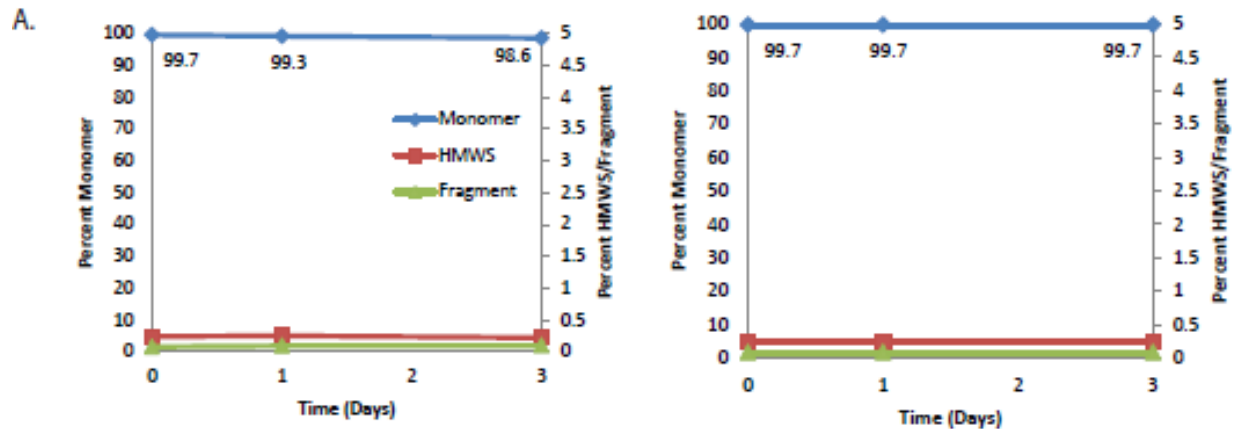
Figure 4.4. The fraction of monomer, high molecular weight species (HMWS), and fragments

for the shake stressed mAb samples in PBS buffer as measured by size exclusion

chromatography (SEC). Values obtained from integrated SEC chromatograms normalized to t=0

values. The SEC was performed in triplicate (n=3) and error bars are plotted as standard

deviation. (A) mAb solution at pH 4.5, and (B) mAb solution at pH 7.4.
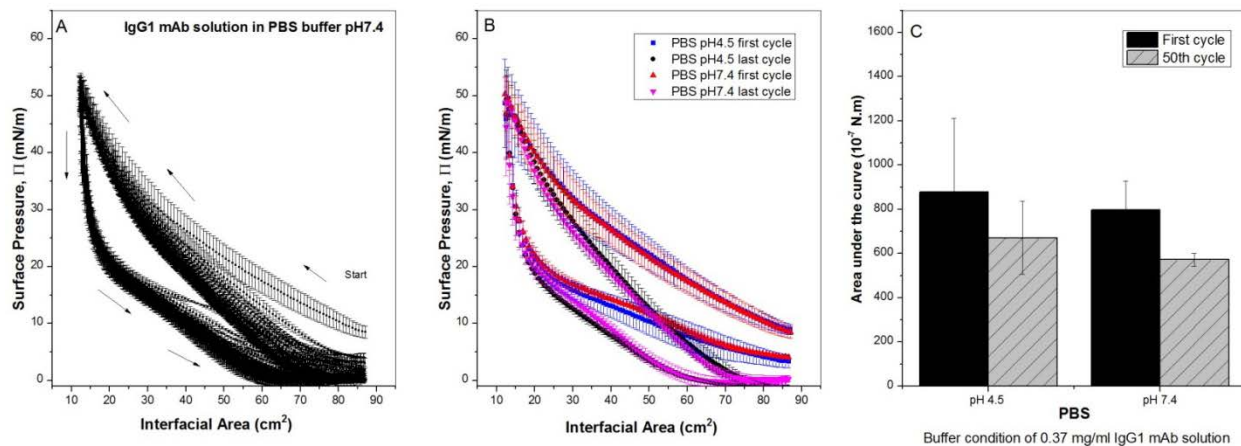
Figure 4.5. (A) Surface pressure vs. area isotherms of 0.37 mg/ml mAb samples in PBS buffer at pH 7.4 subjected to 50 cycles of compressions-expansion during 6 hours (slow rate) in Langmuir trough. Results are presented as mean and SD (n=3). (B) The first and last cycle of compression-expansion isotherms for mAb sample in PBS buffer at pH 7.4 and 4.5. Results are presented as mean and SD, (n=3). (C) Comparing the area under the compression-expansion isotherm (hysteresis) of the first and last cycle for mAb sample in PBS buffer at pH 7.4 and at 4.5. Results are presented as mean and SD (n=3). [10]

---

[10] Figure 4.5 represents experimental work contributed by Saba Ghazvini from the Bioengineering Department at the University of Kansas. The work is included in this thesis to support the conclusions drawn in this chapter.
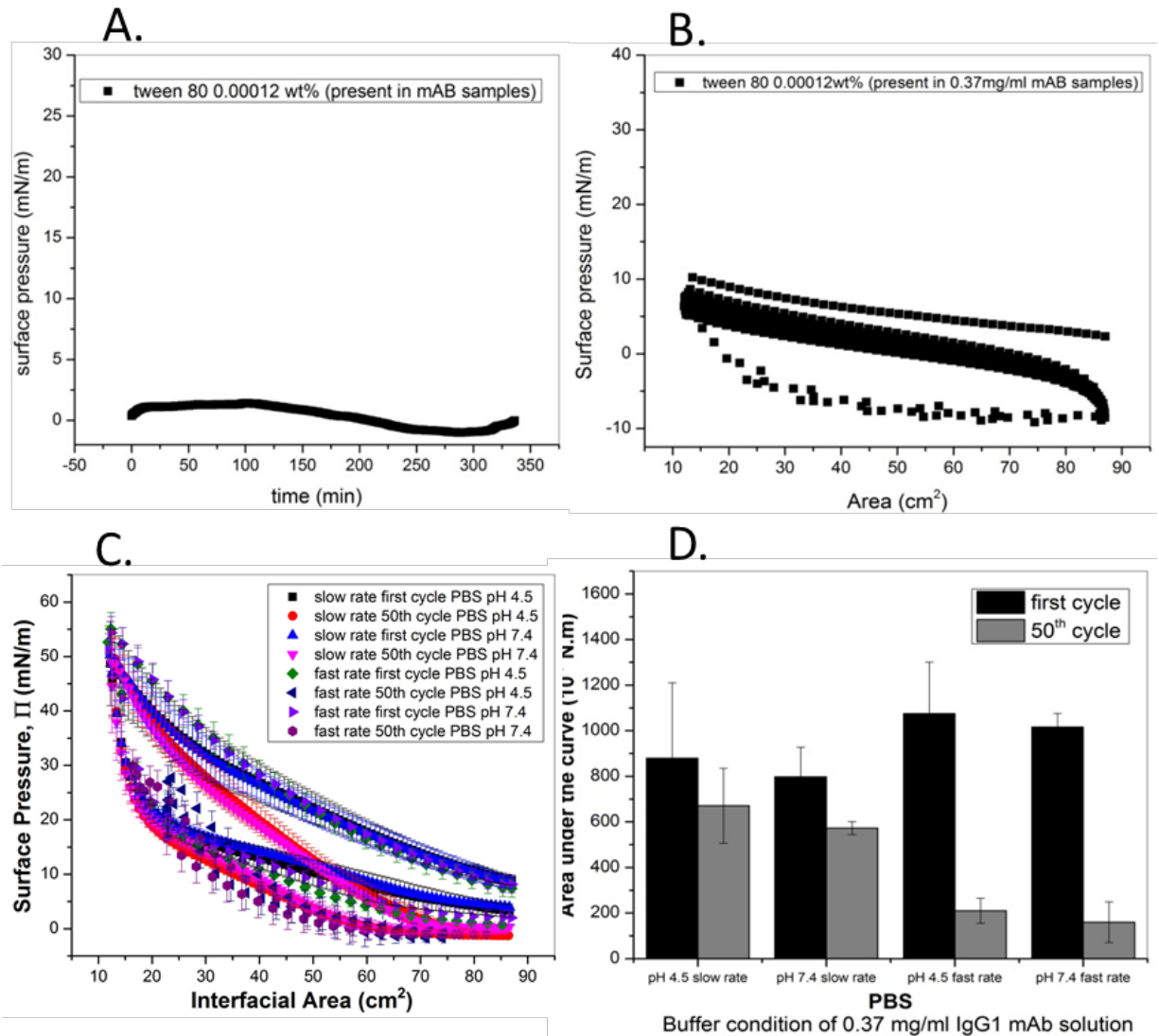
Figure 4.6. (A) Adsorption of polysorbate 80 at 0.00012 wt.% as surface pressure vs time. (B) Surface pressure-area isotherm of polysorbate 80 at 0.00012 wt.% through slow compression-expansion cycles. The samples contain the same concentration of polysorbate 80 in water that is present in the mAb samples throughout the study. The low surface pressure of polysorbate 80 at this concentration indicates the surface pressure that was measured through the study is due to presence of mAb itself. (C) the first and 50th cycle of slow (6hours) and fast rate (25min) of compression-expansion isotherms for mAb sample in 1x PBS buffer at pH7.4 and at 4.5. Results are presented as mean and SD, (n=3). (D) Comparing the area under the compression-expansion

isotherm (hysteresis) of the first and 50th cycle for mAb sample in 1x PBS buffer at pH 7.4 and

at 4.5 for both slow and fast compression. Results are presented as mean and SD (n=3). [11]

---

[11] Figure 4.6 represents experimental work contributed by Saba Ghazvini from the Bioengineering Department at the University of Kansas. The work is included in this thesis to support the conclusions drawn in this chapter.
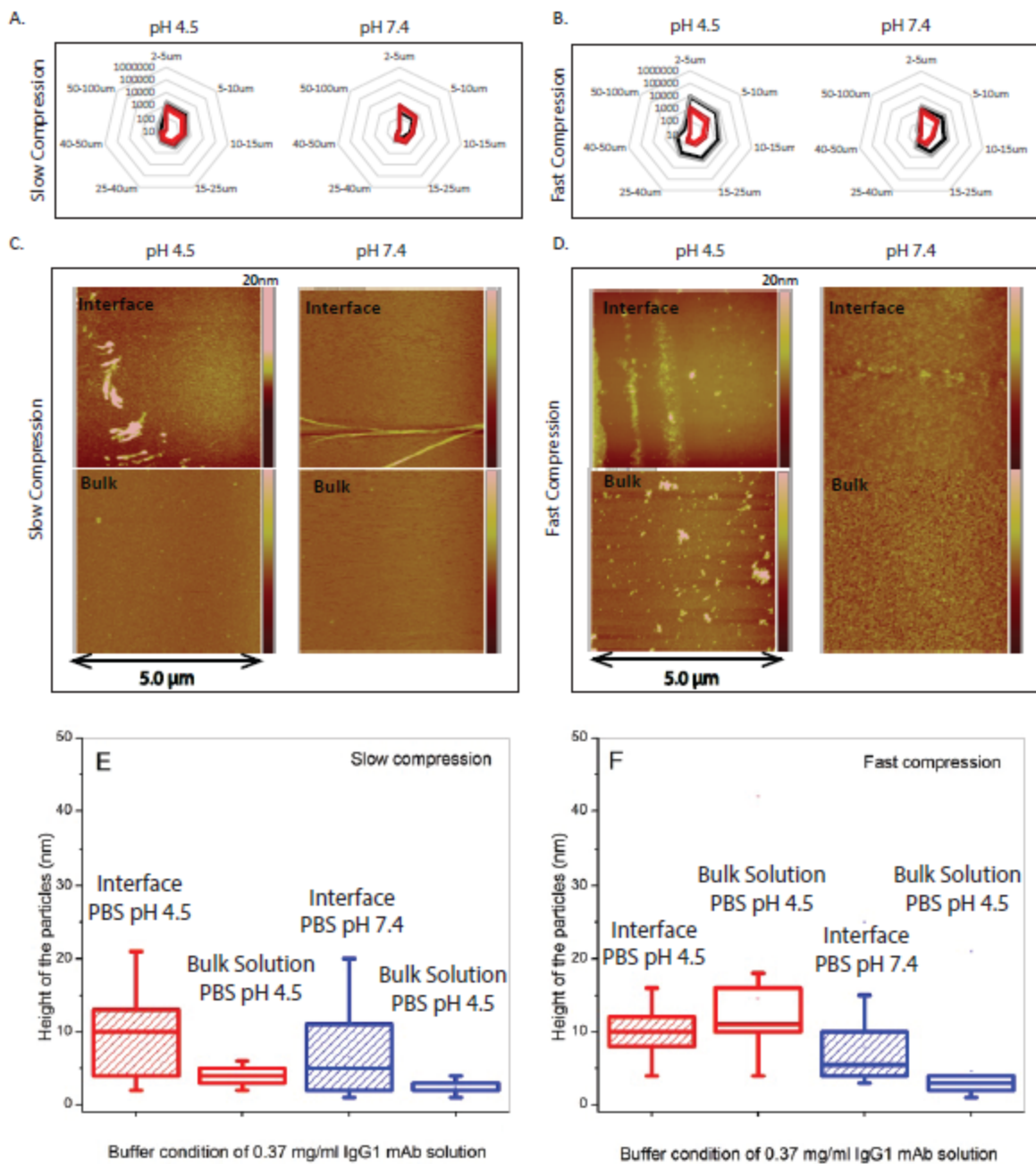
Figure 4.7. (A, B) Radar chart analysis of flow digital images of subvisible particles formed in Langmuir trough for mAb samples in PBS buffer at pH 4.5 and 7.4 after 6 hours of slow compression (panel A), fast compression (Panel B), or room temperature incubation (red trace in panel A and B). Each axis of the radar charts represent a particular particle size range (labelled on figure). The black signal represents the average number of particles (n=3) formed during

stressed conditions and the grey signal represents average plus the standard deviation. The red

signal represents the average number of particles (n=3) formed during a 'no-stress' condition

with the dark red signal representing the average plus standard deviation. The radar charts in this

figure use a logarithmic scale with the center of chart representing 10 particles/ml and each

concentric polygon of the chart marking a 10x increase in the particle number. The outermost

polygon comprising each radar chart marks a particle concentration of 1,000,000 particles/ml for

each corresponding size range. (C, D) AFM images of protein particles formed at air-solution

interface and bulk mAb solution subjected to the slow (Panel C) or fast (Panel D) compression.

The mAb particles at interface or in the bulk solution were transferred on a freshly cleaved mica

sheet by a brief horizontal contact with the interface or being allowed to sit in trough,

respectively. (E, F) the height analysis of AFM images of the mAb particles formed at air-

solution interface or bulk solution of compressed samples in 1x PBS buffer at pH 4.5 or 7.4

subjected to the slow (Panel E) and fast (Panel F) compression (N=9). [12]

---

[12] Panel C–F of Figure 4.7 represents experimental work contributed by Saba Ghazvini from the Bioengineering Department at the University of Kansas. The work is included in this thesis to support the conclusions drawn in this chapter.
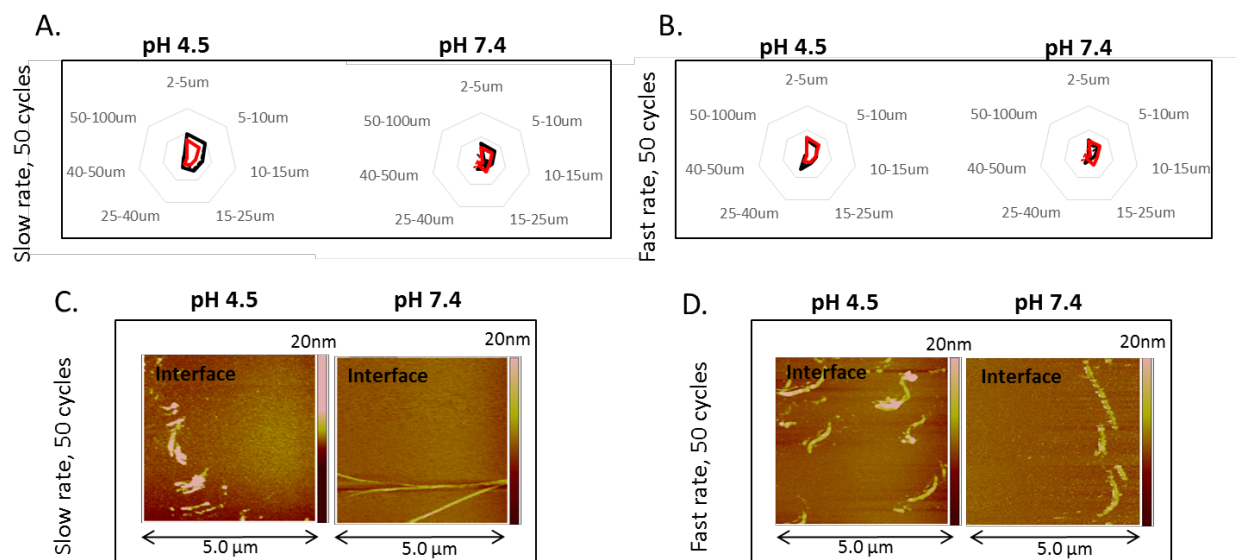
Figure 4.8. (A,B) Radar chart array of mAb particles suspended in bulk solution of pH 4.5 or

7.4 1x PBS buffer after 50 cycles (6 hours) of slow compression (panel A), 50 cycles (25 min) of

fast compression (Panel B), or room temperature incubation (red trace in panel A and B). Each

axis of the radar charts represent a particular particle size range (labelled on figure). The black

signal represents the average number of particles (n=3) formed during stressed conditions and

the grey signal represents average plus the standard deviation. The red signal represents the

average number of particles (n=3) formed during a 'non-stressed condition' with the dark red

signal representing the average plus standard deviation. The radar charts in this figure use a

logarithmic scale with the center of chart representing 10 particles/ml. The outermost polygon

comprising each radar chart marks a particle concentration of 1,000,000 particles/ml for each

corresponding size range. (C,D) representative AFM images of IgG1 mAb particles formed at

air-solution interface subjected to 50 cycles (6 hours) of slow compression (Panel C) or 50 cycles

(25 min) of fast compression (Panel D) compression. MAb particles at interface or bulk solution

were transferred on a freshly cleaved mica sheet by a brief horizontal contact with the interface

or being allowed to sit in trough, respectively.[13]

---

[13] Figure 4.8 represents experimental work contributed by Saba Ghazvini from the Bioengineering Department at the University of Kansas. The work is included in this thesis to support the conclusions drawn in this chapter.
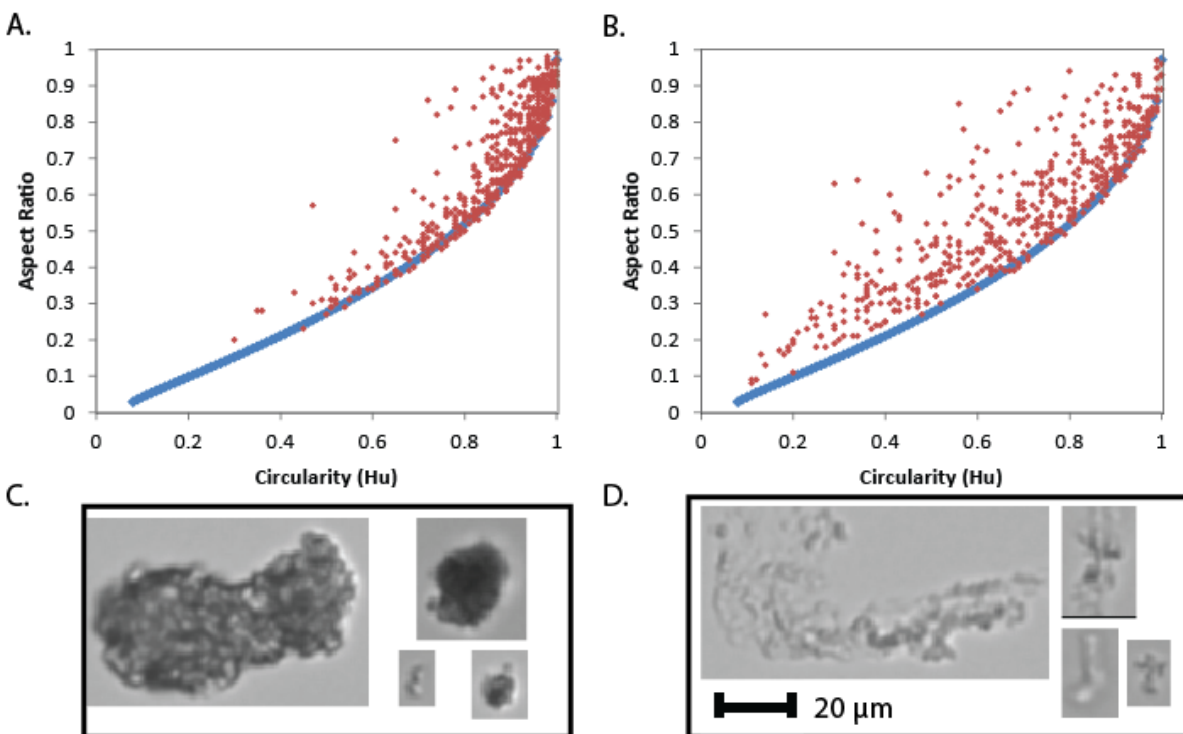
Figure 4.9. Morphology of protein particles detected in bulk solution after stress conditions as measured by flow digital imaging. (A) Scatter plot of the first 500 particles detected in a mAb sample in PBS buffer at pH 4.5 subjected to 8 hours of fast compression. The blue line represents the morphology of an ellipse calculated using the Ellipsoid-Volume method(104) to characterize the morphology of the particles (see text). (B) Scatter plot of the first 500 particles detected in a mAb sample in PBS buffer at pH 4.5 subjected to 3 days of side-to-side shaking in a glass vial at 300 RPM. (C) Representative protein particle images for the fast compression sample. (D) Representative protein particle images of the stressed mAb samples from flow digital imaging analysis.
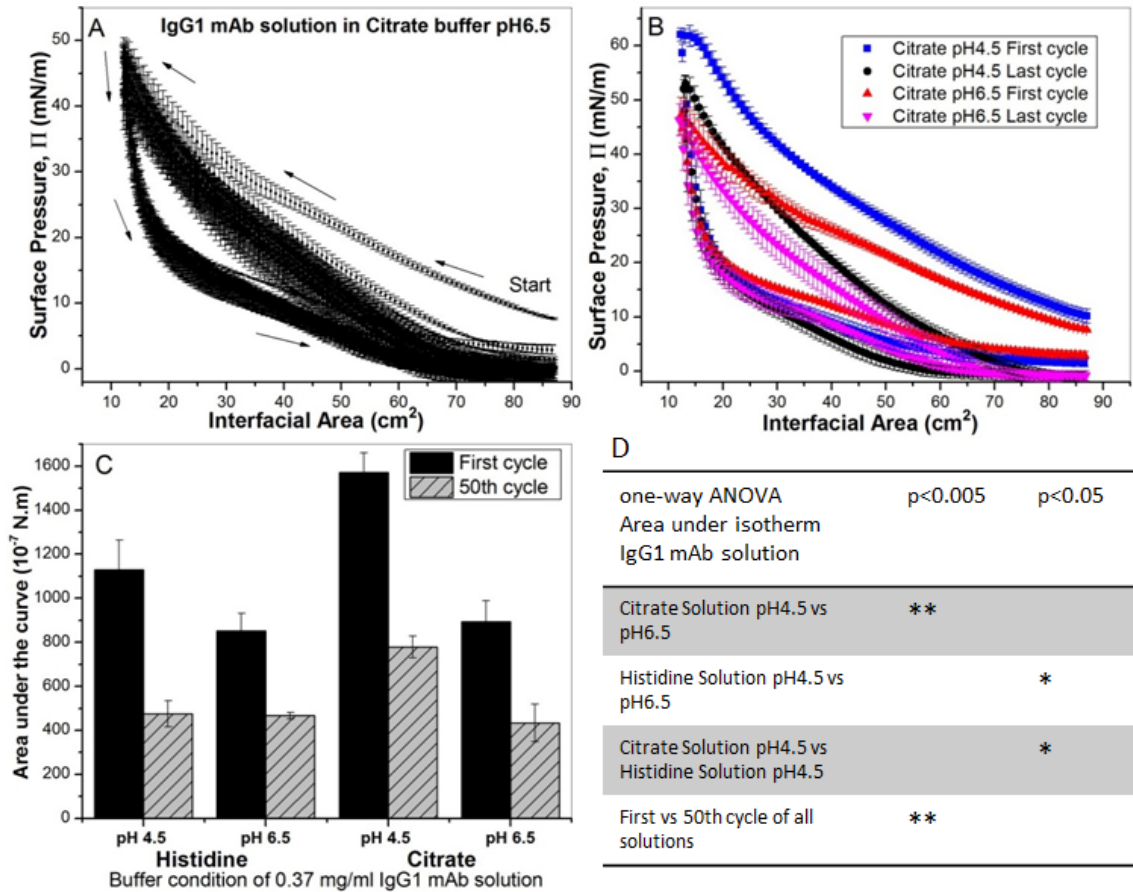
Figure 4.10. (A) Surface pressure vs. area isotherms of 0.37 mg/ml IgG1 mAb in citrate buffer at pH 6.5 subjected to slow compressions-expansions rate in Langmuir trough. Results are presented as mean and SD, (n=3). (B) Comparison of the first and last cycle of compression-expansion isotherms for mAb samples in citrate buffer at pH 4.5 and 6.5. Results are presented as mean and SD, (n=3). (C) Comparison of the area under the compression isotherms of the first and last cycles for mAb samples in histidine or citrate buffer at pH 4.5 and 6.5. Results are presented as mean SD, (n=3). (D) One-way ANOVA analysis of the area under the compression isotherms (hysteresis) of the first and last cycles of mAb samples presented in panel C. [14]

---

[14] Figure 4.10 represents experimental work contributed by Saba Ghazvini from the Bioengineering Department at the University of Kansas. The work is included in this thesis to support the conclusions drawn in this chapter.
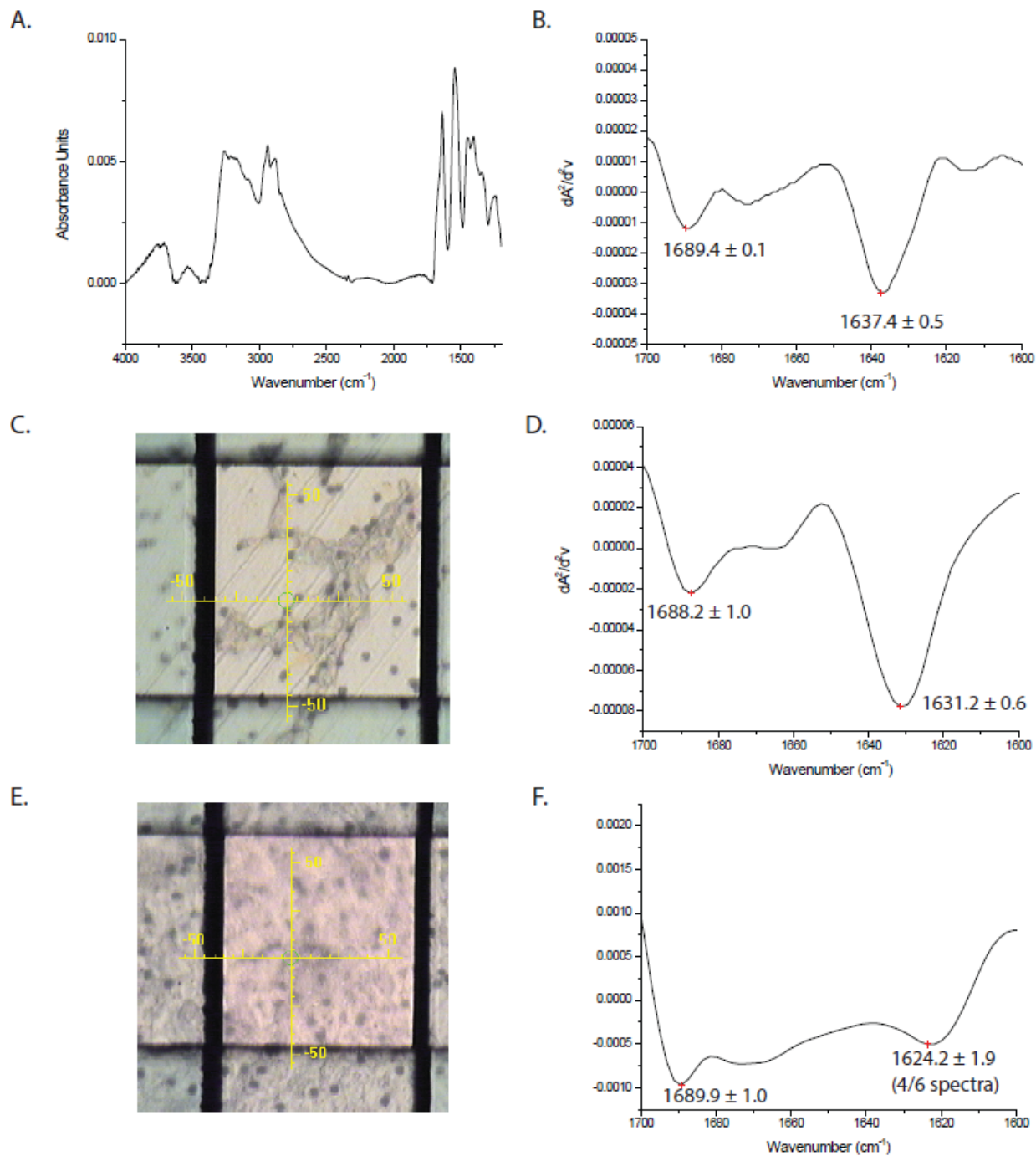
Figure 4.11. Secondary structure analysis of imaged protein particles (formed in pH 7.4 PBS mAb samples subjected to fast compression for 6 hours) as measured by FTIR and FTIR microscopy. A) Representative FTIR spectra of the native mAb control solution. B) Representative second derivative spectra of the amide I region for the native mAb control. Peaks

are given as the average of 3 replicates. C) Representative particle image captured using FTIR microscopy to analyze particles formed during fast compression. D) Representative second derivative FTIR spectra of the amide I region for a particle formed during fast compression. Peak values (mean and SD) are given as the average of 9 particles. E) Representative particle image captured using FTIR microscopy to analyze particles formed after extensive heat denaturation at 90 °C. D) Representative second derivative FTIR spectra of the amide I region for a particle formed during extensive heat denaturation at 90 °C. Peak values (mean and SD) are given as the average of 6 particles.
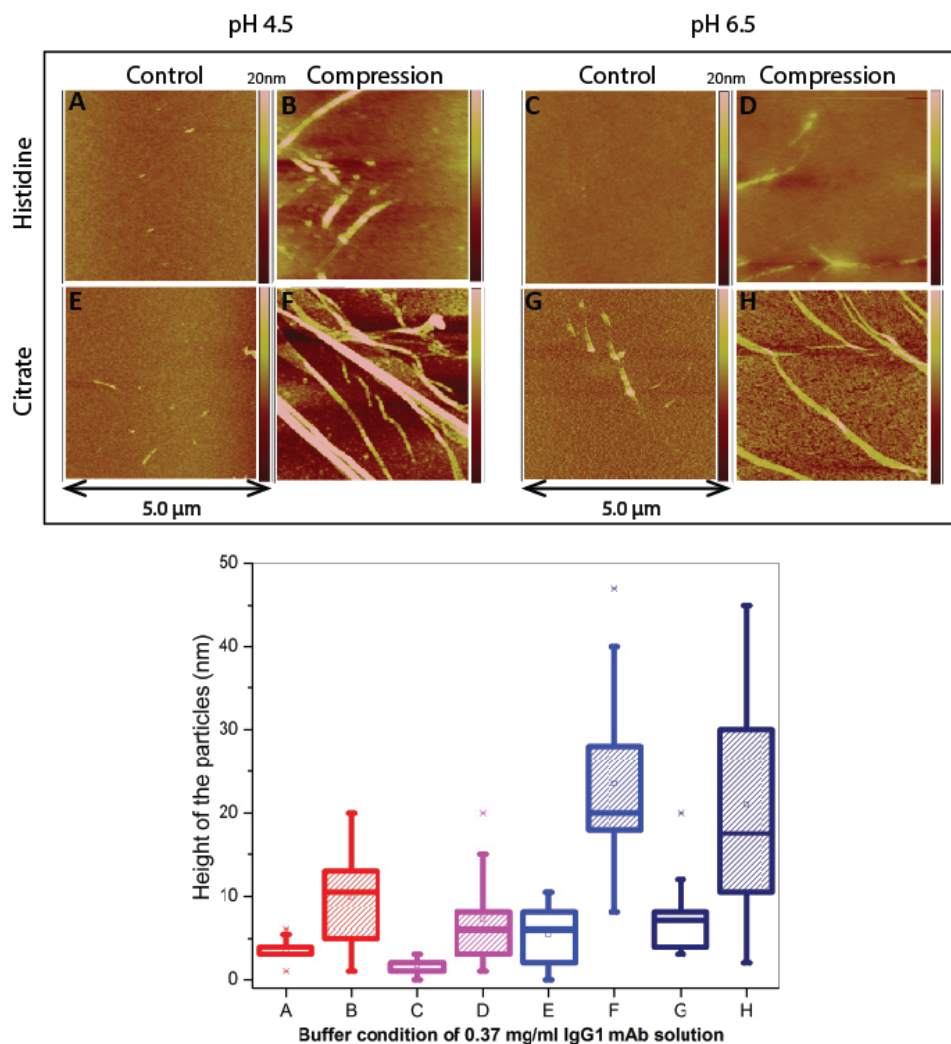
Figure 4.12. (Top Panel) High resolution topographical AFM images of mAb protein films show IgG1 mAb particles formed at air-solution interface of samples formulated in histidine or citrate buffer at pH 4.5 and 6.5 and subjected to slow compression-expansion in Langmuir trough. (Bottom Panel) Height analysis of the AFM images of the mAb particles in slow compression-expansion and control for the same conditions as the top panel (n=9). The control samples correspond to protein films transferred from the air-protein solution interface of mAb samples that were not subjected to any interfacial mechanical stresses. [15]

---

[15] Figure 4.12 represents experimental work contributed by Saba Ghazvini from the Bioengineering Department at the University of Kansas. The work is included in this thesis to support the conclusions drawn in this chapter.
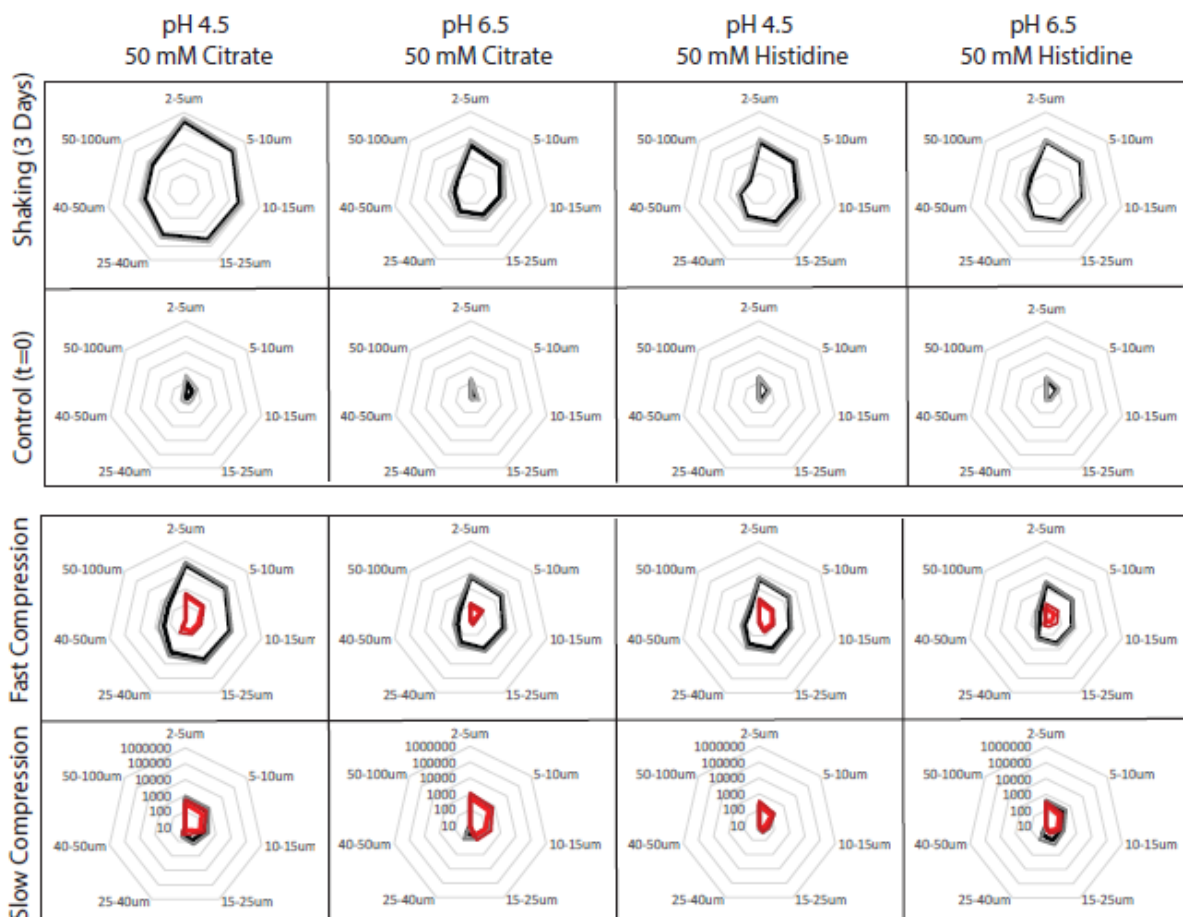
Figure 4.13. Radar chart analysis of flow digital images of subvisible particles formed in bulk mAb samples in histidine or citrate buffers at pH 4.5 or 6.5. (Top) samples subjected to 0 or 3 days of side-to-side shaking in glass vials at 300 RPM. The black signal represents the average number of particles (n=3) and the grey signal represents average plus the standard deviation. (Bottom) samples subjected to 6 hours of fast compression, slow compression, or room temperature incubation in Langmuir trough. The black signal represents the average number of particles (n=3) formed during compression and the grey signal represents average plus the standard deviation. The red signal represents the average number of particles (n=3) formed during room temperature incubation with the dark red signal representing the average plus standard deviation. The radar charts in this figure use a logarithmic scale with the center of chart

representing 10 particles/ml and each concentric polygon of the chart marking a 10x increase in

the particle number. The outermost polygon comprising each radar chart marks a particle

concentration of 1,000,000 particles/ml for each corresponding size range.
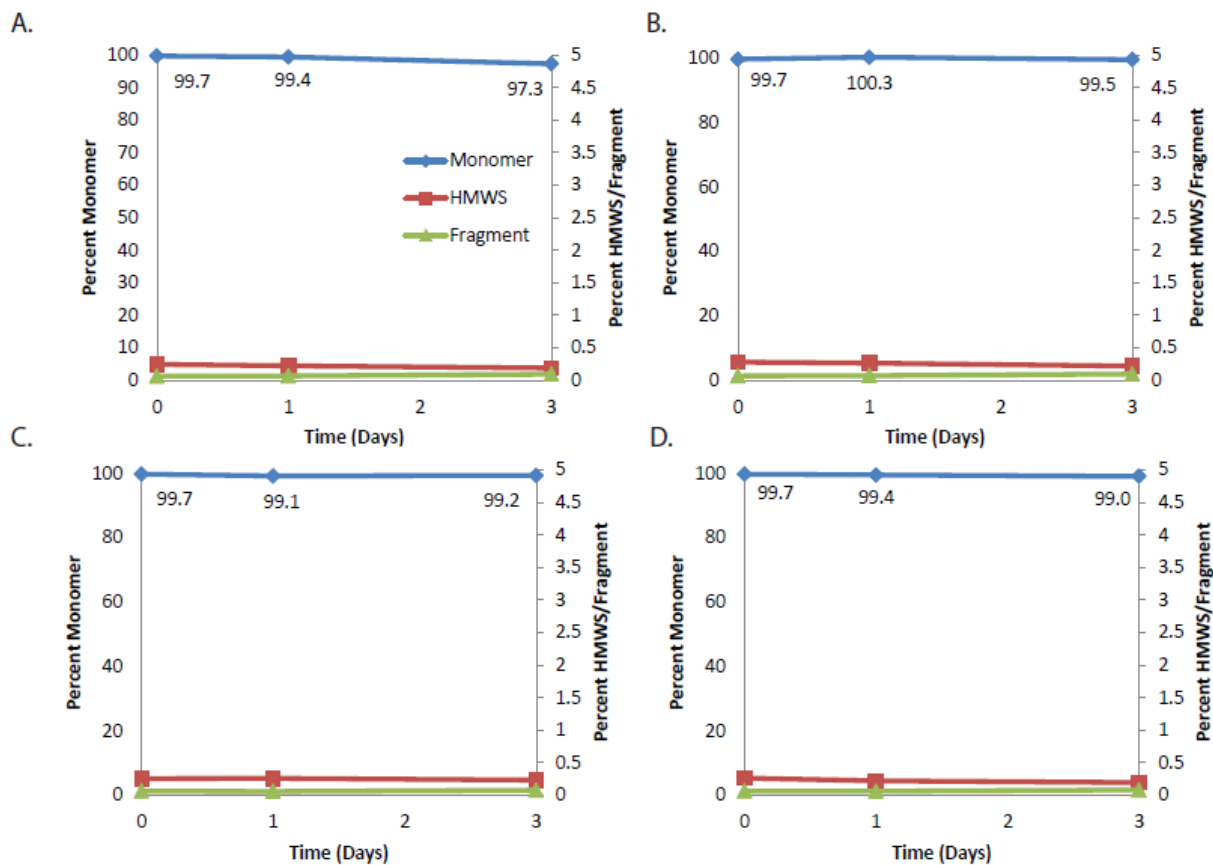
Figure 4.14. The fraction of monomer, high molecular weight species (HMWS), and fragments for the shake stressed mAb samples in different formulations. Values obtained from integrated SEC chromatograms normalized to t=0 values. The SEC is performed in triplicate (n=3), error bars were plotted as standard deviation. MAb solution at (A) pH 4.5 in 50mM citrate buffer, (B) pH 6.5 in 50mM citrate buffer, (C) pH 4.5 in 50mM histidine buffer, and (D) pH 6.5 in 50mM histidine buffer.

Chapter 5: Effects of Protein Conformation, Apparent Solubility, and Protein-Protein Interactions on the Rates and Mechanisms of Aggregation for an IgG1 Monoclonal Antibody

5.1. Introduction

Non-native protein aggregation, or the assembly of proteins into conformationally altered agglomerates, is multistep process that can occur by different mechanisms through various molecular and colloidal steps (10, 44, 45). In the biopharmaceutical industry, non-native aggregation of therapeutic proteins is a highly undesirable phenomenon because the presence of protein aggregates can compromise drug efficacy by decreasing potency and/or by increasing product immunogenicity potential (i.e., formation of anti-drug antibodies) (1, 2, 12-14, 46, 47). The process of non-native, irreversible protein aggregation (hereafter referred to as aggregation) results in aggregates of varying size ranging from soluble dimers to insoluble macroscopic particles (66). The extent of protein aggregation is largely determined by the sequence and structure of the protein itself (67, 68), solution environment (e.g., pH, ionic strength, cosolutes) (51, 54, 69), and stress condition applied to induce aggregation (e.g., temperature, mechanical agitation, light, etc.) (70). Recent studies, for example, suggest that mechanical agitation induces aggregation of protein molecules at the air-solution interface (62) whereas incubation at elevated temperatures promotes aggregation of proteins in bulk solution (71). Cosolutes may affect protein aggregation mechanisms and/or rates by modifying protein conformation, protein structural stability, apparent solubility, and/or protein-protein interactions in solution (11).

Traditionally, protein aggregation has been mechanistically interpreted using the Lumry-Eyring model, in which a reversible conformational change of the protein is followed by an irreversible association step (4). If aggregation follows the Lumry-Eyring model, the kinetics should be highly temperature sensitive (to a greater extent than predicted by the Arrhenius equation) because of the second order dependence on the concentration of partially unfolded species. For this reason, evaluating protein conformational stability is an important

140

consideration for understanding protein aggregation mechanisms. For example, differential scanning calorimetry is commonly employed to measure endothermic transitions attributed to protein unfolding as a function of temperature under different solution conditions.

Contrary to the Lumry-Eyring model, there are examples of native proteins associating prior to undergoing a conformational change to form an aggregate (4, 59). Quantifying the concentration of such transient encounter complexes by direct experimental methods is technically challenging because of the reversible, and thermodynamically unstable, nature of these intermediates, which may cause them to exist for only a short time in extremely small quantities. In several studies, one approach to address this challenge involved the observation that protein aggregation propensity in different solutions correlated to apparent solubility values in the presence of an inert crowding agent (59, 180). Middaugh and coworkers used an extrapolation method to determine the apparent thermodynamic activity of saturated protein solutions from protein precipitation data in solutions with different polyethylene glycol (PEG) concentrations (181). Other studies have used descriptive parameters derived from precipitation profiles (e.g., midpoint values) as a means of rapidly rank ordering different solutions conditions for pharmaceutical development (59, 180, 182). Fundamentally, apparent solubility measurements reflect the free energy difference between amorphous solid and solution phases if the system is at equilibrium. It is suggested that such experimentally determined apparent protein solubility (or extrapolated thermodynamic activity) values can be used as an experimental surrogate for the thermodynamic favorability of reversible encounter complex formation (intermediates) prior to irreversible aggregate formation, and thus correlate with observed propensity of a protein to aggregate under the same conditions (59).

Measures of non-specific, weak protein-protein interactions (referred to hereafter as PPI) under different solution conditions are commonly used to interpret protein aggregation data under those same conditions. The rationale behind such approaches is that mechanistically protein aggregation must have one or more association steps. Weak PPI are often characterized using experimental measures of protein charge and/or the second osmotic virial coefficient (B_2) (5, 7, 71). Using statistical mechanics, the second osmotic virial coefficient can be defined as

$$B_2 = -\frac{N_A}{2M^2} \int \{\exp[-W_{22}(r)/k_B T] - 1\} 4\pi r^2 dr,$$

(5.01)

where M is the molecular weight of the protein, N_A is Avogadro's number, k_B is the Boltzmann constant, T is the absolute temperature and $W_{22}(r)$ is the protein-protein potential of mean force (averaged over all orientations) as a function of center-to center distance, r (6, 28, 30). If a protein is globular, and if two protein molecules effectively stick together irreversibly upon association, the kinetics of protein aggregation should closely follow the theory of slow coagulation (3)

$$k \approx \frac{2\pi(D_1+D_2)}{\int_{R_{s1}+R_{s2}}^{\infty} \exp\{\Phi_{12}(r)/k_b T\}\frac{dr}{r^2}},$$

(5.02)

where k is the rate of association, D_1 and D_2 are the diffusion coefficients of the aggregating species (1 and 2), and R_{s1} and R_{s2} are the spherical radii of the aggregating species. $\Phi_{12}(r)$ is the interaction potential between species 1 and 2 as a function of center-to-center distance r. In the scenario described above, we can assume that protein aggregation should directly correlate to B_2. There are several prominent examples in the literature, however, where observed protein aggregation results do not necessarily show any apparent direct correlation to such PPI values (56, 57).

In this work, we seek to examine the effects of protein conformational stability, apparent solubility, and PPI parameters on the mechanism and rate of aggregation for an IgG1 mAb stored at different incubation temperatures under different solution conditions. In the following section, we develop several theoretical kinetic models to explain why protein aggregation may appear to correlate with weak PPI, apparent solubility, and conformational stability in some cases but not in others. The models are then applied to interpret experimental protein aggregation data collected over a range of incubation temperatures for an IgG1 mAb prepared in different solution conditions possessing varying values of PPI, apparent solubility, and conformational stability.

5.2. Theory

5.2.1. Kinetic Model of Protein Aggregation

This model uses the framework of the Lumry-Eyring Nucleated Polymerization model developed by Roberts and coworkers, to consider protein aggregation, in bulk solution, as a multi-step process that may involve several competing nucleation and growth pathways (84, 85). The formation of an irreversible dimer (nucleation event) may be described by one or more of the following potentially competing pathways:

$$N^* + N^* \xrightarrow{\;\; K_{a1,(N^*,N^*)} \;\;} \{N^*\}_2 \xrightarrow{\;\; k_{nuc,\{N^*\}_2} \;\;} A_{2,\{N^*\}_2}$$

(5.03a)

$$N^* + m \xrightarrow{\;\; K_{a1,(N^*,m)} \;\;} \{N^*m\} \xrightarrow{\;\; k_{nuc,\{N^*m\}} \;\;} A_{2,\{N^*m\}} \qquad (5.03b)$$

$$m + m \xrightarrow{\;\; K_{a1,(m,m)} \;\;} \{m\}_2 \xrightarrow{\;\; k_{nuc,\{m\}_2} \;\;} A_{2,\{m\}_2} \qquad (5.03c)$$
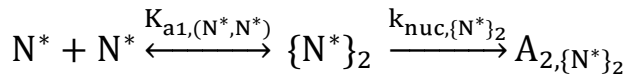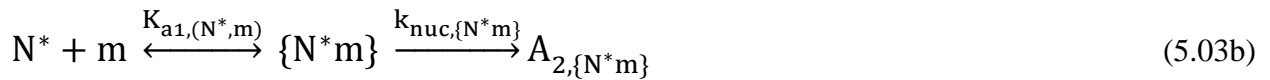
Where N^* is a conformationally altered monomer, m is a native monomer, and $A_{2,\{encounter\ complex\}}$ is an "irreversible" dimer (net thermodynamic irreversibility relative to the

143

current solution environment) that has formed through an encounter complex intermediate. $\{N^*\}_2$, $\{N^*m\}$, and $\{m\}_2$ are reversible encounter complexes whose initial structures should depend upon the structure of the associating species. $K_{a1,(N^*,N^*)}$, $K_{a1,(N^*,m)}$, and $K_{a1,(m,m)}$ are the equilibrium association constants for the reversible dimeric encounter complex formation. The subscript of the equilibrium association constant in parenthesis is used to differentiate between the aggregating monomer species. k_{nuc} is a rate constant describing conformational rearrangement of an encounter complex to an irreversible aggregate (referred to as nucleation in the LENP model). The subscript of k_{nuc} specifies the type of encounter complex undergoing the nucleation event. Figure 5.1 is a visual scheme depicting the nucleation mechanisms described by Equations 5.03a-c.

After the nucleation event, the existing dimer may enter a growth phase where the oligomeric state of the aggregate grows through the addition of a native monomer, conformationally altered monomer, or an aggregate to the existing structure. The nature and extent of any growth event probably depends upon the type of nucleus (e.g. $\{N^*\}_2$, $\{N^*m\}$, or $\{m\}_2$). For practical purposes, however, we ignore these potential differences in this model. This association process is thus represented by the following equations:

$$A_j + N^* \xrightarrow{K_{aj,(N^*)}} \{N^*A_j\} \xrightarrow{k_{g,\{N^*A_j\}}} A_{j+1} \tag{5.04a}$$

$$A_j + m \xrightarrow{K_{aj,(m)}} \{A_j\,m\} \xrightarrow{k_{g,\{A_j\,m\}}} A_{j+1} \tag{5.04b}$$

$$A_j + A_i \xrightarrow{k_{agg(j,i)}} A_{j+i} \ldots \tag{5.05}$$

Where j and i represent the number of monomeric units contained within an aggregate, and $2 \leq (j \text{ or } i) < \infty$. $K_{aj,(N^*)}$ and $K_{aj,(m)}$ represent the equilibrium association constants for growth

of an aggregate, composed of j monomers, by addition of a conformationally altered monomer (N^*) or native monomer (m), respectively. Similar to aggregate nucleation, the brackets "{}" denote a reversible encounter complex composed of two species. The rate constant, k_g, describes the conformational rearrangement of an aggregate-monomer encounter complex to a larger, irreversible aggregate. $k_{agg(j,i)}$ is a rate constant for the formation of an aggregate composed of j + i monomeric units from two aggregates of size j and i. Figure 5.2 is a visual scheme depicting the growth mechanisms for different dimers described by Equations 5.04a, 5.04b and 5.05.

If we define the total monomer concentration as being equal to the concentration of native monomer plus the concentration of partially unfolded monomer (i.e., $m_{tot} = m + N^*$), then Equations 5.03-5.05 can be used to express the rate of monomer loss as

$$-\frac{d[m]}{dt} = 2 * k_{nuc,obs}[m_{tot}]^2 + \sum_{j=2}^{\infty} k_{g,obs,\{A_j\}}[A_j][m_{tot}] , \qquad (5.06)$$

where $k_{nuc,obs}$ and $k_{g,obs}$ are the observed rate constants for nucleation and growth events and will reflect some combination of the competing aggregation pathways. The first term on the left hand side of Equation 5.06 describes monomer loss as a result of a nucleation event, and the second term describes monomer loss as a result of monomers adding to aggregates of all possible sizes. The subscript $\{A_j\}$ on $k_{g,obs}$ is used to differentiate between the observed rate constants of growth events for aggregates of different sizes. Additionally, the subscript $\{A_j\}$ on $k_{g,obs}$ intentionally neglects to specify the monomer type (N^* or m) involved in the growth event since the observed rate constant could be a convolution of both growth mechanisms.

The rate of aggregate formation for an aggregate consisting of j monomers can be described by the following equation:

$$\frac{d[A_j]}{dt} = k_{g,obs,\{A_{j-1}\}}[m_{tot}][A_{j-1}] - k_{g,obs,\{A_j\}}[m_{tot}][A_j] - k_{agg(j,j)}[A_j]^2 - [A_j]\sum_{i=2}^{\infty}k_{agg(j,i)}[A_i] +$$

$$\begin{cases} \sum_{i=2}^{\frac{j}{2}}k_{agg(j-i,i)}[A_{j-i}][A_i] & j \in \text{even integers} \\ \sum_{i=2}^{\frac{j-1}{2}}k_{agg(j-i,i)}[A_{j-i}][A_i] & j \in \text{odd integers} \end{cases} \qquad (5.07)$$

5.2.2. Role of Conformational Stability on Aggregation Rates

Considering that $k_{nuc,obs}$ is the observed rate constant for three potentially competing pathways, it can be expressed in terms of the observed rate constants for each mechanism and the fraction of conformationally distorted protein, f. If we define $N^* = f * m_{tot}$ and $m = (1 - f) * m_{tot}$, then

$$k_{nuc,obs} = k_{nuc,obs,\{N^*\}_2} * f^2 + k_{nuc,obs,\{N^*m\}} * f(1 - f) + k_{nuc,\{m\}_2} * (1 - f)^2 . \qquad (5.08)$$

$k_{g,obs}$ for an aggregate of size j can be similarly defined as

$$k_{g,obs,\{A_j\}} = k_{g,obs,\{N^*A_j\}} * f + k_{g,obs,\{A_j m\}} * (1 - f) . \qquad (5.09)$$

If a protein does not aggregate by a particular pathway, then the observed rate constant can simply be set to 0.

5.2.3. Role of Colloidal Stability and Apparent Solubility on Aggregation Rates

The equilibrium constants describing encounter complex formation for aggregate nucleation (i.e., $K_{a1,(N^*,N^*)}$, $K_{a1,(N^*,m)}$, and $K_{a1,(m,m)}$) and aggregate growth (i.e., $K_{aj,(N^*)}$ and $K_{aj,(m)}$) can be described as an association rate constant divided by a dissociation rate constant.

Assuming steady state kinetics can be applied to nucleation ($\frac{d\{N^*\}_2}{dt} = \frac{d\{N^*m\}}{dt} = \frac{d\{m\}_2}{dt} = 0$), the observed rate constant for a particular nucleation mechanism is given by $k_{nuc,obs,\{\}} =$

$\frac{k_{a1,\{\}}k_{nuc,\{\}}}{k_{-a1,\{\}}+ k_{nuc,\{\}}}$, where {} represents the $\{N^*\}_2$, $\{N^*m\}$, or $\{m\}_2$ pathway. If the same assumption is

applied to aggregate growth, $k_{g,obs,\{\}} = \frac{k_{aj,\{\}}k_{g,\{\}}}{k_{-aj,\{\}}+ k_{g,\{\}}}$. When two protein monomer/aggregates

species diffuse together to form an encounter complex, there are 2 limiting cases of particular interest: (1) the encounter complex rapidly forms a stable aggregate ($k_{nuc,\{\}} \gg k_{-a,\{\}}$ and/or $k_{g,\{\}} \gg k_{-aj,\{\}}$), and (2) the encounter complex tends to diffuse apart ($k_{-a1,\{\}} \gg k_{nuc,\{\}}$ and/or $k_{-aj,\{\}} \gg k_{g,\{\}}$).

Considering limiting case (1) in further detail, $k_{nuc,obs,\{\}} \approx k_{a1,\{\}}$ and/or $k_{g,obs,\{\}} \approx k_{aj,\{\}}$. Under such conditions, the observed rate constant for a particular mechanism will approximately equal the rate of protein association which is directly related to colloidal stability (see introduction). This limiting case could occur if the activation energy barrier for association is sufficiently higher than the activation energy barrier for nucleation. When limiting case (2) is further examined, $k_{nuc,obs,\{\}} \approx k_{nuc,\{\}}K_{a1,\{\}}$ and/or $k_{g,obs,\{\}} \approx k_{g,\{\}}K_{aj,\{\}}$. $K_{a1,\{\}}$ and $K_{aj,\{\}}$ are equilibrium constants describing encounter complex formation for a particular nucleation and growth pathway, respectively. $k_{nuc,\{\}}$ and $k_{g,\{\}}$ are rate constants describing conformational

rearrangement of the encounter complex into a stable aggregate. Under this limiting case, aggregation kinetics will not be related to colloidal stability in a kinetic sense, but will instead depend upon equilibrium encounter complex formation and subsequent structural rearrangement. If apparent solubility (or extrapolated thermodynamic activity) measurements in solutions with inert crowding agents reflect the thermodynamic favorability of protein in solution vs. an amorphous solid phase, it could be used as surrogate parameter to evaluate changes in $K_{a1,\{\}}$ and $K_{aj,\{\}}$ between solution conditions.

5.3. Materials and Methods

5.3.1. Sample Preparation

The IgG1 mAb (pI ~ 9) was donated by Janssen Research & Development, LLC (Horsham, Pennsylvania) at an approximate concentration of ~40 mg/ml. Citrate and histidine stock formulation buffers (50 mM) were prepared at pH 4.5 and 6.5 with and without 100 mM NaCl. L-histidine was obtained from Sigma-Aldrich (St. Louis, Missouri). Citric acid anhydrous and sodium citrate dihydrate were from Fisher Scientific (Hampton, New Hampshire). Buffers were prepared with Milli-Q water (EMD Millipore, Billerica, Massachusetts) and were sterile filtered using a 0.2 μm filter. Final mAb solutions for these studies were prepared at a concentration of 1.0 mg/ml by diluting the mAb stock solution (1/40) into each of the four formulation buffers. The working mAb solutions of 3 mL each were aliquoted into 37.7×16.75 mm Fiolax® glass vials (Schott, Lebanon, Pennsylvania) capped with elastomeric stoppers that were treated with a fluorocarbon film (West Pharmaceutical Services, Exton, Pennsylvania). The sample preparation procedures outlined above are described as well in a separate but complimentary study examining aggregation at the air-water interface in the presence of

mechanical agitation(183). Vials intended for long term incubation were sealed with flip-off

CCS seals (West Pharmaceutical Services). The IgG1 mAb containing sample vials were

subjected to shorter term incubation at 57°C for up to 5 days or longer term incubation for up to

7 months at either 40 °C or 25 °C.

5.3.2. Differential Scanning Calorimetry (DSC)

A VP-Capillary DSC (Malvern Instruments, Worcestershire, United Kingdom) was used

to obtain apparent melting thermograms for 1.0 mg/ml mAb in different solution conditions. The

differential heat capacity between the mAb solution (sample cell) and corresponding buffer

(reference cell) was scanned over a temperature range of 10 to 90°C at a rate of 1°C/min. The

MicroCal LLC DSC plug-in for Origin 7.0 was used for data analysis by iteratively fitting

processed thermograms to a non-two state model for protein unfolding.

5.3.3. Size Exclusion Chromatography (SEC)

SEC was performed using a prominence UFLC HPLC system (Shimadzu, Kyoto, Japan)

equipped with a diode array detector. A TSKgel G3000SWx1 stainless steel column (Tosoh

Biosciences, San Francisco, California) with a TSKgel SWxI guard column were used at 30°C to

separate and quantitate monomer, aggregate, and fragment populations. A pH 6.8, 0.2 M sodium

phosphate buffer was used as the mobile phase to reduce protein adsorption to the column (133).

The flow rate was set to 0.7 ml/min and the column was allowed to equilibrate for 3 h prior to

measurement. For each sample, 30 µl was injected onto the column and the absorbance at 214

nm was collected for 30 min. LC Solution software from Shimadzu was used to integrate

monomer, aggregate, and fragment peaks. Integrated peak areas were normalized by the total

area at t=0 to monitor the loss in peak area between different time points.

5.3.4. Sedimentation Velocity Analytical Ultracentrifugation (SV-AUC)

An Optima XL-I analytical ultracentrifuge (Beckman Coulter, Fullerton, CA) equipped with an interference optical system was used for sedimentation velocity measurements. Experiments were conducted at 20 °C, at a rotor speed of 40,000 RPM. Samples and reference were loaded into Beckman charcoal-epon two sector cells with 12 mm sapphire windows. The samples were incubated within the centrifuge for an additional hour after the chamber reached temperature. Analysis of the sedimentation data was performed using Sedfit software (184). A continuous sedimentation coefficient distribution c(s) was used with 100 scans of the sedimentation data to determine monomer and aggregate content in pH 4.5, fifty mM Histidine mAb samples incubated at 57°C. The partial specific volume, buffer density and viscosity values used to model the data were 0.73 ml/g, 1.00 g/ml, and 1.002 cP, respectively. A range of 0 to 30 s was used (after verifying that there was no signal outside of this range) with a resolution of 300 points per distribution and a confidence level of 0.95. Baseline, radial independent noise, and time independent noise were fit by the software. The meniscus and bottom positions were set manually. Integrated peak areas were normalized by the total area at t=0 to monitor the loss in peak area between different time points.

5.3.5. Static Light Scattering

Composition gradient multi-angle light scattering (CG-MALS) was performed to determine the apparent second virial coefficient (A_2) of the various mAb solutions. The CG-MALS configuration consisted of a Calypso-II equipped with 20 nm polyether sulfone (PES) membrane filters to mix, degas, filter and inject mAb concentration gradients into a Dawn Heleos II multi-angle light scattering (MALS) detector with a 658 nm laser for static light scattering (Wyatt Technology Corp, Santa Barbara, CA), and an in-line Optilab rEX differential

refractive index detector to measure protein concentration. Protein solutions for light scattering were purified by performing four 15x dilution buffer exchanges using Amicon Ultra-15 10kDa molecular weight cutoff centrifugal filter devices (EMD Millipore, Billerica, MA). After the final buffer exchange, the protein and the buffer fractions were collected and filtered using a Whatman 0.1 μm PVDF syringe driven membrane filter (GE Healthcare, Little Chalfont, United Kingdom) to remove large impurities. Protein concentrations were measured with a NanoDrop spectrophotometer (Thermo Fisher Scientific, Waltham, MA) using a 0.1% extinction coefficient of 1.4 at 280 nm. The initial target protein concentration for static light scattering experiments was ~10 mg/ml. If $|2A_2M_wc_2| \leq 0.05$ then the protein concentration was increased to ~30 mg/ml for subsequent experiments, where $|2A_2M_wc_2|$ is a unit-less fraction that reflects the contribution of non-ideal interactions to the total light scattering signal. A_2 is the apparent second virial coefficient, M_w is the weight averaged molecular weight, and c_2 is the protein concentration. The apparent second virial coefficient was determined by regressing SLS data at multiple protein concentrations using the Zimm equation[31]

$$\frac{K^*c_2}{R(\theta)} = \frac{1}{M_w} + 2A_2c_2 \ , \tag{5.10}$$

where $R(\theta)$, the excess Rayleigh ratio, describes the intensity of scattered light. K^* is an optical constant given by

$$K^* = \frac{4\pi^2 n_0^2}{N_A \lambda_0^4} \left(\frac{dn}{dc}\right)^2 , \tag{5.11}$$

where n_0 is the refractive index of the buffer, λ_0 is the wavelength of the laser in a vacuum, N_A is Avogadro's number, and $\frac{dn}{dc}$ is the differential refractive index increment of the protein. The value of $\frac{dn}{dc}$ was set to 0.185 ml/g.

Using statistical mechanical arguments, the theoretical contributions of excluded volume to the second osmotic virial coefficient can be expressed as (3)

$$B_2 = \frac{N_A u}{2M^2}, \tag{5.12}$$

where is M the molecular weight of the protein, and u is the excluded volume. The excluded volume for a spherical system can be expressed as 8V, where V is the volume of a single sphere. Therefore, the theoretical contribution of excluded volume on the apparent second virial coefficient can be calculated for spherical particles (9) by

$$B_2{}^{exc} = \frac{16\pi N_A r^3}{3M^2}. \tag{5.13}$$

Experimental apparent second virial coefficients were then normalized by $B_2{}^{exc}$ to provide a unitless parameter sensitive to protein-protein interactions:

$$a_2 = \frac{A_2 - B_2{}^{exc}}{B_2{}^{exc}}. \tag{5.14}$$

Using $M = 150{,}000$ Da and a spherical diameter of 10 nm, $B_2{}^{exc} = 0.556 * 10^{-4}$ mol ml g^{-2}. The normalized virial coefficient calculations described above are built into the Calypso V2.1.3 software. The reported normalized a_2 values in this manuscript are an average of three separate experiments.

5.3.6. Polyethylene Glycol (PEG) Precipitation

Stock solutions of PEG-10,000 ranging from 0 to 40% w/v were prepared for each buffer condition. 244 µL of each solution (0 to 40% w/v) were added to a 96-well polystyrene filter plate (Corning Life Sciences, Corning, NY). Six µL of an IgG1 mAb stock solution (~40 mg/mL) was added to the wells to achieve final protein concentrations of 1 mg/mL. The plates were incubated overnight at room temperature and centrifuged at 3,500g for 15 min. The filtrate was collected in a clear 96 well collection plate (Greiner Bio-One North America Inc., Monroe, NC). Afterwards, 200 µL of the filtrate was transferred into a 96 well UV Star microplate. The filtrate was measured using SpectraMax M5 UV-Visible plate reader (Molecular Devices LLC, Sunnyvale, CA) at 280 nm to determine the protein concentration. Concentration of IgG1 mAb vs % PEG-10,000 data were fit using a standard four-parameter modified Hill-slope sigmoidal curve equation:

$$y = b + \left(\frac{t-b}{1 + e^{\ s(mid-x)}} \right), \tag{5.15}$$

where t = top plateau, b = bottom plateau, mid = x-axis midpoint, and s = slope. Midpoint values were determined from the resulting curve fit as described in detail elsewhere (182).

5.3.7. Determination of Aggregation Kinetic Rate Constants

Rate constants describing the aggregation process ($k_{nuc,obs}$ and $k_{g,obs}$) were determined by simulating fits to experimental SEC data using an in-house script in Python v2.7.10. The script iteratively solves Equations 5.06 and 5.07 based on user entered values for the number of time steps, range of aggregate polymerization (j), and rate constants $k_{nuc,obs}$, $k_{g,obs}$, and k_{agg}. Simulated monomer loss as a function of time was compared to experimental monomer loss presumably due to aggregation (and with fragment peaks treated as monomer). SV-AUC was

used to measure monomer loss (instead of SEC) for stressed mAb samples in certain

formulations that were determined to adsorb to the SEC column (see text). Aggregate-aggregate

association was set to zero in mathematical simulations, and $k_{g,obs}$ was treated as constant for all

aggregate sizes ($k_{g,obs,\{A_2\}} \approx k_{g,obs,\{A_\infty\}}$). Additionally, the polymerization state j was set to

∞ to reduce the amount of data points required to distinguish between simulations. The effects

and purpose of these modeling parameters and treatments are discussed in the *Supplemental*

Materials section. Simulations were performed for each sample until the residuals (experimental

data point – simulated data point) were within the range of the experimental standard deviation

and randomly distributed about zero.

5.3.8. Empirical Modeling of Net Protein Charge

The molecular modeling and visualization program PyMol v1.5 was used to construct the

Fab, hinge, and Fc regions of an IgG1 antibody model (185). The Fab and hinge coordinates

were obtained from the *in silico* KOL-Padlan structure of an IgG1 molecule (186). Homology

models of the antibody sequence were mapped onto the template Fab regions with Modeller

version 9.12 (187). The Fc region was retrieved from the x-ray structure, 3AVE, maintaining the

linked G0F glycan residues (188).

The homology model was analyzed using PROPKA v3.1, an empirical algorithm that

calculates the pKa of titratable residues based on interactions with nearby functional groups and

desolvation effects due to the structural position of the residue (189) (190). The net charge of the

IgG1 mAb was then calculated using the <u>Henderson–Hasselbalch</u> relationship with user entered

pH values and titratable residue pKa values from the PROPKA 3.1 results.

154

5.3.9. Calculation of the Second Osmotic Virial Coefficient

The theoretical second osmotic virial coefficient for uniformly charged spheres was calculated using an equation developed Winzor and coworkers (9):

$$B_2 = B_{ex} + B_z = \frac{uN_A}{2M^2} + \frac{1000Z^2}{4M^2I}\left(\frac{1+2\kappa r_s}{(1+\kappa r_s)^2} + \cdots\right), \tag{5.16}$$

where B_{ex} is the excluded volume contribution to the second virial coefficient, B_z is the electrostatic contribution, Z is the net charge, I is the ionic strength (mol/L), r_s is the solvated radius, and κ is the Debye inverse screening length. The value of B_{ex} was $0.556 * 10^{-4}$ mol ml g^{-2} (see static light scattering section) and r_s was approximated as 5 nm. The ionic strength was calculated using the relationship $I = \frac{1}{2}\sum c_i z_i^2$ where c_i is the concentration of an electrolyte species and z_i is its valence. The charged state of the citrate buffer was determined by solving equations for triprotic acids with pKa values of 3.1, 4.7, and 6.4 whereas histidine was treated as a weak base with a pKa value of 6.1. To our knowledge, there is no straight forward approach to calculating the ionic strength of an ampholytes solution. Therefore, we decided to approximate the ionic strength of solutions containing histidine by treating histidine as having a total charge of 0 or +1. The inverse Debye screening length was determined at 20 °C using the expression $\kappa = 3.27 * 10^7 \sqrt{I}$ (cm^{-1}). The theoretical normalized second osmotic virial coefficient (b_2) was calculated using the equation:

$$b_2 = \frac{B_2 - B_2{}^{exc}}{B_2{}^{exc}} = \frac{B_z}{B_2{}^{exc}}. \tag{5.17}$$

5.3.10. Flow Microscopy

A FlowCam VS Series (Fluid Imaging Technologies, Scarborough, Maine) benchtop flow microscope was used to image particles with area based diameters (ABD) in the range of 1-

100 μm. The instrumental setup included a 100 μm x 2 mm flow cell and a 10x objective. A

total volume of 0.5 ml was analyzed per sample at a flow rate of 0.15 ml/min with an image

capture speed of 21 frames per second. Each day, the instrument was focused using NIST

traceable 25 μm polystyrene spheres (Thermo Fisher Scientific, Waltham, Massachusetts). The

mass of each particle was calculated using

$$\text{Mass of particle k } (M_k) = \frac{\pi}{6} \times d^3 \times \sqrt{1.70763 - 1.70864 \times (1 - C)^{0.45} - 0.70638\, C} \, * \, 1.41 \frac{g}{ml} * f \qquad (5.18)$$

Where d is the equivalent circular diameter of the particle, C is the circularity of the particle, and

f is the fraction of protein within the calculated volume.(104) The total mass of all the imaged

particles was calculated using

$$\text{Mass of n particles per ml } = \frac{\sum_{k=1}^{n} M_k}{V_a E} \qquad (5.19)$$

V_a is the volume analyzed, and E is a term to correct for the efficiency of imaging.

Experimentally determined values of ABD and circularity (hu) were used for the calculations.

The fraction of protein within a particle was taken to be 0.2 as described previously (104).

5.3.11. Absorbance Spectroscopy

The absorbance at 280 nm was measured for IgG1 mAb samples using an 8453 UV-Vis

Spectrophotometer (Agilent, Santa Clara, California). Baseline correction was applied by

subtracting the average optical density over the range of 500 to 600 nm.   The concentration of

mAb solutions was calculated using Beer's Law ($E_{1\,cm}^{0.1\%}$= 1.4). After 1 day of incubation at 57

°C, the samples were centrifuged at 13,500 g for 15 min to remove insoluble particulates and the

absorbance of the supernatant fraction was measured. In addition to baseline correction, light

scattering correction as suggested by Mach and Middaugh was also applied to account for

increased light scattering by large aggregates (153). The loss of protein in solution due to the formation of large precipitates was approximated by subtracting the mAb concentration after one day of thermal stress from the initial mAb concentration.

5.4. Results and Discussion

5.4.1. Conformational Stability of mAb under Different Solution Conditions

As a first step to better understand the relationship between temperature and observed aggregation rates, differential scanning calorimetry (DSC) was used to assess how changes in solution conditions (pH, ionic strength, buffer ion type) effect the apparent thermal onset (T_0) and thermal melting temperature values (T_m) for an IgG1 mAb. It has previously been shown that IgG1 mAbs undergo thermal unfolding steps which correspond to structural alterations of distinct domains/regions of the antibody (78, 79). We apply the model proposed by Ionescu and coworkers to interpret deconvoluted thermal melting events for this IgG1 mAb in terms of its CH_2 domain, Fab region, and CH_3 domain unfolding events as previously shown for three other IgG1 mAbs (80).

The IgG1 mAb used in this study displays two endothermic transitions at pH 4.5 and 6.5 in histidine buffered solutions as measured by DSC (Figure 5.3A). At pH 4.5, the first melting transition can be attributed to unfolding of the CH_2 domain and the second larger transition is probably a convolution of Fab region and CH_3 domain unfolding events (80). The first apparent melting temperature (T_{m1}) was at 58.3 ± 0.1 ℃, and the second was at 71.7 ± 0.1 ℃. Addition of 100 mM NaCl to the pH 4.5 histidine solution did not change the number or order of the observed transitions in the DSC thermogram, but the T_{m1} value for the mAb decreased to 56.1 ± 0.1 ℃ and the second T_m decreased to 70.3 ± 0.1 ℃ (Table 5.1). The decrease in T_m values, compared to the NaCl absent solution, probably signifies a decrease in the conformational

stability of this mAb, but it could also potentially be an artifact caused by faster aggregation rate constants (48). At pH 6.5, the mAb in the histidine solution also displayed two endothermic transitions (Figure 5.3A). In this case, however, the first transition is probably a convolution of CH_2 domain and Fab region unfolding (80) with an observed T_m value at 72.9 ± 0.1 ℃ while the second transition reflects unfolding of the CH_3 domain with a T_{m3} at 79.2 ± 0.1 ℃. A summary of the apparent thermal onset and thermal melting temperatures are summarized in Table 5.1.

DSC thermograms of the mAb in pH 4.5 and 6.5 citrate solutions had higher onset and melting temperatures compared to the mAb in histidine solution (Figure 5.3B). At pH 4.5, there were 3 endothermic transitions with the first, second, and third corresponding to the CH_2 domain, Fab region, and CH_3 domain, respectively (80). Apparent melting temperatures for the first, second and third transitions were 59.5 ± 0.1, 73.1 ± 0.1, and 79.2 ± 0.1 ℃, respectively. Addition of 100 mM NaCl, to the pH 4.5 citrate formulation decreased the apparent melting temperatures slightly with T_{m1}, T_{m2}, and T_{m3} values decreasing to 59.0 ± 0.1, 72.7 ± 0.1, and 79.0 ± 0.1 ℃, respectively (Table 5.1). Interestingly, mAb melting temperatures decreased more when NaCl was added to the histidine solution than when it was added to the citrate solution. This could be because the ionic strength of the histidine solution was substantially lower than the citrate solution (see calculated ionic strength values for each condition summarized in Table 5.2). At pH 6.5, the mAb in citrate solution displayed 2 endothermic transitions similar to the pH 6.5 mAb histidine solution. The first transition is presumably a convolution of CH_2 domain and Fab region unfolding with an observed T_m occurring at 73.1 ± 0.1 ℃ and the second transition reflecting unfolding of the CH_3 domain with a T_{m3} at 83.1 ± 0.1 ℃.

5.4.2. Apparent Solubility of mAb Under Different Solution Conditions

Apparent protein solubility as a function of polyethylene glycol (PEG) concentration was measured to better understand the thermodynamics of mAb precipitation in different solution environments. The apparent solubility values were extrapolated to determine the apparent thermodynamic activity of saturated mAb solutions without PEG (181). Representative experimental data showing mAb concentration in different solutions as a function of PEG concentration are presented in Figure 5.3C. Extrapolated apparent thermodynamic activity values (in the absence of PEG) and [PEG] midpoint values (i.e., 50% of the mAb in the amorphous phase) were determined. In pH 4.5 histidine solution, the mAb had the highest [PEG] midpoint value of 24.6 % w/v (with an extrapolated apparent activity value of 1.86 ± 0.4 g/ml). Addition of 100 mM NaCl to the pH 4.5 histidine formulation caused the precipitation curve to shift to a midpoint value of 15.1 % w/v PEG (with an extrapolated apparent activity value of 1.10 ± 0.08 g/ml) corresponding to an increase in the ionic strength of the solution. At pH 6.5, the midpoint value was 8.5 % w/v PEG (with an extrapolated apparent activity value of 0.11 ± 0.01 g/ml). The mAb in the citrate solutions had [PEG] midpoint values ranking as follows and the values are summarized in Table 5.2: pH 4.5 citrate + NaCl > pH 4.5 citrate > pH 6.5 citrate. The extrapolated activity values for the mAb were 0.04, 0.01, and 0.02 g/ml for the pH 4.5, pH 4.5 + NaCl, and pH 6.5 citrate solutions, respectively.

Mahadevan and Hall developed a statistical mechanical model to predict trends in apparent solubility in polyethylene glycol solutions by considering excluded volume, osmotic and electrostatic interactions (191). In general, our observed results are consistent with their model because apparent solubility values in mAb solutions with PEG decreased with decreasing calculated values of protein charge and/or increased ionic strength (see calculated charge and

ionic strength values for each condition summarized in Table 5.2). As described previously in other studies (59, 180), and as described in our experiments below, these descriptive parameters derived from the PEG precipitation profile can be valuable for interpreting observed protein aggregation data under different solutions conditions.

The PEG concentration (% w/v) vs. protein concentration (i.e., precipitation) profile of this mAb was fit to a sigmoidal function and the [PEG] midpoint values (Figure 5.3C) were used to compare the relative thermodynamic favorability of non-specific IgG1 mAb associations leading to amorphous precipitation. We hypothesize that differences in the relative apparent solubility values of the mAb in different solutions could indicate the thermodynamic favorability of transient encounter complex formation in the same solutions. At the [PEG] midpoint, the ΔG between protein in the solution and solid amorphous phases is zero if the solution is at equilibrium. Additionally, the protein-protein potential of mean force (PMF), $W_{22}(r)$ can be expressed as (5, 6)

$$W_{22}(r) = W_{HS}(r) + W_Z(r) + W_{disp}(r) + W_{osmotic}(r) + W_{dipole}(r) + W_{assoc}(r). \qquad (5.20)$$

From left to right, the terms on the right hand side of Equation 5.20 represent contributions of excluded volume, electrical double layer, dispersion forces, osmotic forces, dipole interactions, and specific interaction sites to the protein-protein PMF (5, 6). As the concentration of PEG is increased, the short range osmotic potential reflected by the $W_{osmotic}(r)$ term becomes increasingly attractive. These osmotic attractions have been previously modeled using a theory developed by Asakura and Oosawa (192, 193). Based on these models, differences in [PEG] midpoint values should approximately reflect the extent to which osmotic forces are required to overcome other repulsive interactions and induce mAb precipitation. On the other hand, this

approach has some limitations. For example, Sarangapani et al. have demonstrated that such models can be inadequate for describing protein behavior with changes in pH or protein concentration because they neglect to account for changes in intrinsic flexibility and protein conformation (194). Additionally, this approach assumes that the PEG molecules are inert and do not interact with the protein molecules which may not always be the case.

5.4.3. Colloidal Stability of Native mAb under Different Solution Conditions

To compare protein-protein interactions (PPI) in different solution conditions on a relative basis, static light scattering was used to obtain normalized apparent second virial coefficient (a_2) values for the IgG1 mAb as a function of solution pH, ionic strength and buffer ion type (Figure 5.3D). Traditionally, the second virial coefficient A_2, obtained from classical analysis of static light scattering data (Equation 5.10), was equated to the second osmotic virial coefficient, B_2 (3, 195). More recently, however, the two virial coefficients have been shown to formally differ (30, 32, 33). Under sufficiently dilute conditions (e.g., $|2A_2 M_w c_2| \leq 0.12$), differences between A_2 and B_2 may not be significant in terms of statistical uncertainty (33-35). Otherwise, the value of A_2 was theoretically proposed to systematically over estimate repulsive interactions and underestimate attractive interactions compared to B_2 (33). In protein solutions with weak PPI, the second virial coefficient can be dominated by contributions from excluded volume (38). Normalization of the second virial coefficient by correcting for the excluded volume contribution of spheres ($A_2 \rightarrow a_2$) can be used to help tease out weak protein-protein interactions (36, 37).

In solutions containing histidine, the IgG1 mAb was found to have the most repulsive PPI with a_2 values of 1.18 ± 0.29 and 0.58 ± 0.02 at pH 4.5 and 6.5, respectively (Figure 5.3C & Table 5.2). The mAb in these histidine solutions were the only conditions where $|2A_2 M_w c_2| >$

0.12. Addition of 100 mM NaCl to the pH 4.5 histidine solution changed the sign of a_2 from positive to negative, to a value of -0.43 ± 0.03, suggesting that PPI changed from repulsive to slightly attractive for the mAb (Figure 5.3C). In the pH 4.5 and 6.5 citrate containing solutions, the mAb had the lowest values of a_2 which argues that the mAb under these conditions had the most attractive PPI. This result was notable because the pH 4.5 histidine solution with NaCl has a greater calculated ionic strength than the pH 4.5 citrate solution (Table 5.2). Addition of 100 mM NaCl to the pH 4.5 citrate formulation did not significantly change the a_2 value despite substantially increasing the ionic strength of the solution. At pH 6.5, the mAb in the citrate solution had the most attractive PPI. This result was expected because the solution had the highest ionic strength and the mAb had the lowest calculated net charge of all conditions tested (see Table 5.2 for summary of the calculated protein charge and solution ionic effect values; also see next section).

5.4.4. Evaluation of Experimental Apparent Solubility and Colloidal Stability vs. Calculated Values of Various Solution and Protein Properties

Theoretical values of solution ionic strength, protein charge as a function of pH, and the second virial coefficient were calculated to aid in the interpretation of the experimental a_2 and PEG precipitation data sets for this mAb under the different solutions (Table 5.2). The theoretical normalized second osmotic virial coefficient (b_2) for spheres with a uniformly distributed net charge was also determined to better understand how mAb charge and ionic strength might affect colloidal interactions for an idealized case. The value of b_2 for the mAb in pH 4.5 histidine solution indicated that this condition should have the most repulsive protein-protein interactions (Table 5.2), which was in agreement with the experimentally determined a_2. The [PEG] midpoint value, one experimental measure of the relative apparent solubility of the

mAb in different solutions (see previous section), was also the highest in the pH 4.5 histidine solution indicating that the charged state of the mAb could also affect the favorability of forming transient associating species. Neal et al. incorporated anisotropic charge distributions into their models of B_2 and found that electrostatic effects are especially magnified in complementary configurations (196). They also found that attractive molecular orientations can disproportionally affect the value of B_2 compared to repulsive orientations. This is one possible explanation for the large difference between the calculated b_2 and experimental a_2 values.

At pH 6.5, the mAb in histidine solution had the second largest value of b_2 which was also in agreement with the experimentally determined value of a_2 (Table 5.2). The apparent solubility data, however, showed the precipitation profile shifting substantially to the left indicating lower amounts of PEG led to mAb precipitation (Figure 5.3D). This discrepancy between PPI and apparent solubility (in PEG solutions) is not surprising because b_2 describes PPI in dilute solutions and may not accurately represent interactions in more crowded solution environments. On the other hand, b_2 values for the mAb under this solution condition could be related to specific charged amino acid residues within the mAb modulating potential self-association configurations. For example, Arora et al. demonstrated that protonation of histidine residues located within an association interface of a different IgG1 mAb greatly reduced the formation of self-associated mAb species (20).

After increasing the solution ionic strength, the trend of the theoretical b_2 did not agree with the experimental a_2 of the mAb in the pH 4.5 histidine solution containing 100 mM NaCl. The theoretical value indicated that there should be slightly repulsive PPI while the experimental value indicated that slightly attractive interactions were present. The PEG precipitation data showed that mAb in the pH 4.5 histidine solution with NaCl had higher apparent solubility

values than the mAb in the pH 6.5 histidine solution (see previous section and Table 5.2). This result could suggest that the formation of transient complexes becomes less favorable as the molecular charge of this mAb increases. From the discrepancies noted above, we notice that increasing the solution ionic strength did not have as great of an effect on the apparent solubility values measured. The differences between the calculated and experimentally determined virial coefficients could arise from the mAb having a few slightly attractive molecular orientations available while the model only considers a uniform repulsive interaction (197). The discrepancies observed in the PEG precipitation data noted above also support such an argument because double layer repulsions are expected to be largely screened at an ionic strength of 0.124 M (pH 4.5 histidine + NaCl) compared to 0.007 M (pH 6.5 histidine). Thus, it is possible that the charged state of specific titratable residues on the mAb could potentially have a large effect on the thermodynamics of protein association causing the observed differences in PEG concentration required to induce precipitation.

Interesting deviations between a_2 and b_2 were also observed for the mAb in the citrate solutions. At pH 4.5, the calculated b_2 indicated that there should be substantial repulsive colloidal interactions in citrate solution, but slightly attractive PPI were measured for the mAb as reflected by a_2 values (Table 5.2). Surprisingly, a_2 did not decrease when 100 mM NaCl was added to the pH 4.5 citrate formulation despite the calculated ionic strength increasing from 0.089 M (citrate) to 0.189 M (citrate + NaCl). On the other hand, b_2 predicted decreased protein-protein interactions based on the increased ionic strength. It is likely that this discrepancy could be caused by citrate ions preferentially accumulating on the surface of the mAb when histidine residues are charged, as has been described previously for other mAbs (35, 88, 89). Furthermore, the Shultz-Hardy rule suggests that multivalent anions will be more

164

effective at screening the charge on the mAb than monovalent anions or multivalent cations (3). Interestingly, the apparent solubility values observed for the mAb in pH 4.5 citrate solution increased upon addition of 100 mM NaCl. This could suggest that any negative charge imparted by the accumulation of citrate is screened by the addition of NaCl. At pH 6.5, b_2 and a_2 showed good agreement because both values suggest that this condition has the most attractive (or least repulsive) PPI for the mAb. This was an expected result because the mAb has the lowest net charge and the solution had the highest ionic strength out of all conditions examined. It is important to note that the a_2 results suggest that the charges on the mAb is effectively screened in 50 mM citrate solutions because a_2 decreased from -0.84 ± 0.03 at pH 4.5 to only -1.14 ± 0.02 at pH 6.5, despite the ionic strength increasing from 0.089 M to 0.243 M.

In summary, we compared calculated parameters of charge, ionic strength, and b_2 to experimentally measured parameters of a_2, [PEG] precipitation midpoint, and extrapolated apparent thermodynamic activity. These results showed that changes in solution pH affected the experimentally determined apparent solubility (and extrapolated thermodynamic activity) more than ionic strength (i.e., [PEG] midpoint for pH 4.5 histidine with 100 mM NaCl vs. pH 6.5 histidine solution). On the other hand, the calculated b_2 and experimental a_2 values showed that ionic strength substantially decreased the strength of protein-protein interactions under the same solution conditions. It is possible that differences in protein conformation and/or the charged state of specific titratable residues could be responsible for the observed trends in the PEG precipitation data while long range colloidal interactions are responsible for the trends observed in the a_2 data. This is probable because protein-protein interactions measured by a_2 seemed to follow the same trends as the theoretical calculation (b_2) which used spherical geometry to calculate the contribution of excluded volume and Debye-Hückel theory (3) to account for

screening of electrostatic repulsions (except in the case of mAb in pH 4.5 citrate vs. pH 4.5 citrate + NaCl as described earlier).

5.4.5. Experimental and Modeled mAb Aggregation Results in Different Solutions

Using experimental data from either SEC or SV-AUC, monomer loss as a function of time can be used to obtain an apparent reaction order and time scale for protein aggregation. If the size of aggregates remains small, dimers are the smallest aggregate species, and aggregate-aggregate association can be neglected. Then, completely nucleation dominated aggregation should have an effective reaction order of 2. In contrast, aggregation dominated by monomer addition growth mechanisms will have an effective reaction order that approaches 1 if reversible self-association is negligible as is the case for this mAb (data not shown). Under this particular limiting case, monomer loss of this mAb can be modeled and used to obtain rate constants and/or characteristic time scales for both aggregate nucleation and growth by monomer addition (84).

Prior to modelling the kinetics of experimental mAb aggregation data sets, simulations of Equations 5.06 and 5.07 were performed to better understand how nucleation and aggregate growth affect the overall observed rate of the aggregation process. The effect of varying nucleation and growth rate constants on the simulation was investigated systematically over 4 orders of magnitude for nucleation and 3 orders of magnitude for growth (Figure 5.4). Although it was possible to simulate several conditions that resulted in a similar amount of aggregation over a certain time period, the profiles clearly displayed characteristic differences thereby supporting our modeling approach of fitting monomer loss vs time for this mAb. For example, samples with slower nucleation rates and faster growth rates displayed an initial "lag" phase

compared to samples with a faster nucleation rate and slower growth rate. Based on the results

of these initial simulations, we collected a range of experimental mAb aggregation stability data

in different solutions to capture the lag perceived by slower nucleation rates and acceleration

produced by fast growth rates. The timescale of the stability study for each mAb solution

condition needed to be optimized to capture a full range of aggregation data to properly

discriminate between different combinations of nucleation and growth rates.

Simulated fits of experimental mAb aggregation data were then generated for the fraction

of non-aggregated mAb species (monomer + fragment) for each solution and temperature

condition to determine observed rate constants for aggregate nucleation and growth processes.

The rationalization for modeling both monomer and fragments populations as aggregate prone

species is discussed in detail the Supplemental Materials section (see Rationalization of

Assumptions Present in Aggregation Model). Briefly, substantial fragmentation did not appear

to deplete reactive species populations by causing mAb aggregation rates to decelerate. In a

future study, we plan to investigate the effect of considering fragmentation as the initiation step

in separate mAb aggregation pathways to more accurately model such cases. Representative

SEC chromatograms and SV-AUC data demonstrating separation profiles and peak integration

of the different mAb species are presented in Figure 5.5 (panels A-B). In addition, integrated

SEC aggregation profiles for mAb samples under different histidine buffer solution conditions as

a function of time and temperature are presented in Figure 5.5 (panels C-H). Integrated SEC

aggregation profiles for the mAb in different citrate buffer solution conditions at different

temperatures are shown in Figure 5.6.

Figure 5.7 shows the simulation results for the SEC aggregation data for the pH 4.5 mAb

solutions, in both citrate and histidine buffers with/without NaCl, after being incubated at 57 ℃

for up to 5 days. The red squares in the figure represent the average concentration (mg/ml) of non-aggregated species for mAb solutions in three different sample vials measured by SEC or SV-AUC. In the pH 4.5 citrate solution, incubation resulted in rapid monomer loss with no monomer detected in solution after 1 day of incubation (Figure 5.7A, top panel). Absorbance spectroscopy of the supernatant fraction after centrifugation confirmed that loss of monomer was because of non-native amorphous precipitation (Figure 5.8, panel A). Additionally, the modeled observed growth rate constant dominated the overall aggregation kinetics compared to the nucleation process (Table 5.3). The mAb in the pH 4.5 citrate solution with NaCl also had a similar rate of monomer loss (Figure 5.7A, bottom panel) and also underwent phase separation after one day. The overall kinetics of aggregation was also growth dominated (Supplemental Table 5.3). On the other hand, although monomer loss of the mAb in the pH 4.5 histidine solution was also rapid (Figure 5.7B, top panel), no significant increase (compared to t=0) in the calculated mass of larger aggregates (i.e., particles larger than 2 µm in diameter), based on FlowCam particle data, was detected after 3 days (Figure 5.6, panel B). The shape of the simulated result also suggests that the mAb sample has a nucleation dominated aggregation mechanism similar to the light blue trace in Figure 5.4, panel A. Increasing the ionic strength of the mAb in histidine buffer (with NaCl) causes the observed aggregation rate to increase, and resulted in significant non-native phase separation after 1 day of incubation (Figure 5.6, panel A). In this sample condition, neither aggregate nucleation nor growth clearly dominated the aggregation mechanism (Table 5.3).

The pH 4.5 mAb solutions, in both citrate and histidine buffers with/without NaCl were also incubated at 40 ℃ for up to 7 months (Figure 5.9). Integrated SEC results for mAb samples incubated at 40 ℃ as a function of time are presented in Figure 5.6. It is apparent that less mAb

aggregated over the course of 7 months when incubated at 40 ℃ compared to 1 day at 57 ℃.

The mAb in the pH 4.5 citrate solutions with and without NaCl had similar rates of aggregation

at 40 ℃ (Figure 5.7A). In these sample conditions, a slower 'lag phase' in which aggregate

nucleation primarily occurs was observed prior the rate accelerating due to aggregate growth.

The simulated rate constant values support these observations because the observed rate

constants of aggregate growth were ~3 orders of magnitude larger than those of nucleation

(Table 5.3). On the other hand, a lag phase was not readily observable in the pH 4.5 histidine

mAb solutions with and without NaCl, but the profile displayed some early curvature indicative

of both aggregate nucleation and growth processes occurring. The simulated rate constants,

however, suggest that the observed growth rate constant was ~3 orders of magnitude larger than

the nucleation rate constant. Although aggregate growth was non-trivial, no significant increases

in the calculated mass of larger aggregates (i.e., particles greater than 2 µm in diameter), as

calculated from the experimentally determined MFI data, was detected after 7 months (Figure

5.6, panel C).

The mAb samples at pH 6.5 were also incubated at 40 ℃ for up to 7 months and fit to the

kinetic models described by Equations 5.06 and 5.07 (Figure 5.10). The rate and extent of

aggregation at pH 6.5 was much less than at pH 4.5, despite reduced values of apparent solubility

(and extrapolated thermodynamic activity, determined by PEG precipitation) and having more

attractive PPI (A2 values by static light scattering), as presented in the previous section, and as

discussed in the next section. Curvature of the simulated fit to the experimental SEC aggregation

data was also observed for mAb in pH 6.5 citrate solution incubated at 40 ℃. The aggregation

profile for the mAb in the pH 6.5 histidine solution did not display major curvature since both

the modeled nucleation and growth rates were very slow over this time period.

At 25 ℃, the aggregation profiles for the mAb in the pH 4.5 histidine and citrate solutions was even slower with less than 3% monomer loss occurring in both samples after 7 months (Figure 5.11). Although such degradation could be considered significant from a pharmaceutical storage stability perspective, the modeled nucleation and growth rate constants for both conditions were extremely slow and did not show any appreciable differences between the samples. To be more rigorous for modeling aggregation of this mAb at this temperature condition, future work will need to include a longer-term stability study to mechanistically examine mAb aggregation at lower temperatures and to test the applicability of these models to predict protein storage life under lower temperature conditions. Thus, although the results at 25°C do not show any appreciable differences in their modeled rate constants, the data should not be over interpreted due to the lack of an apparent characteristic time scale observed in the monomer loss vs. time data.

5.4.5. The Effect of the Physical Properties of the mAb in Different Solutions on Aggregate Nucleation and Growth

When taken together, the two simulated aggregation rate constants modeled from the mAb stability data in various solution and temperature conditions provide several important results in terms of better understanding the aggregation mechanism of experimental data in relation to the physical properties of the mAb. To this end, as shown in Figure 5.12A, the modeled values of $k_{nuc,obs}$ (mAb aggregation nucleation rate constants) are presented as a function of apparent melting temperature (T_m values from DSC measurements; see Table 5.1) minus incubation storage temperature (T) for all of the examined storage and solution conditions. This temperature scale of $(T_m - T)$ was used to better evaluate the effect of partially unfolded mAb on the observed aggregation nucleation rate constants. The modeled nucleation rate

constants were normalized by the smallest value to observe differences between the solution and temperature conditions on a relative scale (also, it should be noted that for this analysis aggregation data for pH 6.5 mAb samples incubated at 57 ℃, and for mAb samples incubated at 25 ℃, are not included because of the limitations outlined in the previous sections).

At 40 ℃ incubation ($T_m - T$ ranging from ~15 to 20 ℃ in Figure 5.12A), the observed nucleation rate constants for the mAb in pH 4.5 histidine (dark red), pH 4.5 histidine + NaCl (light red), pH 4.5 citrate (dark blue), and pH 4.5 citrate + NaCl (light blue) solutions appear to be similar and randomly distributed. Interestingly, differences in a_2 or the apparent solubility profiles (e.g., midpoint or extrapolated activity values, Table 5.2) were not reflected in the modeled $k_{nuc,obs}$ values for solution conditions with similar $T_m - T$ values (Figure 5.12A). At 57 ℃ incubation ($T_m - T < 5$ ℃), the modeled nucleation rates increased rapidly as $T_m - T$ decreased. This seems intuitive because the nucleation mechanism expected to be fastest at high temperatures has an observed rate constant which scales with the fraction of unfolded protein squared. It was unexpected, however, that the colloidal environment in the different solution conditions did not appear to have any affect on the observed nucleation rate constants, since we had originally hypothesized that conformationally altered proteins were more likely to stick upon collisions and would therefore appear to follow the theory of slow coagulation (see introduction).

In the context of this model, this result from Figure 5.12A implies that the process of aggregate nucleation for this mAb behaves similarly to limiting case 2 as presented in the *Theoretical Role of Colloidal Stability on Aggregation* Rates section. In other words, structural alterations of associated mAb monomers to form a stable irreversible mAb dimer could be the rate limiting component of aggregate nucleation. Additionally, we did not observe any apparent correlation of the experimental aggregation rate in different solutions to the apparent solubility

171

values of the mAb in the same solutions (as measured in PEG precipitation assay). This is probably because partially unfolded intermediates of the mAb would be expected to have lower solubility values. If the equilibrium association constant is high for the mAb in every solution, then we would expect only conformational rearrangement of an encounter complex to be the rate limiting step. In this study, the nucleation mechanism involving encounter complex formation between native mAb molecules, described by Equation 5.03c, did not appear to be a major pathway for this mAb. It would be interesting to see in future work if nucleation of other mAb molecules, which undergo that pathway to a greater extent, correlates with such apparent solubility measurements as seen previously by others with using different mAbs (59, 180).

Using the same approach described above (Figure 5.12A) with the model nucleation rate constants, the modeled values of $k_{g,obs}$ (observed growth rate constants for mAb aggregation) are presented as a function $T_m - T$ to better observe the role of conformational changes (i.e., CH_2 domain unfolding as seen by DSC) on growth processes during aggregation of this mAb (Figure 5.12B). In contrast to Figure 5.12A, it is readily apparent in Figure 5.12B that aggregate growth does not correlate as well to the relative concentration of partially unfolded mAb as approximately given by $T_m - T$. One potential explanation is that the observed growth rate constants (Figure 5.12B) were more sensitive to the colloidal environment of the mAb as measured by a_2 and PEG precipitation values (Table 5.2). The deviations between $k_{g,obs}$ values for the mAb in different solution environments, but at similar $T_m - T$ values, appear to best correlate with the rank ordering of the apparent solubility profiles for the native mAb in different solutions (Figure 5.3C). Furthermore, it is difficult to physically justify how encounter complex formation could be rate limiting at the relatively low a_2 values observed in this study. Therefore, although we conclude that aggregate growth by monomer addition was sensitive to the colloidal

environment of the mAb under these conditions, we suspect that rates were affected by association thermodynamics rather than kinetics. In other words, based on these considerations, it is reasonable to conclude that similar to aggregate nucleation, aggregate growth also follows limiting case 2 as presented in the *Theory - Role of Colloidal Stability and Apparent Solubility on Aggregation Rates* section. Except that in this case, it was probably the equilibrium concentration of associated encounter complex that was rate limiting rather than the structural rearrangement of the encounter complex. For example, although there was substantial monomer loss in the pH 4.5 mAb sample in histidine buffer incubated at 57°C for 3 days, there was limited aggregate growth. Note that this solution condition had the highest solubility in PEG solutions compared to the other mAb solution conditions. Barnett et al. previously rationalized this type of observation by arguing that when protein-protein interactions are strongly repulsive, a monomer diffusing towards an aggregate would be felt simultaneously by all of the monomeric components within the aggregate causing extensive growth to become highly unfavorable (35).

5.4.6. Rationalization of Assumptions Present in Aggregation Model

In our simulations, aggregate-aggregate association was set to zero because accurately quantifying aggregate populations was challenging due the limited size resolution of the SEC column and the potential of aggregates to either adsorb to or be filtered out by the guard column. In the context of this model, however, aggregate-aggregate association will deplete the total aggregate population which could decrease the observed rate of growth by monomer addition for this model (Equation 5.07). Fortunately, the observed rates of aggregate-aggregate association should be very slow until aggregate populations become large enough to overcome the second order concentration dependence. In this study, the last experimental time points for most of the solution and temperature conditions investigated showed no significant particle formation. For

173

sample conditions that did have measurable precipitation at the end of the time scales examined, early time points without significant particle formation were used to simulate the fit of monomer loss. Additionally, we ran simulations which included a large k_{agg} term and found that it did not affect the fit residuals indicating that the modeled time points were sufficiently early to avoid large errors from neglecting aggregate-aggregate growth (data not shown). Another assumption included in the simulation was that $k_{g,obs,\{A_2\}} \approx k_{g,obs,\{A_\infty\}}$. This assumption was made necessary because it was not feasible to individually model each and every growth rate constant due to the challenges of resolving aggregate sizes. Fortunately, this assumption does not affect the number of reactive aggregates within the context of this model and should therefore provide a relative rate constant that describes aggregate growth by monomer addition.

Interestingly, the fragmentation pathway did not appear to interfere with the aggregation pathway (i.e. the rate of area loss of the monomer + fragment peaks did not decelerate or decrease with substantial fragmentation). If the fragmentation pathway prevented mAb species from aggregating, the rate should have decelerated reflecting the reduced population of reactive species. As a result of the previous observation, aggregation rates were modeled without explicitly considering fragmentation pathways. In terms of future work, it will be important to explore ways to explicitly consider fragmentation pathways and integrate them with the aggregation models developed here.

Within the context of this model, the pH 6.5 mAb samples incubated at 57 ℃ were not able to be accurately simulated without constraining the number of aggregate prone monomer species. The early plateau in monomer loss after ~3 days (Figure 5.5 G & H) may reflect depletion in the amount of aggregate prone species. This result further underscores the

challenges and inherent limitations of treating complex proteins as simple colloidal particles (i.e., pH only alters surface charge and fraction of reactive species).

5.5. Conclusions

In this study we evaluated the aggregation vs. storage time profile of an IgG1 mAb under different solution conditions across a range of temperatures by SEC and SV-AUC, and compared results to the physical properties of the mAb in different solutions including those that produced partially unfolded intermediates (conformational stability by DSC), apparent solubility (in PEG solutions), and protein-protein interactions (second virial coefficients by SLS). A kinetic model for aggregation was developed and applied to interpret SEC and SV-AUC aggregation data during storage of the IgG1 mAb at different temperatures in terms of the roles of aggregate nucleation and growth. Additional kinetic equations describing the effects of conformational stability, colloidal stability, and equilibrium encounter complex formation were also proposed.

We found that the modeled nucleation rate constants for aggregation of this mAb in different solutions were most sensitive to the formation of partially unfolded intermediates (i.e., conformational stability of the mAb). In other words, as the incubation temperature approached the thermal melting temperature (as measured by DSC), the observed aggregation nucleation increased as expected. Interestingly, the observed aggregation nucleation rate constants did not appear to be affected by protein-protein interactions and/or apparent solubility values for this mAb under these various solution and temperature conditions. As a result, we conclude that the association processes between protein monomers were not a rate limiting step of aggregate nucleation for this mAb under these solution and storage conditions.

On the other hand, aggregate growth rate constants (by monomer addition) for this mAb in the same solutions were highly sensitive to protein-protein interactions and/or apparent solubility values (i.e., association thermodynamics) as well as to the conformational stability (i.e., concentration of partially unfolded intermediates) when the mAb was incubated at 57 and 40 °C. Based on the relatively low values of a_2 measured in this study, it is difficult to physically justify long range repulsive interactions causing the rate of protein associations to become the rate limiting step; thus, it is more likely that the thermodynamics of encounter complex formation of the mAb in the different solutions was the rate limiting component of aggregate growth in the same solutions during storage. Thus, this work provides a method to model experimentally obtained protein aggregation stability data to enable a better mechanistic understanding of the relative contributions of nucleation and growth components of the aggregation pathway as function of solution conditions and temperature for proteins.

5.6. Figures and Tables

5.6.1 Tables

Solution Condition (1 mg/ml mAb)	T_{onset} (°C)	T_{m1} (°C)	T_{m2} (°C)	T_{m3} (°C)
pH 4.5 histidine	50.1	58.3	71.7	
pH 4.5 histidine w/ 100 mM NaCl	47.8	56.1	70.3	
pH 6.5 histidine	62.8	72.9		83.4
pH 4.5 citrate	51.5	59.5	73.1	79.2
pH 4.5 citrate w/ 100 mM NaCl	50.1	59.0	72.7	79.0
pH 6.5 citrate	62.0	73.1		83.1

Table 5.1. Apparent thermal melting temperatures for mAb in solution conditions as measured by DSC. Apparent thermal melting temperature values are reported as T_{m1}, T_{m2}, and T_{m3} representing the CH_2, Fab, and CH_3 domains of the mAb, respectively (see Figure 5.1 and text). A thermal melting profile that fails to display melting temperatures for each domain/region is considered an observed T_m to highlight that the melting event could be a convolution of two unfolding events. Each reported value is the average of n=3 experiments, and the standard deviation (SD) for each value was less than 0.2 for all conditions.

Solution Conditions (1 mg/ml mAb)	pH	Approx. mAb Net Charge	Approx. Ionic Strength	Theoretical b_2	Experimental a_2		[PEG] midpoint
					Mean	SD	Mean
50 mM Citrate	4.5	104.3	0.089	7.6	-0.84	0.03	6.8
50 mM Citrate	6.5	41.3	0.243	0.3	-1.14	0.02	5.2
50 mM Citrate w/ 100 mM NaCl	4.5	104.3	0.189	2.6	-0.82	0.01	7.9
50 mM Histidine	4.5	104.3	0.024	43.1	1.18	0.29	24.6
50 mM Histidine	6.5	41.3	0.007	31.9	0.58	0.02	8.5
50 mM Histidine w/ 100 mM NaCl	4.5	104.3	0.124	4.8	-0.43	0.03	15.1

Table 5.2. Summary of experimental and calculated physical parameters of different mAb solutions. Values for approximate mAb Net Charge, approximate solution Ionic Strength, and Theoretical b_2 values (theoretical surrogate parameter for protein-protein interactions) were calculated as described in the methods section. The experimental surrogate parameter for protein-protein interactions (a_2) and [PEG] midpoint values (midpoint of mAb vs PEG concentration curves; see text) are presented as the average and standard deviation of 3 experiments. Values of b_2 and a_2 are normalized and therefore have no units. [PEG] midpoint has units of % w/v. The standard deviation for the [PEG] midpoint was less than 0.1 for all conditions.

Solution Condition	$k_{nuc, obs}$	$k_{g,obs}$	T
pH 4.5 Histidine	1.67E-04	2.08E-03	57
pH 4.5 Histidine	3.75E-08	1.35E-05	40
pH 4.5 Histidine	2.29E-08	1.15E-05	25
pH 4.5 Histidine NaCl	1.41E-03	1.63E-02	57
pH 4.5 Histidine NaCl	8.13E-08	1.67E-05	40
pH 6.5 Histidine	2.71E-08	1.77E-05	40
pH 4.5 Citrate	1.00E-05	1.32E+00	57
pH 4.5 Citrate	5.42E-08	7.71E-05	40
pH 4.5 Citrate	2.29E-08	1.46E-05	25
pH 4.5 Citrate NaCl	1.54E-05	1.53E+00	57
pH 4.5 Citrate NaCl	6.88E-08	7.50E-05	40
pH 6.5 Citrate	2.71E-08	2.08E-05	40

Table 5.3. Modeled values of observed rate constants for aggregate nucleation and growth.

The simulated values of $k_{nuc, obs}$ and $k_{g,obs}$ have units of $min^{-1}ml * mg^{-1}$. The incubation

temperature (T) has units of °C.

5.6.2. Figures

Equation	Visual Scheme of Nucleation Mechanisms
3a	
3b	
3c	
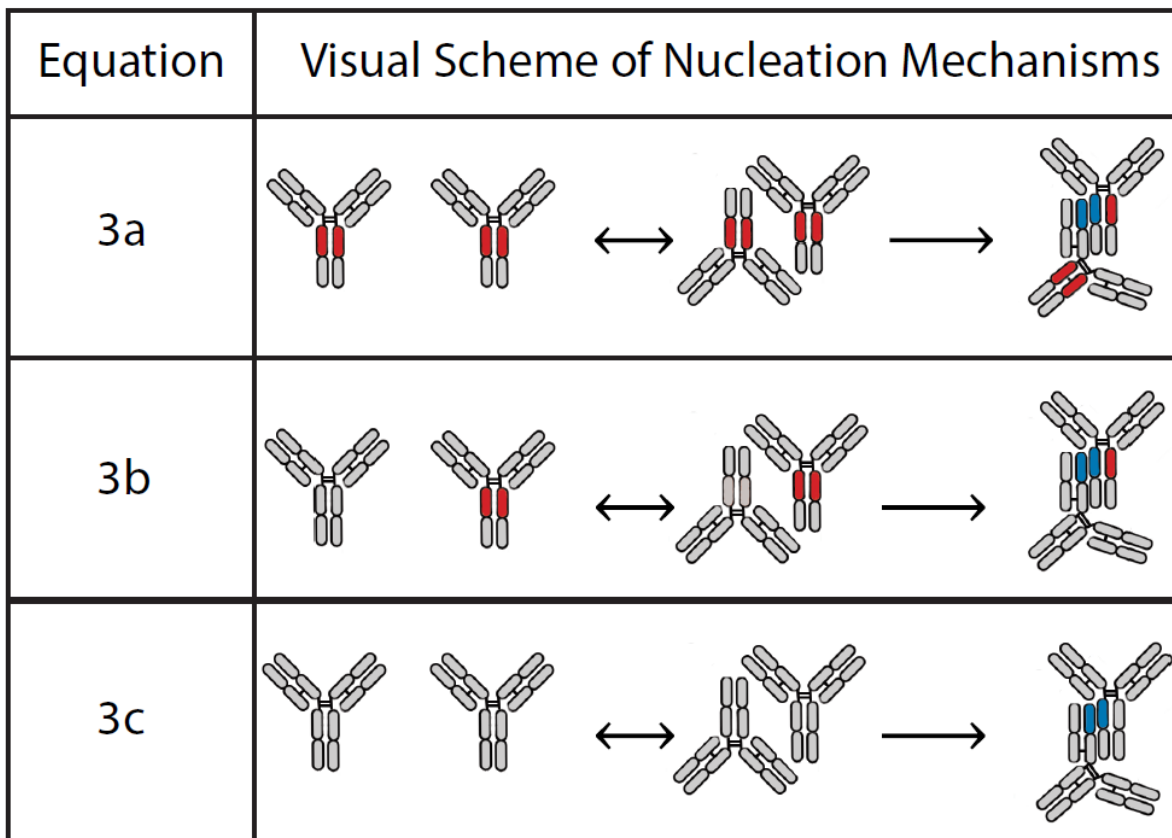
Figure 5.1. Visual scheme of potential mAb nucleation mechanisms. The various mAb nucleation mechanisms of aggregation shown in the figure correspond to Equations 5.03a, 5.03b, and 5.03c. The visual schematic is not intended to be structurally accurate at a molecular level, and therefore should not be over interpreted in terms of actual mAb aggregate structure. Red color represents a disordered domain, grey color a native domain, and blue color an inter-domain structure between two mAbs.

Equations	Visual Scheme of Growth Mechanisms
(N = 3a) G = 4a	
(N = 3a) G = 4b	
(N = 3b) G = 4a	
(N = 3b) G = 4b	
G = 5 (i = 2, j=3)	

Figure 5.2. Visual scheme of growth mechanisms for different dimers produced through nucleation mechanism 3a or 3b. The different mAb growth mechanisms of aggregation shown in the figure correspond to Equations 5.04a, 5.04b, and 5.05. The visual schematic is not intended to reflect accurate structure at a molecular level, and therefore should not be directly interpreted in terms of aggregate structure. Red color represents a disordered domain, a grey color a native domain, and blue color represents an inter-domain structure between two mAbs. The letters G and N represent "growth" and "nucleation," respectively.
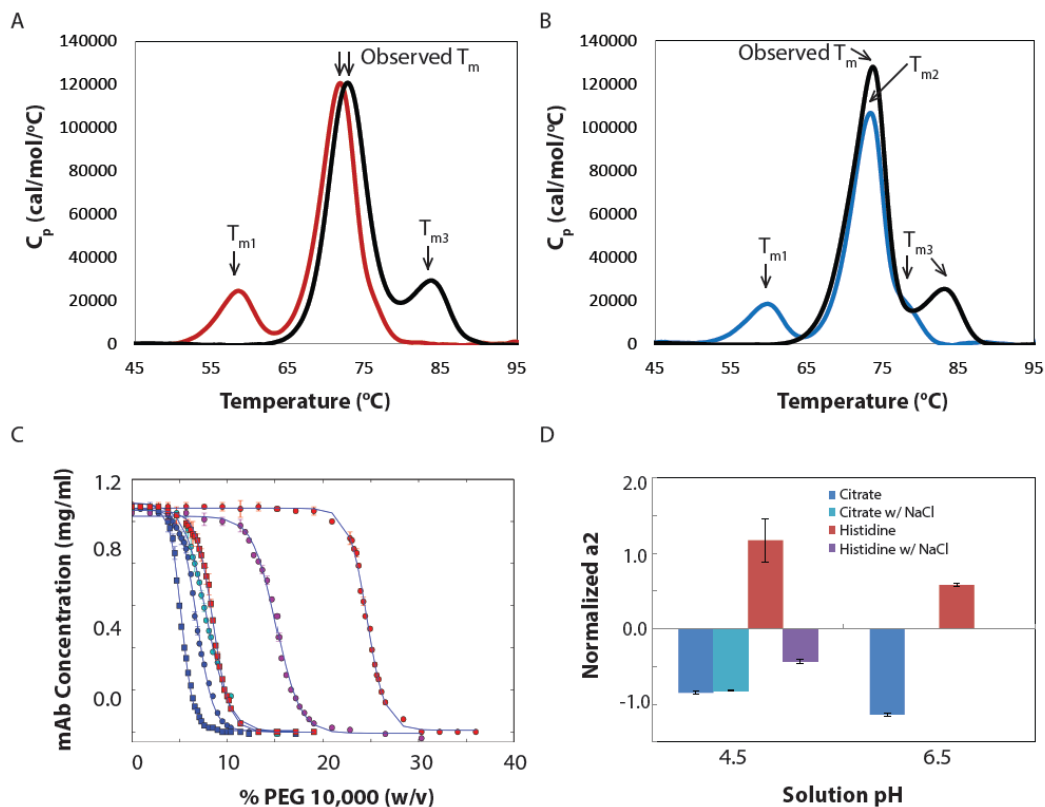
Figure 5.3. Representative conformational stability, apparent solubility, and protein-protein interactions data for IgG1 mAb in different pH and buffer conditions. (A) DSC thermogram of mAb in pH 4.5 (red trace) and pH 6.5 (black trace) histidine buffer. (B) DSC thermogram of mAb in pH 4.5 (blue trace) and pH 6.5 (black trace) citrate buffer. A thermal melting profile that fails to display a melting temperature for each domain is labelled with an observed T_m to highlight that the melting event could be a convolution of two domain unfolding events. (C) Protein-PEG precipitation curves for 1 mg/ml mAb at pH 4.5 (denoted by circles) and pH 6.5 (squares) in histidine buffer (red), histidine buffer w/ 100 mM NaCl (purple), citrate buffer (blue), and citrate buffer w/ 100 mM NaCl (cyan). (D) Normalized second virial coefficient values at pH 4.5 and 6.5 in citrate buffer (blue), citrate buffer w/ 100 mM NaCl (cyan), histidine buffer (red) and histidine buffer w/ 100 mM NaCl (purple) as measured by static light scattering (CG-MALS).

182
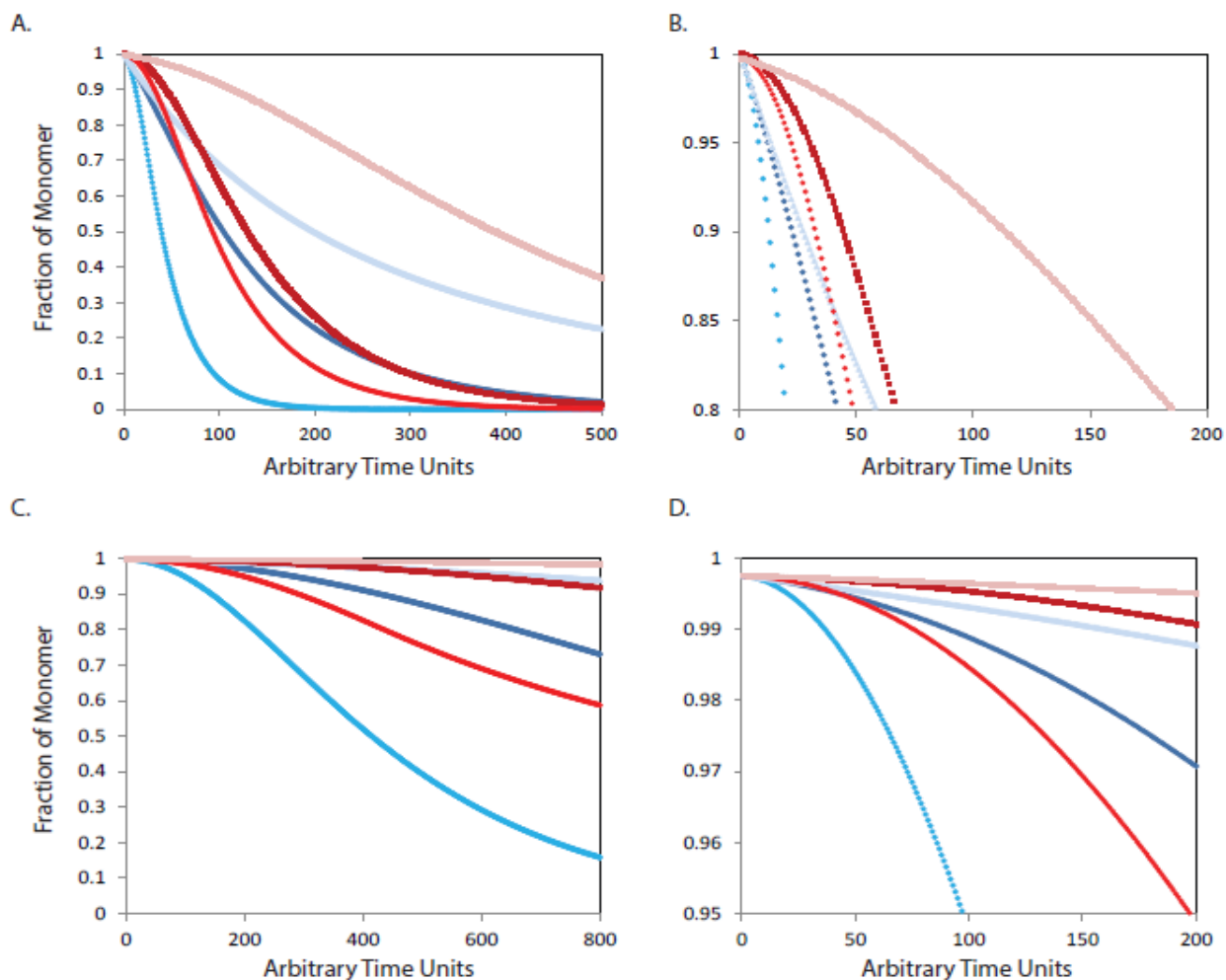
Figure 5.4. Simulated mAb aggregation profiles generated using the LENP-based model (as described in the theory section of the main text) using various nucleation and growth rate constants. Simulations were conducted using arbitrary time units (ATU) causing rate constants to have units of ml/(mg ATU). (A) Aggregation profiles for molecules with "faster" nucleation rates. The red traces have a nucleation rate of 0.0002 and the blue traces have a nucleation rate 10x faster than the red trace. The lightest red color (topmost) trace has a growth rate of 0.05, the darkest red color (middle) trace has a growth rate of 0.5, and the red color (bottom) trace has a growth rate of 0.99. The light blue (topmost) trace has a growth rate of 0.005, the dark blue (middle) trace has a growth rate of 0.05 and the teal (bottom) trace has a growth rate of 0.5. (B)

Zoomed-in version of the early stage of the aggregation profiles displayed in Panel A. (C) Aggregation profiles for molecules with "slower" nucleation rates. The red traces have a nucleation rate of 2 x 10^-6 and the blue traces have a nucleation rate 10x faster than the red trace. The pastel blue and pastel red (topmost) traces have a growth rate of 0.005, the dark blue and dark red (middle) traces have growth rates of 0.05, and the red/teal (bottom) traces have a growth rate of 0.5. (D) Zoomed-in version of the early stages of aggregation profiles displayed in Panel C.
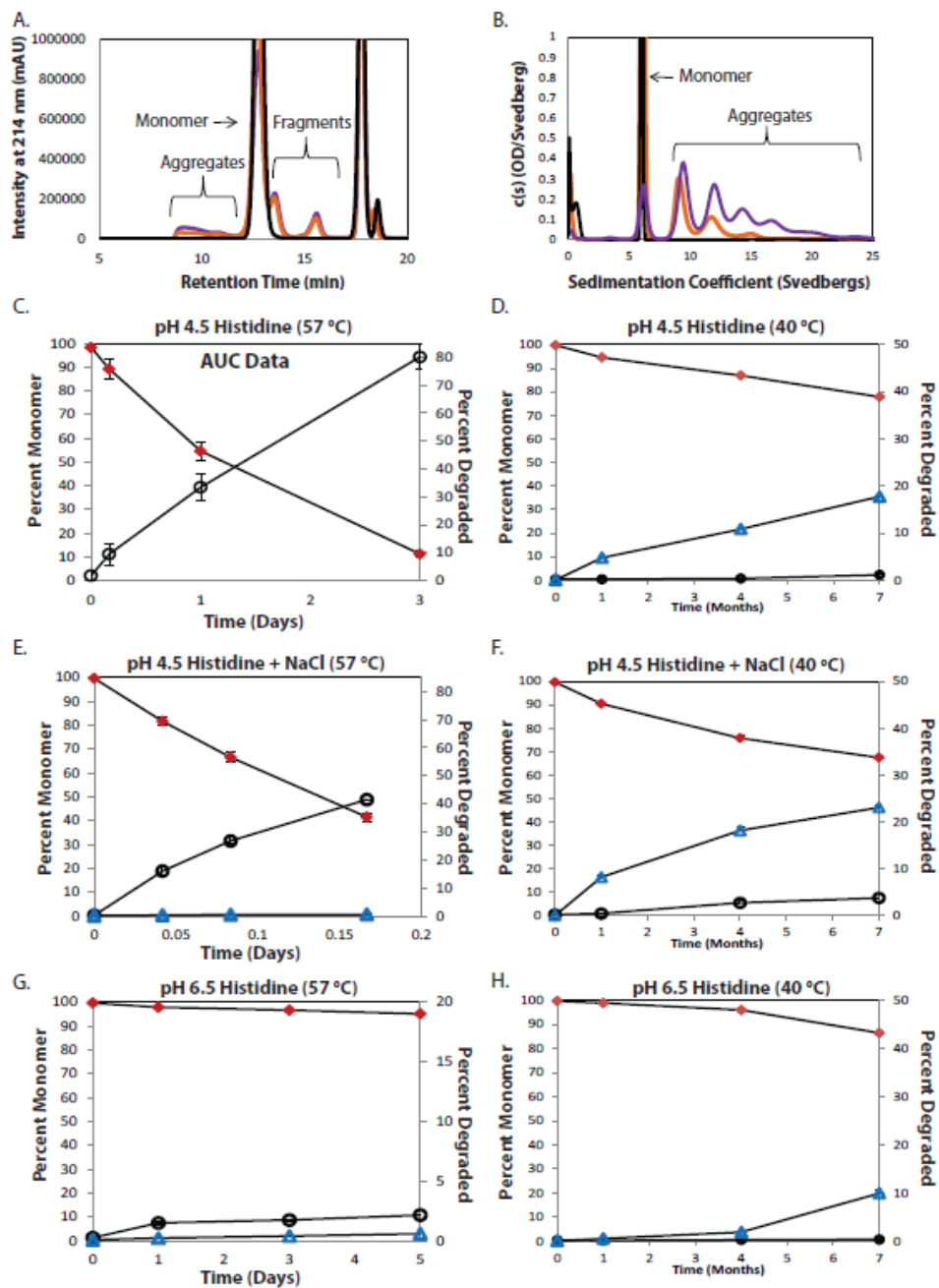
Figure 5.5. SEC and SV-AUC data for mAb incubated at 40 or 57 °C in histidine solutions at different pH/ionic strengths. (A) Representative SEC chromatograms showing mAb aggregate, monomer and fragment peaks changing in area as a function of incubation time. (B) Representative SV-AUC data showing mAb monomer and aggregate peaks changing in area as a function of incubation time. (C-H) Profiles showing loss of mAb monomer (red diamonds) and

increase in mAb aggregates (black open circles), and increase in mAb fragments (blue open triangles) as a function of incubation time. SEC and SV-AUC data normalized to total area at t=0 to capture loss due to insoluble aggregate formation. Data presented as the average of 3 experiments. Error bars reflect the standard deviation. Buffer conditions and incubation temperatures are labelled above each graph. Lines simply connect the data points for ease of interpretation and are not meant to fit the data.
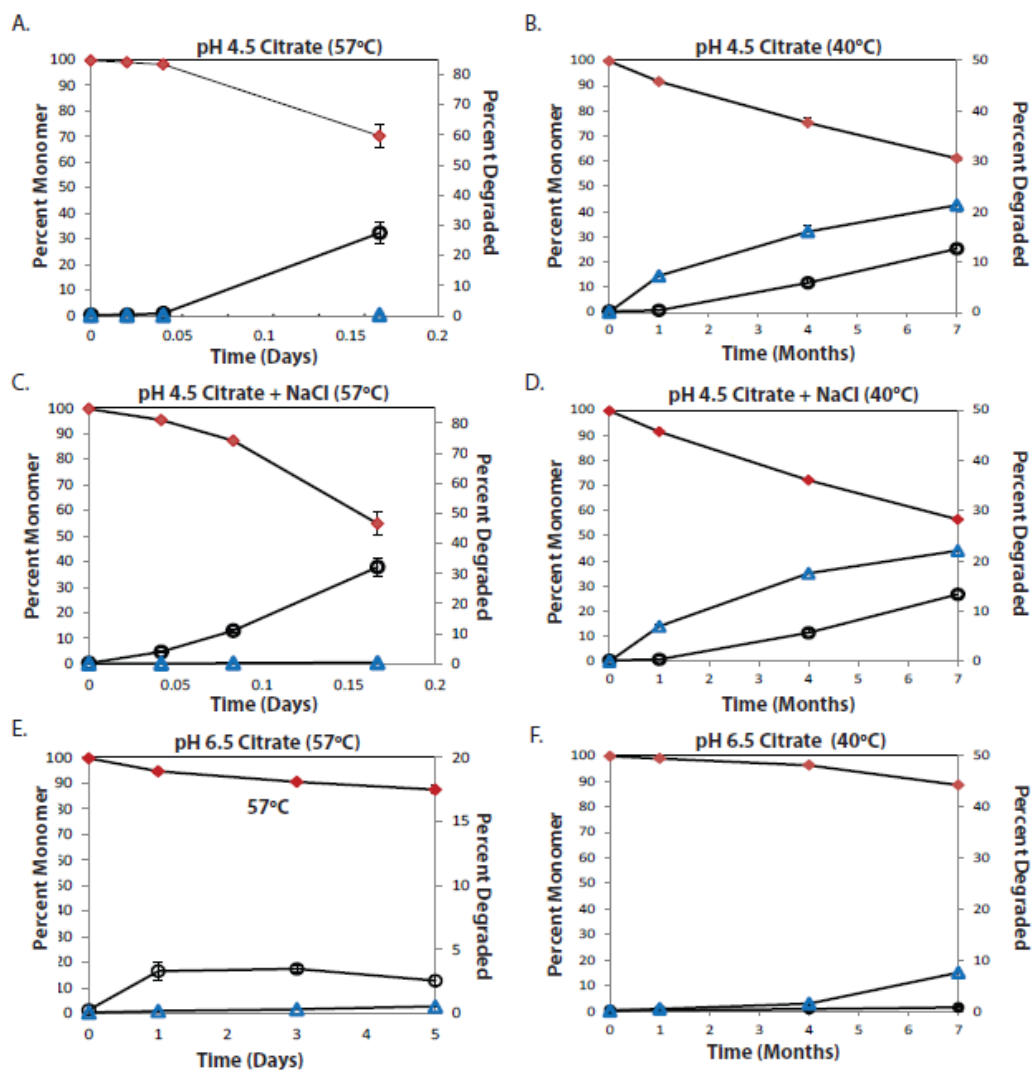
Figure 5.6. SEC data for mAb incubated at 40 or 57 °C in citrate solutions with different pH/ionic strengths. (A-F) Profiles showing loss of mAb monomer (red diamonds) and increase in mAb aggregates (black open circles), and increase in mAb fragments (blue open triangles) as a function of incubation time. SEC data were normalized to total area at t=0 to capture loss due to insoluble aggregate formation. Data presented as the average of 3 experiments. Error bars reflect the standard deviation. Buffer conditions and incubation temperature are labelled above each graph. Lines simply connect the data points for ease of viewing and are not meant to fit the data.
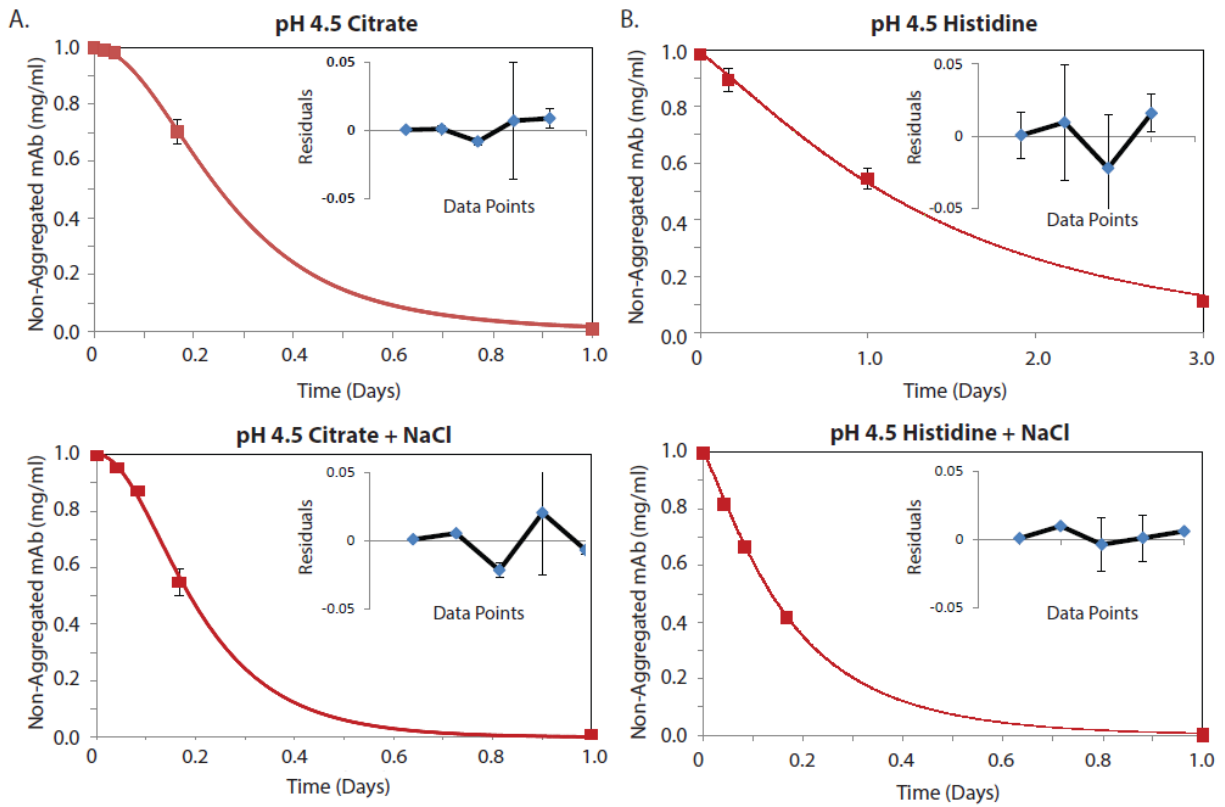
Figure 5.7. Simulated fit of experimental SEC and SV-AUC data of loss of non-aggregated (monomer + fragment) mAb over time at 57°C. Experimental (solid red squares, n= 3) and simulated profiles (solid red line) of non-aggregated mAb concentration in different solution conditions as a function of incubation time. The residuals of each fit are presented in the upper right corner of the corresponding graph. Error bars reflect the experimental standard deviation. Buffer conditions are labelled above each graph. The top panel of (B) was acquired using SV-AUC and all other conditions were measured using SEC.
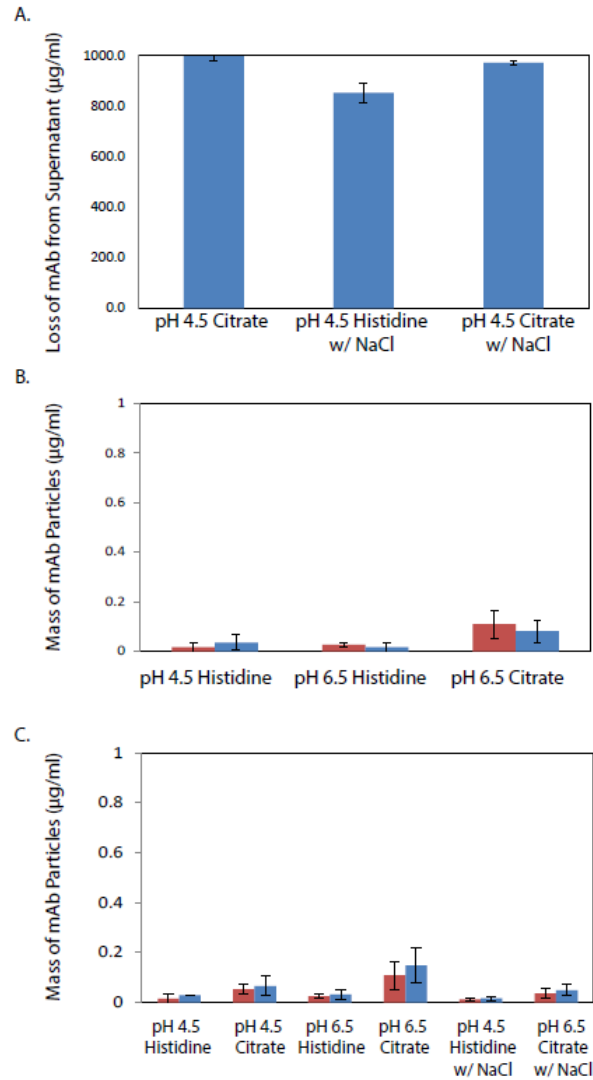
Figure 5.8. Precipitation and particle formation of the mAb after incubation at different temperatures/time scales. (A) Loss of protein mass in solution measured by absorbance spectroscopy after 1 day of incubation at 57 °C. (B) Calculated mass of subvisible protein particles suspended in solution, using particle number and size data from flow imaging measurements using a method developed reported previously (104), after 1 day of incubation at 57 °C. No visible precipitate was observed in these samples. (C) Calculated mass of subvisible sized protein particles suspended in solution after 7 months of incubation at 40 °C. No visible precipitation was observed in these samples.

189
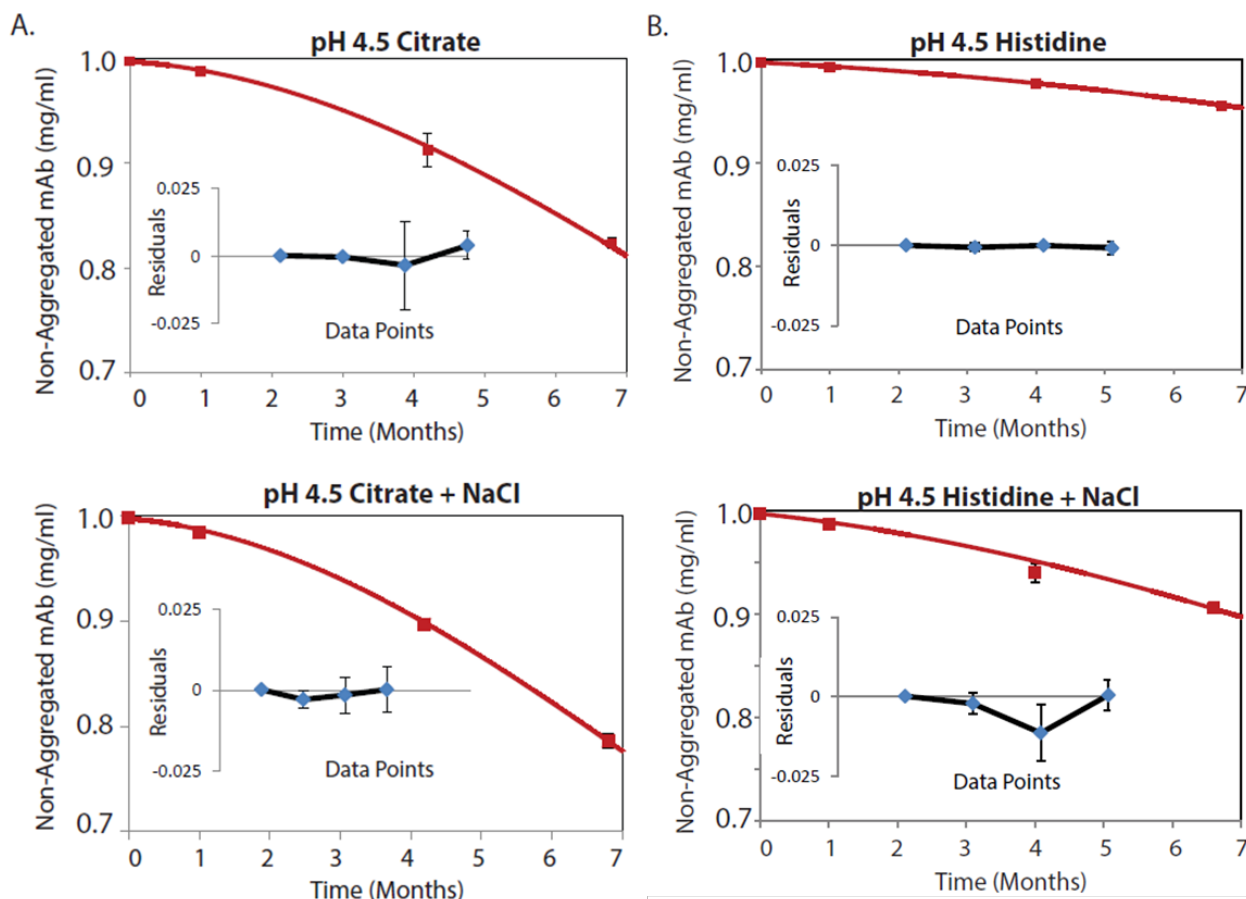
**Figure 5.9. Simulated fit of experimental SEC data of loss of non-aggregated (monomer +
fragment) mAb over time at 40°C.** Experimental (solid red squares, n= 3) and simulated
profiles (solid red line) of non-aggregated mAb concentration in different solution conditions as
a function of incubation time as measured by SEC. The residuals of each fit are presented in the
lower left corner of the corresponding graph. Error bars reflect the experimental standard
deviation. Buffer conditions are labelled above each graph.
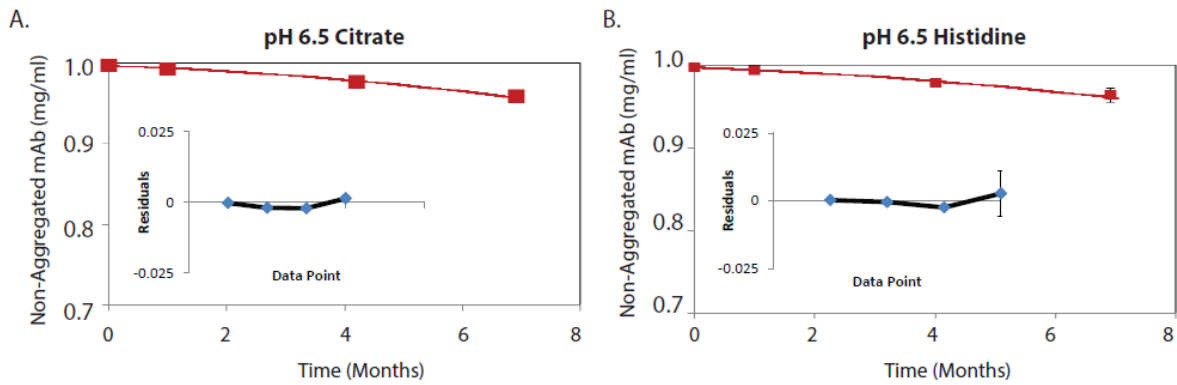
Figure 5.10. Simulated fit of experimental data of non-aggregated (monomer + fragment) mAb at pH 6.5 at 40°C during storage. (A, B) Experimental (solid red squares, n= 3) and simulated profiles (solid red line) of non-aggregated mAb concentration in different solution conditions as a function of incubation time. The residuals of each fit are presented in the lower left corner of the corresponding graph. Error bars reflect the experimental standard deviation. Solution conditions for mAb are labelled above each graph.
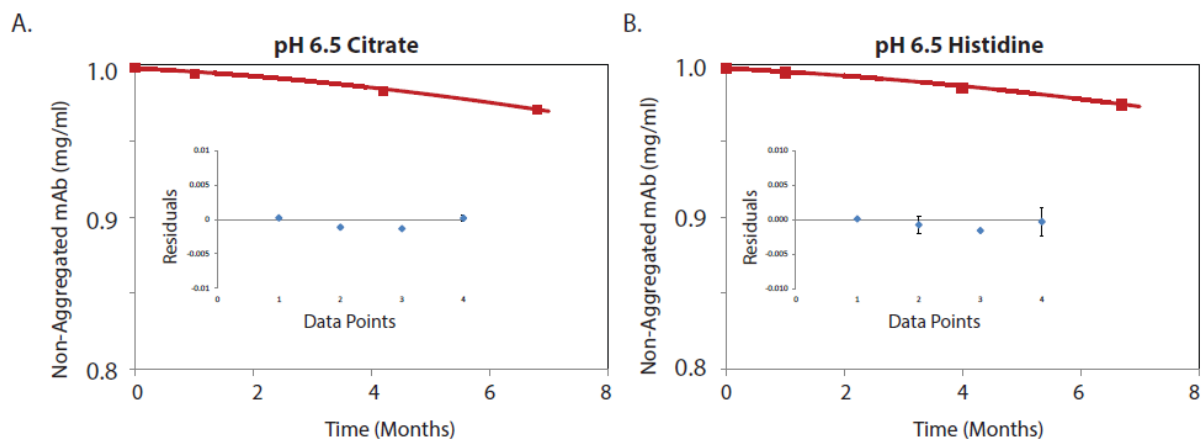
Figure 5.11. Simulated fit of experimental data of non-aggregated (monomer + fragment) mAb at pH 4.5 at 25°C during storage. (A, B) Experimental (solid red squares, n= 3) and simulated profiles (solid red line) of non-aggregated mAb concentration in different solution conditions as a function of incubation time. The residuals of each fit are presented in the lower left corner of the corresponding graph. Error bars reflect the experimental standard deviation. Solution conditions for mAb are labelled above each graph.
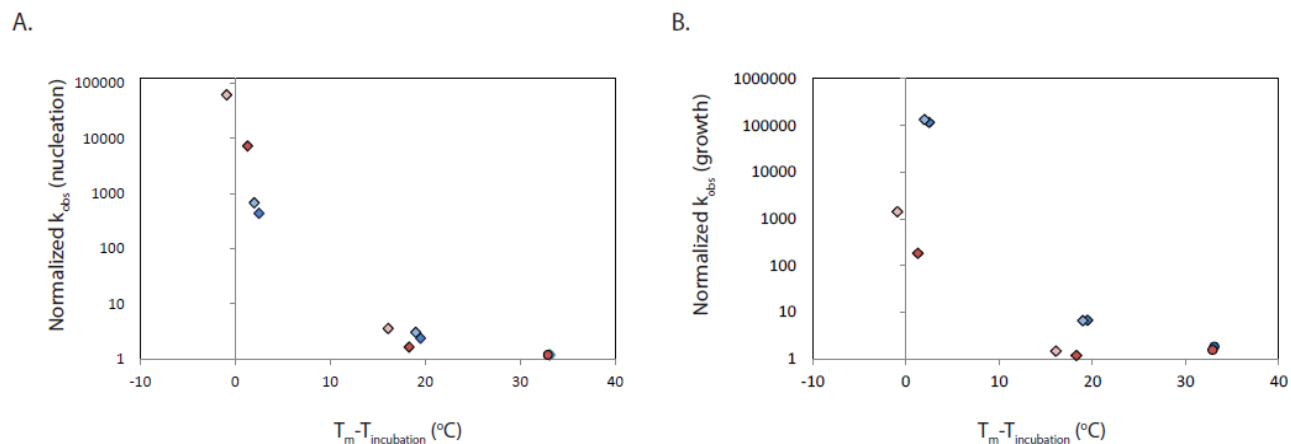
Figure 5.12. The effect of conformational stability (presence of partially unfolded mAb species) on the observed rate constants for mAb aggregate nucleation and growth.

Observed nucleation and growth aggregation rate constants were obtained by fitting simulations of Equations 5.06 and 5.07 to experimental SEC and SV-AUC stability data for mAb stored in different solutions at different temperatures. The values reported are dimensionless numbers which were normalized by the smallest observed rate constant for each process. The colors dark blue, light blue, dark red, and light red correspond to the mAb prepared in the citrate, citrate + NaCl, histidine, and histidine + NaCl solution conditions where the diamond and circle shapes correspond to solution pH values of 4.5 and 6.5, respectively. (A.) Modeled values for the observed nucleation rate constant as a function of the first apparent melting temperature (measured by DSC) minus incubation temperature. (B.) Modeled values for the observed growth rate constant as a function of first apparent melting temperature (measured by DSC) minus incubation temperature.

Chapter 6: Summary, Discussion, and Future Directions

6.1. Summary and Discussion

The presence of protein aggregates in therapeutic biopharmaceuticals is hypothesized to increase the risk of unwanted immunogenicity in patients leading to decreased efficacy or even potentially inducing anaphylaxis (1, 2). Therefore, protein formulations are designed to minimize aggregation during manufacturing, storage and administration through empirical stability testing as well as by maximizing experimental surrogate parameters of protein conformational and colloidal stability. This latter approach is theoretically valid when protein aggregation is understood in terms of the Lumry-Eyring model. In actuality, however, protein aggregation describes a collection of multiple potentially competing pathways that can be initiated through chemical degradation, conformational changes, reversible associations, and/or adsorption to interfaces (44, 58, 61-65). As such, the role of conformational and colloidal stability in preventing protein aggregation induced during long term storage and by various environmental stress conditions remains unclear.

Competing protein aggregation pathways can result in heterogeneous aggregate populations in a protein formulation that possess wide distributions for aggregate size and morphological properties. One outstanding challenge in the preformulation characterization and formulation development of protein drug candidates is how to quantify and present such large protein aggregation/particle data sets without substantially decreasing the resolution of the data. Such methods are critical to interpret the effects of formulation variables on aggregation processes induced through various accelerated stress conditions.

In chapter 2 of this thesis, we develop and propose a data visualization method using radar charts to simultaneously quantify, present and compare the effects of multiple formulation variables on the properties of protein aggregates as a function of their measured size. The first

195

method presented in chapter 2 demonstrates how changes in solution pH, ionic strength, type of external stress condition, and duration of stress exposure can differentially affect the size and number of subvisible particles (~1-100 microns) detected in IgG1 monoclonal antibody solutions. The second method presented considers how the morphology of particles (e.g., aspect ratio and particle intensity) is affected as the formulation variables outlined above are systematically varied. In the third method presented, we demonstrate how data outputs from multiple analytical instruments can be combined to more comprehensively observe the effects of pharmaceutically relevant variables on aggregation pathways. Through application of the radar chart analysis method, we clearly demonstrate that formulations with increased conformational and colloidal stability can be effective at reducing protein aggregation and particle formation induced through specific stress conditions. At the same time, we also demonstrate that these same formulation conditions can also exacerbate aggregation/particle formation that is induced through other stress conditions which may promote aggregation through pathways that are poorly described by the Lumry-Eyring model.

Larger subvisible particles are typically counted and quantified experimentally using digital imaging techniques (e.g., 2-dimensional size). There has been a general desire to quantify such data in terms of a 3-dimensional volume and/or protein particle mass. In the pharmaceutical biotechnology literature, multiple research groups have assumed for simplicity that a 2-dimensional equivalent circular diameter can be equated to a 3-dimensional equivalent spherical diameter without significant error. In chapter 3, we first demonstrate that such assumptions can be highly erroneous depending upon the morphology of protein particles (e.g., error increases as particles become more elongated). As such, we propose using prolate ellipsoid of revolution geometry to more accurately model protein particle volume from 2-dimensional

196

size and morphology parameters. This model was tested on elongated polystyrene standards obtained through collaborators and produced superior results than the common approach of equating 2-D and 3-D diameters. Based on the boundary conditions described by a 3-dimensional prolate ellipsoid of revolution, a protein density value reflecting a 20% protein and an 80% solvent was used to calculate protein particle mass in this work. This assumed density value produced calculated mass values that agreed with experimental measures of protein mass loss in highly aggregated samples.

An observation reviewed in the introductory chapter of this thesis (chapter 1) is that the extent of aggregation induced by mechanical agitation (e.g., side-to-side shaking) of IgG1 mAb solutions does not appear to be reduced by changing the solution composition to increase mAb conformational stability and/or colloidal stability. Recent studies have hypothesized that protein particles can be produced by disrupting a high concentration gel-like layer of protein at the air-solution interface (62). In chapter 4, we collaborate with Professor Prajnaparamita Dhar and Saba Ghazvini, a graduate student in her lab, in the Chemical Engineering Department of the University of Kansas to better characterize and determine the origin of subvisible sized protein particles detected in solution after mechanical agitation.

In this chapter, the same IgG1 mAb was prepared in solutions containing different buffer ions and pH values and evaluated to determine if such changes affect the properties of the gel-like protein layer at the air-solution interface and/or the resulting subvisible particles produced. Saba Ghazvini demonstrated that both slow and fast compression rates of these various mAb solutions in a Langmuir trough system resulted in significant protein particle formation at the air-solution interface. We found that subvisible particles were only detected in significant numbers (relative to t=0 control) in bulk mAb solution for the fast compression rate. These results

197

suggest that mechanical stress can produce subvisible protein particles at the air water interface, but sufficient stress needs to be applied to release the particles from the interface into the bulk solution. Furthermore, while we found that formulation composition had a large effect on the particle formation tendencies of this IgG1 at the air-solution interface, the results could not be entirely explained using conformational stability, colloidal stability, and/or surface pressure vs. area isotherms obtained from the Langmuir trough measurements. This will be a topic of ongoing and future research in the Dhar and Volkin laboratories.

In addition to aggregating at interfaces, proteins can aggregate in bulk solution by mechanisms which are initiated by partial unfolding or reversible association of proteins. In chapter 5, we develop a theoretical model describing aggregation in terms of multiple nucleation (dimer formation) mechanisms and multiple aggregate growth mechanisms. Furthermore, we describe the theoretical role of both conformational and colloidal stability on both aggregate nucleation and growth. Experimentally, we measured conformational stability using DSC and colloidal stability using the second virial coefficient obtained from SLS. Additionally, we used a PEG precipitation assay to determine relative apparent solubility (and extrapolate to obtain the apparent thermodynamic activity) of mAb in different solutions, and compared these values as a potential surrogate for the relative thermodynamic favorability of protein in solution vs. amorphous precipitate. Aggregation data was collected for mAb using SEC and flow microscopy over the same range of formulation conditions incubated for up to 7 months. We found that solutions that resulted in decreased conformational stability of the mAb increased the rate of both nucleation and growth aggregation mechanisms during storage at temperatures well below the thermal onset temperature (as measured by DSC). On the other hand, we found that colloidal stability of the mAb in different solutions, as given by a_2 values from SLS, did not

198

appear to affect the rate of aggregate nucleation. The rate of aggregate growth however, could be controlled by increasing the net charge of the mAb molecule. The extent of aggregate growth of the mAb in different solutions correlated with both a_2 and apparent solubility data from the PEG precipitation experiments for the mAb in the same solutions.

Quantitative data visualization methods, mathematical models and kinetic models were developed in this thesis to better characterize and mechanistically study protein aggregation. The methods developed here were then applied to comprehensively map and better understand the effects of formulation composition and environmental stress on the aggregation pathways of an IgG1 mAb. A rigorous understanding of the different protein aggregation mechanisms is important to properly formulate proteins, especially because the classically used Lumry-Eyring type aggregation mechanisms, which may occur at elevated temperatures, may not be predictive of protein aggregation during long term storage or under mechanical agitation. The various tools developed here in this thesis offer a broad range of approaches which could be applied to the topic of protein aggregation for both pharmaceutical development and basic research purposes.

6.2. Future Directions

There are several exciting possibilities to build upon the research results, data visualization methods, and mathematical modeling tools presented here. This section will briefly highlight some outstanding challenges in the field of protein aggregation with a focus on work that could build upon the methods presented in this thesis. The projects suggested below could offer new insights into protein aggregation from a basic science perspective, and mechanistic information learned could be applied to better optimize the protein formulation development process.

One major limitation in the current understanding of protein subvisible particles is a lack of knowledge about their packing (i.e., density). As presented in the introduction of this thesis, part of the problem is an unclear definition of the "boundary" of a subvisible sized (~1-100 micron) protein particle. Protein particle density is an extremely important value that is used in resonant mass measurements to calculate protein particle size and is also used in calculations of protein particle mass from flow microscopy data. One potential way to define the boundaries of protein particle is to use inert molecules which are too large to diffuse into particle "channels." Various sized polymer molecules could be used to change the size of the "probe." Subvisible particles of various proteins could be spiked into these solutions and particle density could be calculated using a standard densitometer by varying the inert polymer concentration. A potential complication of this approach is that high polymer concentration could induce protein precipitation through unbalanced osmotic forces at high excluded volumes.

Another potential avenue for future research would be to understand the link between protein solution properties (e.g., protein charge, ionic strength, conformational integrity) and aggregation at the air-solution by creating mathematical models to account for the relative concentration of adsorbed protein at the interface. Currently, most industry and academic studies published to date are focused on finding parameters which correlate or can predict surface induced aggregation. As demonstrated in this thesis, aggregation is a multi-step process any of which can become rate limiting at different solution conditions. Development of such a model could help to clarify how and when parameters such as protein conformational stability and surface pressure correlate with surface induced aggregation.

A third exciting possibility would be to further improve the kinetic models for protein aggregation developed in chapter 5. Other degradation pathways can occur which remove

reactive monomer from solution. One major pathway which can affect aggregation in such a manner is mAb fragmentation. Additional terms could be developed to account for cases where fragments are either aggregate prone or unreactive. Furthermore, the simulation scripts used to model protein aggregation data could be equipped with statistical analysis to report confidence intervals. Such statistical analysis will become critical as the number of simulated parameters increases. Unfortunately, the models developed here cannot be used for prediction of protein aggregation until protein-protein interactions can be better predicted.

Performing these future studies would go a long way towards advancing the understanding of protein aggregation from a basic biophysics and colloid science perspective. One potential reason for why these studies have not been performed to date is because of their complicated nature requiring both theoretical and technical expertise in several different fields. This is one major reason why our collaboration with Professor Dhar at the University of Kansas and conversations Professor Christopher Roberts at the University of Delaware have been so beneficial towards developing the work in this Thesis.

Bibliography

1. Carpenter, J. F., T. W. Randolph, W. Jiskoot, D. J. Crommelin, C. R. Middaugh, G. Winter, Y. X. Fan, S. Kirshner, D. Verthelyi, S. Kozlowski, K. A. Clouse, P. G. Swann, A. Rosenberg, and B. Cherney. 2009. Overlooking subvisible particles in therapeutic protein products: gaps that may compromise product quality. Journal of pharmaceutical sciences 98:1201-1205.

2. Rosenberg, A. S. 2006. Effects of protein aggregates: an immunologic perspective. The AAPS journal 8:E501-507.

3. Hiemenz, P. C., and R. Rajagopalan. 1997. Principles of Colloid and Surface Chemistry. Marcel Dekker, Inc., New York.

4. Chi, E. Y., S. Krishnan, T. W. Randolph, and J. F. Carpenter. 2003. Physical stability of proteins in aqueous solution: mechanism and driving forces in nonnative protein aggregation. Pharmaceutical research 20:1325-1336.

5. Saluja, A., and D. S. Kalonia. 2008. Nature and consequences of protein-protein interactions in high protein concentration solutions. International journal of pharmaceutics 358:1-15.

6. Curtis, R. A., A. Montaser, J. M. Prausnitz, and H. W. Blanch. 1998. Protein-protein and protein-salt interactions in aqueous protein solutions containing concentrated electrolytes. Biotechnology and bioengineering 58:451.

7. Zhang, J. 2012. Protein-Protein Interactions in Salt Solutions. In Protein-Protein Interactions -Computational and Experimental Tools. W. Cal, and H. Hong, editors. Intech.

8. Israelachvili, J. 1991. Intermolecular & Surface Forces. Academic Press, London.

9. Harding, S. E., J. C. Horton, S. Jones, J. M. Thornton, and D. J. Winzor. 1999. COVOL: An interactive program for evaluating second virial coefficients from the triaxial shape or dimensions of rigid macromolecules. Biophysical journal 76:2432-2438.

10. Amin, S., G. V. Barnett, J. A. Pathak, C. J. Roberts, and P. S. Sarangapani. 2014. Protein aggregation, particle formation, characterization & rheology. Curr Opin Colloid In 19:438-449.

11. Kamerzell, T. J., R. Esfandiary, S. B. Joshi, C. R. Middaugh, and D. B. Volkin. 2011. Protein-excipient interactions: Mechanisms and biophysical characterization applied to protein formulation development. Advanced drug delivery reviews 63:1118-1159.

12. Bi, V., V. Jawa, M. K. Joubert, A. Kaliyaperumal, C. Eakin, K. Richmond, O. Pan, J. Sun, M. Hokom, T. J. Goletz, J. Wypych, L. Zhou, B. A. Kerwin, L. O. Narhi, and T. Arora. 2013. Development of a human antibody tolerant mouse model to assess the immunogenicity risk due to aggregated biotherapeutics. Journal of pharmaceutical sciences 102:3545-3555.

13. Joubert, M. K., M. Hokom, C. Eakin, L. Zhou, M. Deshpande, M. P. Baker, T. J. Goletz, B. A. Kerwin, N. Chirmule, L. O. Narhi, and V. Jawa. 2012. Highly Aggregated Antibody Therapeutics Can Enhance the in Vitro Innate and Late-stage T-cell Immune Responses. Journal of Biological Chemistry 287:25266-25279.

14. Telikepalli, S., H. E. Shinogle, P. S. Thapa, J. H. Kim, M. Deshpande, V. Jawa, C. R. Middaugh, L. O. Narhi, M. K. Joubert, and D. B. Volkin. 2015. Physical characterization

and in vitro biological impact of highly aggregated antibodies separated into size-enriched populations by fluorescence-activated cell sorting. Journal of pharmaceutical sciences 104:1575-1591.

15. Connolly, B. D., C. Petry, S. Yadav, B. Demeule, N. Ciaccio, J. M. Moore, S. J. Shire, and Y. R. Gokarn. 2012. Weak interactions govern the viscosity of concentrated antibody solutions: high-throughput analysis using the diffusion interaction parameter. Biophysical journal 103:69-78.

16. Liu, J., M. D. Nguyen, J. D. Andya, and S. J. Shire. 2005. Reversible self-association increases the viscosity of a concentrated monoclonal antibody in aqueous solution. Journal of pharmaceutical sciences 94:1928-1940.

17. Esfandiary, R., D. B. Hayes, A. Parupudi, J. Casas-Finet, S. Bai, H. S. Samra, A. U. Shah, and H. A. Sathish. 2013. A systematic multitechnique approach for detection and characterization of reversible self-association during formulation development of therapeutic antibodies. Journal of pharmaceutical sciences 102:3089-3099.

18. Yadav, S., A. Sreedhara, S. Kanai, J. Liu, S. Lien, H. Lowman, D. S. Kalonia, and S. J. Shire. 2011. Establishing a link between amino acid sequences and self-associating and viscoelastic behavior of two closely related monoclonal antibodies. Pharmaceutical research 28:1750-1764.

19. Kanai, S., J. Liu, T. W. Patapoff, and S. J. Shire. 2008. Reversible self-association of a concentrated monoclonal antibody solution mediated by Fab-Fab interaction that impacts solution viscosity. Journal of pharmaceutical sciences 97:4219-4227.

20. Arora, J., J. M. Hickey, R. Majumdar, R. Esfandiary, S. M. Bishop, H. S. Samra, C. R. Middaugh, D. D. Weis, and D. B. Volkin. 2015. Hydrogen exchange mass spectrometry reveals protein interfaces and distant dynamic coupling effects during the reversible self-association of an IgG1 monoclonal antibody. mAbs 7:525-539.

21. Mason, B. D., L. Zhang, R. L. Remmele, Jr., and J. Zhang. 2011. Opalescence of an IgG2 monoclonal antibody solution as it relates to liquid-liquid phase separation. Journal of pharmaceutical sciences 100:4587-4596.

22. Nishi, H., M. Miyajima, H. Nakagami, M. Noda, S. Uchiyama, and K. Fukui. 2010. Phase separation of an IgG1 antibody solution under a low ionic strength condition. Pharmaceutical research 27:1348-1360.

23. Raut, A. S., and D. S. Kalonia. 2015. Opalescence in monoclonal antibody solutions and its correlation with intermolecular interactions in dilute and concentrated solutions. Journal of pharmaceutical sciences 104:1263-1274.

24. Roberts, C. J., and M. A. Blanco. 2014. Role of anisotropic interactions for proteins and patchy nanoparticles. J Phys Chem B 118:12599-12611.

25. Neal, B. L., D. Asthagiri, and A. M. Lenhoff. 1998. Molecular origins of osmotic second virial coefficients of proteins. Biophys J 75:2469-2477.

26. Cole, C., and J. Warwicker. 2002. Side-chain conformational entropy at protein-protein interfaces. Protein science : a publication of the Protein Society 11:2860-2870.

27. Warwicker, J., S. Charonis, and R. A. Curtis. 2014. Lysine and arginine content of proteins: computational analysis suggests a new tool for solubility design. Molecular pharmaceutics 11:294-303.

28.   Mcmillan, W. G., and J. E. Mayer. 1945. The Statistical Thermodynamics of Multicomponent Systems. Journal of Chemical Physics 13:276-305.

29.   Minton, A. P. 2001. The influence of macromolecular crowding and macromolecular confinement on biochemical reactions in physiological media. The Journal of biological chemistry 276:10577-10580.

30.   Siderius, D. W., W. P. Krekelberg, C. J. Roberts, and V. K. Shen. 2012. Osmotic virial coefficients for model protein and colloidal solutions: Importance of ensemble constraints in the analysis of light scattering data. J Chem Phys 136.

31.   Wyatt, P. J. 1993. Light-Scattering and the Absolute Characterization of Macromolecules. Anal Chim Acta 272:1-40.

32.   Asthagiri, D., A. Paliwal, D. Abras, A. M. Lenhoff, and M. E. Paulaitis. 2005. A consistent experimental and modeling approach to light-scattering studies of protein-protein interactions in solution. Biophysical journal 88:3300-3309.

33.   Blanco, M. A., E. Sahin, Y. Li, and C. J. Roberts. 2011. Reexamining protein-protein and protein-solvent interactions from Kirkwood-Buff analysis of light scattering in multi-component solutions. J Chem Phys 134.

34.   Blanco, M. A., T. Perevozchikova, V. Martorana, M. Manno, and C. J. Roberts. 2014. Protein-Protein Interactions in Dilute to Concentrated Solutions: alpha-Chymotrypsinogen in Acidic Conditions. Journal of Physical Chemistry B 118:5817-5831.

35.   Barnett, G. V., V. I. Razinkov, B. A. Kerwin, T. M. Laue, A. H. Woodka, P. D. Butler, T. Perevozchikova, and C. J. Roberts. 2015. Specific-Ion Effects on the Aggregation Mechanisms and Protein-Protein Interactions for Anti-streptavidin Immunoglobulin Gamma-1. Journal of Physical Chemistry B 119:5793-5804.

36.   Bonnete, F., and D. Vivares. 2002. Interest of the normalized second virial coefficient and interaction potentials for crystallizing large macromolecules. Acta Crystallogr D 58:1571-1575.

37.   Dumetz, A. C., A. M. Chockla, E. W. Kaler, and A. M. Lenhoff. 2008. Effects of pH on protein-protein interactions and implications for protein phase behavior. Bba-Proteins Proteom 1784:600-610.

38.   Minton, A. P. 2007. Static light scattering from concentrated protein solutions, I: General theory for protein mixtures and application to self-associating proteins. Biophysical journal 93:1321-1328.

39.   Teraoka, I. 2002. Polymer solutions, an introduction to physical properties. Wiley-Interscience, New York.

40.   Li, S., D. Xing, and J. Li. 2004. Dynamic light scattering application to study protein interactions in electrolyte solutions. Journal of biological physics 30:313-324.

41.   Neergaard, M. S., D. S. Kalonia, H. Parshad, A. D. Nielsen, E. H. Moller, and M. van de Weert. 2013. Viscosity of high concentration protein formulations of monoclonal antibodies of the IgG1 and IgG4 subclass - prediction of viscosity through protein-protein interaction measurements. European journal of pharmaceutical sciences : official journal of the European Federation for Pharmaceutical Sciences 49:400-410.

42.   Yadav, S., T. M. Scherer, S. J. Shire, and D. S. Kalonia. 2011. Use of dynamic light scattering to determine second virial coefficient in a semidilute concentration regime. Anal Biochem 411:292-296.

43. Menzen, T., and W. Friess. 2014. Temperature-ramped studies on the aggregation, unfolding, and interaction of a therapeutic monoclonal antibody. Journal of pharmaceutical sciences 103:445-455.

44. Philo, J. S., and T. Arakawa. 2009. Mechanisms of protein aggregation. Current pharmaceutical biotechnology 10:348-351.

45. Roberts, C. J. 2014. Nucleation, Aggregation, and Conformational Distortion. In Biophysical Methods for Biotherapeutics: Discovery and Development Applications. T. K. Das, editor. John Wiley & Sons, Inc, Hoboken. 125-144.

46. Ratanji, K. D., J. P. Derrick, R. J. Dearman, and I. Kimber. 2014. Immunogenicity of therapeutic proteins: influence of aggregation. Journal of immunotoxicology 11:99-109.

47. Shankar, G., E. Shores, C. Wagner, and A. Mire-Sluis. 2006. Scientific and regulatory considerations on the immunogenicity of biologics. Trends in biotechnology 24:274-280.

48. Sanchezruiz, J. M. 1992. Theoretical-Analysis of Lumry-Eyring Models in Differential Scanning Calorimetry. Biophysical journal 61:921-935.

49. Sanchezruiz, J. M., J. L. Lopezlacomba, M. Cortijo, and P. L. Mateo. 1988. Differential Scanning Calorimetry of the Irreversible Thermal-Denaturation of Thermolysin. Biochemistry 27:1648-1652.

50. Lumry, R., and H. Eyring. 1954. Conformation Changes of Proteins. J Phys Chem-Us 58:110-120.

51. Baynes, B. M., and B. L. Trout. 2004. Rational design of solution additives for the prevention of protein aggregation. Biophysical journal 87:1631-1639.

52. Lee, J. C., and S. N. Timasheff. 1981. The Stabilization of Proteins by Sucrose. Journal of Biological Chemistry 256:7193-7201.

53. Timasheff, S. N. 2002. Protein-solvent preferential interactions, protein hydration, and the modulation of biochemical reactions by solvent components. Proceedings of the National Academy of Sciences of the United States of America 99:9721-9726.

54. Kalonia, C., O. S. Kumru, J. H. Kim, C. R. Middaugh, and D. B. Volkin. 2013. Radar chart array analysis to visualize effects of formulation variables on IgG1 particle formation as measured by multiple analytical techniques. Journal of pharmaceutical sciences 102:4256-4267.

55. Chi, E. Y., S. Krishnan, B. S. Kendrick, B. S. Chang, J. F. Carpenter, and T. W. Randolph. 2003. Roles of conformational stability and colloidal stability in the aggregation of recombinant human granulocyte colony-stimulating factor. Protein science : a publication of the Protein Society 12:903-913.

56. Bajaj, H., V. K. Sharma, A. Badkar, D. Zeng, S. Nema, and D. S. Kalonia. 2006. Protein structural conformation and not second virial coefficient relates to long-term irreversible aggregation of a monoclonal antibody and ovalbumin in solution. Pharmaceutical research 23:1382-1394.

57. Sahin, E., A. O. Grillo, M. D. Perkins, and C. J. Roberts. 2010. Comparative effects of pH and ionic strength on protein-protein interactions, unfolding, and aggregation for IgG1 antibodies. Journal of pharmaceutical sciences 99:4830-4848.

58. Mehta, S. B., J. S. Bee, T. W. Randolph, and J. F. Carpenter. 2014. Partial unfolding of a monoclonal antibody: role of a single domain in driving protein aggregation. Biochemistry 53:3367-3377.

205

59.   Banks, D. D., R. F. Latypov, R. R. Ketchem, J. Woodard, J. L. Scavezze, C. C. Siska, and V. I. Razinkov. 2012. Native-state solubility and transfer free energy as predictive tools for selecting excipients to include in protein formulation development studies. Journal of pharmaceutical sciences 101:2720-2732.

60.   Banks, D. D., J. Zhang, and C. C. Siska. 2014. Relationship between native-state solubility and non-native aggregation of recombinant human granulocyte colony stimulating factor: practical implications for protein therapeutic development. Mol Pharm 11:3431-3442.

61.   Bee, J. S., M. Davis, E. Freund, J. F. Carpenter, and T. W. Randolph. 2010. Aggregation of a monoclonal antibody induced by adsorption to stainless steel. Biotechnology and bioengineering 105:121-129.

62.   Bee, J. S., D. K. Schwartz, S. Trabelsi, E. Freund, J. L. Stevenson, J. F. Carpenter, and T. W. Randolph. 2012. Production of particles of therapeutic proteins at the air–water interface during compression/dilation cycles. Soft matter 8:10329-10335.

63.   Bee, J. S., D. Chiu, S. Sawicki, J. L. Stevenson, K. Chatterjee, E. Freund, J. F. Carpenter, and T. W. Randolph. 2009. Monoclonal antibody interactions with micro- and nanoparticles: adsorption, aggregation, and accelerated stress studies. Journal of pharmaceutical sciences 98:3218-3238.

64.   Gerhardt, A., K. Bonam, J. S. Bee, J. F. Carpenter, and T. W. Randolph. 2013. Ionic strength affects tertiary structure and aggregation propensity of a monoclonal antibody adsorbed to silicone oil-water interfaces. Journal of pharmaceutical sciences 102:429-440.

65.   Mehta, S. B., R. Lewus, J. S. Bee, T. W. Randolph, and J. F. Carpenter. 2015. Gelation of a monoclonal antibody at the silicone oil-water interface and subsequent rupture of the interfacial gel results in aggregation and particle formation. Journal of pharmaceutical sciences 104:1282-1290.

66.   Joubert, M. K., Q. Luo, Y. Nashed-Samuel, J. Wypych, and L. O. Narhi. 2011. Classification and characterization of therapeutic antibody aggregates. The Journal of biological chemistry 286:25118-25133.

67.   Chennamsetty, N., V. Voynov, V. Kayser, B. Helk, and B. L. Trout. 2010. Prediction of aggregation prone regions of therapeutic proteins. The journal of physical chemistry. B 114:6614-6624.

68.   Neudecker, P., P. Robustelli, A. Cavalli, P. Walsh, P. Lundstrom, A. Zarrine-Afsar, S. Sharpe, M. Vendruscolo, and L. E. Kay. 2012. Structure of an intermediate state in protein folding and aggregation. Science 336:362-366.

69.   Baynes, B. M., D. I. Wang, and B. L. Trout. 2005. Role of arginine in the stabilization of proteins against aggregation. Biochemistry 44:4919-4925.

70.   Telikepalli, S. N., O. S. Kumru, C. Kalonia, R. Esfandiary, S. B. Joshi, C. R. Middaugh, and D. B. Volkin. 2014. Structural characterization of IgG1 mAb aggregates and particles generated under various stress conditions. Journal of pharmaceutical sciences 103:796-809.

71.   Roberts, C. J., T. K. Das, and E. Sahin. 2011. Predicting solution aggregation rates for therapeutic proteins: approaches and challenges. International journal of pharmaceutics 418:318-333.

72. Volkin, D. B., S. Hershenson, R. J. Ho, S. Uchiyama, G. Winter, and J. F. Carpenter. 2015. Two decades of publishing excellence in pharmaceutical biotechnology. Journal of pharmaceutical sciences 104:290-300.

73. Ducry, L., and B. Stump. 2010. Antibody-drug conjugates: linking cytotoxic payloads to monoclonal antibodies. Bioconjugate chemistry 21:5-13.

74. Wu, A. M., and P. D. Senter. 2005. Arming antibodies: prospects and challenges for immunoconjugates. Nature biotechnology 23:1137-1146.

75. Wakankar, A. A., M. B. Feeney, J. Rivera, Y. Chen, M. Kim, V. K. Sharma, and Y. J. Wang. 2010. Physicochemical stability of the antibody-drug conjugate Trastuzumab-DM1: changes due to modification and conjugation processes. Bioconjugate chemistry 21:1588-1595.

76. Guo, J., S. Kumar, A. Prashad, J. Starkey, and S. K. Singh. 2014. Assessment of physical stability of an antibody drug conjugate by higher order structure analysis: impact of thiol- maleimide chemistry. Pharmaceutical research 31:1710-1723.

77. Natsume, A., R. Niwa, and M. Satoh. 2008. Improving effector functions of antibodies for cancer treatment: Enhancing ADCC and CDC. Drug Des Dev Ther 3:7-16.

78. Vermeer, A. W. P., and W. Norde. 2000. The thermal stability of immunoglobulin: Unfolding and aggregation of a multi-domain protein. Biophysical journal 78:394-404.

79. Vermeer, A. W. P., W. Norde, and A. van Amerongen. 2000. The unfolding/denaturation of immunogammaglobulin of isotype 2b and its F-ab and F-c fragments. Biophysical journal 79:2150-2154.

80. Ionescu, R. M., J. Vlasak, C. Price, and M. Kirchmeier. 2008. Contribution of variable domains to the stability of humanized IgG1 monoclonal antibodies. Journal of pharmaceutical sciences 97:1414-1426.

81. Brummitt, R. K., D. P. Nesta, L. Chang, S. F. Chase, T. M. Laue, and C. J. Roberts. 2011. Nonnative aggregation of an IgG1 antibody in acidic conditions: part 1. Unfolding, colloidal interactions, and formation of high-molecular-weight aggregates. Journal of pharmaceutical sciences 100:2087-2103.

82. Brummitt, R. K., D. P. Nesta, L. Q. Chang, A. M. Kroetsch, and C. J. Roberts. 2011. Nonnative Aggregation of an IgG1 Antibody in Acidic Conditions, Part 2: Nucleation and Growth Kinetics with Competing Growth Mechanisms. Journal of pharmaceutical sciences 100:2104-2119.

83. Roberts, C. J. 2014. Therapeutic protein aggregation: mechanisms, design, and control. Trends in biotechnology 32:372-380.

84. Andrews, J. M., and C. J. Roberts. 2007. A Lumry-Eyring nucleated polymerization model of protein aggregation kinetics: 1. Aggregation with pre-equilibrated unfolding. The journal of physical chemistry. B 111:7897-7913.

85. Li, Y., and C. J. Roberts. 2009. Lumry-Eyring nucleated-polymerization model of protein aggregation kinetics. 2. Competing growth via condensation and chain polymerization. The journal of physical chemistry. B 113:7020-7032.

86. Andersen, C. B., M. Manno, C. Rischel, M. Thorolfsson, and V. Martorana. 2010. Aggregation of a multidomain protein: A coagulation mechanism governs aggregation of a model IgG1 antibody under weak thermal stress. Protein Science 19:279-290.

87.	Arosio, P., S. Rima, and M. Morbidelli. 2013. Aggregation mechanism of an IgG2 and two IgG1 monoclonal antibodies at low pH: from oligomers to larger aggregates. Pharmaceutical research 30:641-654.

88.	Esue, O., S. Kanai, J. Liu, T. W. Patapoff, and S. J. Shire. 2009. Carboxylate-Dependent Gelation of a Monoclonal Antibody. Pharmaceutical research 26:2478-2485.

89.	Esue, O., A. X. Xie, T. J. Kamerzell, and T. W. Patapoff. 2013. Thermodynamic and structural characterization of an antibody gel. mAbs 5:323-334.

90.	Gokarn, Y. R., R. M. Fesinmeyer, A. Saluja, V. Razinkov, S. F. Chase, T. M. Laue, and D. N. Brems. 2011. Effective charge measurements reveal selective and preferential accumulation of anions, but not cations, at the protein surface in dilute salt solutions. Protein science : a publication of the Protein Society 20:580-587.

91.	Rudiuk, S., L. Cohen-Tannoudji, S. Huille, and C. Tribet. 2012. Importance of the dynamics of adsorption and of a transient interfacial stress on the formation of aggregates of IgG antibodies. Soft matter 8:2651-2661.

92.	Shieh, I. C., and A. R. Patel. 2015. Predicting the agitation-induced aggregation of monoclonal antibodies using surface tensiometry. Molecular pharmaceutics 12:3184-3193.

93.	Mahler, H. C., W. Friess, U. Grauschopf, and S. Kiese. 2009. Protein aggregation: pathways, induction factors and analysis. Journal of pharmaceutical sciences 98:2909-2934.

94.	Narhi, L. O., J. Schmit, K. Bechtold-Peters, and D. Sharma. 2012. Classification of protein aggregates. Journal of pharmaceutical sciences 101:493-498.

95.	Narhi, L. O., Y. Jiang, S. Cao, K. Benedek, and D. Shnek. 2009. A critical review of analytical methods for subvisible and visible particles. Current pharmaceutical biotechnology 10:373-381.

96.	Xiang, S. D., A. Scholzen, G. Minigo, C. David, V. Apostolopoulos, P. L. Mottram, and M. Plebanski. 2006. Pathogen recognition and development of particulate vaccines: does size matter? Methods 40:1-9.

97.	Ripple, D. C., and M. N. Dimitrova. 2012. Protein Particles: What We Know and What We Do Not Know. Journal of pharmaceutical sciences.

98.	Fischer, H., I. Polikarpov, and A. F. Craievich. 2004. Average protein density is a molecular-weight-dependent function. Protein science : a publication of the Protein Society 13:2825-2828.

99.	Folzer, E., T. A. Khan, R. Schmidt, C. Finkler, J. Huwyler, H. C. Mahler, and A. V. Koulov. 2015. Determination of the Density of Protein Particles Using a Suspended Microchannel Resonator. Journal of pharmaceutical sciences.

100.	Demeule, B., S. Messick, S. J. Shire, and J. Liu. 2010. Characterization of particles in protein solutions: reaching the limits of current technologies. The AAPS journal 12:708-715.

101.	Scherer, T. M., S. Leung, L. Owyang, and S. J. Shire. 2012. Issues and challenges of subvisible and submicron particulate analysis in protein solutions. The AAPS journal 14:236-243.

102. Zolls, S., M. Gregoritza, R. Tantipolphan, M. Wiggenhorn, G. Winter, W. Friess, and A. Hawe. 2013. How subvisible particles become invisible-relevance of the refractive index for protein particle analysis. Journal of pharmaceutical sciences 102:1434-1446.

103. Barer, R., and S. Tkaczyk. 1954. Refractive index of concentrated protein solutions. Nature 173:821-822.

104. Kalonia, C., O. S. Kumru, I. Prajapati, R. Mathaes, J. Engert, S. Zhou, C. R. Middaugh, and D. B. Volkin. 2015. Calculating the mass of subvisible protein particles with improved accuracy using microflow imaging data. Journal of pharmaceutical sciences 104:536-547.

105. Filipe, V., A. Hawe, and W. Jiskoot. 2010. Critical evaluation of Nanoparticle Tracking Analysis (NTA) by NanoSight for the measurement of nanoparticles and protein aggregates. Pharmaceutical research 27:796-810.

106. Patel, A. R., D. Lau, and J. Liu. 2012. Quantification and characterization of micrometer and submicrometer subvisible particles in protein therapeutics by use of a suspended microchannel resonator. Analytical chemistry 84:6833-6840.

107. Sharma, D. K., P. Oma, M. J. Pollo, and M. Sukumar. 2010. Quantification and characterization of subvisible proteinaceous particles in opalescent mAb formulations using micro-flow imaging. Journal of pharmaceutical sciences 99:2628-2642.

108. Das, T. K. 2012. Protein particulate detection issues in biotherapeutics development--current status. AAPS PharmSciTech 13:732-746.

109. Weinbuch, D., S. Zolls, M. Wiggenhorn, W. Friess, G. Winter, W. Jiskoot, and A. Hawe. 2013. Micro-flow imaging and resonant mass measurement (Archimedes) - complementary methods to quantitatively differentiate protein particles and silicone oil droplets. Journal of pharmaceutical sciences 102:2152-2165.

110. Zolls, S., M. Gregoritza, R. Tantipolphan, M. Wiggenhorn, G. Winter, W. Friess, and A. Hawe. 2013. How subvisible particles become invisible-relevance of the refractive index for protein particle analysis. Journal of pharmaceutical sciences.

111. Wang T, J. S., Kumru O, Telikepalli S, Middaugh C, Volkin D. 2013. Case Studies Applying Biophysical Techniques to Better Characterize Protein Aggregates and Particulates of Varying Size. In Biophysics for Therapeutic Protein Development. N. LO, editor. Springer.

112. Burg, T. P., M. Godin, S. M. Knudsen, W. Shen, G. Carlson, J. S. Foster, K. Babcock, and S. R. Manalis. 2007. Weighing of biomolecules, single cells and single nanoparticles in fluid. Nature 446:1066-1069.

113. Luo, Q., M. K. Joubert, R. Stevenson, R. R. Ketchem, L. O. Narhi, and J. Wypych. 2011. Chemical modifications in therapeutic protein aggregates generated under different stress conditions. The Journal of biological chemistry 286:25134-25144.

114. Filipe, V., W. Jiskoot, A. H. Basmeleh, A. Halim, H. Schellekens, and V. Filipe. 2012. Immunogenicity of different stressed IgG monoclonal antibody formulations in immune tolerant transgenic mice. mAbs 4.

115. Liu, L., T. W. Randolph, and J. F. Carpenter. 2012. Particles shed from syringe filters and their effects on agitation-induced protein aggregation. Journal of pharmaceutical sciences 101:2952-2959.

116. Kroetsch, A. M., E. Sahin, H. Y. Wang, S. Krizman, and C. J. Roberts. 2012. Relating particle formation to salt- and pH-dependent phase separation of non-native aggregates of alpha-chymotrypsinogen A. Journal of pharmaceutical sciences 101:3651-3660.

117.   Kim, N., R. L. Remmele, Jr., D. Liu, V. I. Razinkov, E. J. Fernandez, and C. J. Roberts. 2013. Aggregation of anti-streptavidin immunoglobulin gamma-1 involves Fab unfolding and competing growth pathways mediated by pH and salt concentration. Biophysical chemistry 172:26-36.

118.   Fesinmeyer, R. M., S. Hogan, A. Saluja, S. R. Brych, E. Kras, L. O. Narhi, D. N. Brems, and Y. R. Gokarn. 2009. Effect of ions on agitation- and temperature-induced aggregation reactions of antibodies. Pharmaceutical research 26:903-913.

119.   Zolls, S., R. Tantipolphan, M. Wiggenhorn, G. Winter, W. Jiskoot, W. Friess, and A. Hawe. 2012. Particles in therapeutic protein formulations, Part 1: overview of analytical methods. Journal of pharmaceutical sciences 101:914-935.

120.   Kumru, O. S., J. Liu, J. A. Ji, W. Cheng, Y. J. Wang, T. Wang, S. B. Joshi, C. R. Middaugh, and D. B. Volkin. 2012. Compatibility, physical stability, and characterization of an IgG4 monoclonal antibody after dilution into different intravenous administration bags. Journal of pharmaceutical sciences 101:3636-3650.

121.   Sharma, D. K., D. King, P. Oma, and C. Merchant. 2010. Micro-flow imaging: flow microscopy applied to sub-visible particulate analysis in protein formulations. The AAPS journal 12:455-464.

122.   Barnard, J. G., S. Singh, T. W. Randolph, and J. F. Carpenter. 2011. Subvisible particle counting provides a sensitive method of detecting and quantifying aggregation of monoclonal antibody caused by freeze-thawing: insights into the roles of particles in the protein aggregation pathway. Journal of pharmaceutical sciences 100:492-503.

123.   Wuchner, K., J. Buchler, R. Spycher, P. Dalmonte, and D. B. Volkin. 2010. Development of a microflow digital imaging assay to characterize protein particulates during storage of a high concentration IgG1 monoclonal antibody formulation. Journal of pharmaceutical sciences 99:3343-3361.

124.   Strehl, R., V. Rombach-Riegraf, M. Diez, K. Egodage, M. Bluemel, M. Jeschke, and A. Koulov. 2011. Discrimination Between Silicone Oil Droplets and Protein Aggregates in Biopharmaceuticals: A Novel Multiparametric Image Filter for Sub-visible Particles in Microflow Imaging Analysis. J Pharm. Res.

125.   Maddux, N. R., S. B. Joshi, D. B. Volkin, J. P. Ralston, and C. R. Middaugh. 2011. Multidimensional methods for the formulation of biopharmaceuticals and vaccines. Journal of pharmaceutical sciences.

126.   Clark, N. R., and A. Ma'ayan. 2011. Introduction to statistical methods to analyze large data sets: principal components analysis. Science signaling 4:tr3.

127.   Cheng, W., S. B. Joshi, F. He, D. N. Brems, B. He, B. A. Kerwin, D. B. Volkin, and C. R. Middaugh. 2012. Comparison of high-throughput biophysical methods to identify stabilizing excipients for a model IgG2 monoclonal antibody: conformational stability and kinetic aggregation measurements. Journal of pharmaceutical sciences 101:1701-1720.

128.   Bhambhani, A., J. M. Kissmann, S. B. Joshi, D. B. Volkin, R. S. Kashi, and C. R. Middaugh. 2012. Formulation design and high-throughput excipient selection based on structural integrity and conformational stability of dilute and highly concentrated IgG1 monoclonal antibody solutions. Journal of pharmaceutical sciences 101:1120-1135.

129.	Thakkar, S. V., S. B. Joshi, M. E. Jones, H. A. Sathish, S. M. Bishop, D. B. Volkin, and C. R. Middaugh. 2012. Excipients differentially influence the conformational stability and pretransition dynamics of two IgG1 monoclonal antibodies. Journal of pharmaceutical sciences 101:3062-3077.

130.	Iyer, V., N. Maddux, L. Hu, W. Cheng, A. K. Youssef, G. Winter, S. B. Joshi, D. B. Volkin, and C. R. Middaugh. 2013. Comparative signature diagrams to evaluate biophysical data for differences in protein structure across various formulations. Journal of pharmaceutical sciences 102:43-51.

131.	Kim, J. H., V. Iyer, S. B. Joshi, D. B. Volkin, and C. R. Middaugh. 2012. Improved data visualization techniques for analyzing macromolecule structural changes. Protein science : a publication of the Protein Society 21:1540-1553.

132.	Manikwar, P., R. Majumdar, J. M. Hickey, S. V. Thakkar, H. S. Samra, H. A. Sathish, S. M. Bishop, C. R. Middaugh, D. D. Weis, and D. B. Volkin. 2013. Correlating excipient effects on conformational and storage stability of an IgG1 monoclonal antibody with local dynamics as measured by hydrogen/deuterium-exchange mass spectrometry. Journal of pharmaceutical sciences 102:2136-2151.

133.	Bond, M. D., M. E. Panek, Z. Zhang, D. Wang, P. Mehndiratta, H. Zhao, K. Gunton, A. Ni, M. L. Nedved, S. Burman, and D. B. Volkin. 2010. Evaluation of a dual-wavelength size exclusion HPLC method with improved sensitivity to detect protein aggregates and its use to better characterize degradation pathways of an IgG1 monoclonal antibody. Journal of pharmaceutical sciences 99:2582-2597.

134.	Simler, B. R., G. Hui, J. E. Dahl, and B. Perez-Ramirez. 2012. Mechanistic complexity of subvisible particle formation: links to protein aggregation are highly specific. Journal of pharmaceutical sciences 101:4140-4154.

135.	Wilson, G. A., and M. C. Manning. 2013. Flow imaging: moving toward best practices for subvisible particle quantitation in protein products. Journal of pharmaceutical sciences 102:1133-1134.

136.	Lubiniecki, A., D. B. Volkin, M. Federici, M. D. Bond, M. L. Nedved, L. Hendricks, P. Mehndiratta, M. Bruner, S. Burman, P. Dalmonte, J. Kline, A. Ni, M. E. Panek, B. Pikounis, G. Powers, O. Vafa, and R. Siegel. 2011. Comparability assessments of process and product changes made during development of two different monoclonal antibodies. Biologicals : journal of the International Association of Biological Standardization 39:9-22.

137.	Federici, M., A. Lubiniecki, P. Manikwar, and D. B. Volkin. 2013. Analytical lessons learned from selected therapeutic protein drug comparability studies. Biologicals : journal of the International Association of Biological Standardization 41:131-147.

138.	Li, J., S. Pinnamaneni, Y. Quan, A. Jaiswal, F. I. Andersson, and X. Zhang. 2012. Mechanistic understanding of protein-silicone oil interactions. Pharmaceutical research 29:1689-1697.

139.	Seidl, A., O. Hainzl, M. Richter, R. Fischer, S. Bohm, B. Deutel, M. Hartinger, J. Windisch, N. Casadevall, G. M. London, and I. Macdougall. 2012. Tungsten-induced denaturation and aggregation of epoetin alfa during primary packaging as a cause of immunogenicity. Pharmaceutical research 29:1454-1467.

140. Razinkov, V. I., M. J. Treuheit, and G. W. Becker. 2013. Methods of high throughput biophysical characterization in biopharmaceutical development. Current drug discovery technologies 10:59-70.

141. Samra, H. S., and F. He. 2012. Advancements in high throughput biophysical technologies: applications for characterization and screening during early formulation development of monoclonal antibodies. Molecular pharmaceutics 9:696-707.

142. Glover, Z. W., L. Gennaro, S. Yadav, B. Demeule, P. Y. Wong, and A. Sreedhara. 2013. Compatibility and stability of pertuzumab and trastuzumab admixtures in i.v. infusion bags for coadministration. Journal of pharmaceutical sciences 102:794-812.

143. Sreedhara, A., Z. K. Glover, N. Piros, N. Xiao, A. Patel, and B. Kabakoff. 2012. Stability of IgG1 monoclonal antibodies in intravenous infusion bags under clinical in-use conditions. Journal of pharmaceutical sciences 101:21-30.

144. Torosantucci, R., V. Brinks, G. Kijanka, L. A. Halim, M. Sauerborn, H. Schellekens, and W. Jiskoot. 2014. Development of a transgenic mouse model to study the immunogenicity of recombinant human insulin. Journal of pharmaceutical sciences 103:1367-1374.

145. Brinks, V., D. Weinbuch, M. Baker, Y. Dean, P. Stas, S. Kostense, B. Rup, and W. Jiskoot. 2013. Preclinical models used for immunogenicity prediction of therapeutic proteins. Pharmaceutical research 30:1719-1728.

146. Bai, S., Y. Murugesan, M. Vlasic, L. B. Karpes, and M. L. Brader. 2013. Effects of submicron particles on formation of micron-sized particles during long-term storage of an interferon-beta-1a solution. Journal of pharmaceutical sciences 102:347-351.

147. Werk, T., D. B. Volkin, and H. C. Mahler. 2014. Effect of solution properties on the counting and sizing of subvisible particle standards as measured by light obscuration and digital imaging methods. European journal of pharmaceutical sciences : official journal of the European Federation for Pharmaceutical Sciences 53:95-108.

148. Sharma, D. K., D. King, and C. Merchant. 2011. Reference material development for calibration and verification of image-based particle analyzers. International journal of pharmaceutics 416:293-295.

149. Murphy, D. B. 2001. Fundamentals of Light Microscopy and Electronic Imaging. John Wiley & Sons.

150. Brown, L. 2011. Characterizing Biologics Using Dynamic Imaging Particle Analysis. Biopharm Int 24:S4-S9.

151. Quillin, M. L., and B. W. Matthews. 2000. Accurate calculation of the density of proteins. Acta crystallographica. Section D, Biological crystallography 56:791-794.

152. Champion, J. A., Y. K. Katare, and S. Mitragotri. 2007. Making polymeric micro- and nanoparticles of complex shapes. Proceedings of the National Academy of Sciences of the United States of America 104:11901-11904.

153. Mach, H., and C. R. Middaugh. 2011. Ultraviolet spectroscopy as a tool in therapeutic protein development. Journal of pharmaceutical sciences 100:1214-1227.

154. Ripple, D., Wayment, JR, Carrier, MJ,. 2011. Standards for the optical detection of protein particles. American pharmaceutical review.

155. White, E. T., W. H. Tan, J. M. Ang, S. Tait, and J. D. Litster. 2007. The density of a protein crystal. Powder Technol 179:55-58.

156. Zhao, H. Y., P. H. Brown, and P. Schuckt. 2011. On the Distribution of Protein Refractive Index Increments. Biophysical journal 100:2309-2317.

157. Ball, V., and J. J. Ramsden. 1998. Buffer dependence of refractive index increments of protein solutions. Biopolymers 46:489-492.

158. Voros, J. 2004. The density and refractive index of adsorbing protein layers. Biophysical journal 87:553-561.

159. Narhi, L. O., V. Corvari, D. C. Ripple, N. Afonina, I. Cecchini, M. R. Defelippis, P. Garidel, A. Herre, A. V. Koulov, and T. Lubiniecki. 2015. Subvisible (2–100 µm) Particle Analysis During Biotherapeutic Drug Product Development: Part 1, Considerations and Strategy. Journal of pharmaceutical sciences 104:1899-1908.

160. Bukofzer, S., J. Ayres, A. Chavez, M. Devera, J. Miller, D. Ross, J. Shabushnig, S. Vargo, H. Watson, and R. Watson. 2015. Industry perspective on the medical risk of visible particles in injectable drug products. PDA journal of pharmaceutical science and technology / PDA 69:123-139.

161. Singh, S. K., N. Afonina, M. Awwad, K. Bechtold-Peters, J. T. Blue, D. Chou, M. Cromwell, H. J. Krause, H. C. Mahler, B. K. Meyer, L. Narhi, D. P. Nesta, and T. Spitznagel. 2010. An industry perspective on the monitoring of subvisible particles as a quality attribute for protein therapeutics. Journal of pharmaceutical sciences 99:3302-3321.

162. Andersen, C. B., M. Manno, C. Rischel, M. Thorolfsson, and V. Martorana. 2010. Aggregation of a multidomain protein: a coagulation mechanism governs aggregation of a model IgG1 antibody under weak thermal stress. Protein science : a publication of the Protein Society 19:279-290.

163. Kumru, O. S., J. Liu, J. A. Ji, W. Cheng, Y. J. Wang, T. Wang, S. B. Joshi, C. R. Middaugh, and D. B. Volkin. 2012. Compatibility, physical stability, and characterization of an IgG4 monoclonal antibody after dilution into different intravenous administration bags. Journal of pharmaceutical sciences 101:3636-3650.

164. Kiese, S., A. Papppenberger, W. Friess, and H. C. Mahler. 2008. Shaken, not stirred: mechanical stress testing of an IgG1 antibody. Journal of pharmaceutical sciences 97:4347-4366.

165. Kamerzell, T. J., R. Esfandiary, S. B. Joshi, C. R. Middaugh, and D. B. Volkin. 2011. Protein–excipient interactions: Mechanisms and biophysical characterization applied to protein formulation development. Advanced drug delivery reviews 63:1118-1159.

166. Khan, T. A., H.-C. Mahler, and R. S. Kishore. 2015. Key interactions of surfactants intherapeutic proteinformulations: A review. European Journal of Pharmaceutics and Biopharmaceutics.

167. Lee, H. J., A. McAuley, K. F. Schilke, and J. McGuire. 2011. Molecular origins of surfactant-mediated stabilization of protein drugs. Advanced drug delivery reviews 63:1160-1171.

168. Kerwin, B. A. 2008. Polysorbates 20 and 80 used in the formulation of protein biotherapeutics: structure and degradation pathways. Journal of pharmaceutical sciences 97:2924-2935.

169. Liu, L., W. Qi, D. K. Schwartz, T. W. Randolph, and J. F. Carpenter. 2013. The effects of excipients on protein aggregation during agitation: an interfacial shear rheology study. Journal of pharmaceutical sciences 102:2460-2470.

213

170.   Graham, D., and M. Phillips. 1979. Proteins at liquid interfaces: I. Kinetics of adsorption and surface denaturation. Journal of colloid and interface science 70:403-414.

171.   Razavi, S., K. D. Cao, B. Lin, K. Y. C. Lee, R. S. Tu, and I. Kretzschmar. 2015. Collapse of Particle-Laden Interfaces under Compression: Buckling vs Particle Expulsion. Langmuir : the ACS journal of surfaces and colloids 31:7764-7775.

172.   Pocivavsek, L., R. Dellsy, A. Kern, S. Johnson, B. Lin, K. Y. C. Lee, and E. Cerda. 2008. Stress and fold localization in thin elastic membranes. Science 320:912-916.

173.   Esue, O., A. X. Xie, T. J. Kamerzell, and T. W. Patapoff. 2013. Thermodynamic and structural characterization of an antibody gel. In mAbs. Taylor & Francis. 323-334.

174.   Rajagopalan, R., and P. C. Hiemenz. 1997. Principles of colloid and surface chemistry. Marcel Dekker, New-York, 3e édition, ISBN 0 8247:8.

175.   Chen, B., R. Bautista, K. Yu, G. A. Zapata, M. G. Mulkerrin, and S. M. Chamow. 2003. Influence of histidine on the stability and physical properties of a fully human antibody in aqueous and solid forms. Pharmaceutical research 20:1952-1960.

176.   Katdare, A., and M. Chaubal. 2006. Excipient development for pharmaceutical, biotechnology, and drug delivery systems. CRC Press.

177.   Salinas, B. A., H. A. Sathish, S. M. Bishop, N. Harn, J. F. Carpenter, and T. W. Randolph. 2010. Understanding and modulating opalescence and viscosity in a monoclonal antibody formulation. Journal of pharmaceutical sciences 99:82-93.

178.   Mahler, H. C., F. Senner, K. Maeder, and R. Mueller. 2009. Surface activity of a monoclonal antibody. Journal of pharmaceutical sciences 98:4525-4533.

179.   Serno, T., J. F. Carpenter, T. W. Randolph, and G. Winter. 2010. Inhibition of agitation-induced aggregation of an IgG-antibody by hydroxypropyl-β-cyclodextrin. Journal of pharmaceutical sciences 99:1193-1206.

180.   Banks, D. D., J. Zhang, and C. C. Siska. 2014. Relationship between Native-State Solubility and Non-Native Aggregation of Recombinant Human Granulocyte Colony Stimulating Factor: Practical Implications for Protein Therapeutic Development. Molecular pharmaceutics 11:3431-3442.

181.   Middaugh, C. R., W. A. Tisel, R. N. Haire, and A. Rosenberg. 1979. Determination of the apparent thermodynamic activities of saturated protein solutions. The Journal of biological chemistry 254:367-370.

182.   Gibson, T. J., K. McCarty, I. J. McFadyen, E. Cash, P. Dalmonte, K. D. Hinds, A. A. Dinerman, J. C. Alvarez, and D. B. Volkin. 2011. Application of a high-throughput screening procedure with PEG-induced precipitation to compare relative protein solubility during formulation development with IgG1 monoclonal antibodies. Journal of pharmaceutical sciences 100:1009-1021.

183.   Ghazvini, S., C. Kalonia, D. Volkin, and P. Dhar. 2015. Evaluating the Role of the Air-Solution Interface on the Mechanism of Subvisible Particle Formation Caused by Mechanical Agitation for an IgG1 mAb. Journal of pharmaceutical sciences Submitted.

184.   Schuck, P. 2000. Size-distribution analysis of macromolecules by sedimentation velocity ultracentrifugation and lamm equation modeling. Biophysical journal 78:1606-1619.

185.   DeLano, W. L., and J. W. Lam. 2005. PyMOL: A communications tool for computational models. Abstr Pap Am Chem S 230:U1371-U1372.

186.   Padlan, E. A. 1994. Anatomy of the Antibody Molecule. Mol Immunol 31:169-217.

187. Sali, A., and T. L. Blundell. 1993. Comparative Protein Modeling by Satisfaction of Spatial Restraints. Journal of molecular biology 234:779-815.

188. Matsumiya, S., Y. Yamaguchi, J. Saito, M. Nagano, H. Sasakawa, S. Otaki, M. Satoh, K. Shitara, and K. Kato. 2007. Structural comparison of fucosylated and nonfucosylated Fc fragments of human immunoglobulin G1. Journal of molecular biology 368:767-779.

189. Olsson, M. H. M., C. R. Sondergaard, M. Rostkowski, and J. H. Jensen. 2011. PROPKA3: Consistent Treatment of Internal and Surface Residues in Empirical pK(a) Predictions. J Chem Theory Comput 7:525-537.

190. Li, H., A. D. Robertson, and J. H. Jensen. 2005. Very fast empirical prediction and rationalization of protein pK(a) values. Proteins 61:704-721.

191. Mahadevan, H., and C. K. Hall. 1990. Statistical-Mechanical Model of Protein Precipitation by Nonionic Polymer. Aiche J 36:1517-1528.

192. Asakura, S., and F. Oosawa. 1954. On Interaction between 2 Bodies Immersed in a Solution of Macromolecules. Journal of Chemical Physics 22:1255-1256.

193. Asakura, S., and F. Oosawa. 1958. Interaction between Particles Suspended in Solutions of Macromolecules. J Polym Sci 33:183-192.

194. Sarangapani, P. S., S. D. Hudson, R. L. Jones, J. F. Douglas, and J. A. Pathak. 2015. Critical Examination of the Colloidal Particle Model of Globular Proteins. Biophysical journal 108:724-737.

195. Dumetz, A. C., A. M. Snellinger-O'Brien, E. W. Kaler, and A. M. Lenhoff. 2007. Patterns of protein - protein interactions in salt solutions and implications for protein crystallization. Protein Science 16:1867-1877.

196. Neal, B. L., D. Asthagiri, and A. M. Lenhoff. 1998. Molecular origins of osmotic second virial coefficients of proteins. Biophysical journal 75:2469-2477.

197. Roberts, C. J., and M. A. Blanco. 2014. Role of Anisotropic Interactions for Proteins and Patchy Nanoparticles. Journal of Physical Chemistry B 118:12599-12611.